UNIVERSIDAD COMPLUTENSE DE MADRID

FACULTAD DE CIENCIAS QUÍMICAS

Departamento de Química Inorgánica

TESIS DOCTORAL

Synthesis, structures and magnetic properties of Mn_2MsbO_6 (M=Cr, Fe and R-Rare earth) high pressure polymorphs

Síntesis, estructuras y propiedades magnéticas de los polimorfos de alta presión de Mn_2MsbO_6 (M=Cr, Fe y R-Tierra rara)

MEMORIA PARA OPTAR AL GRADO DE DOCTOR

PRESENTADA POR

Elena Solana Madruga

Directores

Regino Sáez Puche
Antonio J. Dos Santos García

Madrid, 2017

Synthesis, structures and magnetic properties of Mn_2MSbO_6 (M = Cr, Fe and R-Rare earth) high pressure polymorphs

---

Síntesis, estructuras y propiedades magnéticas de los polimorfos de alta presión de Mn_2MSbO_6 (M = Cr, Fe y R-Tierra rara)

Elena Solana Madruga

Universidad Complutense de Madrid

Facultad de Ciencias Químicas

Departamento de Química Inorgánica

Dirigida por:

Prof. Regino Sáez Puche

Dr. Antonio J. Dos Santos García

Synthesis, structures and magnetic properties of Mn_2MSbO_6 (M = Cr, Fe and R-Rare earth) high pressure polymorphs

---

Síntesis, estructuras y propiedades magnéticas de los polimorfos de alta presión de Mn_2MSbO_6 (M = Cr, Fe y R-Tierra rara)

Elena Solana Madruga

Memoria presentada para optar al grado de Doctor en Ciencias Químicas

Universidad Complutense de Madrid
Facultad de Ciencias Químicas
Departamento de Química Inorgánica

Dirigida por:

Prof. Regino Sáez Puche

Dr. Antonio J. Dos Santos García

Agradecimientos

En primer lugar quisiera agradecer a los directores de esta tesis su constante interés y su dedicación en la supervisión de todas las fases del proceso. Ambos han sabido transmitirme, de principio a fin, la pasión que sienten por la ciencia. Una pasión que no he podido evitar heredar y que espero ser capaz de transmitir algún día con la mitad de la facilidad y el cariño que ellos me han mostrado.

Un aspecto sin duda relevante en ámbito de la investigación es la financiación. Por ello, no podría comenzar a redactar esta tesis de otra forma que no fuera mostrando mi agradecimiento a los órganos responsables de la financiación de los proyectos que la sustentan. No debe faltar, por ello, referencia a la Comunidad de Madrid y al Ministerio de Economía Industria y Competitividad, que han apoyado durante estos años la investigación en que se enmarca esta tesis doctoral a través de los proyectos S-2013/MIT-12753 y MAT2013-44964-R.

Así mismo, esta tesis no habría sido posible sin la inestimable colaboración del Profesor J.P. Attfield, que me acogió durante unos meses en su grupo de investigación en CSEC, University of Edinburgh, poniendo sus medios y su consejo a mi disposición.

Por supuesto debo mencionar también otras instituciones que han permitido el desarrollo de medidas realmente importantes para la culminación de esta tesis, entre las que destacan los centros de difracción de radiación sincrotrón, ALBA-Lightsource, y de neutrones, Institut Laue-Langevin, que siempre han sido generosos con el tiempo de haz solicitado. En especial quiero agradecer su apoyo al Dr. C. Ritter, que no sólo ha representado a la perfección su papel de contacto local sino que ha mostrado el interés y la paciencia necesarios para asesorarme en la interpretación de las medidas.

De la misma forma, muestro mi máximo reconocimiento al Dr. Á. Arévalo López, que ha tenido una parte realmente importante en mi evolución profesional, por la que tanto tanto le debo.

En el ámbito profesional cotidiano no podría olvidarme del Dr. J. M. Gallardo Amores, al que mucho más allá de las lecciones sobre alta presión le debo los consejos sin filtro. Al Dr. J. Romero de Paz, por no limitarse a la realización de las medidas sino por haberme aconsejado en lo que consideró necesario. A los compañeros de fatigas, con los que he compartido momentos tanto de desesperación como de distensión. Tampoco podría faltar aquí el Profesor L. C. Díaz Otero, que día tras día ha generado tensiones y distensiones con sus míticos consejos y al que tanto respeto y admiro.

En un ámbito más personal, le debo mi mayor agradecimiento a mi familia. En primer lugar, por supuesto, a mis padres, que han dado lo mejor de sí mismos cada día durante tantos años para que yo haya podido llegar hasta aquí. Merecen especial mención mis abuelos, que me han enseñado las cosas más importantes que jamás haya aprendido. A mis hermanos, por seguir al pie del cañón cuando es necesario. No podría haber acabado hoy esta etapa sin el soporte informático-fenicio de Jorge ni el insomnio de Blanca. A Quique, por aguantarme cada día desde hace ocho años aún teniendo la posibilidad de huir. Gracias por el constante apoyo.

Y por último, pero no menos importante, a los amigos. A Iris, por asegurarse de mantenerme con vida hasta el fin de mi tesis. A Víctor, por su incontable ayuda gramatical. A Ana y a Márquez, por seguir siendo los mejores anfitriones, mejores incluso en la distancia. A Amalia, a Sandra y a Andrés, por seguir siendo capaces de mantener, cada uno desde su sitio y a su manera, la gran amistad que une. Y a todas las personas que se olvidan en el tintero por cuestiones logísticas (mis niñas de la parro, mis chicas de Boadilla…y por supuesto María, siempre ahí) pero que de un modo u otro han contribuido a mi persona y a mi ciencia.

Apunta siempre a la luna y quizá así alcanzarás a dar a la campana.

(A la memoria de Sor Consuelo, por el primer empujón hacia la química).

Outline

Summary ····1

Resumen ····3

I.- Introduction

1.- Interest and background ····6

1.1 - Perovskite structure ···· 8

1.1.1 - General overview···· 8

Geometric distortions in perovskites····8

Cation ordering in perovskites····9

- $A_2BB'O_6$ double perovskites ····9

- $AA'B_2O_6$ double perovskites ····11

- $AA'BB'O_6$ double-double perovskites····12

1.1.2 - Extrinsic factors: High Pressure and/or High Temperature conditions in perovskites ····13

1.2 - Corundum derivatives····15

1.2.1 - Ilmenite and Lithium niobate polymorphs····15

1.2.2 - Ni_3TeO_6 - type structure····16

1.2.3 - Extrinsic factors: High Pressure and/or High Temperature conditions in corundum derivatives····18

1.3 - Site exchanging substitutions inducing mixed-charged A sites ····19

2.- Aims of this work ····21

3.- Bibliography ····23

II.- Experimental techniques

1.- Sample preparation ····34

1.1 - Ceramic method ····34

1.2 - High pressure synthesis····34

1.2.1 - One - stage devices ····36

1.2.2 - Multi-anvil device ····38

2. - Structural characterisation ····40
2.1 - Diffraction techniques. General overview ····40
2.1.1 - X-ray diffraction ····42
2.1.2 - Neutron Diffraction ····44
2.1.3 - Electron diffraction and electron microscopy experiments ····46
3. - Magnetic characterisation ····47
4.-Bibliography ···· 48

III.- Results and discussion
Mn_2MSbO_6 with M = d^n transition metals

1.-General introduction ····52
2.-Mn_2CrSbO_6 ···· 53
2.1- Double perovskite ····53
2.1.1 - Synthesis and structural characterisation ····53
2.1.2 - Magnetic behaviour ····58
2.1.3 - Thermal stability···· 61
2.2- Ilmenite ···· 63
2.2.1 - Synthesis and structural characterisation ····63
2.2.2 - Magnetic behaviour ····67
3.-Mn_2FeSbO_6 ···· 72
3.1- Double perovskite ····72
3.1.1 - Synthesis and structural characterisation ····72
3.1.2 - Magnetic behaviour ····73
3.1.3 - Electric behaviour ····79
3.1.4 - Thermal stability···· 81
3.2- Ilmenite ···· 82
3.2.1 - Synthesis and structural characterisation ····82
3.2.2 - Magnetic behaviour ····84
4.-Bibliography ···· 91

IV.- Results and discussion
Mn_2MSbO_6 with M = d^0 transition metals

1.-General introduction ····· 98
2.-NTO_Mn_2ScSbO_6 ····· 102
2.1. - Synthesis and structural characterisation ····· 102
2.2. - Magnetic behaviour ····· 109
2.3. - Electric behaviour ····· 113
3.-DPv_Mn_2ScSbO_6 ····· 114
3.1. - Synthesis and structural characterisation ····· 114
3.2. - Magnetic behaviour ····· 116
3.3. - Thermal stability ····· 119
4.-Bibliography ····· 121

V.- Results and discussion
Mn_2MSbO_6 with M = f^n transition metals

1.-General introduction ····· 124
2.-Room pressure:
$(Mn_{0.66}R_{1.34})(Mn_{0.66}Sb_{1.34})O_7$ pyrochlores ····· 125
2.1. - Synthesis and structural characterisation ····· 125
2.2. - Magnetic behaviour ····· 131
2.3. - Thermal stability ····· 140
3.-High pressure:
$MnRMnSbO_6$ double perovskites ····· 142
2.1. - Synthesis and structural characterisation ····· 142
2.2. - Magnetic behaviour ····· 157
4.-Bibliography ····· 172

VI- Conclusions ····· 175

Appendix I- Determination of tilt angles in DPv and DDPv polymorphs 179

Appendix II- Magnetic interactions in ordered corundum derivatives 185

Appendix III- Publications arising from this thesis 193

1) Magnetic and crystal structure determination of Mn_2FeSbO_6 double perovskite. Journal of Physics: Condensed Mater, 2013, 25, 206004.

2) Synthesis, structures and magnetic properties of the dimorphic Mn_2CrSbO_6 oxide. Dalton transactions, 2015, 44, 10665.

3) High pressure synthesis of polar and non-polar cation-ordered polymorphs of Mn_2ScSbO_6. Dalton transactions, 2015, 44, 20441.

4) Double Double Cation Order in the High-Pressure Perovskites $MnRMnSbO_6$. Angewandte Chemie International Edition 2016, 55, 9340

The most widely studied family of functional materials is that of perovskites, with ABO_3 stoichiometry. Recently, rock-salt ordered $A_2BB'O_6$ double perovskites and more complex $AA'BB'O_6$ compounds have shown the coexistence of two ferroic orders. Despite their similar chemical formula, ABO_3 and $A_2BB'O_6$ ordered corundum derivative structures have been lees explored, though they can achieve not only ferroelectricity but also multiferroicity. High pressure can induce phase transitions from the corundum derivatives to the denser perovskite structure, thus relating two phases with potential functional interest.

In this context, this study aims the synthesis and structural characterisation of Mn_2MSbO_6 (M = Cr, Fe and R - rare earth) oxides, along with the determination of their structure-properties relationship.

Synthesis considerations.

The synthesis of these oxides at moderate pressures (~ 3-5.5 GPa) yields the formation of ordered corundum derivatives, e.g. ilmenite-type (ILO, $R\bar{3}$) or Ni_3TeO_6-type (NTO, $R3$) structures. Otherwise, the use of higher pressures (~ 7-12 GPa) induces the crystallisation of Mn_2MSbO_6 with a B-site rock-salt ordered double perovskite (DPv, $P2_1/n$) structure. It is worth noting the special case observed in the synthesis of Mn_2RSbO_6 compounds:

i) at room pressure, these oxides crystallise with a pyrochlore $A_2B_2O_7$ structure with an uncommon cationic stoichiometry ($Mn_{0.66}R_{1.34}Mn_{0.66}Sb_{1.34}O_7$).

ii) when synthesised under high pressure, the largest R^{3+} cations (La, Pr, Nd and Sm) stabilise a novel perovskite derivative that combines the simultaneous order of A/A' and B/B' cations into a so-called double double perovskite (DDPv, $P4_2/n$) structure. This $MnRMnSbO_6$ is the first example of a perovskite showing a rock-salted motif among B (Mn^{2+}) and B' (Sb^{5+}) cations and a columnar arrangement of A (Mn^{2+}) and A' (R^{3+}) cations. This DDPv structure is notable for having five different cation sites, three of them occupied by Mn^{2+} in tetrahedral, square planar and octahedral environments. Compositional substitutions by smaller R-cations lead to conventional monoclinic DPv $(MnR)MnSbO_6$. Among them, R = Eu and Gd modifications are studied in this work, where Mn^{2+} and R^{3+} are disordered over the A sites while Mn^{2+} and Sb^{5+} are rock salt ordered at the B sites.

An important conclusion from this experimental work is that the crystallisation of Mn_2MSbO_6 into different ordered corundum derivatives can be controlled. The gradual size enlargement of M^{3+} cations has been found to induce increasing exchange proportions among A- and B-site cations. This process yields the crystallisation of ILO polymorphs for Mn_2MSbO_6 (M = Cr and Fe) and an NTO-structure for Mn_2ScSbO_6 (better formulated as $MnScMnSbO_6$). Details of the structural characterisation for Mn_2MSbO_6 compounds with M = $3d^n$ (Cr^{3+}, Fe^{3+}), $3d^0$ (Sc^{3+}) and $4f^n$ (R^{3+}) are discussed along chapters III, IV and V respectively.

Structure-magnetic properties relationship.

Exploring the corundum structure, there are octahedral-site cations sharing edges within a (00z) layer (A) and faces (B) along the *c*-axis. Therefore, up to three different superexchange magnetic interactions operate in these ordered-corundum polymorphs: 90º A-O-A (edge-sharing), 90º A-O-B (face-sharing) and 90º B-O-B. On the other hand, direct A-B, A-A and B-B interactions can compete with the superexchange mechanism. ILO-Mn_2FeSbO_6 and ILO-Mn_2CrSbO_6 have antiferromagnetic (AFM) couplings between the ferromagnetic (FM) Mn^{2+} and M^{3+} sublattices below T_N=260 K and 60 K respectively. The presence of two extra electrons

in the e_g-orbitals of Fe^{3+} *vs.* Cr^{3+} strengthens the Mn-M (A-B) interactions, which results in the increase of T_N. However, the presence of a number of magnetic interactions different in sign and strength induces a strong magnetic frustration upon cooling, giving rise to complex helical magnetic structures at low temperatures. That of Mn_2CrSbO_6 is notable for showing a strong temperature dependence of its incommensurate propagation vector. On the other hand, the diamagnetic character of the Sc^{3+} ($3d^0$) cation into the NTO-Mn_2ScSbO_6 compound suppresses the frustration observed in the ILO polymorphs, thus stabilising an AFM structure. Unexpectedly, the large site-selective antisite exchange of Sc with one of the Mn positions acts as an unconventional origin of a net FM component.

Magnetic interactions in DPv structures are usually governed by the 180º B-O-B' superexchage interactions, but the diamagnetic character of the Sb^{5+} (B') cations prevents this coupling. As a consequence, Mn-O-M (A-O-B) are the strongest interactions in Mn_2MSbO_6 DPv. The electronic configuration of the M^{3+} cation and the <Mn-O-M> angle will determine the strength and sign of these interactions. AFM behaviours are observed for M = Sc^{3+}, Cr^{3+} and Fe^{3+}, but the increase in the number of electrons in M = Fe^{3+} induces the frustration between magnetic interactions of equivalent strength but opposed in sign, thus originating an elliptical helix magnetic structure at low temperatures.

The magnetic behaviour of the DPv and DDPv $MnRMnSbO_6$ polymorphs is rather complex due to both the emergence of 4f-3d magnetic interactions and the presence of magnetic anisotropy introduced by the rare earth elements. The negative Weiss temperature shows that AFM interactions are dominant in these perovskites. The DDPv phases with magnetic R^{3+} cations show consecutive magnetic transitions, in general arising from the independent magnetic order of Mn^{2+} and R^{3+} sublattices. Moreover, the strongest rare earth anisotropy has been found to induce the spin-reorientation of the Mn^{2+} sublattice in $MnNdMnSbO_6$.

Powder neutron diffraction data were used to explore the low temperature magnetic orderings in all these Mn_2MSbO_6 compounds.

Finally, the magnetic behaviour of $Mn_{0.66}R_{1.34}Mn_{0.66}Sb_{1.34}O_7$ compounds is governed by the AFM ordering of the spins in a pyrochlore structure. It induces a magnetic frustration that ends in a glassy behaviour. The analysis of the entropy variation (ΔS_T) through this magnetic transition shows a large magnetocaloric effect, as high as $|\Delta S_T| \sim 20.7$ J/kgK at 8 K for a magnetic field increment $\Delta H = 9T$ in the R = Gd compound.

The relation between the structural and magnetic evolution of the Mn_2MSbO_6 family is detailed along this work, providing the basis for the development of new perovskite and corundum ordered derivatives in the search for new functional materials.

Los compuestos con estructura tipo perovskita, de fórmula general ABO_3 y sus polimorfos ordenados ($AA'BB'O_6$) han sido ampliamente estudiados debido a que pueden presentar coexistencia de dos o más órdenes ferroicos. Sin embargo, los compuestos con estructuras derivadas del corindón han suscitado un menor interés a pesar de poseer la misma estequiometría ABO_3/ $A_2BB'O_6$ y similar potencial como materiales multiferroicos. Además, la utilización de altas presiones permite inducir transformaciones de fase entre estos polimorfos.

En este contexto, el principal objetivo de este trabajo es la síntesis, caracterización estructural y determinación de la relación estructura-propiedades en los óxidos Mn_2MSbO_6 (M = Cr, Fe Sc y R-tierra rara-).

Síntesis de los compuestos Mn_2MSbO_6.

La síntesis de estos óxidos a presiones moderadas (~ 3-5.5 GPa) conduce a la formación de compuestos con estructuras derivadas del corindón con distinto orden catiónico: ilmenita (ILO, $R\bar{3}$) o tipo-Ni_3TeO_6 (NTO, $R3$). El empleo de presiones más elevadas (~ 7-12 GPa) produce la estabilización de estructuras más compactas, como la perovskita, en la que Sb y M adoptan un orden tipo-NaCl originando una doble perovskita (DPv, $P2_1/n$). Entre estos compuestos, conviene puntualizar el particular caso de Mn_2RSbO_6:

i) su síntesis en condiciones de presión ambiente, origina la formación de estructuras tipo-pirocloro con la inesperada estequiometria $Mn_{0.66}R_{1.34}Mn_{0.66}Sb_{1.34}O_7$.

ii) la síntesis a alta presión de los compuestos Mn_2RSbO_6 con R= La, Pr, Nd y Sm produce la formación de un nuevo tipo de perovskita, que combina orden catiónico en ambas posiciones (A y B) en una doble-doble-perovskita (DDPv, $P4_2/n$) cuya formulación más adecuada es $MnRMnSbO_6$. Esta nueva estructura, nunca observada antes en estos compuestos, presenta orden tipo-NaCl en las posiciones B entre los cationes Mn^{2+} y Sb^{5+} y orden columnar entre Mn^{2+} y R^{3+} en las posiciones A. Es destacable que esta DDPv presenta cinco posiciones catiónicas en sitios cristalográficos independientes, tres de ellos ocupados por Mn^{2+} en coordinación tetraédrica, planocuadrada y octaédrica. La sustitución de R por tierras raras de menor tamaño (R^{3+} = Gd y Eu) conduce a la formación de DPv convencionales, $(MnR)MnSbO_6$, donde Mn^{2+} y R^{3+}se encuentran desordenados en la posición A y Mn^{2+} y Sb^{5+} mantienen el orden tipo-NaCl en las posiciones B.

A partir de los resultados obtenidos se puede concluir que es posible controlar el tipo estructural de los compuestos Mn_2MSbO_6 atendiendo a las condiciones de síntesis y al tamaño del catión M. El progresivo incremento de tamaño de los cationes M^{3+} induce una creciente proporción de intercambio catiónico entre las posiciones A y B de estos óxidos, produciendo la cristalización de Mn_2MSbO_6 con estructuras tipo ilmenita (M = Cr y Fe) y tipo-NTO (M = Sc, mejor formulado como $MnScMnSbO_6$). Los detalles de la síntesis y caracterización estructural de los compuestos Mn_2MSbO_6 con M = $3d^n$ (Cr^{3+}, Fe^{3+}), $3d^0$ (Sc^{3+}) y $4f^n$ (R^{3+}) se describe en los capítulos III, IV y V respectivamente.

Relación estructura-propiedades magnéticas

Una descripción sencilla de la estructura tipo-corindón permite diferenciar octaedros que comparten aristas con otros situados en la misma capa (00z) (A) y una cara con un octaedro de distinta capa (B) a lo largo del eje *c*. Como consecuencia de esta eleva conectividad, los polimorfos ordenados derivados de esta estructura presentan tres tipos de interacciones magnéticas de superintercambio a través de oxígeno: 90º A-O-A y 90º B-O-B (ambas a través

de arista) y 90º A-O-B (compartiendo cara). Además, estas interacciones compiten con las interacciones directas A-B, A-A y B-B. Los compuestos ILO-Mn_2FeSbO_6 y ILO-Mn_2CrSbO_6 presentan el acoplamiento antiferromagnético (AFM) de las subredes ferromagnéticas (FM) Mn^{2+} y M^{3+} por debajo de T_N = 260 K y 60 K respectivamente. La diferencia existente entre sus T_N es debida a que el Fe^{3+} posee 2 electrones desapareados en los orbitales e_g que aumenta la intensidad de las interacciones Mn-Fe. Sin embargo, la coexistencia de varios tipos de interacciones magnéticas que difieren en signo y magnitud, produce una frustración magnética que da lugar a estructuras magnéticas inconmensurables a baja temperatura. El caso del compuesto ILO_Mn_2CrSbO_6 es especialmente relevante, ya que el vector de propagación presenta una fuerte dependencia con la temperatura. Por otra parte, la presencia del catión diamagnético Sc^{3+} ($3d^0$) en el NTO_Mn_2ScSbO_6 suprime la frustración observada en las ilmenitas. En su lugar, estabiliza un orden AFM entre los espines de Mn^{2+}, con una débil componente ferromagnética originada como consecuencia del desorden selectivo entre dos cationes de las posiciones A y B.

Las principales interacciones magnéticas en los polimorfos tipo DPv son de superintercambio a 180º B-O-B'. Sin embargo, debido al carácter diamagnético del Sb^{5+} (B'), las interacciones Mn-O-M (A-O-B) cobran mayor importancia en Mn_2MSbO_6. La naturaleza e intensidad de esta interacción vendrá determinada por la configuración electrónica del catión M^{3+} y por el ángulo de esta interacción. Se ha observado un comportamiento AFM en las perovskitas Mn_2MSbO_6 con M = Sc, Cr y Fe, si bien es destacable que Mn_2FeSbO_6 presenta una estructura magnética helicoidal inconmensurable a baja temperatura.

El comportamiento magnético de los polimorfos DPv y DDPv_$MnRMnSbO_6$ presenta una alta complejidad debido a la anistropía magnética asociada a la tierra rara y a la presencia de interacciones 4f-3d. Todos ellos presentan una temperatura de Weiss negativa, lo que indica la predominancia de interacciones AFM. En términos generales, las DDPv que contienen cationes R^{3+} paramagnéticos presentan dos transiciones magnéticas debido al orden independiente de las subredes de Mn^{2+} y R^{3+}. Además, se ha observado la reorientación de los spines de Mn^{2+} inducida por la fuerte anistropía de R en $MnNdMnSbO_6$.

Las estructuras magnéticas de todos los compuestos han sido determinadas por difracción de neutrones a baja temperatura.

El comportamiento magnético de los compuestos $Mn_{0.66}R_{1.34}Mn_{0.66}Sb_{1.34}O_7$ está gobernado por el orden AFM de los espines dentro de la estructura pirocloro. Esto produce una frustración magnética que origina un comportamiento tipo vidrio de espín. La variación de entropía (ΔS_T) producida en esta transición toma el valor de $|\Delta S_T| \sim 20.7$ J/kg K a 8 K, para un incremento de campo magnético ΔB = 9T para R=Gd, que puede considerarse como un efecto magnetocalórico elevado.

La determinación de la relación entre las evoluciones estructural y magnética de la familia de compuestos Mn_2MSbO_6, detallada a lo largo de esta tesis, permitirá desarrollar nuevos materiales de interés funcional con estructuras derivadas de las tipo-perovskita y –corindón.

I. Introduction

1.- Interest and background

The structural and functional versatility of ABO_3 oxides make them interesting not only from the fundamental point of view but also for their potential applications. Regarding the fundamental aspects, the question to be answered is which structure will adopt a given chemical composition under different pressure (*P*) and temperature (*T*) conditions. On the other hand, their potential applications will be governed by their structure-properties relationship. A wide variety of structures are known for ABO_3 compounds, arising from both different anionic packings and different arrangements of the cations to occupy the interstices between anionic layers. However, predicting the resulting structure for a given ABO_3 composition is not a trivial topic as a number of factors including lattice energy (Coulombic contribution), crystal-field energy (electronic contribution) and geometric packing effects (steric contribution) affect the coordination number and/or the nature of M – O bonds [1]. The ionicity / covalency of these bonds is decisive on the lattice and crystal field stabilisation energies and the geometric effects stabilising the structure. Moreover, not only compositional but also external variables, such as synthesis conditions (*P*, *T* and time), must be taken into account, what adds kinetic considerations to thermodynamics.

The consequently high complexity has motivated several approaches to develop a good method for predicting the structure of ABO_3 compounds [1–6]). These are based on general empirical rules that allow one to predict the structure in ionic, or predominantly so, compounds. The most commonly accepted criterion was put forward by V. M Goldschmidt (1926), who noticed that the cell dimensions of a perovskite (Pv) structure can be determined from the framework of linked BO_6 octahedra and the size of the A - site cation, which occupy the cuboctahedral void. The ideal relation between the radii of A - and B - site cations and the anions (X) is defined in equation *Eq. 1*:

$$r_A + r_X = \sqrt{2}(r_B + r_X) \quad Eq.\ 1$$

In the general ABO_3 case, X is oxygen, B is the 6-fold coordinated cation and A is the large cation, which for the ideal perovskite structure adopts a 12-fold coordination. Since their ionic radii are dependent on their charge and coordination environment, *Eq. 1* is usually corrected by including the so-called "tolerance factor" (*t*), to allow a certain tolerance of fit, so that the modified ionic relation is expressed as in equation *Eq. 2*:

$$r_A + r_X = t\sqrt{2}(r_B + r_X) \quad Eq.\ 2$$

Therefore, *t*, which is close to unity, will change with the chemical composition, thus providing a certain control on the manipulation of the structure which will be stabilised. The main ABO_3 structural types are summarised in Figure 1.1 attending to their *t*-values. The ideal cubic Pv structure is only found if *t* is very close to unity while other distorted Pv occur for $0.75 < t < 1$. When $t > 1$, AO_3 layers are hexagonal close-packed and BO_6 octahedra share faces along the hexagonal *c*-axis. If *t* is lower than 0.75 different structures appear, generally corundum (α-Al_2O_3) and its ordered derivatives (e.g. ilmenite-, $LiNbO_3$- or Ni_3TeO_6-type) or, exceptionally, bixbyite-type (α-Mn_2O_3) when the A-site cation is rather small. Other examples of ABO_3 structures are the Rh_2O_3-II and $CaIrO_3$-type, renamed as post-perovskite since experimental evidences showed that $MgSiO_3$ perovskite [7] transforms into a new high-pressure layered form with $CaIrO_3$-type structure. In general terms, high pressure

overcomes steric atomic interactions and can induce phase transformations into denser structures [8,9]. For instance, corundum transforms into the Rh_2O_3-II structure [10] and then to post-Pv at higher pressure[11]. The cubic bixbyite α-Mn_2O_3 transforms into an unquenchable post-Pv structure above 28 GPa [12,13], but high pressure-high temperature (HPHT) synthesis also allows the isolation of different polymorphs with corundum- and distorted Pv-type structures at 15 GPa and ~ 18 GPa respectively [14]. On the other hand, subsequent phase transitions are reported for the corundum-type Fe_2O_3 to Pv and post-Pv structures [15]. $ScVO_3$ bixbyite irreversibly transforms into Pv [16] and the non-polar $MnTiO_3$ ilmenite phase adopts an acentric $LiNbO_3$-type structure at moderate pressures and a Pv one at higher pressures [17,18].

The polymorphism observed in ABO_3 ternary compounds can also be extended to quaternary $A_2BB'O_6$ or $AA'B_2O_6$ oxides. In fact, there are plenty of examples in the literature for chemically controlled structural transitions, where the progressive substitution of a cation in the structure by another one induces structural variations and distortions [19,20] which can evolve towards the stabilisation of an ordered derivative of the parent structure [21,22] or to a different structural-type [23]. The charge and size mismatch between those exchanging cations is the most important factor determining the long range ordering in compounds which maintain the same structural type [24]. However, synthesis conditions, oxidation state stability or cation bonding preferences can also affect the degree of ordering [25,26]. Hence, not only different polymorphs of the same compound but also isostructural compounds may present completely different properties as a result of their compositional substitution.

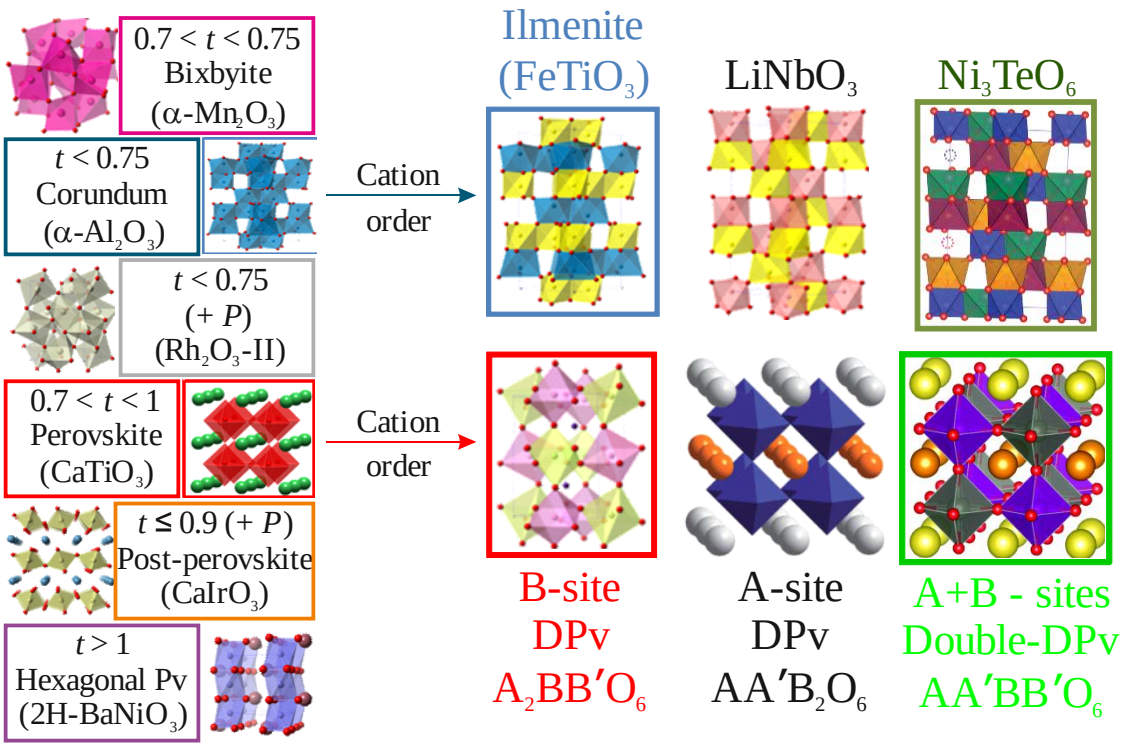

Fig 1.1 Schematised polymorphism in ABO_3 oxides classified in terms of the tolerance factor (t). ($+P$) included in Rh_2O_3 – II and post-Pv polymorphs indicates the requirement of high pressure synthesis. The main perovskite and corundum ordered derivatives are included in the right-hand side. Coloured titles indicate the structures studied in this work.

In the next sections, the crystal structures of the compounds synthesised during this work are described. The structural derivatives arising from cation ordering phase transformations are also investigated. The most extended example of ordering in quaternary compounds belongs to the perovskite family [27,28]. Upon going from the ternary ABO_3 Pv to the quaternary $A_2BB'O_6$ or $AA'B_2O_6$ oxides, B- or A-site orderings can be expected as a function of the cation size and charge mismatch between B/B' and A/A' pairs respectively. The different A- and B-site cation orderings could be further combined by introducing two aliovalent A-site cations in an already B-site ordered structure, i.e. $AA'BB'O_6$.

Regarding the Mn_2MSbO_6 general composition studied along this work, it is worth noting that high pressure conditions are often needed to stabilise the small Mn^{2+} cation into the large A site of the Pv structure [29–36]. The use of moderate pressures leads to the formation of the more stable corundum ordered derivatives. In particular, quaternary oxides with the ilmenite- and Ni_3TeO_6-type structures have been isolated in this work [32,33]. The relative stability of these related structures is carefully examined and thermally induced phase transformations have been encountered from the metastable high pressure form to the most stable polymorph. A final section concerning site exchanging cation substitutions is included. By this, the pyrochlore compounds discussed in chapter V, with unusual uncompensated mixed charge in both A and B sites, are related to the main Mn_2MSbO_6 oxides starring this work.

Finally, the interest of these compounds from the materials science point of view is also discussed, establishing by that the background for the current study and setting the basis for the subsequently proposed objectives.

1.1 - Perovskite structure

1.1.1 - General overview

One of the most commonly studied ABO_3 families of compounds is that crystallising with the perovskite structure. It can be described as a cubic close packing (ccp) of oxide anions with ¼ of them substituted by A cations in an ordered manner. Oxygens are placed in the eight corners and four faces of the cubic unit cell with the A cations centring the other two faces. The B cations occupy one of the four available octahedral voids, that which is not adjacent to the A cations. Another description of the perovskite structure is a 3D framework of BO_6 octahedral units sharing corners along the three crystallographic axes originating cuboctahedral voids in between eight octahedra, which are occupied by 12-fold coordinated A cations (AO_{12}).

Geometric distortions in perovskites

The ideal perovskite structure, crystallising in the $Pm\bar{3}m$ space group, is exemplified by the mineral Tausonite $SrTiO_3$ [37]. The ideal cubic perovskite is expected to crystallise for compositions where the Golsdmidth relation favours a tolerance factor $t = 1$. However, as the A – site cation decreases in size for a constant r_B or as B is substituted for a bigger element with remaining r_A, different lengths are achieved by the corresponding B – O and A – O bonds thus giving rise to irregular BO_6 and AO_{12} polyhedra. These alterations induce a stress that destabilises the ideal structure, producing a distorted one and a further decrease of t down to the limit value of $t = 0.75$ [28]. As a consequence of this geometrically induced destabilisation, the A – site coordination number ranges from 12 down to 6

and BO_6 octahedra develop a cooperative rotation about one, two or the three crystallographic axes, commonly known as tilt. Depending on the relative octahedral rotation with respect to the adjacent polyhedra, different tilt systems can be achieved, as it was early investigated by Glazer [38], Megaw [39], Aleksandrov [40], O'Keeffe and Hyde [41,42] and lately reviewed by Woodward [43], Howard [44] and Stokes [45]. However, the standard notation most commonly used to describe octahedral tilting is that described by Glazer (1972, [38]). Concomitantly to this distortion, the crystal symmetry is reduced, giving rise to rhombohedral , hexagonal , tetragonal ($PbTiO_3$ [46]), orthorhombic ($GdFeO_3$ [47] and in fact, the perovskite mineral itself $CaTiO_3$ [48]) or monoclinic ($BiMnO_3$ [49]) derivatives.

In addition to these tilting distortions, other factors could appear, such as cooperative octahedral distortions or ionic displacements from the centre of the octahedron [50]. The first of these phenomena can be induced through shortening or elongating effects on the B – O bonds. Such effects may arise from metallic electronic configurations favouring anisotropic octahedral environments, e.g. Jahn-Teller distortions as those commonly observed for Mn^{3+} (d^4) or Cu^{2+} (d^9). A different origin for distortion is exemplified by the charge-ordered insulator $BaBiO_3$, in which bismuth atoms appear in two different oxidation states (3+ and 5+). There are two different bismuth-oxygen bond lengths: the shorter one is attributed to Bi^{5+}-O bonds and the larger one to Bi^{3+}-O bonds [51,52]. It is also worth mentioning that, upon K or Pb doping, $Ba_{1-x}M_xBiO_3$ perovskite at A and B sites respectively, it becomes superconducting [53,54]. In the case of A site, severe distortions can be induced through the insertion of cations containing lone-pair electrons, as it occurs for Pb^{2+} or Bi^{3+} cations, which induce asymmetric A – O bonds of different strengths. These cooperative distortions produce the breaking of crystallographic symmetry constrains allowing thereby spontaneous electric polarisation to occur, which provide access to new ferroelectric and multiferroic materials.

Cation ordering in perovskites

When A– or B– site cations are half substituted, different long range cationic orderings can be achieved, giving rise to a large variety of derivatives defined with the generic formulae $AA'B_2O_6$ or $A_2BB'O_6$, also known as double perovskites (DPv). In general terms, these compounds are governed by the same geometric and electronic restraints as simple ABO_3 perovskites, but the higher complexity of their structures induces the emergence of more complex properties including superconductivity, magnetoresistance, ferroelectricity, multiferroicity and thermoelectricity among others [54–58].

The main types of ordered DPv derivatives are summarised in Figure 1.2 and analysed in detail along this section:

- $A_2BB'O_6$ double perovskites: The most influent factor determining the type of B – site ordering is primarily the charge difference between B and B' cations and secondarily their size difference [24]. It is generally assumed that when the charge mismatch between B and B' cations is 0 or 1, no long range ordering exists at B site; otherwise, when the charge difference is 3 or higher, only the ordered structure is observed. There are three B-cation ordered sublattices known for double perovskites: rock-salt (RS), columnar (C) and layer (L) which are schematised in the upper part of Fig. 1.2.

The most common B-cation arrangement is the RS-type, often arising from the intermittent location of a large cation with low oxidation state and a small one with higher oxidation state, minimising by that their steric and electrostatic repulsions.

The ideal RS_DPv crystallises with a cubic $2a_p$ unit cell in the space group $Fm\bar{3}m$ in the absence of any BO_6 and $B'O_6$ octhahedral tilts. However, lower-symmetric structures reflecting octahedral tiltings normally occur. For instance, the symmetry lowers through tetragonal (e.g. $I4/m$ $Sr_2FeB'O_6$ derivatives with B' = Mo or Os [59,60]) down to monoclinic distorted ~ $\sqrt{2}$ $a_p \times \sim \sqrt{2}$ $a_p \times 2a_p$ unit cells within the $P2_1/n$ or $I2/m$ space groups. $Sr_{2-x}Ca_xFeSbO_6$ system with x = 0, 1 and 2 constitutes a good example of DPv crystallising in these space groups [61]. It is not always easy to distinguish $P2_1/n$ from $I2/m$ space groups through X-ray diffraction and the symmetry has to be confirmed by means of zone axis microdiffraction patterns [62]. Ba_2BiSbO_6 crystallises in the $R\bar{3}$ space group, with BiO_6 and SbO_6 octahedra ordered in a rock-salt configuration [63]. The ~ 97% of the reported RS_DPv crystallise within these 5 space groups [64] although there are some other few perovskites with $I4/mmm$ and $Pn\bar{3}$ symmetries, such as Ba_2CuUO_6 [65] and $CaCu_3Fe_2Re_2O_{12}$ [66], where B-site cations order in a rock-salt fashion.

However, $A_2BB'O_6$ DPv with columnar and layered B-site cationic arrangements have also been found [67]. For instance, $NdSrMn^{3+}Mn^{4+}O_6$ [68] and La_2CuSnO_6 [69] compounds were the first columnar and layered B-site DPv respectively ever reported. Since the charge difference between B and B' cations is only 1 in $NdSrMn^{3+}Mn^{4+}O_6$ and 2 in La_2CuSnO_6 and the differences in the ionic radii are less than 0.12 Å [70] in both compounds, these cannot still be considered the key factors controlling the sublattice type.

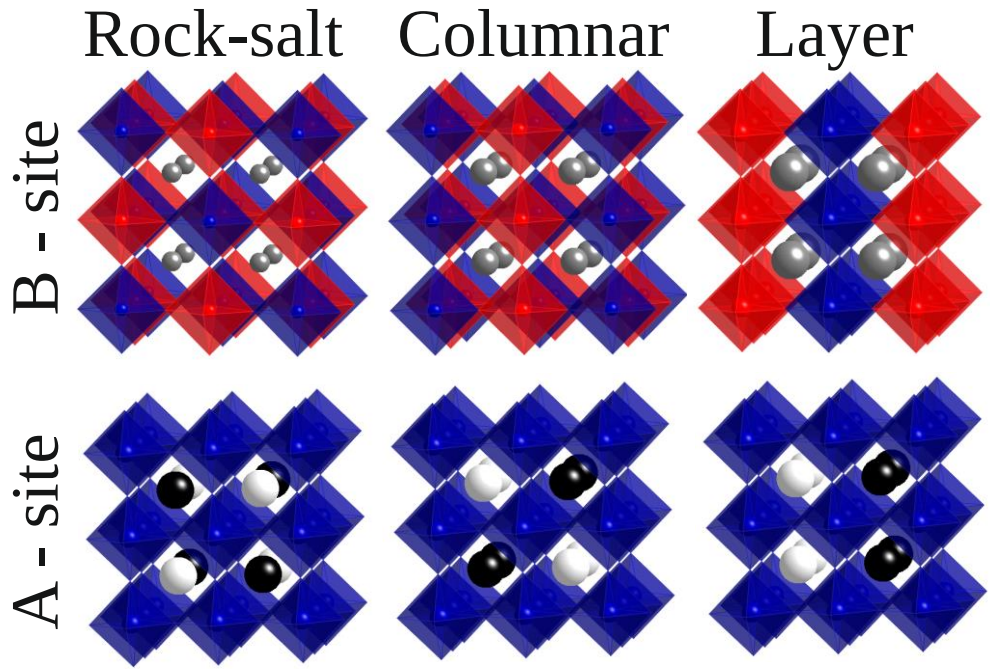

Fig. 1.2. Main types of A – (bottom) and B – site (up) ordered $AA'B_2O_6$ and $A_2BB'O_6$ double perovskite derivatives. Blue and red octahedra represent different BO_6 and $B'O_6$ positions and black and white spheres stand for independent A and A' sites.

Additional factors are thus expected to favour these columnar and layered types of ordering. The fifth Pauling's rule states that all ions of the same type tend to have the same environment in order to optimise the bonding and electrostatic repulsions. Therefore, the most favourable situation is the RS order, where each B-site cation is surrounded by six B' cations, thus minimising electrostatic repulsions and keeping all the anion sites chemically and crystallographically equivalent. However, as B is surrounded by 4 B' + 2 B in the columnar- and 2 B' + 4 B in the layered-orderings, non-equivalent anion environments are created, which could be understood as a violation of Pauling's fifth rule. Hence, the electrostatic repulsions progressively increase making columnar and layered arrangements gradually less stable. Nevertheless, the combination of B-site cations allowing cooperative first order Jahn-Teller (FOJT) distortions, as Mn^{3+} and Cu^{2+} cations, can stabilise these orderings as observed in the C_DPv $LaCaMn^{3+}Mn^{4+}O_6$ [71] and $NdSrMn^{3+}Mn^{4+}O_6$ [68] and the L_DPv La_2CuSnO_6 [69] and La_2CuZrO_6 [72] oxides.

- $AA'B_2O_6$ double perovskites: Concerning the A – site orderings these are less common than those observed at the B site because the oxidation state differential among A and A' cations is two or less. Therefore, A – site cations are not as prone to order as B – site ones but when the A/A' size mismatch is high enough to induce order the layered arrangement (see bottom right corner in Fig. 1.2) is preferred over the rock salted one. The differences of preferential order between A/A' against B/B' sites is attributed to the presence of different anionic environments: the site of an oxide anion in a RS_$AA'B_2O_6$ is centrosymmetric, as it is surrounded by two A and two A' cations alternated in both directions. Consequently, it cannot shift towards A/A' cations to optimise the bonding, i.e. A-O and A'-O are forced to be the same, what induces a high destabilisation of the compound. In fact, up to date there are only two examples of long-range RS_A – site ordered DPv compounds (bottom left corner in Fig. 1.2), namely $NaBaLiNiF_6$ and $Na_2BaFe_4F_{12}$, and one example exhibiting just short-range order ($PbCaTi_2O_6$) [67]. On the other hand, the layered configuration of A and A' cations creates three distinct anion environments, allowing anion shifts to stabilise strains in the structure. Consequently, $RA'B_2O_6$ compounds (where R is a rare earth) usually develop this kind of order [73].

As in the case of B – site ordered DPv, the columnar arrangement (middle part in bottom row of Fig. 1.2) has an intermediate stability between those of the RS_DPv and the L_DPv. The existence of compounds exhibiting A-site columnar ordering is scarce although some of them, such as $CaFeTi_2O_6$ [74] and $CaMnTi_2O_6$ [75], have been isolated. They show a $a^+a^+c^-$ tilt system, which was initially assigned to the orthorhombic *Pmmn* space group by Glazer [38], but these compounds surprisingly crystallise within a more symmetric tetragonal structure, with $P4_2/nmc$ and $P4_2mc$ symmetries. Among them, the Mn compound is notable for its polar space group, which ~~allows its ferroelectric behaviour~~.

Despite the unusual existence of A – site DPv compounds, these exotic orderings can be stabilised through adequate octahedral tilting, anion vacancies or A – site vacancies [67]. -There are only four tilt systems that allow to break the symmetry and create non-equivalent A sites. Two of them ($a^0b^+b^+$ and $a^0b^-b^+$) have never been observed in a $AA'B_2O_6$ DPv. $a^+a^+a^+$ is the most common tilt system adopted by $AA'_3B_4O_{12}$ cubic double perovskites, where A-site cations are ordered in two different sites [76–82]. A-site columnar ordering is adopted by tetragonal DPvs with $a^+a^+c^-$ tilt system, of which only two examples are reported: $CaA'Ti_2O_6$ (A' = Fe, Mn) [74,75]. Furthermore, as it is pointed out in Chapter V, we have found a new type of ordered DPv that combines rock salt ordering at the B site

with A-site columnar arrangement in the $MnRMnSbO_6$ double-double perovskites (DDPv) (R = La, Pr-Sm) [83].

On the other hand, the presence of A – site vacancies increases the concentration of anions able to shift towards A/A' cations and the existence of anion vacancies decreases the concentration of anions not able to do it. Therefore, these two types of non-stoichiometry also stabilise the $AA'_2B_2O_6$ double perovskites, what justifies the latest interest on these materials.

- $AA'BB'O_6$ double-double perovskites: Once studied the different A– and B– site possible orders, the next point to be considered should be devoted to check the available combinations among them. Theoretical studies performed through group theory analysis revealed that a total of 147 possible phases resulted, including 26 ternary phases (i.e. $A_2BB'O_6$ and $AA'_2B_2O_6$, just ordered within one sublattice) and 93 quaternary ($AA'BB'O_6$) ordered low symmetry phases plus 28 additional possible arrangements with more than four positions allowed for each sublattice [84]. The resulting doubly ordered superstructures exhibit tetragonal, orthorhombic or monoclinic symmetries, all of them presenting a total of four types of possible combinations of both A and B sublattices, namely i) 1:1 (A-site) and 1:1 (B-site), i.e. $AA'BB'O_6$; ii) 1: 1 (A-site) and 1:3 (B-site), i.e. $A_2A'_2BB'_3O_{12}$; iii) 1:3 (A-site) and 1:1 (B-site), i.e. $AA'_3B_2B'_2O_{12}$ and iv) 3:1 (A-site) and 3:1 (B-site), i.e. $AA'_3BB'_3O_{12}$.

Despite the high number of possible combinations of A- and B-site orderings, only layered A– site arrangement has been experimentally found to coexist with rock-salt B – site order up to date [67,73,85], excluding the new $MnRMnSbO_6$ DDPv reported in chapter V of this thesis [83]. The reason for the existence of a single type of $AA'BB'O_6$ perovskite oxide showing simultaneous ordering at both sites must be the synergy of the highest possible degree of stabilisation within each sublattice. The presence of rock-salt B – site order usually originates the tilt of BO_6 octahedra, which is one of the stabilising factors for the A sublattice ordering. For instance, the rock salt ordering among B and B' cations in the $AA'BWO_6$ compounds [73,85] produces two non-equivalent A sites leading to a layered arrangement of A and A' cations. It originates a lowering of the crystal symmetry that leads to the crystallisation of most of these compounds in the non-centrosymmetric $P2_1$ space group, allowing thereby ferroic orderings to occur. Actually, 15 out of the theoretically modelled 56 phases arising from improper octahedral rotations are predicted to be improper ferroelectrics [84,86,87].

As a consequence of the low stability of both columnar and rock-salt A– site orders, none of them had ever been found in combination with any ordered B sublattice. Nevertheless, the discussed effect of BO_6 tilting on the A sublattice would theoretically allow the synthesis of $AA'BB'O_6$ doubly ordered perovskites with columnar A/A' motif. The synthesis of double-double ordered perovskites is not an easy task, but it represents an interesting challenge for chemists, as finding new types of perovskite derivatives would open up a new pathway to develop multifunctional materials. In fact, different combinations have been stabilised in $AA'BB'O_{6-x}$ oxygen deficient and $AA'BB'O_{6+x}$ A – site deficient DPv. The challenge and functional interest now is to develop new types of stoichiometric ordered derivatives, as the presence of A vacant positions partially defeats the potential spontaneous polarisation and the introduction of oxygen deficiency perturbs the development of magnetic B – O – B' superexchange interactions.

To sum up, the perovskite structure accepts a high degree of distortion, enabling the stabilisation of perovskitic compounds for a wide range of A and B cations. In fact, it allows the stabilisation of almost any stoichiometric mixture with the adequate A / B ionic radii or charge ratios. The charge relation between both site cations in the ideal cubic simple perovskite is (A:B) = (2:4), but as exemplified along this section it can stabilise (3:3) and (1:5) ratios [88]. The compositional variation of the generic ABO_3 formula induces different ionic sites, orders and occupancies, originating diverse types of double perovskites. The magnetic and electric behaviours can then be tailored by combining different electronic environments through the insertion of transition metals and/or rare earths and elements with lone pairs within the different crystallographic sites, thus giving rise to compounds with potential applications such as sensors (piezoelectric $Pb(Zr_{1-x}Ti_x)O_3$ [89]), magnetic memories (ferromagnetic $LaMnO_3$ [90]), electrodes for Solid Oxide Fuel Cells (SOFCs) or Li^+ ion batteries (Li^+ ion conductor $(Li_{0.5-3x}La_{0.5+x})TiO_3$ [91]), magnetic detectors (superconductor $Y_{1/3}Ba_{2/3}CuO_{3-x}$ [92]), etc. Moreover, the combination of at least two of these properties within the same material, coupled at the same temperature, provides access to new multifunctional compounds. For instance, the magnetoelectric coupling allows changes in polarisation tailored by a variation of a magnetic field and vice versa. Multiferroicity turns these materials optimal for their use in electronic devices as electrically induced magnetic stores and read heads for hard disks ($LaMnO_{3-x}$).

1.1.2 - Extrinsic factors: High Pressure and/or High Temperature conditions in perovskites

It is, however, worth noting that the chemical composition is not the only influent factor on the structural symmetry of the perovskite family but synthesis conditions can also be used to allow access to new compounds. Symmetry transitions are very common in perovskites upon heating as consequence of changes in the tilt system [93,94]. In particular, the high pressure – high temperature (HPHT) method is traditionally used to synthesise metastable structures, as it is the case of the highly distorted perovskites and the corundum derivatives studied in this work. It also allows the stabilisation of small cations at the A- perovskite sites, even for chemical compositions where *t* is below 0.75. This is possible because the use of high pressures compress the unit cell, thus decreasing the volume of the A site and making A – O distances short enough to create bonds [95]. This method is reminiscent of that of the so-called chemical pressure [96] induced when substituting A by a smaller cation under room pressure conditions, originating distorted perovskites. However, the smaller the cation the lower its stability, and for a given $t < 0.75$ the perovskite structure cannot be stabilised at room pressure.

HPHT synthesis has traditionally been used to obtain other metastable structures different from perovskites such as Rh_2O_3-II, post-perovskite, bixbite, ilmenite, $LiNbO_3$ and Ni_3TeO_6 structures [97] (see Fig. 1.1). Additionally, the increase of pressure can induce phase transitions among different polymorphs [98].

Among the ABO_3 systems treated under HPHT conditions, Mn-containing double perovskites have attracted an especial interest during the last years, due to their spin, charge and orbital degrees of freedom, which induce complex orderings featuring their properties. Mn accommodates differently into the A or B sites depending on its oxidation state, size and coordination environment preferences. For instance, Mn^{4+} and Mn^{3+} ($r^{VI} = 0.53$ Å and $r^{VI} = 0.645$ Å, respectively [70]) are only stable at the B position, but Mn^{2+} can be stabilised under high pressure conditions in the highly coordinated A site of the perovskite structure despite its relatively small ionic radius (which ranges from $r^{VI} = 0.83$Å to

r^{VIII} = 0.96 Å as a function of its coordination number [70]).The magnetic and electronic properties of A site doped $RMnO_3$ manganites are strongly dependent on the existence of charge and orbital orders of Mn^{3+} / Mn^{4+} cations at the B site [99], which are sometimes accessible by applying high pressures, e.g. $RSrMn_2O_6$ [100].

The ambition of combining A –and B – site orders in $AA'BB'O_6$ DDPv potentiates the interest of introducing Mn^{3+} into the B site due to the discussed stabilising effect of its Jahn-Teller distortion. Notable examples of this effect are $RA'MnWO_6$ compounds, which combine L_A – and RS_B – arrangements [85]. Moreover, this stabilisation originates complex superstructures, commonly known as quadrupole perovskites, in compounds of general formula AMn_7O_{12}, where different oxidation states can be modulated for Mn within A', B and B' sites depending on the A^{n+} cation ($1 \leq n \leq 3$). As a result, their different Mn^{3+} / Mn^{4+} ratios induce complex spin, charge and orbital orders [101–103], originating interesting electromagnetic properties which include multiferroic and giant improper ferroelectric behaviours combined with spin - wave like magnetic structures [104,105].

On the other hand, the mentioned positive result of high pressure synthesis on the stabilisation of small A – site cations in the perovskite structure has lately motivated the study of $Mn^{2+}{}_2BB'O_6$ DPv polymorphs [29–36]. Within this family of oxides, which constitute the parent composition of the compounds studied here, several types of magnetic and transport properties appear. For instance, room temperature magnetoresistance is observed in Mn_2FeReO_6 [34,35] and an exotic spiral magnetic structure is induced from magnetic frustration in Mn_2FeSbO_6 [30,31]. It is also worth noting that the related $Mn_2FeB'O_6$ compounds with B' = Mo, W and Ta present rhombohedral structures but up to date none of their perovskite polymorphs have been isolated. This also affects some Mn_2BSbO_6 compounds [106].

1.2 - Corundum derivatives

For tolerance factors lower than 0.75, ABO_3 compounds crystallise with corundum structure or some of its derivatives, or even with the bixbyite structure (for a narrow range of A / B ionic radii relation) (see Figure 1.1). As it has been pointed out in the previous section, the use of moderate pressures stabilise corundum derivative structures of $Mn_2BB'O_6$ compounds and applying higher pressures induces the formation of their perovskite polymorph. In fact, this phenomenon has been observed in most of the compounds presented in this work. Although the corundum structure (α-Al_2O_3) is more rigid than the perovskite one for stabilising high distortions, cationic ordering can also originate various derivatives. Corundum structure crystallises with $R\bar{3}c$ space group and can be described as a hexagonal packing of oxide anions with cations lying in two thirds of the octahedral sites. The cationic distribution into these 2/3 sites originates pairs of MO_6 octahedra sharing faces along the *z* direction and each of them share edges with other three octahedra within the basal plane (see Fig. 1.3-left). This structure is also adopted when two different isovalent cations similar in size are distributed randomly in the octahedral sites, e.g. by doping $Al^{3+}{}_2O_3$ with Cr^{3+}, Fe^{3+} or Ti^{3+} [107]. However, it is also possible to observe long range ordering among both cations if their atomic radii or charges are different enough to stabilise ordered polymorphs. Then, they must be stated as ABO_3 oxides and will be briefly described in the next subsections.

1.2.1 - Ilmenite and Lithium niobate polymorphs

Among the ABO_3 corundum derivatives the most common are the ilmenite ($FeTiO_3$, ILO) and the $LiNbO_3$-type (LNO) structures. In general terms, the first of them is favoured for divalent A-site and tetravalent B-site cations ($A^{2+}B^{4+}O_3$) while $A^{+}B^{5+}O_3$ compounds usually crystallise with the latter [28]. ILO crystallises with $R\bar{3}$ space group and its structure can be described on the basis of the corundum structure, where A and B cations segregate onto alternated planes perpendicular to the *z* axis (Fig. 1.3 middle-left). The cationic order between (00z) layers, highlighted with dashed black lines in Fig. 1.3, results in pairs of AO_6 and BO_6 face sharing octahedra (depicted in blue and red respectively). As a consequence, the glide plane along the *z* axis which featured the corundum structure is lost in its ILO derivative, so that (003) and (101) reflections are visible in its diffraction patterns. Similar to corundum, cations are displaced from the centre of the octahedra due to the strong cation-cation repulsions across shared faces. This octahedral off-centring results in the so-called *puckering* of the cations above and below their ideal z coordinate into the (00z) planes, thus originating undulated layers. This distortion is schematised in the figure with white arrows pointing towards opposite directions. For the sake of clarity, such arrows are only depicted over the ILO-type structure, where the discussed ideal (00z) layers are also drawn. As it will be deeply discussed in chapters III and IV for the different ordered corundum derivatives studied in this work, this kind of distortion, common to all the corundum derivative structures, strongly affects their functional properties.

Up to this point, the mentioned ILO–type structure is defined for the general ABO_3 compounds but it can also be observed when introducing two different cations at the B sites, that is $A_2BB'O_6$. The alternated (00z) layers are constituted by AO_6 and $B/B'O_6$ octahedra, where there is a random distribution of B and B' cations within their respective layer. Since B-site cations are disordered, the structure remains centrosymmetric, so the $R\bar{3}$ space group is kept.

On the other hand, LNO-type structure (Fig. 1.3 middle-right) can also be described in terms of a corundum derivative, where AO_6 (blue) and BO_6 (red) octahedra are ordered in layers parallel to (012) planes (highlighted with grey dashed lines in Figure 1.3). Cations are arranged to avoid octahedral edge-sharing with any contiguous like cation, thus obtaining 1:1 cationic ordering along the three crystallographic directions. This atomic distribution implies the loss of centrosymmetry and the presence of the *c*-glide plane, thus crystallising in the *R*3*c* space group and resulting in the suppression of (003) and (101) reflections in the diffraction patterns.

The organisation of cations comes, as happened for the perovskite derivatives, from the need for minimising electrostatic repulsions. Therefore, the charge mismatch between A and B cations is the order parameter that acts as the driving force for determining the final cationic distribution. For that reason, the LiO_6 and NbO_6 octahedra in the $LiNbO_3$-type structure order by sharing both faces and edges, achieving by that a maximal homogeneity of the electronic distribution and minimising cationic repulsions. The lower charge difference between A and B cations in ILO-type structure allows the simpler face sharing of TiO_6 and FeO_6 octahedra along the *z* axis in $Fe^{2+}Ti^{4+}O_3$, so that the strongest repulsions are distributed through edge sharing octahedra (longer metal-metal distances) within (00z) layers.

1.2.2 - Ni_3TeO_6 – type structure

Apart from the described ILO and LNO polymorphs, there exist other further ordered derivatives of the corundum structure based on these two phases. Herein, the *R*3 Ni_3TeO_6-type (NTO) derivative, depicted in Figure 1.3-rigth, is detailed since one of the compounds studied along this work crystallises with its structure. It has two different oxygen positions and four independent cationic sites, schematised in the figure as A, B' (dark and pale blue), A' and B (dark and pale red). This structure can be described as a corundum derivative with (00z) layers alternatively occupied by $AO_6/B'O_6$ and $A'O_6/BO_6$ edge sharing octahedra. The cation arrangement in this NTO-type structure is such that the polyhedra sharing faces along the *z* axis are always A against B and B' against A'. The presence of four independent cationic sites originates different cationic displacements from their ideal sites, thus inducing an uncompensated dipolar moment giving rise to a net polarisation along the *z* axis [20,108]

It is worth to highlight that this further cation order needs for the location of four different cations into different crystallographic sites in an ordered manner. Therefore, the origin of the differences between the equal nuclei in both the archetypal Ni_3TeO_6 and the $Mn_2BB'O_6$ oxides studied in this work are not intrinsic differences between the three Ni^{2+} or the two Mn^{2+} cations themselves, but they are induced from their different relations with the rest of the cations in the structure. In this context, it is useful to understand the NTO-type structure as an additional order of two different cations within the (00z) layers of a ILO-like structure or within the (012) layers of a LNO-like derivative. As discussed for the related ILO and LNO structures, the cation distribution into different sites is induced by the charge mismatches. The extreme charge difference of Ni^{2+} / Te^{6+} pairs in the Ni_3TeO_6 originates their preference to order into a LNO-like distribution. However, the presence of uncompensated proportions of Ni and Te, determines the formation of alternated Ni^{2+} / Te^{6+} and Ni^{2+} / Ni^{2+} (012) layers. The presence of Te in the first of those layers induces the symmetry breaking between the two NiO_6 octahedra of the later, since one of them will face the TeO_6 and the other one will only share an

edge within the (00z) plane: their different distances from Te will involve different cationic repulsions.

In the case of $Mn_2BB'O_6$ oxides, different chemical compositions can be expected to induce a ILO or a LNO structure if B and B' cations do not show a charge mismatch high enough to originate their additional order within their corresponding B-site (00z) or (012) layer respectively. Some examples of $Mn_2BB'O_6$ compounds crystallising with ILO and LNO orders are Mn_2MSbO_6 (M = Cr^{3+}, Fe^{3+})[30,32,106,109] and $Mn_2FeB'O_6$ (B' = Ta^{5+}, Nb^{5+}) [110] respectively. If, otherwise, B and B' cations are different enough to order into independent sites, then the two Mn^{2+} cations reveal their preference to locate at the most distant octahedra, which only share a corner, due to their large repulsion, as it occurs, e.g. in Mn_2MSbO_6 (M = Sc^{3+}) [33] and $Mn_2FeB'O_6$ (B' = Mo^{5+}, W^{6+}) [111,112].

The coexistence of polarisation with ferromagnetism makes the compounds crystallising with NTO-type structure potential candidates to present multiferroicity. Therefore, the location of different paramagnetic cations within the four possible cationic sites opens up a new pathway to develop multiferroic materials [111]. Applying high pressures may induce not just the described phase transitions among different polymorphs but moderate pressures may allow the transformation of one corundum derivative into another one with different cationic order.

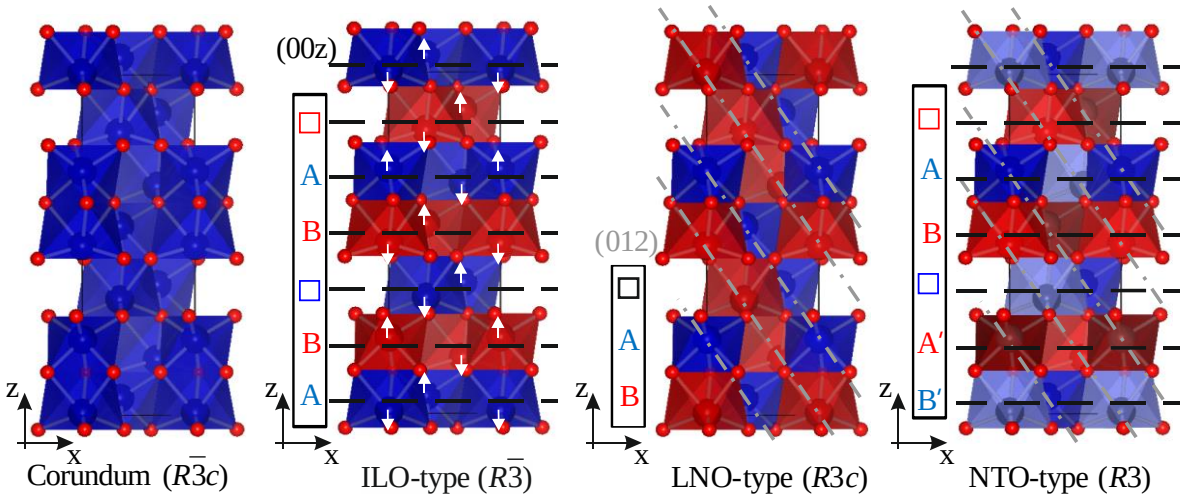

Figure 1.3. Unit cells of corundum-related structures showing the different cationic ordered planes. From left to right: disordered corundum, ILO-type structure ordered in alternated (00z) layers (highlighted with dashed black lines), LNO-type alternating (012) layers (dashed grey lines) and NTO-type combining both (00z) and (012) layers. White arrows on the ILO-type structure schematise the puckering featuring all these derivatives. The groups of letters included on the left hand side of each polymorph schematise the cationic site – sequences along the *z*-axis, where red and blue squares stand for A – and B – site vacancies, respectively, and the black one is a general cationic vacancy. Blue and red octahedra in the ILO and LNO structures are AO_6 and BO_6 respectively. The NTO-type structure shows A / B' cations (dark and pale blue respectively) and A' /B (dark and pale red) positions ordered into alternated (00z) layers. The blue and red squares in the leyend of this polymorph represent a vacant site of the A / B' and A' / B layers respectively.

1.2.3 - Extrinsic factors: High Pressure and/or High Temperature conditions in corundum derivatives

It is well known that the isolation of the different phases, either corundum derivatives or perovskite polymorphs implies a compromise between pressure and temperature. For instance, $MnTiO_3$ undergoes consecutive phase transitions upon increasing pressure. In a first step, increasing pressure induces the ILO to LNO-type transition through a reorientation process in which half of the cations are implied and oxygens rotate to accommodate them [17]. Under higher pressures the LNO-type polymorph transforms directly into a highly distorted orthorhombic perovskite structure through the cooperative rotation of TiO_6 octahedra and the consequent displacement of Mn into the highly coordinated A site [18].

In the particular case of Mn_2MSbO_6 (M = Fe, Cr) oxides, studied in this work, it is possible to induce the DPv to ILO transition through a thermal treatment under room pressure conditions. By that, both polymorphs, which exhibit very different properties, can be not just isolated under different HPHT synthesis conditions but also transformed at ambient pressure. This is quite surprising since LNO-phase, but not ILO, appears to be the quench product of the perovskite structure [113][98]. This is because the perovskite structure can indeed be derived geometrically from LNO-type through a topological transformation with a continuous displacement of atoms. Surprisingly, it has been reported by Megaw that a similar transition is forbidden for the ilmenite structure, since a cationic interchange between A and B cations would be needed [114]. In fact, the phase transformation from the DPv_Mn_2CrSbO_6 polymorph to the ILO_Mn_2CrSbO_6 modification found out in our study represents the first example in the literature [32], as detailed in chapter III. Then, a rearrangement and redistribution of atoms via diffusion is required in the perovskite to ilmenite phase transformation. The transition requires high temperatures to aid kinetics, but the transition in Mn_2CrSbO_6 is clearly completed at 1 atm and 973 K. This kind of synthesis/transformation, where an already prepared high pressure material is the precursor for a following room pressure chemical process, can be described as *hard-soft* chemistry [96]. These hard-soft reactions alter the local chemistry or even the crystal structure due to the partial instability of the high pressure phase, thus leading to unusual properties [115]. Moreover, post synthesis DPv – LNO phase transtitions have been observed under heating treatments at room pressure for compounds undergoing a synthetic ILO – DPv phase transition under HPHT conditions, which constitutes another example of hard-soft chemistry [98].

1.3 - Site exchanging substitutions inducing mixed-charged A sites

Up to here, the interest and background for most of the compounds studied during this work have already been settled. The cationic substitution of different M^{3+} ions in Mn_2MSbO_6 oxides has been considered but always keeping constant 2 Mn^{2+} cations at the A site. This approach originated double perovskite polymorphs and different corundum derivatives with $Mn^{2+}{}_2M^{3+}Sb^{5+}O_6$ stoichiometry. The substitution of such M^{3+} transition metal cations for larger trivalent metals is expected to induce different cationic arrangements, as it is the case of the NTO Mn_2ScSbO_6 compound, better formulated as $(Mn^{2+}Sc^{3+})(Mn^{2+}Sb^{5+})O_6$ [33]. However, this effect does not limit to the corundum derivatives, but it also occurs among structures favoured by higher tolerance factors, such as perovskites. In fact, the DPv polymorph of Mn_2ScSbO_6 already presents a considerable anti-site disorder between Sc and Mn [33]. In this line, larger M^{3+} cations, such as Bi^{3+} or R^{3+} (rare earths), often tend to locate in the highly coordinated A site of the perovskite structure producing the exchange of one of the A-site Mn^{2+} cations to the B site.

On the one hand, there are plenty of examples in the literature of double perovskites $RA'B_2O_6$, where R stands for a trivalent rare earth cation while A' is a large divalent metal, often an alkaline-earth element [116–118]. These phases are accessible via conventional ceramic method at room pressure. Otherwise $MnRMnSbO_6$ perovskites need for HPHT to be obtained as metastable phases. It is notable that the synthesis of the related Mn_2MSbO_6 oxides with M = transition metals under room pressure conditions usually leads to a combination of $MnSb_2O_6$, $Mn_2Sb_2O_7$ and spinel phases with MnM_2O_4 composition. However, when M is substituted by the large R^{3+} cations these antimoniates showed an energetic preference for a new family of non-stoichiometric structural derivatives of the cubic Mn_2RSbO_7 pyrochlore structure, further discussed in chapter V to be $(Mn^{2+}{}_{0.66}R^{3+}{}_{1.34})(Mn^{3+}{}_{0.66}Sb^{5+}{}_{1.34})O_7$.

The pyrochore structure (Figure 1.4) can be described as an oxygen deficient fluorite derivative, with 1/8 of anion vacancies in an ordered manner. The ideal pyrochlore structure crystallises in the space group $Fd\bar{3}m$ and consists on a three dimensional network of corner sharing BO_6 octahedra originating triangular and hexagonal tunnels in two perpendicular directions. A-site cations (grey spheres in Figure 1.4) locate in the hexagonal tunnels, giving rise to OA_4 tetrahedra (highlighted with a red dashed line). A further view of the structure locates the large A cation at the 16d site (0.5, 0.5, 0.5), the smaller B cation at 16c (0,0,0) and two different positions can be distinguished for the O anions, namely 48f (x, 0.125, 0.125) and the so-called O' anion (red spheres in Figure 1.4) at 8b (0.375, 0.375, 0.375). Therefore, this compound is better formulated as $A_2B_2O_6O'$. This crystal structure tolerates ionic vacancies at the A and O' sites to a certain extent [119], what could result in ionic conductivity.

In fact, oxygen deficient pyrochlore structures have lately been studied for their potential use as fast ionic conductors. Theoretical studies demonstrate that the high O^{2-} mobility occurs through a vacancy mechanism implying the 48f oxygen hopping, while the 8b O' sites do not often play an important role [120,121]. This high conductivity is associated to order/disorder phase transitions, either induced by compositional variations or thermally activated. It is common to find in the literature $R_2B_{1-x}B'_xO_7$ pyrochlore oxides where the progressive substitution of B cations induces the slow disorder among A – and B – site cations and the O – site displacement towards their ideal positions in the disordered fluorite structure. It is interesting to note that up to three different ionic diffusion rates (one for both cationic sites all together and independent rates for O and O') have been determined for these

compounds. The distortion features induced upon heating have been probed to behave in a similar manner [122].

Analogous order/disorder transitions have also been observed to occur under irradiation, paving the way for their use for immobilization of actinides in nuclear waste [123]. Another interesting potential use of these systems is catalysis, as a promising catalytic activity has recently been tested in a cathode with a high reversible capacity for lithium – O_2 batteries [124]. There, the pyrochlore compound was synthesised as a mesoporous phase, thus allowing the interplay of oxygen stoichiometry on the high proportion of surface defects.

In addition to the recently focus on their electric applicability, the magnetic properties of $R_2B_2O_7$ pyrochlores have traditionally attracted a high interest. The corner sharing of cation tetrahedra (see Figure 1.4-right), which is a general feature of the pyrochlore structure, yields a classical geometrically frustrated lattice [125]. Therefore, it shows the ideal environment to study exotic magnetic ground states when the A site is occupied by paramagnetic cations that order antiferromagnetically. This is because the location of magnetic cations into the highly coordinated A site of this structure couples the geometric frustration to the magnetic one. As a consequence, many possible favoured spin configurations of near stabilities coexist, and interesting quantum effects may occur either induced by freezing [126] or under the application of an external magnetic field [127]. Some of the most exciting phases develop spin-glass [128–130], spin-ice [131,132] or spin-liquid [126,133,134] behaviours. Moreover, the non-stoichiometric $(Mn^{2+}_{0.66}R^{3+}_{1.34})(Mn^{3+}_{0.66}Sb^{5+}_{1.34})O_7$ pyrochlores found in this project to crystallise at room pressure, which include paramagnetic cations in both A and B sites, revealed an unprecedented magnetocaloric effect as a consequence of the entropy variation in the frustrated system, as further discussed in chapter V.

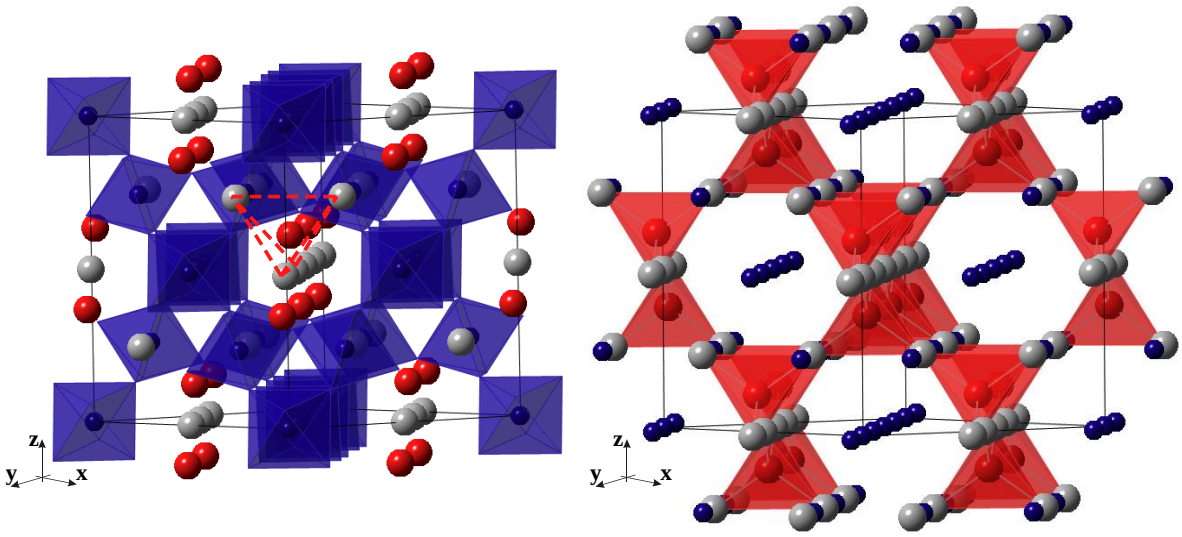

Figure 1.4. Unit cell of the ideal cubic pyrochlore structure along the [110] direction. B cations locate into the blue octahedra and O' anions are depicted as red spheres. A-site cations (grey spheres) occupy the hexagonal tunnels. Red dashed lines schematise the tetrahedral coordination of O' sites. The right-hand side shows the corner sharing tetrahedral lattice of A cations.

2.-Aims of this work

Considering the high interest of the A – site Mn containing perovskite family, a series of new $Mn_2MB'O_6$ double perovskites are intended to be stabilised under high pressure-high temperature conditions. In a first stage, M will be substituted by different paramagnetic transition metal cations (Fe^{3+}, Cr^{3+}) in order to induce additional magnetic interactions ensuring the blossoming of interesting magnetic properties. The use of moderate pressures is expected to allow the isolation of less dense corundum derivative structures for these compounds, as it also occurs in the related $Mn_2MB'O_6$ (B' = Nb, Mo, Ta, W) [110–112] family of oxides.

Taking into account the related systems recently studied, the selected B' cation for this work is Sb^{5+}. Although it does present neither lone pair electrons contributing to the development of electric properties nor unpaired electrons inducing spin couplings affecting the magnetic properties, this element is interesting from the structural point of view. On the one hand, the absence of π character in the Sb-O bonds induces the need for bond length or angle distortions to satisfy the necessity of polarisation induced by the charge and size mismatches among different site cations. In addition, its unusual small size favours the disorder with small transition metal ions located in B site thus allowing the stabilisation of ILO-type structures among the rhombohedral polymorphs. On the contrary, the ionic radii differences with larger non-transition metal trivalent cations are maximised, so this B' element will also permit the stabilisation of different polymorphs. A general rule which must also be considered regarding the determination of the crystal structure of these polymorphs is that the repulsive forces between the highly charged Sb^{5+} cations are too strong for face-shared octahedra to be stable, so that the use of Sb as B' cation involves the confidence that the nearest Sb^{5+} cations will locate at edge sharing octahedra.

Therefore, one of the main objectives of this work is to study the effect exerted by mechanical pressures on the stabilisation of different structures among Mn_2MSbO_6 compounds. Their magnetic and electric properties and the relation between the structure and properties will also be studied.

In a second stage of the work, M^{3+} cations are proposed to be substituted by larger non-transition metals, what should induce progressive structural changes implying rearrangements of both cationic and anionic sublattices, thus originating different ordered derivatives and polymorphs. The repulsions arising from the increasing average ionic radii of B-site cations is expected to be stabilised by partially exchanging the large M^{3+} with Mn^{2+} originally located at the A site, so the chemical pressure released through these compositional variations will induce antisite disordering up to a limit value above which this exchange actually means obtaining a different type of ordered derivative.

The final result of this process among the corundum related structures has already been exemplified with the transition from the ILO-type order to the NTO-polymorph for the extreme case that the exceedingly large volume of the introduced metal (M) prevents the structure to accept any antisite disorder. The controlled substitution through the synthesis of $Mn_2M_{(1-x)}M'_xSbO_6$ solid solutions would allow a more detailed study towards the determination of the exact stability limits of each structure, as this effect, directly depending on the physic-chemical nature of the M' metal, induces much more subtle differences than those arising from the application of an external mechanical pressure. Nevertheless, this is not intended in this project, as we aim to study the global impact resulting from this effect, what means the stabilisation of different polymorphs as a consequence of the complete compositional variation.

In the case of the perovskite structures the progressive antisite disorder among A and B site cations may induce an increasing disorder process within the previously ordered B sublattice and/or the appearance of some kind of order within the A sublattice for high values of exchanged elements. At some point during this process partial orders of both sites may coexist. The introduction of R^{3+} cations, in particular, is proposed as an especially interesting target, due to the wide background concerning $R_2BB'O_6$ B-site and $RA'B_2O_6$ A-site ordered DPv structures and the small amount of known $AA'BB'O_6$ DPv combining ordered configurations in both sublattices. Moreover, the only type of DPv known to show variable degrees of order in both sites up to date has been described as layered-A and rock-salted-B, but the considerably larger size difference between R^{3+} and Mn^{2+} cations may originate a different arrangement as it occurs for the columnar A-site ordered Ca-Mn and Ca-Fe titanates [74,75].

Through these compositions, new functional compounds, their polymorphism arising from pressure effects, their structural distortions and their relative stability are intended to be studied. Additionally, the reversibility of the different phase transitions and their consequences on the studied properties will be discussed.

Concerning the influence of stoichiometric variations, room pressure synthesis under oxidising conditions of R^{3+} A-site containing compounds is proposed to originate Mn_2MSbO_7 pyrochlore derivatives. Their resulting unusual stoichiometry and its influence on their structure and properties will be argued.

3.- Bibliography

[1] Giaquinta D.M., zur Loye H-C. Structural Predictions in the ABO_3 Phase Diagram. Chem. Mater. 1994;6:365–72. doi:10.1021/cm00040a007.

[2] Roth R.S. Classification of Perovskite and Other ABO_3-Type Compounds. J. Res. Natl. Bur. Stand. (1934) 1957;58:75–88. doi:org/10.6028/jres.058.010.

[3] Roth R.S., Schneider S.J. Phase Equilibria in Systems Involving the Rare-Earth Oxides . Part 1 . Polymorphism of the Oxides of the. J. Res. Natl. Bur. Stand. Chem. 1960;64:309–16.

[4] Schneider S.J., Roth R.S. [a]Phase equilibria in systems involving the rare-earth oxides. Part II. Solid state reactions in trivalent rare-earth oxide systems. J. Res. Natl. Bur. Stand. Sect. A Phys. Chem. 1960;64A:317–32. doi:10.6028/jres.064A.031.

[5] Schneider S.J., Roth R.S., Waring J.L. Solid state reactions involving oxides of trivalent cations. J. Res. Natl. Bur. Stand. Sect. A Phys. Chem. 1961;65A:345. doi:10.6028/jres.065A.037.

[6] Goldschmidt V.M., Mat-Naturu Kl 1926:2, 117.

[7] Oganov A.R., Ono S. Theoretical and experimental evidence for a post-perovskite phase of $MgSiO_3$ in Earth's D" layer. Nature 2004;430:445–8. doi:10.1038/nature02701.

[8] Belik A.A., Yi W. High-pressure synthesis, crystal chemistry and physics of perovskites with small cations at the A site. J. Phys. Condens. Matter. 2014;26:163201. doi:10.1088/0953-8984/26/16/163201.

[9] Grochala W., Hoffmann R., Feng J., Ashcroft N.W. The chemical imagination at work in very tight places. Angew. Chemie. - Int Ed 2007;46:3620–42. doi:10.1002/anie.200602485.

[10] Lin J., Degtyareva O., Prewitt C., Dera P., Sata N., Gregoryanz E., et al. Crystal structure of a high-pressure/high-temperature phase of alumina by in situ X-ray diffraction. Nat. Mater. 2004;3:389–93. doi:10.1038/nmat1121.

[11] Oganov A.R., Ono S. The high-pressure phase of alumina and implications for Earth's D'' layer. Proc. Natl. Acad. Sci. U S A 2005;102:10828–31. doi:10.1073/pnas.0501800102.

[12] Santillán J., Shim S.H., Shen G., Prakapenka V.B. High-pressure phase transition in Mn_2O_3: Application for the crystal structure and preferred orientation of the $CaIrO_3$ type. Geophys. Res. Lett. 2006;33:2–6. doi:10.1029/2006GL026423.

[13] Yamanaka T., Nagai T., Okada T., Fukuda T. Structure change of Mn_2O_3 under high pressure and pressure-induced transition. Z Krist 2005;220:938–45.

[14] Ovsyannikov S.V., Abakumov A.M., Tsirlin A.A., Schnelle W., Egoavil R., Verbeeck J., et al. Perovskite-like Mn_2O_3: A path to new manganites. Angew. Chemie. - Int. Ed. 2013;52:1494–8. doi:10.1002/anie.201208553.

[15] Ono S., Kikegawa T., Ohishi Y. High-pressure phase transition of hematite, Fe_2O_3. J. Phys. Chem. Solids 2004;65:1527–30. doi:10.1016/j.jpcs.2003.11.042.

[16] Castillo-Martínez E., Bieringer M., Shafi S.P., Cranswick L.M.D., Alario-Franco M.Á. Highly

stable cooperative distortion in a weak Jahn-Teller d^2 cation: Perovskite-type $ScVO_3$ obtained by high-pressure and high-temperature transformation from bixbyite. J. Am. Chem. Soc. 2011;133:8552–63. doi:10.1021/ja109376s.

[17] Ko J., Prewitt C.T. High-pressure phase transition in $MnTiO_3$ from the ilmenite to the $LiNbO_3$ structure. Phys. Chem. Miner. 1988;15:355–62. doi:10.1007/BF00311040.

[18] Ross N., Ko J., Prewitt C. A new phase transition in $MnTiO_3$: $LiNbO_3$-perovskite structure. Phys. Chem. Miner. 1989;16:621–9. doi:10.1007/BF00223309.

[19] Ball C.J., Begg B.D., Cookson D.J., Thorogood G.J., Vance E.R. Structures in the System $CaTiO_3$ / $SrTiO_3$. J. Solid State Chem. 1998;139:238–47.

[20] Lefevre C., Roulland F., Thomasson A., Meny C., Porcher F., Andre G., et al. Magnetic and Polar Properties? Optimization in the Magnetoelectric $Ga_{2?x}Fe_xO_3$ Compounds BT - The Journal of Physical Chemistry C 2013.

[21] Arnold D.C. Composition-Driven Structural Phase Transitions in Rare-Earth-Doped $BiFeO_3$ Ceramics : A Review. Ieee. Trans. Ultrason. Ferroelectr. Freq. Control. 2015;62:62–82.

[22] Belik A.A., Rusakov D.A., Furubayashi T., Takayama-Muromachi E. $BiGaO_3$-based perovskites: A large family of polar materials. Chem. Mater. 2012;24:3056–64. doi:10.1021/cm301603v.

[23] Kaleva G.M., Politova E.D., Ivanov S.A., Mosunov A.V., Sadovskaya N.V., Mathieu R., et al. Phase Transitions of $(Cu,Ni)_3TeO_6$ Solid Solutions 2011;47:1132–40. doi:10.1134/S0020168511100104.

[24] Anderson M., Greenwood K., Taylor G., Poeppelmeier K. B-cation arrangements in double perovskites. Prog. Solid State Chem. 1993;22:197–233. doi:10.1016/0079-6786(93)90004-B.

[25] Woodward P.M. Long range order in quaternary oxides. 1996.

[26] Dos Santos-Garcia A.J., Árevalo-López A.M., Fernández-Sanjulián J., Alario-Franco M.Á., Frost D. Synthesis, structural and magnetic disordering in the $IrSr_2RECu_2O_{8+x}$ family of metalo-cuprates by HP+HT oxidation. High Press Res. 2010;30:17–23. doi:10.1080/08957951003617388.

[27] Vasala S., Karppinen M.. $A_2B'B''O_6$ perovskites: A review. Prog. Solid State Chem. 2015;43:1–36. doi:10.1016/j.progsolidstchem.2014.08.001.

[28] Mitchell R.H. Perovskites: Modern and Ancient. Ontario, Canada: Almaz Press; 2002.

[29] Tyutyunnik A.P., Bazuev G.V., Kuznetsov M.V., Zainulin Y.G. Crystal structure and magnetic properties of double perovskite Mn_2FeSbO_6. Mater. Res. Bull. 2011;46:1247–51. doi:10.1016/j.materresbull.2011.04.001.

[30] Mathieu R., Ivanov S.A., Solovyev I.V., Bazuev G.V., Anil Kumar P., Lazor P., et al. Mn_2FeSbO_6: A ferrimagnetic ilmenite and an antiferromagnetic perovskite. Phys. Rev. B 2013;87:14408. doi:10.1103/PhysRevB.87.014408.

[31] Dos Santos-García A.J., Ritter C., Solana-Madruga E., Sáez-Puche R. Magnetic and crystal structure determination of Mn_2FeSbO_6 double perovskite. J. Phys. Condens. Matter.

2013;25:206004. doi:10.1088/0953-8984/25/20/206004.

[32] Dos santos-García A.J., Solana-Madruga E., Ritter C., Ávila-Brande D., Fabelo O., Sáez-Puche R. Synthesis, structures and magnetic properties of the dimorphic Mn_2CrSbO_6 oxide. Dalt. Trans. 2015;44:10665. doi:10.1039/c4dt03849e.

[33] Solana-Madruga E., Dos santos-García A.J., Arévalo-López A.M., Ávila-Brande D., Ritter C., Attfield J.P., et al. High pressure synthesis of polar and non-polar cation-ordered polymorphs of Mn_2ScSbO_6. Dalt. Trans. 2015;44:20441–8. doi:10.1039/c5dt03445k.

[34] Li M-R., Retuerto M., Deng Z., Stephens P.W., Croft M., Huang Q., et al. Giant Magnetoresistance in the Half-Metallic Double-Perovskite Ferrimagnet Mn_2FeReO_6. Angew. Chemie. 2015;127:12237–41. doi:10.1002/ange.201506456.

[35] Arévalo-López A.M., McNally G.M., Attfield J.P. Large Magnetization and Frustration Switching of Magnetoresistance in the Double-Perovskite Ferrimagnet Mn_2FeReO_6. Angew. Chemie. Int. Ed. 2015;54:12074–7. doi:10.1002/anie.201506540.

[36] Arévalo-López A.M., Stegemann F., Attfield J.P. Competing antiferromagnetic orders in the double perovskite $Mn_2MnReO_6(Mn_3ReO_6)$. Chem. Commun. 2016;147:2–4. doi:10.1039/C6CC01290F.

[37] Megaw H.D. Crystal structure of double oxides of the perovskite type. Proc. Phys. Soc. 2002;58:340–340. doi:10.1088/0959-5309/58/3/514.

[38] Glazer A.M. The classification of tilted octahedra in perovskites. Acta Crystallogr. Sect. B Struct. Crystallogr. Cryst. Chem. 1972;28:3384–92. doi:10.1107/S0567740872007976.

[39] Megaw, H.D.; Darlington C.N.W. Geometrical and Structural Relations in the Rhombohedral Perovskites. Acta Crystallogr. A 1975;31:161–73.

[40] Alexandrov K.S., Besnosikov B.V., Posdnjakova L.A. Successive phase transitions in perovskites. II. Structures of distorted phases. Ferroelectrics 1976;12:197–8. doi:10.1080/00150197608241424.

[41] O'Keeffe M., Hyde B.G. Some structures topologically related to cubic perovskite (E21), ReO_3 (D09) and Cu_3Au (L12). Acta Crystallogr. Sect. B Struct. Crystallogr. Cryst. Chem. 1977;33:3802–13. doi:10.1107/S0567740877012114.

[42] O'Keeffe M., Hyde B.G., Bovin J.O. Contribution to the crystal chemistry of orthorhombic perovskites: $MgSiO_3$ and $NaMgF_3$. Phys. Chem. Miner. 1979;4:299–305. doi:10.1007/BF00307533.

[43] Lufaso M.W., Woodward P.M., Goldberger J. Crystal structures of disordered $A_2Mn^{3+}M^{5+}O_6$ (A=Sr, Ca; M=Sb, Nb, Ru) perovskites. J Solid State Chem 2004;177:1651–9. doi:10.1016/j.jssc.2003.12.020.

[44] Howard C.J., Kennedy B.J., Woodward P.M. Ordered double perovskites -- a group-theoretical analysis. Acta Crystallogr. Sect. B Struct. Sci. 2003;B59:463–71.

[45] Stokes H.T., Hatch D.M., Campbell B.J. ISOTROPY Tutorial. 2013.

[46] Kuroiwa Y., Aoyagi S., Sawada A., Harada J., Nishibori E., Takata M., et al. Evidence for Pb-

O Covalency in Tetragonal $PbTiO_3$. Phys. Rev. Lett. 2001;87:217601. doi:10.1103/PhysRevLett.87.217601.

[47] Geller S. Crystal Structure of Gadolinium Orthoferrite, $GdFeO_3$. J. Chem. Phys. 1956;24:1236. doi:10.1063/1.1742746.

[48] Sasaki S., Prewitt C.T., Bass J.D., Schulze W.A.. Orthorhombic perovskite $CaTiO_3$ and $CdTiO_3$: structure and space group. Acta Crystallogr. Sect. C 1987;43:1668–74. doi:10.1107/S0108270187090620.

[49] Kimura T., Kawamoto S., Yamada I., Azuma M., Takano M., Tokura Y. Magnetocapacitance effect in multiferroic $BiMnO_3$. Phys. Rev. B 2003;67:180401. doi:10.1103/PhysRevB.67.180401.

[50] Woodward P.M. Octahedral Tilting in Perovskites. II. Structure Stabilizing Forces. Acta Crystallogr. B 1997;53:44–66. doi:10.1107/S0108768196012050.

[51] Cox D.E., Sleight A.W. Crystal structure of $Ba_2Bi_3+Bi_5+O_6$. Solid State Commun. 1976;19:969–73. doi:10.1016/0038-1098(76)90632-3.

[52] Harrison W.A. Valence-skipping compounds as positive-U electronic systems. Phys. Rev. B - Condens. Matter. Mater. Phys. 2006;74:1–4. doi:10.1103/PhysRevB.74.245128.

[53] Pei S., Jorgensen J.D., Dabrowski B., Hinks D.G., Richards D.R., Mitchell A.W., et al. Structural phase diagram of the $Ba_{1-x}K_xBiO_3$ system. Phys. Rev. B 1990;41:4126. doi:10.1103/PhysRevB.41.4126.

[54] Climent-Pascual E., Ni N., Jia S., Huang Q., Cava R.J. Polymorphism in $BaPb_{1-x}Bi_xO_3$ at the superconducting composition. Phys. Rev. B - Condens. Matter. Mater. Phys. 2011;83:1–8. doi:10.1103/PhysRevB.83.174512.

[55] Hwang H.Y., Cheong S.W., Radaelli P.G., Marezio M., Batlogg B. Lattice effects on the magnetoresistance in doped $LaMnO_3$. Phys. Rev. Lett. 1995;75:914–7. doi:10.1103/PhysRevLett.75.914.

[56] Eerenstein W., Mathur N.D., Scott J.F., F. J. Multiferroic and magnetoelectric materials. Nature 2006;442:759–65. doi:10.1038/nature05023.

[57] Robert R., Aguirre M.H., Hug P., Reller A., Weidenkaff A. High-temperature thermoelectric properties of $Ln(Co, Ni)O_3$ (Ln = La, Pr, Nd, Sm, Gd and Dy) compounds. Acta Mater. 2007;55:4965–72. doi:10.1016/j.actamat.2007.05.020.

[58] Hu Y., Hernandez O., Broux T., Bahout M., Hermet J., Ottochian A., et al. Oxygen diffusion mechanism in the mixed ion-electron conductor $NdBaCo_2O_{5+x}$. J. Mater. Chem. 2012;22:18744. doi:10.1039/c2jm34396g.

[59] Taylor D.D., Schreiber N.J., Brown C.M., Arevalo-Lopez A.M., Rodriguez E.E.. Stabilization of cubic Sr_2FeMoO_6 through topochemical reduction. Chem. Commun. 2015;51:12201–4. doi:10.1039/C5CC04145G.

[60] Paul A.K., Jansen M., Yan B., Felser C., Reehuis M., Abdala P.M. Synthesis, crystal structure, and physical properties of Sr_2FeOsO_6. Inorg. Chem. 2013;52:6713–9. doi:10.1021/ic400740f.

[61] Faik A., Igartua J.M., Iturbe-Zabalo E., Cuello G.J. A study of the crystal structures and the phase transitions of Sr_2FeSbO_6, $SrCaFeSbO_6$ and Ca_2FeSbO_6 double perovskite oxides. J. Mol. Struct. 2010;963:145–52. doi:10.1016/j.molstruc.2009.10.027.

[62] Stoyanova-Lyubenova T., Dos santos-García A.J., Urones-Garrote E., Torralvo M.J., Alario-Franco M.Á. High-pressure synthesis, structural and complex magnetic properties of the ordered double perovskite Pb_2NiReO_6. Dalton. Trans. 2014;43:1117–24. doi:10.1039/c3dt52073k.

[63] Fu W.T. A neutron powder diffraction study on $BaBi_{0.5}Sb_{0.5}O_3$. Solid State Commun. 2000;116:461–4.

[64] Lufaso M.W., Barnes P.W., Woodward P.M. Structure prediction of ordered and disordered multiple octahedral cation perovskites using SPuDS. Acta Crystallogr. Sect. B Struct. Sci. 2006;62:397–410. doi:10.1107/S010876810600262X.

[65] Marcos M.D., Attfield J.P. Quaternary uranium copper oxides: the structure and properties of UBa_2CuO_6. J. Mater. Chem. 1994;4:475–7. doi:10.1039/jm9940400475.

[66] Chen W., Mizumaki M., Seki H., Senn M.S., Saito T., Kan D., et al. A half-metallic A- and B-site-ordered quadruple perovskite oxide $CaCu_3Fe_2Re_2O_{12}$ with large magnetization and a high transition temperature. Nat. Commun. 2014;5:3909. doi:10.1038/ncomms4909.

[67] King G., Woodward P.M. Cation ordering in perovskites. J. Mater. Chem. 2010;20:5785. doi:10.1039/b926757c.

[68] Caignaert, V.; Millange, F.; Hervieu, M.; Suard, E.; Raveau B. The manganite $Nd_{0.5}Sr_{0.5}MnO_3$: a rare distortion of the perovskite. Solid State Commun. 1996;99:173–7.

[69] Anderson M.T., Poeppelmeier K.R. New Perovskite-Related Compound with an Unusual Arrangement of B Cations. Chem. Mater. 1991;3:476–82. doi:10.1021/cm00015a022.

[70] Shannon R.D., Prewitt C.T. Effective Ionic Radii in Oxides and Fluorides. Acta Crystallogr. Sect. B-Structural Crystallogr. Cryst. Chem. 1969;B 25:925–46. doi:10.1107/s0567740869003220.

[71] Woodward P.M., Vogt T., Cox D.E., Arulraj A., Rao C.N.R., Karen P., et al. Influence of Cation Size on the Structural Features of $Ln_{1/2}A_{1/2}MnO_3$ Perovskites at Room Temperature. Chem. Mater. 1998;10:3652–65. doi:10.1021/cm980397u.

[72] Azuma M., Kaimori S., Takano M. High-Pressure Synthesis and Magnetic Properties of Layered Double Perovskites Ln_2CuMO_6 (Ln = La, Pr, Nd, and Sm; M = Sn and Zr). Chem. Mater. 1998;10:3124–30. doi:10.1021/cm980217g.

[73] Knapp M.C., Woodward P.M. A-site cation ordering in $AA'BB'O_6$ perovskites. J. Solid State Chem. 2006;179:1076–85. doi:10.1016/j.jssc.2006.01.005.

[74] Leinenweber K., Parise J. High-Pressure Synthesis and Crystal Structure of $CaFeTi_2O_6$, a New Perovskite Structure Type. J. Solid State Chem. 1995;114:277–81. doi:10.1006/jssc.1995.1040.

[75] Aimi A., Mori D., Hiraki K., Takahashi T., Shan Y.J., Shirako Y., et al. High-Pressure Synthesis of A -Site Ordered Double Perovskite $CaMnTi_2O_6$ and Ferroelectricity Driven by

Coupling of A -Site Ordering and the Second-Order Jahn–Teller Effect. Chem. Mater. 2014;26:2601–8. doi:10.1021/cm500016z.

[76] Deschizeaux M.N., Joubert J.C., Vegas A., Collomb A., Chenavas J., Marezio M. Synthesis and crystal structure of $(ThCu_3)(Mn^{3+}{}_2Mn^{4+}{}_2)O_{12}$, a new ferrimagnetic perovskite-like compound. J. Solid State Chem. 1976;19:45–51. doi:10.1016/0022-4596(76)90148-1.

[77] Ozaki Y., Ghedira M., Chenavas J., Joubert J.C., Marezio M. High-pressure synthesis and bond lengths of calcium copper germanium oxide $[CaCu_3](Ge_4)O_{12}$. Acta Crystallogr. Sect. B Struct. Crystallogr. Cryst. Chem. 1977;33:3615–7. doi:10.1107/S0567740877011686.

[78] Bochu B., Deschizeaux M.N., Joubert J.C., Collomb A., Chenavas J., Marezio M. Synthèse et caractérisation d'une série de titanates pérowskites isotypes de $[CaCu_3](Mn_4)O_{12}$. J. Solid State Chem. 1979;29:291–8. doi:10.1016/0022-4596(79)90235-4.

[79] Subramanian M.A.A., Li D., Duan N., Reisner B.A.A., Sleight A.W.W. High Dielectric Constant in $ACu_3Ti_4O_{12}$ and $ACu_3Ti_3FeO_{12}$ Phases. J. Solid State. Chem. 2000;151:323–5. doi:10.1006/jssc.2000.8703.

[80] Subramanian M.A., Sleight A.W. $ACu_3Ti_4O_{12}$ and $ACu_3Ru_4O_{12}$ perovskites: High dielectric constants and valence degeneracy. Solid State Sci. 2002;4:347–51. doi:10.1016/S1293-2558(01)01262-6.

[81] Prakash B.S., Varma K.B.R.Ã. Effect of the addition of B_2O_3 and $BaO - B_2O_3 - SiO_2$ glasses on the microstructure and dielectric properties of giant dielectric constant material $CaCu_3Ti_4O_{12}$ 2007;180:1918–27. doi:10.1016/j.jssc.2007.04.018.

[82] Liu L., Fan H., Fang P., Jin L. Electrical heterogeneity in $CaCu_3Ti_4O_{12}$ ceramics fabricated by sol-gel method. Solid State Commun. 2007;142:573–6. doi:10.1016/j.ssc.2007.04.005.

[83] Solana-Madruga E., Arévalo-López Á.M., Dos santos-García A.J., Urones-Garrote E., Ávila-Brande D., Sáez-Puche R., et al. Double Double Cation Order in the High-Pressure Perovskites $MnRMnSbO_6$. Angew. Chemie. - Int. Ed. 2016;55:9340–4. doi:10.1002/anie.201603526.

[84] Talanov M.V., Shirokov V.B., Talanov V.M. Combined atomic ordering in the A and B sublattices of perovskite structure. Crystallogr. Reports. 2014;59:662–78. doi:10.1134/S1063774514050198.

[85] King G., Thimmaiah S., Dwivedi A., Woodward P.M. Synthesis and characterization of new $AA'BWO_6$ perovskites exhibiting simultaneous ordering of A-site and B-site cations. Chem. Mater. 2007;19:6451–8. doi:10.1021/cm0716708.

[86] Levanyuk A.P., Sannikov D.G. Improper ferroelectrics. Sov. Phys. Uspekhi. 1974;17:199–214. doi:10.1070/PU1974v017n02ABEH004336.

[87] Matyjasik S., Shaldin Y.V. Spontaneous polarization and pyroelectric effect in the improper ferroelectrics-ferroelastics $Gd_2(MoO_4)_3$ and $Tb_2(MoO_4)_3$ at low temperatures. Low Temp. Phys. 2013;39:967–72. doi:10.1063/1.4830258.

[88] Hu C-C., Tsai C-C., Teng H. Structure Characterization and Tuning of Perovskite-Like $NaTaO_3$ for Applications in Photoluminescence and Photocatalysis. J. Am. Ceram. Soc.

2009;92:460–6. doi:10.1111/j.1551-2916.2008.02869.x.

[89] Kuwata J., Uchino K., Nomura S. Phase transitions in the $Pb(Zn_{1/3}Nb_{2/3})O_3$- $PbTiO_3$ system. Ferroelectrics 1981;37:579–82. doi:10.1080/02687030244000554.

[90] Xu Z.T., Jin K.J., Gu L., Jin Y.L., Ge.C., Wang C., et al. Evidence for a crucial role played by oxygen vacancies in $LaMnO_3$ resistive switching memories. Small 2012;8:1279–84. doi:10.1002/smll.201101796.

[91] Inaguma Y., Chen L., Itoh M., Nakamura T. Candidate compounds with perovskite structure for high lithium ionic conductivity. Solid State Ionics 1994;70/71:196–202. doi:10.1016/0167-2738(94)90309-3.

[92] West A.R. Solid State Chemistry and its Applications. Chichester: Wiley; n.d.

[93] Howard C.J., Knight K.S., Kennedy B.J., Kisi E.H. The structural phase transitions in strontium zirconate revisited. J. Phys. Condens. Matter. 2000;12:L677–83. doi:10.1088/0953-8984/12/45/101.

[94] Mountstevens E.H., Redfern S.A.T., Attfield J.P. Order-disorder octahedral tilting transitions in $SrSnO_3$ perovskite. Phys. Rev. B - Condens. Matter. Mater. Phys. 2005;71:2–5. doi:10.1103/PhysRevB.71.220102.

[95] MALTA-Consolider. An introduction to high-pressure science and technology. 2016.

[96] Gopalakrishnan J. Chimie Douce Approaches to the Synthesis of Metastable Oxide Materials. Chem. Mater. 1995;7:1265–75. doi:10.1021/cm00055a001.

[97] Tsuchiya J., Tsuchiya T., Wentzcovitch R.M. Transition from the Rh_2O_3(II) to $CaIrO_3$ structure and the high-pressure-temperature phase diagram of alumina. Phys. Rev. B 2005;72:20103. doi:10.1103/PhysRevB.72.020103.

[98] Yusa H, Akaogi M, Sata N, Kojitani H, Yamamoto R, Ohishi Y. High-pressure transformations of ilmenite to perovskite, and lithium niobate to perovskite in zinc germanate. Phys Chem Miner 2006;33:217–26. doi:10.1007/s00269-006-0070-5.

[99] Peña A., Gutiérrez J., Barandiarán J.M., Chapman J.P., Insausti M., Rojo T. Correlation between structure and magnetic properties of Cd-substituted $La_{0.7}(Ca_{0.3-x}Cd_x)MnO_3$ CMR manganites. J. Solid State Chem. 2003;174:52–9. doi:10.1016/S0022-4596(03)00173-7.

[100] Kuriki A., Moritomo Y., Machida A., Nishibori E., Takata M., Sakata M., et al. High-pressure structural analysis of $(Nd,Sm)_{1/2}Sr_{1/2}MnO_3$. Phys. Rev. B 2002;65:113105. doi:10.1103/PhysRevB.65.144404.

[101] Prodi A., Gilioli E., Gauzzi A., Licci F., Marezio M., Bolzoni F., et al. Charge, orbital and spin ordering phenomena in the mixed valence manganite $(NaMn^{3+}_{(3)})(Mn^{3+}_{(2)}Mn^{4+}_{(2)})O_{12}$. Nat. Mater. 2004;3:48–52. doi:10.1038/nmat1038.

[102] Streltsov S.V., Khomskii D.I. Jahn-Teller distortion and charge, orbital, and magnetic order in $NaMn_7O_{12}$. Phys. Rev. B 2014;89:201115. doi:10.1103/PhysRevB.89.201115.

[103] Prodi A., Daoud-Aladine A., Gozzo F., Schmitt B., Lebedev O., van Tendeloo G., et al. Commensurate structural modulation in the charge- and orbitally ordered phase of the

quadruple perovskite $(NaMn_3)Mn_4O_{12}$. Phys. Rev. B 2014;90:180101. doi:10.1103/PhysRevB.90.180101.

[104] Perks N.J., Johnson R.D., Martin C., Chapon L.C., Radaelli P.G. Magneto-orbital helices as a route to coupling magnetism and ferroelectricity in multiferroic $CaMn_7O_{12}$. Nat. Commun. 2012;3:1277. doi:10.1038/ncomms2294.

[105] Johnson R.D., Chapon L.C., Khalyavin D.D., Manuel P., Radaelli P.G., Martin C. Giant Improper Ferroelectricity in the Ferroaxial Magnet $CaMn_7O_{12}$. Phys. Rev. Lett. 2012;108:67201. doi:10.1103/PhysRevLett.108.067201.

[106] Bazuev G.V., Golovkin B.G., Lukin N.V., Kadyrova N.I., Zainulin Y.G. High Pressure Synthesis and Polymorphism of Complex Oxides Mn_2BSbO_6(B= Fe, V, Cr, Ga, Al). J. Solid State Chem. 1996;124:333–7. doi:10.1006/jssc.1996.0246.

[107] Gaudry E., Cabaret D., Sainctavit P., Brouder C., Mauri F., Goulon J., et al. Structural relaxations around Ti, Cr and Fe impurities in alpha-Al_2O_3 probed by x-ray absorption near edge structure combined with first-principles calculations. J. Phys. Condens. Matter. 2005;17:5467–80. doi:10.1088/0953-8984/17/36/003.

[108] Spaldin N.A.A. beginners guide to the modern theory of polarization. J. Solid State Chem. 2012;195:2–10. doi:10.1016/j.jssc.2012.05.010.

[109] Mathieu R., Ivanov S.A., Bazuev G.V., Hudl M., Lazor P., Solovyev I.V., et al. Magnetic order near 270 K in mineral and synthetic Mn_2FeSbO_6 ilmenite. Appl. Phys. Lett. 2011;98:202505-1-202505–3. doi:10.1063/1.3593194.

[110] Li M-R., Walker D., Retuerto M., Sarkar T., Hadermann J., Stephens P.W., et al. Polar and Magnetic Mn_2FeMO_6 (M=Nb, Ta) with $LiNbO_3$ -type Structure: High-Pressure Synthesis. Angew. Chemie. 2013;125:8564–8. doi:10.1002/ange.201302775.

[111] Li M-R., Retuerto M., Walker D., Sarkar T., Stephens P.W., Mukherjee S., et al. Magnetic-Structure-Stabilized Polarization in an Above-Room-Temperature Ferrimagnet. Angew. Chem. Int. Ed. Engl. 2014;53:10774–8. doi:10.1002/anie.201406180.

[112] Li M-R., Croft M., Stephens P.W., Ye M., Vanderbilt D., Retuerto M., et al. Mn_2FeWO_6: a New Ni_3TeO_6-Type Polar and Magnetic Oxide. Adv. Mater. 2015 doi:10.1002/adma.201405244.

[113] Inaguma Y., Tanaka K., Tsuchiya T., Mori D., Katsumata T., Ohba T., et al. Synthesis, structural transformation, thermal stability, valence state, and magnetic and electronic properties of $PbNiO_3$ with perovskite- and $LiNbO_3$-type structures. J. Am. Chem. Soc. 2011;133:16920–9. doi:10.1021/ja206247j.

[114] Megaw H.D. Ferroelectricity in crystals 1957.

[115] Arévalo-López A.M., Rodgers J.A., Senn M.S., Sher F., Farnham J., Gibbs W., et al. "Hard-Soft" Synthesis of $SrCrO_{3-\delta}$ Superstructure Phases. Angew. Chemie. Int. Ed. 2012;51:10791–4. doi:10.1002/ange.201206203.

[116] Ueda Y., Nakajima T. The A-site ordered manganese perovskite and its colossal magnetoresistance. Prog. Solid State Chem. 2007;35:397–406.

doi:10.1016/j.progsolidstchem.2007.01.025.

[117] Nakajima T., Tsuchiya T., Daoudi K. Epitaxial A-Site Ordered Perovskite Manganite $SmBaMn_2O_6$ Film on $SrTiO_3$ (001): Fabrication, Structure, and Physical Property. Chem … 2007;3:5355–62.

[118] Nakajima T., Kageyama H., Yoshizawa H., Ueda Y. Structures and Electromagnetic Properties of New Metal-Ordered Manganites: $RBaMn_2O_6$ (R = Y and Rare-Earth Elements). J. Phys. Soc. Japan 2002;71:2843–6. doi:10.1143/JPSJ.71.2843.

[119] Subramanian M.A., Aravamudan G., Subba Rao G.V. Oxide pyrochlores — A review. Prog. Solid State Chem. 1983;15:55–143. doi:10.1016/0079-6786(83)90001-8.

[120] Wilde P. Defects and diffusion in pyrochlore structured oxides. Solid State Ionics 1998;112:173–83. doi:10.1016/S0167-2738(98)00190-8.

[121] Pirzada M., Grimes R.W., Minervini L., Maguire J.F., Sickafus K.E. Oxygen migration in $A_2B_2O_7$ pyrochlores. Solid State Ionics 2001;140:201–8. doi:10.1016/S0167-2738(00)00836-5.

[122] Wuensch B.J., Eberman K.W., Heremans C., Ku E.M., Onnerud P., Yeo E.M.E., et al. Connection between oxygen-ion conductivity of pyrochlore fuel-cell materials and structural change with composition and temperature. Solid State Ionics 2000;129:111–33. doi:10.1016/S0167-2738(99)00320-3.

[123] Sickafus K.E., Minervini L., Grimes R.W., Valdez J.A., Ishimaru M., Li F., et al. Radiation tolerance of complex oxides. Science (80-) 2000;289:748–51.

[124] Oh S.H., Black R., Pomerantseva E., Lee J-H., Nazar L.F. Synthesis of a metallic mesoporous pyrochlore as a catalyst for lithium–O_2 batteries. Nat. Chem. 2012;4:1004–10. doi:10.1038/nchem.1499.

[125] Greedan J.E. Geometrically frustrated magnetic materials. J. Mater. Chem. 2001;11:37–53. doi:10.1039/b003682j.

[126] Kassner E.R., Eyvazov A.B., Pichler B., Munsie T.J.S., Dabkowska H.A., Luke G.M., et al. Supercooled spin liquid state in the frustrated pyrochlore $Dy_2Ti_2O_7$. Proc. Natl. Acad. Sci. 2015;112:8549–54. doi:10.1073/pnas.1511006112.

[127] Ross K.A., Ruff J.P.C., Adams C.P., Gardner J.S., Dabkowska H.A., Qiu Y., et al. Two-Dimensional Kagome Correlations and Field Induced Order in the Ferromagnetic XY Pyrochlore $Yb_2Ti_2O_7$. Phys. Rev. Lett. 2009;103:227202. doi:10.1103/PhysRevLett.103.227202.

[128] Raju N.P., Gmelin E., K. K.R. Magnetic susceptibility and specific-heat studies of spin-glass-like ordering in the pyrochlore compounds $R_2Mo_2O_7$ (R = Y, Sm, or Gd). Phys. Rev. B 1992;46.

[129] Gingras M.J.P., Stager C.V., Raju N.P., Gaulin B.D., Greedan J.E. Static Critical Behavior of the Spin-Freezing Transition in the Geometrically Frustrated Pyrochlore Antiferromagnet $Y_2Mo_2O_7$ 1996:947–50. doi:10.1103/PhysRevLett.78.947.

[130] Harris M.J., Bramwell S.T., Zeiske T., McMorrow D.F., King P.J.C. Magnetic structures of

highly frustrated pyrochlores. J. Magn. Magn. Mater. 1998;177:757–62. doi:10.1016/S0304-8853(97)00796-8.

[131] Mostame S., Castelnovo C., Moessner R., Sondhi S.L. Tunable nonequilibrium dynamics of field quenches in spin ice. Proc. Natl. Acad. Sci. 2014;111:640–5. doi:10.1073/pnas.1317631111.

[132] Chang L-J., Onoda S., Su Y., Kao Y-J., Tsuei K-D., Yasui Y., et al. Higgs transition from a magnetic Coulomb liquid to a ferromagnet in $Yb_2Ti_2O_7$. Nat. Commun. 2012;3:992. doi:10.1038/ncomms1989.

[133] Savary L., Balents L. Coulombic Quantum Liquids in Spin- 1/2 Pyrochlores. Phys. Rev. Lett. 2012;108:37202. doi:10.1103/PhysRevLett.108.037202.

[134] Enjalran M., Gingras M.J.P., Kao Y-J., Maestro a Del, Molavian H.R. The spin liquid state of the $Tb_2Ti_2O_7$ pyrochlore antiferromagnet: a puzzling state of affairs. J. Phys. Condens. Matter. 2004;16:S673–8. doi:10.1088/0953-8984/16/11/014.

II. Experimental Techniques

1.- Sample preparation

1.1 - Ceramic method

The room pressure samples synthesised during this work were prepared with the conventional solid state ceramic method. The stoichiometric amounts of the precursor binary oxides were ground under acetone in an agate mortar until reaching homogeneity and subsequently pelletized with a manual hydraulic press. For those compounds incorporating rare earths in their compositions the reactant sesquioxide was previously decarbonised through a heat treatment in air at 1173 K for 12 hours, except in the case of Pr_2O_3, which tendency to oxidise required the heating of Pr_6O_{11} at 1323 K under a N_2/H_2 (5%) flow.

This kind of room pressure synthesis was developed for all the studied compositions in order to check the existence of any unknown room pressure polymorph of the Mn_2MSbO_6 oxides. With this purpose, the precursors were treated under temperatures ranging 1173 K - 1773 K. For Mn_2MSbO_6 oxides with M = $3d^n$ transition metals (Cr^{3+} and Fe^{3+}), the room pressure heating was always found to yield the formation of binary and mixed oxides with undesired cationic stoichiometries, such as Sb_2O_4, MnM_2O_4 or $Mn_2Sb_2O_7$, in agreement with the literature [1]. In the case of the M = $3d^0$ transition metal (Sc^{3+}), a cationic disordered structure with $R\bar{3}$ symmetry is formed under room pressure conditions [2,3]. The absence of long range magnetic order in this compound and the evidence of high pressure accessible phases with ordered corundum derivative and double perovskite structures for Mn_2MSbO_6 oxides, motivated the exploration of their synthesis under high pressure conditions.

The room pressure synthesis of Mn_2RSbO_6 oxides (R = rare earth element) resulted in an unexpected non-stoichiometric derivative with pyrochlore structure. The finding of this new family of room pressure compounds, formulated as $(Mn_{0.66}R_{1.34})(Mn_{0.66}Sb_{1.34})O_7$, promoted the optimisation of their synthesis conditions and the study of their magnetic properties, as detailed in chapter V.

1.2 - High pressure synthesis

Mn_2MSbO_6 high pressure polymorphs constitute the main part of the samples studied along this work. As detailed in chapter I, $Mn_2MB'O_6$ compounds often crystallise with DPv [4–7], ILO [6,8,9], LNO [10] and NTO [11–13] structures when synthesised under high pressure – high temperature conditions. In particular, moderate pressure polymorphs of Mn_2MSbO_6 with ILO and NTO structures have been isolated for M = $3d^n$ and $3d^0$ transition elements respectively. Their synthesis under higher pressure conditions yield the formation of conventional rock-salt ordered double perovskites. On the other hand, the synthesis of the high pressure polymorphs of Mn_2RSbO_6 oxides has been found to need much higher pressures, under which only the perovskite derivative structure can be stabilised. As it will be detailed in chapter V, these compounds crystallise with a conventional DPv structure similar to those of Mn_2MSbO_6 (M = Cr, Fe and Sc) for sufficiently small rare earths (R = Eu and Gd among the compounds studied here) but the use of larger R elements (La – Sm) induces an additional order among the A-site cations with a columnar arrangement [14].

In general terms, the synthesis approach for all these Mn_2MSbO_6 and $MnRMnSbO_6$ oxides can be explained on the same bases. A precursor mixture is prepared by grinding the stoichiometric amounts of the needed binary oxides under acetone in an agate mortar. The use of R_2O_3 oxides require their decarbonation in the same conditions detailed for the ceramic method.

Depending on the synthesis temperature conditions to be applied these precursors are packed into a gold (T < 1373 K) or a platinum capsule (T > 1373 K).. The capsule is introduced into the pressure cell, further detailed below, and the target pressure, 3 - 13 GPa for all the samples studied along this thesis, is applied. Once stabilised the target pressure the sample is rapidly heated up to the synthesis temperature. Under these conditions, solid state reactions are well-known to complete very fast, so the synthesis temperature is maintained during short reaction times, ranging from 6 to a maximum of 35 minutes for all the compounds discussed herein. For the optimal synthesis conditions of a particular compound see the text in the corresponding chapter. After the reaction time, temperature is quenched and pressure is slowly released, providing access to metastable phases kinetically favoured. The recoverability of a thermodynamical product at ambient pressure is conditioned to symmetry constraints [15].

Different *"large volume"* high pressure devices have been used as a function of the required pressure. In general terms, these instruments are often constituted by three main components: i) a hydraulic press, which provides the force to induce the uniaxial high pressure conditions; ii) a high pressure module, formed by the anvils which transmit the pressure from the press to the sample; and iii) the sample assembly, i.e. the pressure cell. Among these components, is the complexity of the pressure module what best characterises the different setups, since the hydraulic press is similar for all of them, just varying their force limits, and the sample assembly depends on the selected module. Attending to this factor HPHT devices can be classified into one- or two-stage types.

Both kinds of setups have been used to prepare the different polymorphs of Mn_2MSbO_6 compounds presented in this dissertation. On the one hand, moderate pressures have been accessed through the use of simple (one-stage) devices. For instance, a Belt-type press located at the *"Laboratorio de Altas Presiones"*of Universidad Complutense de Madrid (UCM), was used to achieve pressures up to 8 GPa and a Conac-type press, placed at the same laboratory, allowed the synthesis of larger amounts of sample treated under pressures up to 9 GPa . The need for higher pressures required the use of a two-stage Multianvil device, located at the School of Chemistry at the University of Edinburgh, accessed through the collaboration with the Center for Science at Extreme Conditions (CSEC). The specific characteristics of each press and the different sample assemblies used to develop the synthesis in each of them are detailed in the next subsections.

The accurate pressure and temperature applied during an experiment can be measured through different methods, although for all the experiments performed during this study, both magnitudes were controlled by the use of calibration curves. These curves are developed for each sample assembly design by applying different forces to the hydraulic fluid and power supplies to the furnace, using well known standard samples. Hence, the experimental pressure and temperature conditions during a synthesis process can be determined as a function of the applied force and electric power.

1.2.1 - One - stage devices

These setups allow the application of moderate pressures and the synthesis of relatively large amounts of sample. The setup used for the preparation of most of the compounds presented in this work belong to this type of instruments. In particular, a Belt- and a Conac-type presses, described below, have been used. It is worth noting that, although Diamond Anvil Cells (DAC), which are commonly used to study diverse properties of chemical compounds under HPHT conditions [16], should also be included among the one - stage devices uniaxially applying high pressures, they are not considered here for various reasons: i) DAC cells allow the manipulation of very small amounts of sample and they provide a limited access to heating the precursor in the synthesis process; since we have access to large-volume devices allowing the synthesis of larger amounts of sample under higher temperature conditions, necessary for the preparation of Mn_2MSbO_6 oxides, DAC cells are not optimal in our case. ii) DAC cells are often designed to apply high pressures during the performance of some measurements. This feature makes them an interesting tool for studying metastable compounds which do not persist back to room pressure; however, the Mn_2MSbO_6 high pressure phases stabilised under HPHT conditions are quenchable to room pressure, and their structural and functional characterisation do not require the use of any pressure cell.. Therefore, in this case there is no need to use these devices so, despite their importance in the high pressure science, the main contribution of this subsection is dedicated to more adequate devices for the objectives of this work: Belt- and Conac- setups.

Figure 2.1 depicts the indicated main components for this type of device, where both similarities and differences among these two equipment are evidenced. Their main difference relay on the pressure cell, which components are represented in the lower part of Figure 2.1a. Above them, their assemblies are schematised. In both cases, the precursor is compacted into a gold or platinum capsule. In the Belt-type cell, the capsule is introduced into an Al_2O_3 sleeve provided with two MgO stoppers. These pieces act as insulators, thus avoiding the appearance of hot spots which could induce the sample melting. This is placed into a graphite furnace, responsible for the sample heating during the experiment, in which extremes conic pieces of pyrophyllite are included. This material acts as a thermal and electric insulator and, when heated under high temperatures, behaves as a fluid, thus resulting an optimal pressure media enhancing the hydrostaticity of the induced pressure. On top of and below these pieces, Teflon rings prevent the pyrophyllite to flow away during the heating process.

In contrast, the Conac-type cell confines the sample capsule into a calcite ($CaCO_3$) container inside the graphite furnace and this one into two concentric $CaCO_3$ cylindrical sleeves provided with stoppers, what insulates the inner part of the assembly. An outer steel capsule is used in order to reinforce the cell insulation and Ta and Mo disks ensure the electric contact. In the outer part, two $CaCO_3$ pieces accommodate the pistons which induce the high pressures to the cell and three cardboard rings ensure the correct alignment.

A detail of the pressure module used in these devices is shown in Figure 2.1b for the Belt-type press, but a similar one is used for the Conac-type module. In both setups, the cell is placed in between two parallel plates made of different concentric materials: the centre, which includes the pistons inducing the pressure to the cell, needs for a higher mechanical resistance, so it is made of WC. The outer rings are designed to withstand not so high pressures, for which stainless steel is hard enough. Pressure is uniaxially induced though these plates to the cell along the direction shown by the arrows in Figure 2.1a.

Figure 2.1c depicts the complete Belt-equipment formed by the hydraulic press including the pressure module where the cell is aligned, a power supply and a temperature controller. A similar assembly forms the Conac-type press. Therefore, for both instruments the synthesis process is completely automated, allowing an accurate and precise control of both pressure and temperature conditions.

Chambers of different volumes can be adapted to these equipment, thus enabling the adequate optimisation of the pressure conditions as a function of the sample volume. In particular, the Belt-type press has a large chamber which can work up to 4 GPa producing a maximum of 300 mg of sample and a smaller one applying up to 8 GPa to a maximum sample amount of 100 mg. Temperatures up to 1973 K can be reached with this press. On the other hand, up to 2073 K can be attained with a Conac-type press, which possess three different chambers: the larger one allows the synthesis of 2.0 g under a maximum pressure of 5.5 GPa; the intermediate chamber produces a maximum of 750 mg under 7.5 GPa and the small one reaches up to 10 GPa in detriment of the sample amount, which cannot exceed 200 mg [17].

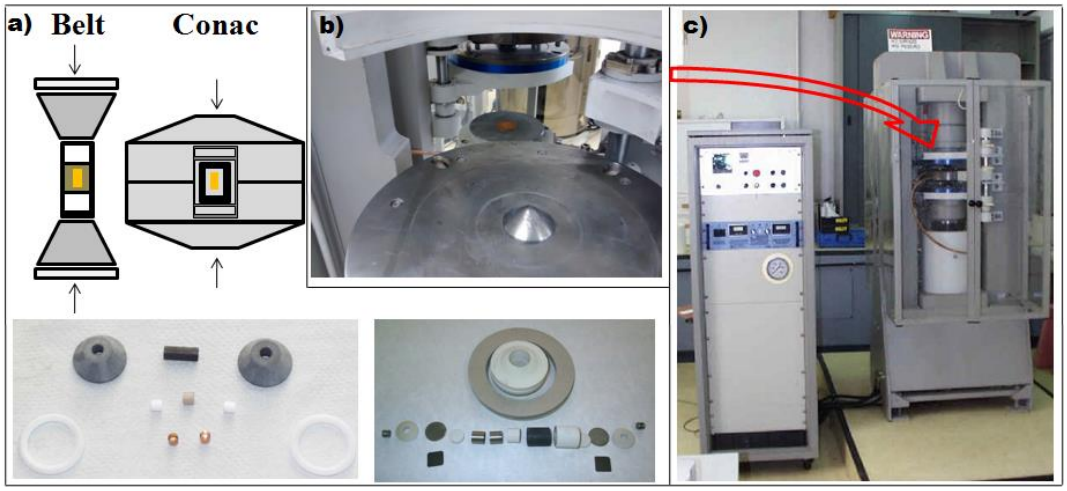

Figure 2.1. a) Schematic cell assemblies (up) for Belt- and Conac- type high pressure setups. The arrows indicate the uniaxial direction along which the pressure is applied to the cell. The cell components for each device are shown at bottom in the same relative position as the schemes. The color code used in the upper part of the Figure can be related to those of their respective real components at the bottom. b) Lower plate of the pressure module of the Belt equipment. In the middle of the plate the WC piston can be appreciated. Concentric stainless steel fragments are also visible around it. In this Figure the module is not aligned, so that the copper films inducing the electric contact to the lower part of this plate can also be seen besides it. The red arrow connecting Figures b and c points the place where the aligned module (constituted by both upper and lower plates) is located in the whole equipment. c) The complete press including the power supply and temperature controller on the left-hand side of the Figure and the hydraulic press with the aligned pressure module on the right.

1.2.2 - Multi-anvil device

Figure 2.2 shows the different parts of the more complex assembly characteristic of the Walker – type module [18] of the Multianvil apparatus used for the highest pressure synthesis. As in the simpler setups explained in the previous subsection, the sample is introduced into a Pt capsule which is surrounded by concentric layers of different materials in order to ensure the correct heating and transmission of pressure to the sample. As it can be observed in Figure 2.2a, the capsule is introduced into an h-BN cylinder provided with stoppers. The selection of this material is due to its soft, refractory and chemical inert features, so that it acts as an adequate confining media which protects the sample from the furnace, thus preventing its melting. Two different sized concentric graphite furnaces minimise the thermal gradient of the sample and additional thermal insulation of the capsule inside the furnaces is ensured by the presence of MgO stoppers and reinforced by an outer ZrO_2 sleeve. On both extremes Mo disks act as electric contacts and MgO rings around them insulate their environment, thus preventing the appearance of hotspots.

The whole cell is fixed into a drilled MgO octahedron, which induces the high pressure to the sample. The correct alignment of this assembly into the press comes through the insertion of the octahedron in between eight WC cubic anvils. These inner anvils, the so called second-stage anvils, are corner truncated cubes. The truncation of their corners originates an octahedral void in the centre of the eight cubes when connecting them through squared face sharing. Therefore, the octahedron is placed in the middle, sharing its triangular faces with the anvils triangular truncated sections. As a consequence, the pressure is symmetrically induced over the sample: the direction of the applied force from the hydraulic press into the sample through the press module is represented in Figure 2.2. with a blue arrow.

As schematised in Figures 2.2a and 2.2b, these second-stage anvils are differently prepared: four of them, the so called type 1 in Figure 2.2, are covered with adhesive tape and the other four (type 2 in Figure 2.2) with card paper, both over three consecutive faces. Pyrophyllite gaskets of different lengths are strategically fixed around the truncated corner of these second type of cubes, so that each type 1 – cube fixes next to the three adequate type 2 – cubes.

The large cube formed by the eight joined cubes holding the cell assembly is glued and stabilised by stacking it into pads of fibre glass. Two Cu sheets are contacted to opposite cubes (those connected through the blue arrow in the Figure), so that the electric current will pass through them across the furnace. This larger cube with the cell inside is introduced, as depicted at the bottom part of Figure 2.2b, in between six big anvils made of hardened steel. These anvils are known as first-stage anvils or wedges and they transmit the high pressure coming from the hydraulic press to the second-stage anvils, which finally transfer it to the cell. The function of the fibre glass pads is to relieve any stress caused by irregularities on the interface between the inner and outer anvils. All the assembly is confined into a containment ring (see left hand-side of Figure 2.2c) where all pieces, homogeneously lubricated, are placed as shown in the section included as an inset in Figure 2.2c. This Figure shows the hydraulic press, which is connected to the power supply and a temperature controller. As in the previous cases, the complete synthesis process is automated, ensuring the correct control of the synthesis conditions.

The sample assembly used for all the experiments run in this press during this study includes second-stage anvils with 14 mm of truncation edge length (TEL). The use of these anvils imply the use of an

8 mm octahedron, which can induce pressures up to 16 GPa to the sample. Given these dimensions this setup is often referred to as 14/8. The transmission of higher pressures is accessible through the use of anvils with shorter TEL, as this decreases the surface area in contact with the cell. A maximum pressure of 26 GPa can be achieved with the Walker - type multianvil apparatus using the 7/3 setup. The maximum temperature that can be supported with this module depends on the material used as furnace. During this work, all the sample assemblies included graphite heaters, which can induce up to 1773 K under the most extreme pressure conditions.

A limitation of this setup is the obtained sample amount, which is considerably smaller than those obtained with the Belt- or Conac-modules (not more than 10-20 mg) due to the higher pressures accessed.

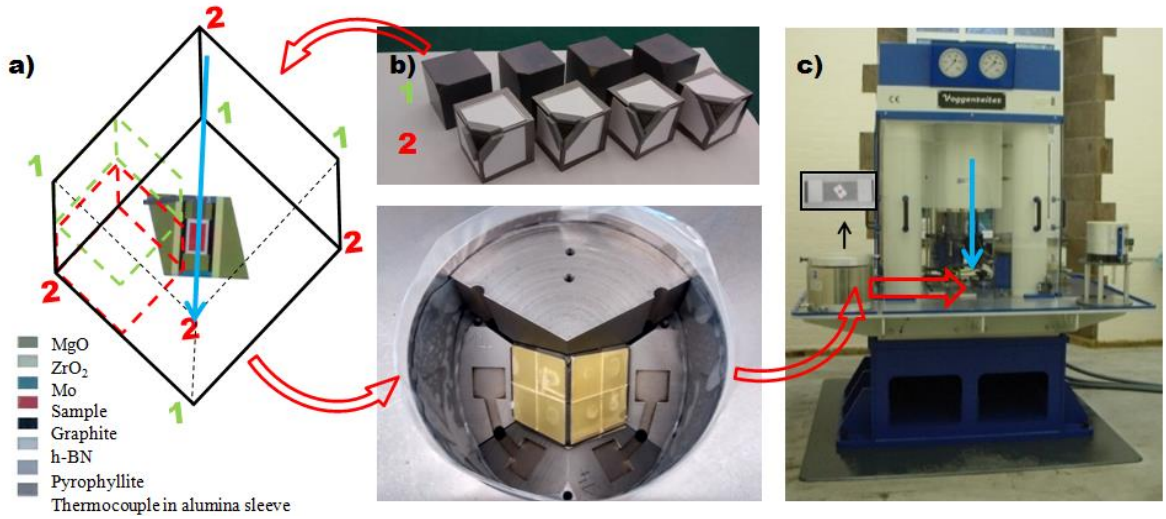

Figure 2.2. a) Scheme showing the components of the cell assembly and the arrangement of the eight inner anvils. Two different types of anvils are identified here as types 1 and 2 (green and red dashed cubes, respectively). b) in the upper part of Figure b the real appearance of both types of cubes is shown. At the bottom, the large cube constituted by the eight cubic anvils can be seen located into the containment ring within four out of the six wedges. The red arrow connecting this figure to Figure c identifies the containment ring among the components of the press. c) The complete hydraulic press. A section of the prepared containment ring is included above it as an inset. The red arrow in Figure c points the location of the containment ring during the HPHT experiment and the blue one points the direction along which pressure is applied to it. Note that the orientation of the cell along the diagonal direction of the cube coincides with this direction.

2. - Structural characterisation

The structural characterisation of the samples includes a large variety of experimental techniques. The complementary information provided by all of them leads to the complete determination of all structural features. In general terms, the main structural characterisation of the materials studied along this work has been performed in terms of diffraction methods. Therefore, this section is focussed on the description of the different diffraction techniques.

2.1 - Diffraction techniques. General overview

In general terms, diffraction techniques are non-destructive characterisation methods based on the coherent dispersion of the incident radiation as a consequence of the crystal periodicity. When a compound acquires long range atomic order, the location of atoms within the unit cell can be related through the appearance of planes with common features, generally called (hkl), where h, k and l are the well-known Miller indices. Moreover, parallel (hkl) planes are packed along their normal crystallographic direction, separated from the consecutive (hkl) planes by a constant distance *d*. These equidistant planes of common characteristics are altogether referred to as a family of planes {hkl}. An incident electromagnetic beam on the sample may give rise to a number of complex radiation - sample interactions. Among them, diffraction occurs as a consequence of dispersion effects: all atoms located in the same {hkl} are said to diffract the incident radiation when the angle of the diffracted beam equals the incident one. Under these conditions, Bragg Law, i.e., $n\lambda = 2d\sin\theta$ [19], is always satisfied.

It can be, thus, easily deduced that, under a monochromatic beam, only the irradiation under determined angles can satisfy this relation so that *n* is an integer. For those angles, the so-called Bragg angles, the phase difference between the incident and the diffracted beams is zero so both waves are said to be in phase. In other words, their interference is totally constructive. As consequence, diffraction peaks can be observed at those angles. When varying the incident angle partially destructive interferences appear, decreasing the peak intensity until it becomes null for totally destructive interferences, i.e., for semi-integer values of *n*.

The presence of different families {hkl} featured by different *d* values originates similar interference patterns under different Bragg angles. Hence, an incident beam scanning a continuous angular range results in the formation of a continuous pattern with peaks arising from different families of planes. This basic aspect of the diffraction pattern is, therefore, characteristic of the structural packing.

Up to here, only *d* spacing is taken into account as the basic feature determining the peak positions. However, some instrumental parameters, such as the axial divergence of the beam or the sample-beam alignment, and some sample properties, as absorption effects, may also influence the position of the reflections [20]. On the other hand, their intensities [21] mainly depend on the structure factor, $\left|F_{hkl}^2\right|$, which includes multiple contributions determined, among other parameters, by the distribution of atoms in the unit cell. Therefore, the different atomic scale factors induce a variation on the relative peak intensities of the diffraction patterns collected for compounds with common structures but different compositions.

Atomic positions can be related through symmetry operations, so equivalencies can be settled. By that, the structure can be explained in terms of the group of symmetry elements relating all the atoms

in the unit cell. This means the classification of the structure into one out of the 230 space groups described in the International Tables for Crystallography [22], what simplifies its description. It is worth noting that the different location of atoms within the reticular positions, i.e., different cation orderings in the structure, can induce important modifications on the diffraction result. A systematic cation ordering along any crystallographic direction may imply the definition of new {hkl}, where d_{hkl} spacing changes. As consequence, the position of the peaks can also be affected by cation ordering. Furthermore, the appearance of cell centring or translational symmetry elements creates new equivalences of planes, what nullifies the structure factor for some atomic positions, originating the systematic extinction of their related peaks. Hence, the observation of systematic absences is important information which facilitates the structural determination. In the end, cation ordering affects both peak intensities and positions.

In summary, the peak position is featured by the relative position of the atoms in the structure, so it is indicative of the dimensions of the unit cell and the location of the atoms inside. On the other hand, the intensity of the peaks depends on the nature of the nuclei originating them, so it allows differentiate which atom is located in each position.

These techniques allow, thus, a quick qualitative interpretation with no sample damage. The observation of a low number of peaks is related to a high symmetry, where most planes are related. As the symmetry decreases peaks are progressively split through the distinction of new {hkl}, so common general features can be observed for diffraction patterns of similar structures. As both the nature and location of the atoms are important factors, different polymorphs of a compound will present different patterns, with noticeable peak position differences. For the sake of our aims, this technique is, thus, optimal for studying the expected structural phase transitions induced under high pressures. Compositional differences for compounds with a common structure will present different relative peak intensities, also allowing their distinction and the study of the structural modifications induced by chemical pressure.

However, quantitative information can also be achieved from these methods. Small structural differences, such as atomic displacements from their ideal sites or their thermal vibrations, may induce subtle changes in the diffraction pattern. Note, anyway, that the structural features observed through diffraction methods are only those arising from the average structure. The determination of local effects needs the combination of different techniques.

The interest of combining different diffraction techniques is that the appreciation of different structural features is enhanced by each beam nature. The Rietveld refinement [23] of different diffraction data usually yields the complete structural determination of the studied compound. For that purpose, FullProf suite software was used [24].The optimisation [25] of the difference between experimental diffraction data and a reference theoretical pattern allows the determination of the exact structural features.

Among the parameters to take into account when refining a nuclear structure, some of them can be commonly considered for all the samples studied in this work. The most important are the background and the peak shape. Background was modelled either through the use of a six coefficient polynomial or through the linear interpolation of intermediate values for a given list of equidistant experimental points. The simulation of the experimental peak shape was developed through the use of a Thompson-Cox-Hastings type function. It is worth noting that the experimental peak shape is usually distorted

from the ideal Gaussian belt as consequence of diverse factors. The key parameters determining the final result arise from the used beam; in particular, its spectral purity and conditioning are the most important parameters, as the divergence of the incident beam induces uncertainty on the Bragg angle resulting in an asymmetric peak broadening arising from overlapped signals. The employed diffraction geometry also adds some uncertainty on the signal detection. Additionally, some sample properties may also have a significant influence on the peak shape, among which the grain size and strain / stress effects are the most usual. In order to reproduce the shape modifications originated from the main instrumental factors a number of mathematical corrections can be used [24], among which the Thompson-Cox-Hastings pseudo-Voigt approximation was selected for these samples due to its accurate determination of Gaussian and Lorentzian contributions with different origins. For the most complex cases, the use of a resolution file provided the instrumental (U, V, W) parameters so that the refinement of the additional (X, Y) shape-factors determines additional peak distortions arising from the structural features. Common instrumental parameters were coupled for secondary phases through the use of the general pseudo Voigt function.

On the other hand, some specific considerations were taken for each structural refinement, as site-coupling or constraint models used for the optimization of thermal parameters, occupancies, antisite disorders, etc. These particular details, along with the complex symmetry analysis needed for the determination of some magnetic structures, are detailed in the adequate subsequent chapters for each compound.

It is clear from this general introduction about diffraction methods that not only the sample but also the nature of the beam irradiating it exerts an important influence on their interaction. For that reason, the particularities of each diffraction technique are detailed in the next subsections. The features determining the relative reliability of their results and which information is more accurate for each method is explained.

2.1.1 - X-ray diffraction

Powder X-ray diffraction (PXRD) has been used as the basic tool for structural characterisation. The easy and cheap generation of X-rays along with the useful and easy interpretation of the results make XRD a classical method to determine crystal structures.

The wavelength of the X-ray radiation is of the order of 1 Å. The atomic scale of this value allows the X-ray radiation to interact with the outer electron shell of the elements in the structure. Therefore, the main contribution to the determination of non-equivalent positions is the difference on the electronic environment of each site - located elements. As a consequence, XRD is a good technique for characterising the average position of heavy elements. The larger the difference on the atomic number (Z) is, the easier the cationic distinction. However, this technique is limited in the determination of light atoms, so oxygen is commonly fixed in its ideal positions when refining the structure. Moreover, distinguishing between two elements with similar Z numbers among different crystallographic sites is also difficult through XRD. In that case, apparent disorder effects might occur, thus leading to an incorrect symmetry assignment [3]. In order to correctly determine both the accurate position for light atoms and the correct positions of similar cations, complementary techniques are necessary. As explained in the next subsection, the different nature of neutron beams induce a different radiation - matter interaction, adequate for solving these problems.

During the experimental period of this study different X-ray diffractometers working in Bragg-Brentano geometry have been used for qualitative determinations. In all cases, quick scans of 15-30 minutes were collected in a maximum angular range 10 º ≤ 2θ ≤ 90 º. With this aim, a Siemens D 5000 (Bruker) and a PANanalytical X'pert POWDER diffractometers were used in the *"Centro de Asistencia a la Investigación (CAI)-Difracción de Rayos X"* at UCM [26]. Both use Cu K_α radiation. The first of them works under a voltage of 40 kV and a current intensity of 30 mA while the second one works under 45 kV and 40 mA. Patterns were collected at room temperature with step sizes of 0.02 º - 0.04 º depending on the sample crystallinity. Additionally, the samples with the lowest diffraction intensity were measured under a rotation time of 8 seconds in order to improve the collection statistics.

Additionally, a D2 Phaser-Bruker diffractometer [27] was used with the same purpose at the School of Chemistry in the University of Edinburgh. This instrument works under 30 kV and 10 mA. Routine patterns were collected with a step size of 0.0365 º. Complete patterns can be collected in 15 minutes with this diffractometer due to the proximity between the font and the detector. However, the resulting data, which include small peaks arising from Cu K_β radiation, are only valid for phase identification and subsequent high resolution measurements are needed.

This necessity is mandatory for pure samples after any routine XRD measurement, as the determination of crystallographic information requires a high resolution. Therefore, slow scans were measured with an X'Pert PRO ALPHA1 multi-purpose diffractometer working in Bragg-Brentano geometry with θ - 2θ configuration. This instrument uses Cu $K_{\alpha1}$ radiation and is equipped with a Ge (111) monochromator and an X'Celerator detector. Diffraction patterns were taken between 10 º and 120 º with a step size of 0.017º.

The study of temperature effects on the structure was developed through thermodiffraction experiments by heating the sample. This technique was used in order to study the thermal activation of perovskite – ilmenite phase transition in Mn_2MSbO_6 oxides with M = trivalent transition metal ions. A PANanalytical X'pert Pro MPD diffractometer provided with an Anton Paar HTK1200 high temperature chamber was used under temperatures up to 1223 K. Cu K_α radiation and θ – θ configuration were employed to measure diffractograms between 10 º and 70 º with a step size of 0.033 º.

High resolution XRD measurements at low temperatures were developed by using synchrotron radiation. The high energy reached by the accelerated electrons allows the beam interaction with deeper electronic layers thus providing a better resolution, so the use of this technique provided reliable data for small samples at room temperature. BLO4-MSPD ALBA lightsource beam line [28] was accessed in order to collect HRXRD patterns under a λ = 0.44214 Å wavelength beam in the angular range 0.021 º < θ < 44.001 º with a step width of 0.003 º. Further symmetry reduction and temperature variations of the lattice parameters were studied at low temperatures.

2.1.2 - Neutron Diffraction

The basic aspects of the fundamental theory concerning Neutron Powder Diffraction (NPD) are the same already explained for XRD. Despite its similar wavelength, the uncharged nature of the neutron beam promotes its interaction with the nuclei of the atoms. It is also worth noting that neutrons have a magnetic moment, so that NPD is used with a double intention: on the one hand, room temperature measurements allow the determination of nuclear structures, just as XRD did. Furthermore, the interacting nuclei are about 10^{-4} times smaller than the neutron beam wavelength, so phase effects are suppressed. On the other hand, NPD measurements detect the neutron - spin interaction when magnetic ordering is present in the sample. Therefore, neutron magnetic scattering is used to determine the magnetic structures of the compounds.

Obviously, the most evident advantage of NPD against XRD is the possibility of determining magnetic structures. However, when analysing nuclear structures some important advantages can also be noted. To start with, the direct interaction of the incident beam with nuclei and not just with their electronic environment enhances the diffraction induced by atoms with small Z values. As a consequence, NPD allows the accurate determination of light atoms. In the case of the compounds studied here, this feature is particularly interesting in order to determine the accurate positions of oxygen atoms, thus obtaining reliable values for polyhedral distortions and octahedral tilting in DPv polymorphs. Moreover, the dispersive power is not the electronic density anymore, but the coherent cross section [29]. This magnitude is very sensitive to both light and heavy atoms, and is often useful to distinguish even isotopes. Among the structures presented here, as detailed in chapter IV, the mentioned apparent cation disorder effects appearing through XRD between two crystallographic positions occupied by heavy atoms similar in weight, can be solved through NPD as a consequence of their different cross sections [3].

The main disadvantage of this technique is that some nuclei, e.g. some R^{3+} cations, strongly absorb neutron radiation. This effect obscures the diffraction phenomenon, so compounds containing these specific rare earth elements are not good candidates to determine their structures through NPD and different techniques or non-absorbing isotopes must be used.

Two different methods are commonly used in large scale facilities to generate the neutron beam: nuclear fission and spallation. The first of them is a continuous source of neutron beams with a very high energy. It is generated when a slow neutron impacts into an active nucleus, often enriched uranium, which absorbs the energy and produces an accelerated neutron in the decay process as a consequence of the division of the excited nucleus into two stable nuclei in their ground states. Spallation sources generate a higher proportion of secondary neutrons of lower energy by impacting an accelerated proton or electron into a nucleus which losses mass by releasing different particles. Therefore, pulsed beams of *cold* neutrons are generated in these sources, which are afterwards accelerated up to the desired velocity. Because of the variable energy, diffraction of these neutron beams is commonly detected in terms of the time of flight (TOF) of the diffracted neutrons instead of their angular range.

During this work, both CW and TOF NPD techniques have been used. Among those using fixed λ, D1B, D2B and D20 instruments located at *Institut Laue - Langevin* (ILL) [30] were selected due to their high intensity and resolution, because of the small amounts of sample for HPHT products. For the same reason the selected diffractometer using variable λ was WISH, located at ISIS source [31].

In general terms, the structural determination of small samples using NPD was carried out through the Rietveld refinement of D2B high resolution data. Long scans were collected under 300 K in the 0 º - 160 º 2θ range with a step-width of 0.05 º using a neutron wavelength λ = 1.594 Å. Magnetic structures were determined through the Rietveld refinement of D2B NPD data collected under temperatures below the magnetic order temperature, previously determined from magnetic susceptibility measurements, in the same experimental conditions using a standard orange He cryostat. The small amount of sample usually required the use of small vanadium cans and the shortest accessible sample - collimator distance. Figure 2.3a shows a general view of D2B instrument indicating its most important components (see figure caption for details).

The thermal evolution of the magnetic structures was studied in terms of the sets of patterns collected each degree from 2 K to a temperature well above the magnetic order on the high intensity D1B instrument. Each pattern was measured in the angular range 0 º≤ 2θ ≤ 130 º with a step-width of 0.1 º using λ = 2.520 Å. Long scans were also collected at both the highest and the lowest temperatures in the same experimental conditions in order to properly compare the complete pattern including nuclear and magnetic reflections with that obtained from purely nuclear diffraction. The main components of this instrument are labelled on Figure 2.3b.

D20 is a very high intensity 2-axis instrument equipped with a large one-dimensional multidetector (see Figure 2.3c). The combination of this detector along with the high flux received by this diffractometer enables real-time measurements in small samples. For that reason, it was used in order to determine the nuclear structure of some HPHT samples. These measurements were collected with a λ = 2.4 Å radiation in the range 0 º - 130 º with a step size of 0.1 º.

Some of the samples prepared at CSEC were also diffracted in collaboration at WISH instrument. This diffractometer [32] is located in the target station 2 at ISIS facility. It provides high resolution in detriment of flux intensity and it is commonly used for determining nuclear and magnetic structures of powder samples with large *d* spacing. The especially small amount of sample and the large cell parameters determined for $MnRMnSbO_6$ compounds from XRD and electron microscopy techniques are specific features making WISH the ideal instrument for them.

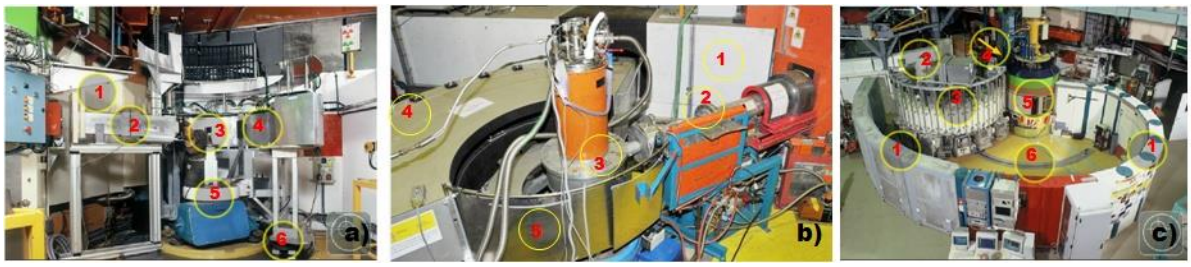

Figure 2.3. General views of D2B (a), D1B (b) and D20 (c) diffractometers located at ILL. Their main components are labelled as follows: a) 1-Shielding of the thermal beam H11; 2-Collimator of the incoming monochromatic beam; 3-Sample position; 4-Multidetector; 5-Sample table (ω rotation) and 6-Air cushion (2θ rotation). b) 1-Thermal neutron guide H22; 2-Collimator of the incoming monochromatic beam; 3-Sample position, provided with a He cryostat; 4-Multidetector (Position Sensitive Detector) and 5-Beam stop. c) 1-Anti-backgroung shielding walls; 2-Sample position; 3-Position sensitive detector (microstrip gas-chamber assembly); 4-Direction of the neutron beam; 5-Monochromator housing and 6-rotation of the diffractometer around the monochromator axis.

2.1.3 - Electron diffraction and electron microscopy experiments

A high-energy electron beam focused over the sample produces a number of different types of interactions. For instance, absorption, transmission, and scattering (elastic and inelastic) effects are commonly observed. Moreover, backscattered, secondary and Auger electrons, X-rays and visible light are also produced. Therefore, electron microscopy is a useful technique providing access to a wide range of structural and microstructural information [33].

In general terms, two main techniques can be discerned, namely transmission and diffraction modes. Modern microscopes include a large variety of qualitative and quantitative analysis. Those used during this study are briefly explained in this subsection.

The negative nature of electrons implies their coulombic interactions with the electronic shells of the atoms in the structure. Therefore, as it occurs in XRD, the larger the difference between the Z number of two elements, the easier their distinction. The particularity of electron diffraction (ED) against XRD and NPD is that diffraction patterns are converted through Fast Fourier Transform (FFT) from images collected in the transmission mode or directly collected in reciprocal space in the diffraction mode. As a consequence, the distance between diffraction spots increases with increasing incident angle, what means shorter *d* spacing in real space. Hence, this technique is of special interest when studying structures with a high atomic density, as the proximity of their atoms in real space is easier to determine in reciprocal space.

The transmission mode enables the collection of contrast images. Recording different crystallographic orientations allows a complete cell reconstruction, thus facilitating the determination of cationic order in unknown structures. The main disadvantages of these techniques are the complex interpretation of results, e.g., dynamic diffraction effects, and the similarities between atoms with near Z values, what may prevent the distinction between elements similar in weight, leading to an apparent disorder.

However, the complementarity of different techniques is a clear advantage. All the samples were studied in the *"Centro Nacional de Microscopía Luis Bru"* at UCM [34]. High resolution transmission electron microscopy (HRTEM) images were taken in a JEOL JEM 3000F microscope operating at 300 kV, provided with a double tilt (±20°) goniometer and point resolution 0.17 nm. Accurate composition and oxidation states were studied through electron energy loss spectroscopy (EELS) in the same microscope, fitted with an energy-dispersive X-ray spectroscopy (XEDS) microanalysis system (OXFORD INCA) and ENFINA spectrometer with an energy resolution of 1.3 eV. Selected area electron diffraction (SAED) and microdiffraction were carried out in a JEOL JEM2100 microscope operating at 200 kV with a double tilt (±45°) goniometer. Additional Scanning-Transmission Electron Microscopy (STEM) images were collected for the samples with the most complex cation orderings in a JEOL JEM ARM200cF microscope with corrected aberration in the condenser lens providing atomic resolution. This microscope, provided with a digital X-ray mapping, operates at 200 kV and has a point resolution of 0.2 nm in TEM mode and 0.08nm in STEM mode.

Simulations of the HRTEM images were performed with the software MacTempas X [35], using the refined structures from PND data as a reference. In all cases, the results showed good fits to the experimental images, as discussed in the results chapters. Therefore, the different diffraction techniques always provided complementary information fully confirming the results.

3. - Magnetic characterisation

The determination of the magnetic properties was carried out from the magnetisation and magnetic susceptibility measurements at different temperatures and magnetic fields. A MPMS-SQUID (Magnetic Property Measurement System - Superconducting Quantum Interference Device) Quantum Design Magnetometer was used in order to measure temperature effects on the magnetisation (M) of the samples under different magnetic field strengths (H). With that purpose, all the samples were measured under similar conditions: the first step is cooling the sample down to 2 K without any magnetic field and measure how heating up back to room temperature affects the magnetisation. The results of this measurement are commonly known as ZFC (Zero Field Cooling) data. Then a magnetic field is applied and stabilised to a constant value and the sample is cooled again down to 2 K. The magnetic field used for most of the measurements developed during this project is 0.1 T; any exceptions for additional measurements under different magnetic fields are detailed in the corresponding chapter for each sample. Under this FC (Field Cooling) conditions, the sample magnetisation is again measured under heating up to room temperature.

Magnetic susceptibility is then calculated as the M / H ratio per molar unity. Direct and reciprocal representations of this magnitude and their differentiate products provide useful information including the number of spin sublattices ordering at different temperatures and their approximate temperature values, the Curie and Weiss constants and the effective magnetic moment.

The global type of magnetic ordering can be deduced from these measurements in terms of the maximum susceptibility values, the tendency of the direct ZFC curve at low temperatures, the relative behaviour of ZFC *vs.* FC curves and the sign of the Weiss constant determined from the linear fit of the paramagnetic range in the reciprocal data. However, the presence of magnetic interactions between the different magnetic sublattices, common among the compounds studied here, may complicate the interpretation of these results. Additional information is obtained through the measurement of field effects on the magnetisation at constant temperatures. With that purpose, different magnetic fields up to 9T were applied. These measurement temperatures are selected from the previous susceptibility data. As a general approach, temperatures above, near and below the magnetic transitions are often selected. By that, the different curves can be compared: the saturation of the magnetisation curve below the magnetic transition temperature typically indicates a ferromagnetic (FM) behaviour, as the increase of the applied magnetic field cannot increase the magnetisation any more, i.e. the maximum ordered magnetic moment is reached so the maximum value may be the saturation of the magnetic moments in the structure. Antiferromagnetic (AFM) components are easily identified as the magnetic moments cancel and their orientation with the magnetic field is a long process which do not reach saturation, and the onset of a net maximum in the susceptibility versus temperature determines the Néel temperature. Moreover, complete loops in the $-5\ T < H < 5\ T$ field range include hysteresis effects for FM compounds facilitating their identification. Intermediate situations as pure ferrimagnetic behaviors arising from the antiparallel orientation of two different FM sublattices, or net ferrimagnetic compounds with different AFM sublattices are easily identified but difficult to quantitatively characterise. Further NPD experiments are necessary to determine the magnetic structures which finally explain the magnetic behaviour observed from these bulk susceptibility and magnetisation measurements.

4.-Bibliography

[1] Bazuev G.V., Golovkin B.G., Lukin N.V., Kadyrova N.I., Zainulin Y.G. High Pressure Synthesis and Polymorphism of Complex Oxides Mn_2BSbO_6 (B= Fe, V, Cr, Ga, Al). J. Solid State Chem. 1996;124:333–7. doi:10.1006/jssc.1996.0246.

[2] Ivanov S., Nordblad P., Mathieu R., Tellgren R., Politova E., André G. Short-Range Spin Order and Frustrated Magnetism in Mn_2InSbO_6 and Mn_2ScSbO_6. Eur. J. Inorg. Chem. 2011;30:4691–9. doi:10.1002/ejic.201100381.

[3] Solana-Madruga E., Dos santos-García A.J., Arévalo-López A.M., Ávila-Brande D., Ritter C., Attfield J.P., et al. High pressure synthesis of polar and non-polar cation-ordered polymorphs of Mn_2ScSbO_6. Dalt. Trans. 2015;44:20441–8. doi:10.1039/C5DT03445K.

[4] Tyutyunnik A.P., Bazuev G.V., Kuznetsov M.V., Zainulin Y.G. Crystal structure and magnetic properties of double perovskite Mn_2FeSbO_6. Mater. Res. Bull. 2011;46:1247–51. doi:10.1016/j.materresbull.2011.04.001.

[5] Dos santos-García A.J., Ritter C., Solana-Madruga E., Sáez-Puche R. Magnetic and crystal structure determination of Mn_2FeSbO_6 double perovskite. J. Phys. Condens. Matter 2013;25:206004. doi:10.1088/0953-8984/25/20/206004.

[6] Dos santos-García A.J., Solana-Madruga E., Ritter C., Ávila-Brande D., Fabelo O., Sáez-Puche R. Synthesis, structures and magnetic properties of the dimorphic Mn_2CrSbO_6 oxide. Dalt Trans 2015:10665–72. doi:10.1039/C4DT03849E.

[7] Mathieu R., Ivanov S.A., Solovyev I.V., Bazuev G.V., Anil Kumar P., Lazor P., et al. Mn_2FeSbO_6: A ferrimagnetic ilmenite and an antiferromagnetic perovskite. Phys. Rev. B 2013;87:014408. doi:10.1103/PhysRevB.87.014408.

[8] Mathieu R., Ivanov S.A., Bazuev G.V., Hudl M., Lazor P., Solovyev I.V., et al. Magnetic order near 270 K in mineral and synthetic Mn_2FeSbO_6 ilmenite. Appl. Phys. Lett. 2011;98:202505–1 – 202505–3. doi:10.1063/1.3593194.

[9] Hudl M., Mathieu R., Nordblad P., Ivanov S.A., Bazuev G.V., Lazor P. Investigation of the magnetic phase transition and magnetocaloric properties of the Mn_2FeSbO_6 ilmenite. J. Magn. Magn. Mater. 2013;331:193. doi:10.1016/j.jmmm.2012.11.040.

[10] Li M-R, Walker D., Retuerto M., Sarkar T., Hadermann J., Stephens P.W., et al. Polar and Magnetic Mn_2FeMO_6 (M=Nb, Ta) with $LiNbO_3$ -type Structure: High-Pressure Synthesis. Angew. Chemie 2013;125:8564–8. doi:10.1002/ange.201302775.

[11] Li M-R, Croft M., Stephens P.W., Ye M., Vanderbilt D., Retuerto M., et al. Mn_2FeWO_6: a New Ni_3TeO_6-Type Polar and Magnetic Oxide. Adv. Mater. 2015, doi:10.1002/adma.201405244.

[12] Li M-R, Retuerto M., Walker D., Sarkar T., Stephens P.W., Mukherjee S., et al. Magnetic-Structure-Stabilized Polarization in an Above-Room-Temperature Ferrimagnet. Angew. Chem Int. Ed. Engl. 2014;53:10774–8. doi:10.1002/anie.201406180.

[13] Solana-Madruga E., Dos santos-García A.J., Arévalo-López A.M., Ávila-Brande D., Ritter C., Attfield J.P., et al. High pressure synthesis of polar and non-polar cation-ordered polymorphs

of Mn_2ScSbO_6. Dalt. Trans. 2015;44:20441–8. doi:10.1039/c5dt03445k.

[14] Solana-Madruga E., Arévalo-López Á.M., Dos santos-García A.J., Urones-Garrote E., Ávila-Brande D., Sáez-Puche R., et al. Double Double Cation Order in the High-Pressure Perovskites $MnRMnSbO_6$. Angew. Chemie - Int. Ed. 2016;55:9340–4. doi:10.1002/anie.201603526.

[15] Grochala W., Hoffmann R., Feng J., Ashcroft N.W. The chemical imagination at work in very tight places. Angew. Chemie - Int. Ed. 2007;46:3620–42. doi:10.1002/anie.200602485.

[16] Jayaraman A. Diamond anvil cell and high-pressure physical investigations. Rev. Mod. Phys. 1983;55:65–108. doi:10.1103/RevModPhys.55.65.

[17] Laboratorio de Altas Presiones, UCM. http://pendientedemigracion.ucm.es/info/labcoap/INSTRU.htm.

[18] Walker D., Carpenter M.A., Hitch C.M., Street D., Kingdom U. Some simplifications to multianvil devices for high pressure experiments. Am Mineral 1990;75:1020–8.

[19] Tilley RJD. Crystal and crystal structures. 2006.

[20] Pecharsky V., Zavalij P.Y. Fundamentals of Powder Diffraction and Structural Characterization of Materials. 2005. doi:10.1007/978-0-387-09579-0.

[21] Woolfson M.M. An Introduction to X-Ray Crystallography. doi:10.1524/zkri.1998.213.5.308.

[22] Crystallography TIUO. International Tables for Crystallography Volume A: Space-Group Symmetry. 2005. doi:10.1107/97809553602060000100.

[23] McCusker L.B., Von Dreele R.B., Cox D.E., Louër D., Scardi P. Rietveld refinement guidelines. J. Appl. Crystallogr. 1999;32:36–50. doi:10.1107/S0021889898009856.

[24] Rodríguez-carvajal J. An introduction to the program FullProf 2000. 2001.

[25] Toby B.H. R factors in Rietveld analysis: How good is good enough? Powder Diffr. 2006;21:67–70. doi:10.1154/1.2179804.

[26] Centro de Asistencia a la Investigación: DRX, http://pendientedemigracion.ucm.es/centros/webs/cai5084/index.php?tp=Difracci%F3n de Polvo&a=dir3&d=23115.php.

[27] Bruker, http://www.d2phaser.com/en/#129-technical-data.

[28] ALBA Lightsource, http://www.cells.es/en/beamlines/bl04-mspd.

[29] Sears V.F. Neutron scattering lengths and cross sections. Neutron News 1992;3:26–37. doi:10.1080/10448639208218770.

[30] Institut Laue Langevin, https://www.ill.eu/

[31] ISIS, http://www.isis.stfc.ac.uk/instruments/wish/wish-6465.html.

[32] Chapon L.C., Manuel P., Radaelli P.G., Benson C., Perrott L., Ansell S., et al. Wish: The New Powder and Single Crystal Magnetic Diffractometer on the Second Target Station. Neutron News 2011;22:22–5. doi:10.1080/10448632.2011.569650.

[33] Williams D.B., Carter C.B. Transmission Electron Microscopy: A Textbook for Materials Science. vol. V1-V4. 2009. doi:10.1007/978-1-61779-415-5_23.

[34] Centro Nacional de Microscopía Luis Bru, http://www.cnme.es.

[35] Mac Tempas X. Version 2.3.7. A program for simulating HRTEM images and diffraction patterns.

III. Results and discussion

Mn_2MSbO_6 with M = d^n transition metals

1.-General introduction

$Mn^{2+}{}_2M^{3+}SbO_6$ oxides present mainly two different polymorphs under different (high) pressure and (high) temperature (HPHT) conditions. When synthesised under moderate pressures, the corundum derivative ilmenite (ILO) and Ni_3TeO_6-type (NTO) structures are usually stabilised in these systems [1,2], but their synthesis under higher pressure conditions favours the stabilisation of a B-site rock-salt double perovskite (DPv) structure [3]. The progressive structural distortion upon introducing larger M^{3+} cations and the evolution of the magnetic behaviour of both polymorphs upon changing the number of electrons in the outer shell of the M metal will be studied through the next chapters. In particular, this chapter is devoted to the study of $Mn^{2+}{}_2M^{3+}SbO_6$ compounds with M = Cr^{3+} and Fe^{3+} cations, which paramagnetic nature is expected to induce complex magnetic behaviours through the coupling of two different magnetic sublattices.

As a consequence of the results discussed during this chapter, a further structural evolution will be pursued through the substitution of M by much larger metals along chapters IV and V. In this context, the next chapter studies the Mn_2MSbO_6 with M being a closed shell d^0 transition metal, such as Sc^{3+}, what will enable an easier understanding of the magnetic behaviour of the A-site Mn^{2+} lattice. This will set the starting point for introducing $4f^n$ rare earths, which will be the main task of chapter V.

The occurrence of a representative collection of both common (AFM, ferrimagnetic) and exotic magnetic behaviours (helical spin structures and spin reorientation processes from commensurate to incommensurate propagation vectors) is studied along this chapter through the substitution of M by two different $3d^n$ transition elements (Cr^{3+}, Fe^{3+}) into two polymorphs of Mn_2MSbO_6 oxides. Their synthesis under HPHT conditions was optimised through the detailed study of the effects of the three main parameters determining the resulting structure, i.e. pressure, temperature and reaction time [4,5]. In general terms, increasing pressure leads to the stabilisation of denser structures during the synthesis process [6]. Consequently, DPv polymorphs are obtained under the highest pressure conditions applied (up to 8 GPa), while the corundum derivative structures are found at moderate pressures (3 GPa for the ILO-compounds). The DPv is the kinetic product, according to its fast crystallisation under extreme conditions, but the larger thermodynamic stability of the corundum related polymorph competes at high temperatures and when the reaction time is long enough.

This interplay between the preferential formation of the kinetic / thermodynamic product is usually found in the context of HPHT synthesis, which often allows the isolation of both polymorphs upon optimising the reaction conditions. However, the high pressure phases are often metastable products, which frequently revert to the thermodynamic phase either upon heated at room pressure (e.g., DPv to ILO transition of Mn_2CrSbO_6 [1]), heated at high pressures (e.g., possible DPv to NTO transformation of Mn_2ScSbO_6, see next chapter for details) / pressed at room temperature (e.g. $ZnGeO_3$ [7]) or even just as a function of time at room pressure and temperature conditions (e.g. diamond to graphite transition of C in the presence of oxidising agents [8]). Therefore, the thermal treatment of the high pressure phase will also be studied as an alternative method for the isolation of the thermodynamic product, i.e. the moderate pressure polymorph.

Along the next sections, a complete structural and functional characterisation is discussed for both polymorphs of Mn_2MSbO_6 (M = Cr and Fe) to determine the structure – properties relationship in these compounds.

2.-Mn_2CrSbO_6

2.1- Double perovskite

2.1.1 - Synthesis and structural characterisation

The DPv polymorph of Mn_2CrSbO_6 was synthesised under HPHT conditions. The precursor mixture was prepared by grinding the stoichiometric amounts of the binary Mn_2O_3, Cr_2O_3 and Sb_2O_3 oxides under acetone in an agate mortar. The resulting homogeneous powder was pressed into a platinum capsule, placed in a Conac-type press at 8 GPa and 1473 K during 15 minutes. Once the reaction was completed, temperature was quenched and pressure was slowly released.

A first structural characterisation through XRD (Figure 3.1a-top) shows that Bragg reflections of the resulting powdered sample can be fitted to the $P2_1/n$ space group with cell parameters $\sqrt{2}a_p * \sqrt{2}a_p * 2a_p$, where a_p is the cubic perovskite cell parameter (~ 3.8 Å). Minor secondary $MnCr_2O_4$ (4.2 %w.t.), Sb_2O_4 (4.8 %w.t.) and $Mn_2Sb_2O_7$ (< 1 %w.t.) phases were also identified and taken into account in the refinement.

Further structural characterisation was developed by NPD studies. Since all the elements in this compound present sufficiently different coherent neutron scattering lengths (coh b = -3.73 fm, 3.635 fm, 5.57 fm and 5.803 fm for Mn, Cr, Sb and O respectively [9]) the atomic positions could be accurately determined. The Rietveld refinement of the high resolution NPD data collected at room temperature at D2B diffractometer, depicted in Figure 3.1a-bottom, confirm the XRD model. Mn_2CrSbO_6 crystallised in the $P2_1/n$ space group with a = 5.2180 (2) Å, b = 5.3710 (2) Å, c = 7.5874 (1) Å and β = 90.36 (1)º lattice parameters. The structural details, including lattice parameters, atomic potions and selected bond lengths and angles, are summarised in Table 3.1

The DPv structure of Mn_2CrSbO_6 compound locates the small Mn^{2+} at the large cuboctahedral A site (4e), while Cr^{3+} and Sb^{5+} cations alternate in a rock-salt fashion among the B (2d) and B' (2c) sites. There are three different oxygen positions within the general 4e site, identified as O_1, O_2, and O_3. A portion of the crystal structure, including the crystallographic unit cell, is depicted in Figure 3.1b, where Cr and Sb cations are denoted as dark and pale blue octahedra. $P2_1/n$ gives rise to the $a^-a^-c^+$ tilt system commonly observed in $A_2BB'O_6$ double perovskites [10]. This tilt system determines the out-of-phase and in-phase rotations of BO_6 / $B'O_6$ octahedra along [110] and [001] directions respectively, visible in the top and bottom projections of Figure 3.1b.

Both the cation order and the described octahedral tilting originate the so-called diagonal $\sqrt{2}a_p * \sqrt{2}a_p * 2a_p$ cell commonly found for similar B-site rock-salt ordered double perovskites [11]. It is worth noting that a certain proportion of cationic disordering is commonly promoted in DPv by the coexistence of different cationic size/charge ratios. The varying Mn^{2+} / M^{3+} and M^{3+} / Sb^{5+} size relations could induce a progressive A-B site exchange determining the different properties and polymorphism of Mn_2MSbO_6 oxides. However, no antisite disorder was found either between B and B' sites or among A and B sites in Mn_2CrSbO_6 perovskite.

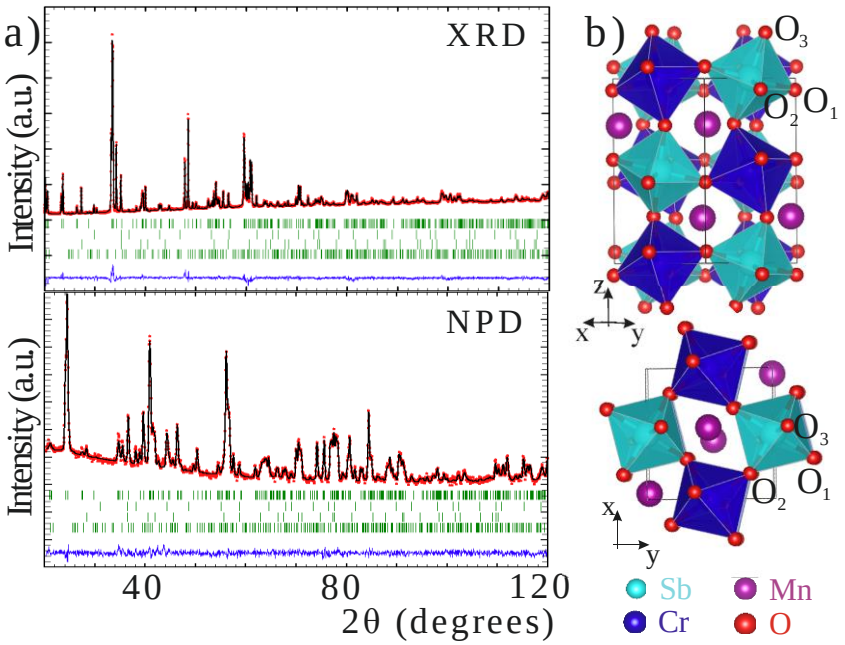

Figure 3.1. a) Rietveld refinements of Mn_2CrSbO_6 DPv polymorph from XRD (up) and NPD (bottom) data; $MnCr_2O_4$, Sb_2O_4 and $Mn_2Sb_2O_7$ secondary phases are included (2nd to 4th rows of Bragg positions respectively). b) Structural model determined from the Rietveld fit of the NPD. Out-of-phase and in-phase $a^-a^-c^+$ tilts are visible along [110] and [001] directions respectively.

Table 3.1.Crystallographic parameters, selected bond distances and angles for the DPv polymorph of Mn_2CrSbO_6 obtained from the Rietveld refinement of NPD data collected at D2B at 300 K.[a)]

P*2₁/*n	a = 5.2180 (2) Å, b = 5.3710 (2) Å, c = 7.5874 (1) Å, β = 90.36 (1) º				
Atom-site	x	y	z	Occ	BVS [b)]
Mn– 4e	0.0149 (8)	0.0471 (7)	0.7463 (7)	1	1.8
Cr– 2d	0.5	0	0	1	2.8
Sb – 2c	0	0.5	0	1	5.4
O_1 – 4e	0.3116 (7)	0.3073 (9)	0.9386 (5)	1	—
O_2 – 4e	0.3143 (6)	0.3073 (9)	0.5640 (4)	1	—
O_3 – 4e	0.8788 (5)	0.4454 (5)	0.7540 (4)	1	—

A-O	**d (Å)**	**B-O**	**d (Å)**
Mn- O_1	2.539 (6)	Cr - O_1 (x2)	1.975 (5)
Mn - O_1	2.113 (6)	Cr - O_2 (x2)	1.997 (4)
Mn- O_2	2.517 (6)	Cr - O_3 (x2)	2.053 (3)
Mn- O_2	2.123 (6)	$d_{av.}$(Cr - O)	2.008 (2)
Mn- O_3	2.255 (5)	Sb - O_1 (x2)	1.986 (4)
Mn- O_3	2.126 (5)	Sb - O_2 (x2)	1.976 (4)
$d_{av.}$(Mn- O)	2.279 (4)	Sb - O_3 (x2)	1.989 (3)
		$d_{av.}$(Sb - O)	1.984 (2)
$\Delta(CrO_6)$ =	$2.7*10^{-4}$	$\Delta(SbO_6)$ =	$7.4*10^{-6}$

< Mn-O_1-Cr >	**< Mn-O_2-Cr >**	**< Mn-O_3-Cr >**
88.7 (3); 116.8 (3)	84.8 (2); 101.0 (3)	90.7 (2); 105.4 (3)

[a)] Fitting residuals: R_p= 2.31%, R_{wp}= 2.68%, R_B = 4.89% and R_F = 3.89%,. [b)] $V_i = \Sigma_j S_{ij} i = \exp(r_0 - r_{ij}/0.37)$. Values calculated using r_{ij}= 1.79 Å (Mn^{2+}), 1.724 Å (Cr^{3+}) and 1.942Å (Sb^{5+}).

According to the three O positions, three different M-O bonds can be appreciated for each type of octahedra. From those distances, the use of equation *Eq. 3* allowed the determination of $B/B'O_6$ polyhedral distortions (Δ).

$$\Delta = \frac{1}{n}\sum_{1}^{n}\left(\frac{d_i - \overline{d}}{\overline{d}}\right)^2 \quad Eq.\ 3$$

The results, $\Delta(SbO_6) = 7.4\ 10^{-6}$ and $\Delta(CrO_6) = 2.7\ 10^{-4}$, point to an almost symmetric SbO_6 and highly distorted CrO_6 octahedra. This difference can be explained on the basis of the electronic environments of each cation and their influence over surrounding O^{2-} anions. On the one hand, Sb^{5+} has a closed shell d^{10} electron configuration, which makes it a strongly polarising cation. This effect induces a large but isotropic distortion on the electron charge cloud of oxygen, so that the six Sb-O distances are similar. Moreover, these bonds usually present a certain covalent character [12], which shortens the experimental distance thus inducing its apparent over-bonding (see BVS in Table 3.1). On the other hand, the non-equivalent occupancy of the 3d orbitals in Cr^{3+} ($[Ar]d^3$) induces a certain tetrahedral distortion of the CrO_6 octahedron: the four equatorial Cr-O distances summarised in Table 3.1 shorten while the two apical ($Cr\text{-}O_3$) elongate.

M-O distances were also used to determine the average oxidation states from bond valence calculations (BVS) through a standard interpolation method [13]. The obtained results, $Mn^{1.8+}$, $Cr^{2.8+}$ and $Sb^{5.4+}$, are close to the expected Mn^{2+}, Cr^{3+} and Sb^{5+} values from the nominal Mn_2CrSbO_6 composition. The slight deviations found for Mn and Sb may originate from the described covalent character of the Sb-O bond, which induces the attraction of the oxygen electrons towards Sb centres, thus originating a charge excess over them. On the other hand, Mn^{2+} cations are rather small ($^{VI}r_{Mn^{2+}} = 0.83$ Å) [14] to be placed at the 12^{th} coordinated A-site of the perovskite decreasing its coordination number from the ideal value of 12 down to 6, thus reducing as well their apparent BVS.

The effective sixfold coordination of Mn is supported by the good accordance between the experimental averaged Mn-O distance (2.279 Å) and the theoretical one determined from the sum of the ionic radii of Mn^{2+} and O^{2-} (2.23 Å). The slight mismatch indicates the elongation of the experimental bonds as a consequence of the discussed Sb-O shortening, which indeed justifies the low experimental oxidation state for Mn.

The main structural features summarised in Table 3.1 have already been detailed and discussed to be related to the structural distortion. However, it has been pointed out in the general introduction of this chapter that one of the key points would be the determination of the evolving structural distortions, so that a structure-properties relation can be set. In this context, a further study on the distortion features will be performed, so the $a^-a^-c^+$ tilt system defining the RS B-site ordered DPv structure will be carefully studied. With this objective, Appendix I details the three main different methods available for the calculation of both in-phase and out-of-phase tilt angles along $[001]_C$ (ϕ), $[110]_C$ (θ) and $[111]_C$ (Φ) pseudo-cubic directions: from i) lattice dimensions, ii) bond angles and iii) the relation between atomic positions.

That detailed discussion on the determination of the different tilt angles will apply for all the double perovskites studied along this work. The tilt angles of Mn_2CrSbO_6 have been calculated from the three described methods, which results are summarised in Table 3.2. The use of the lattice parameters yields different tilt values compared to those obtained from the other methods. The slight mismatch

observed between ϕ (13.45º) and θ (13.71º) angles for Mn_2CrSbO_6 can be attributed to the small β monoclinic angle (90.36º), which makes the monoclinic character of the crystallographic cell similar to a pesudo-orthorhombic cell. The higher value determined for the third tilt angle Φ (19.11º), along [111] direction, agrees with that calculated from cos Φ = cos ϕ * cos θ.

On the other hand, the ϕ tilt angle determined from < B – O – B' > bond angles and that determined from atomic positions yield the same 20.185º value. Since there are two independent potions at the B-site, ϕ was calculated as the average of the different ϕ_M values determined for CrO_6 (19.89 º) and SbO_6 (20.48 º) octahedra (equation *Eq.25* in Appendix I). It is notable that, as discussed in Appendix I, the tilt angles determined from the lattice parameters are less accurate than those determined from both bonding angles and the trigonometric relations between the ideal and the experimental atomic positions, which is reasonable since the last two methods do consider the symmetry differences with the pseudo-orthorhombic-related structure.

Concerning the θ angle, a similar behaviour is observed: the tough determination of independent θ values for Cr (19.24 º) and Sb (19.48 º) polyhedra through the different O_n positions includes both the [110] and $[\bar{1}10]$ components; which averaged value results in 19.36 º, indeed very close to the 19.28º determined from *Eq. 4*. Since the β-monoclinic angle is close to 90 º, all the tilt angles defining the monoclinic DPv studied along this project will be determined from the half difference of 180 º and <B – O – B' > angles along the corresponding directions:

$$\phi = \frac{180^o - < B - O - B' >}{2} \quad Eq.\ 4$$

Table 3.2. Tilt angles along $[001]_C$ (ϕ), $[110]_C$ (θ) and $[111]_C$ (Φ) directions determined for the DPv polymorph of Mn_2CrSbO_6 through the use of the three described methods: using lattice parameters, bond angles and atomic positions. [a)]

Method	**ϕ (º)**		**θ (º)**		**Φ (º)**
Lattice parameters	13.45		13.71		19.11
Bond angles	20.185		19.28		27.91
Atomic positions	O_3	O_3	O_1	O_2	27.97
	ϕ_{Cr} = 19.89	ϕ_{Sb} = 20.48	θ_{Cr} =19.02 θ_{Sb} = 18.95	θ_{Cr} = 19.45 θ_{Sb} = 20.01	
	ϕ = 20.185		θ =19.36		

[a)] see Appendix I for further details: the calculation through the relation between atomic positions allow the determination of independent BO_6 and $B'O_6$ octahedral rotations through the different oxygen sites.

It is worth noting that Glazer's definition of the tilt system for the discussed $P2_1/n$ space group ($a^-a^-c^+$) [15], determines out-of-phase tilts equivalent in magnitude about *x* and *y* axes (a_x^- and a_y^-) and a different magnitude for an in-phase rotation about the *z* axis (c^+). The combination of a_x^- and a_y^- can therefore be described as one single θ, and c^+ term stands for a unique ϕ angle. The classical description of this tilt system thus considers the distinction of axial and equatorial tilts but it does not take into account the different BO_6 and $B'O_6$ octahedral rotations.

The resulting tilt angles, ϕ ~ 20.2 º and θ ~ 19.3 º, can be observed in the nuclear structure depicted in Figure 3.1b. The experimental values are rather high compared to other double perovskites with similar compositions at the B sites. For instance, ϕ values determined through the same method for A_2CrSbO_6 (A = Ca, Sr) $P2_1/n$ double perovskites are 5.5 º and 13.5 º [16,17]. The effective coordination for the larger A-site cations in these room pressure compounds is tenfold for Sr^{2+} ($^{X}r_{Sr^{2+}}$ = 1.36 Å) and eightfold for Ca^{2+} ($^{VIII}r_{Ca^{2+}}$ = 1.12 Å) [14], whereas the stabilisation of sixfold coordination for the smaller Mn^{2+} ($^{VI}r_{Mn^{2+}}$ = 0.83 Å) cation requires the use of high pressures during the synthesis process. By that, the averaged Mn-O bond distance is 2.279 Å (see Table 3.1 above), which is in agreement to that calculated from the ionic radii sums (2.23 Å).

However, other high pressure double perovskites with Mn^{2+} in the A site have similar tilt angles, e.g. Mn_2BReO_6 (B = Fe, Mn) oxides have ϕ = 19.7 º and 22.4 º respectively [18,19] and Mn_2BSbO_6 (B = Fe, Sc) oxides have ϕ = 20.4 º and 19.5 º respectively [2,3]. It can therefore be concluded that the distortion observed in the DPv polymorph of Mn_2CrSbO_6 is a consequence of the high tilt angles originated for the stabilisation of the small Mn^{2+} cation in the highly coordinated A site.

It is striking that only a few $Mn_2BB'O_6$ DPv polymorphs have been stabilised, even under high pressure conditions [10]. Otherwise, their ordered corundum derivative polymorphs (ILO, LNO, NTO) are often easily stabilised under moderate pressures. In this context, the study of the phase boundary between polymorphs is an interesting target to be developed throughout this thesis, as the determination of the phase diagram will allow to find single phases and the P and T conditions needed to induce phase transformations. Similar studies have been carried out in the literature for other perovskites, which reveal that increasing tilt angles up to 25º are stable for $A^{2+}GeO_3$ and $A^{2+}TiO_3$ compounds upon decreasing the ionic radii of the A-site cations and / or increasing the synthesis pressures. The instability of larger tilt angles is reported to induce their transformation into the rhombohedral ILO or LNO polymorphs [7,20]. In an analogous manner, the stabilisation of Mn^{2+} at the A site of the DPv structure of Mn_2MSbO_6 through the use of high pressures must be limited. Increasing the synthesis pressure stabilises smaller cations into the A sites, such as Mn^{2+} [1–3,21–24], Cu^{2+} [25–27], Sc^{3+} and In^{3+} [28–31], and concomitantly increases the tilt angles. The higher the distortion, the lower the stability. Therefore, the chemical composition of the DPv polymorph must satisfy a compromise for stabilising both Mn^{2+} and the high octahedral tilting. Consequently, their stability limit could be monitored by using their tilt angles as a critical parameter, which induces a phase transition into the ILO (Mn_2CrSbO_6 and Mn_2FeSbO_6 [1]) or the NTO (Mn_2ScSbO_6 [2]) polymorphs under pressure conditions where the tilt angles of the DPv polymorph are above their stability limit.

Microstructural characterisation has also been performed through HRTEM. Figure 3.2 shows high resolution micrographs taken along the $[010]_C$ (a) and $[110]_C$ (b) zone axes. The periodic stripes observed along the [001] direction in both images correlates with the doubling of the *c* cell parameter that is confirmed by the measured distance (~ 7.5 Å) obtained from the FFT of the experimental images. The cation ordering among Cr and Sb at the B sites is observed along the cubic *x* axis and is exemplified by the linear profile of intensity values depicted as an inset on the top-right corner of the image. The distance between the Cr and Sb maxima amounts to ~ 2.6 Å and correlates with that obtained from the FFT of the experimental image along $[\bar{1}00]_C$ direction.

The calculated image obtained from the crystallographic information derived from the Rietveld refinement of the NPD data, using the Mac Tempas X software [32], is superimposed over the experimental image. It was calculated using a thickness of t = 30 Å and a defocus of -425 Å and is in good agreement with the experimental image. The projected structural model is also suited along the $[110]_C$ zone axis (Figure 3.2b), where B and B' cations are overlapped giving rise to a periodicity of ~ 3.7 Å, close to the ideal a_p. The structural model oriented through this projection is also superimposed on the figure, showing a good fit.

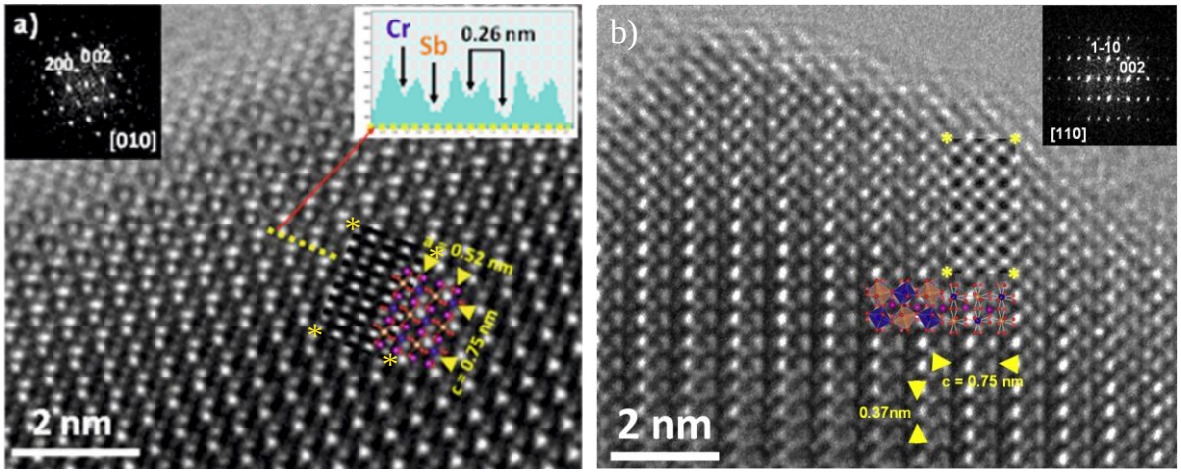

Figure 3.2. HRTEM images of the DPv polymorph of Mn_2CrSbO_6 along the $[010]_C$ (a) and $[110]_C$ (b) zone axes. Insets show the linear profile of intensities (top-right corner in a), the simulated image (delimited by yellow asterisks) calculated for a thickness of 30 Å and a defocus of -425 Å and the structural model obtained from the Rietveld refinements of NPD data.

2.1.2 - Magnetic behaviour

The magnetic properties of the DPv polymorph of Mn_2CrSbO_6 were studied from the temperature (T) dependence of the magnetic susceptibility (χ) and the magnetic field (H) dependent magnetisation (M) measurements. χ *vs.* T curves, plotted in Figure 3.3a - left axis, were measured under FC and ZFC conditions at 0.1 T. χ increases below T_N ~ 60 K followed by a maximum in the ZFC curve and a slight divergence between ZFC / FC branches below ~ 20 K. The presence of AFM correlations is evidenced through the appearance of the maximum in susceptibility and the observed χ values,

namely ~ 0.7 emu mol^{-1}·Oe^{-1} at 10 K. Moreover, the fit of the reciprocal susceptibility χ^{-1} *vs.* T (Figure 3.3a - right axis) to a Curie-Weiss (CW) law χ (T) = c / (T - θ) resulted in a highly negative value for the Weiss constant, θ = -219.7 (1) K, which confirms the AFM behaviour. From this fit, the Curie constant, c = 10.5 (1) emu K mol^{-1} Oe^{-1}, yields a total effective moment μ_{eff} = 9.2 (1) μ_B, in agreement with the expected value (9.22 μ_B) for the contributions of $2Mn^{2+}$ (S = 5/2) and Cr^{3+} (S = 3/2) cations. The AFM behaviour is also supported by the M *vs.* H curves, depicted in Figure 3.3b, which show a linear trend both above and below T_N.

However, this trend slowly deviates at low temperatures giving rise to a remanent magnetisation as low as ~ 0.2 μ_B. Such a small net magnetisation, enlarged in the inset of Figure 3.3.b, shows a small hysteresis at 2 K below H_C ~ 0.05 T, that could be explained in terms of a small spin canting originated by antisymmetric Dzyaloshinskii-Moriya interactions (DM) [33].

Therefore, both Mn^{2+} and Cr^{3+} sublattices order antiferromagnetically below the Néel temperature T_N ~ 60 K. The < Mn - O_n - Cr > angles (84.8º - 116.8º) determined from the nuclear structure refinement (see Table 3.1), are near the ideal 90º originating d^5 - d^3 AFM superexchange interactions through oxygen according to Goodenough-Kanamori-Anderson rules [34]. The small FM net component arises from the spin canting.

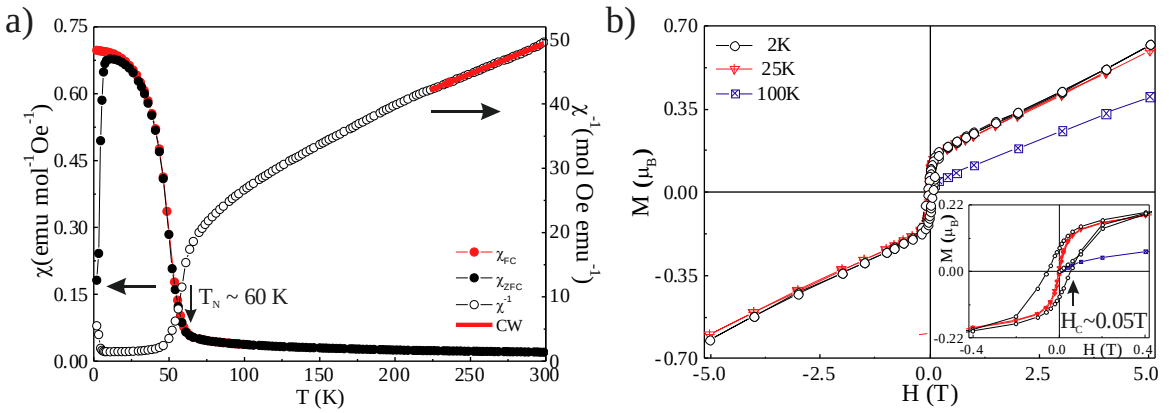

Figure 3.3. Magnetic behaviour of Mn_2CrSbO_6 double perovskite polymorph in terms of a) thermal dependence of the susceptibility and b) field dependent magnetisation measurements. The inset in b) shows the magnification of the -0.4 T < H < 0.4 T range of the M *vs.* H measurements, were a small hysteresis is observed at 2 K with a coercive field of H_C ~ 0.05 T

However, a complete magnetic characterisation requires the determination of the magnetic structure from the neutron diffraction data. The appearance of new Bragg peaks in the 2K diffraction pattern confirmed the AFM behaviour (see Figure 3.4a). The magnetic structure was initially determined from the Rietveld refinement of the low temperature NPD data. All the magnetic peaks can be indexed with a magnetic propagation vector κ = [½ 0 ½], what indicates that *a* and *c* cell parameters of the magnetic structure are doubled with respect to those of the nuclear structure. Provided this propagation vector, the AFM alignment of the spins along *x* and *z* directions is expected.

The magnetic symmetry analysis was developed in terms of BasIreps software [35] for the determined propagation vector κ = [½ 0 ½] and the two independent atomic positions of Mn^{2+} and Cr^{3+} cations in the $P2_1/n$ space group. The results indicate that Mn can follow four different irreducible representations (Ireps) containing three basis vectors (BV) each, which determine the alignment of the spins along the three main crystallographic directions. These Ireps ($\Gamma_1 - \Gamma_4$) are summarised in Table 3.3, where only the real components of each BV are shown as the imaginary component is 0 in all cases. Cr is only represented by the Ireps Γ_2 and Γ_4, and the lower multiplicity of its Wyckoff site only applies at the two first symmetries indicated in Table 3.3.

Γ_2 stands for the AFM alignment of both Cr and Mn, while Γ_4 yields the FM correlations of Cr spins. The evidence of the AFM nature of this compound from magnetic susceptibility and magnetisation measurements reveal that Cr must follow Γ_2. The simplest solution for the discussed macroscopic magnetic behaviour is that both cations follow the same Irep, though Mn could still have some alternatives: Γ_3 is FM along *x* and *z* directions, so it can be neglected, but Γ_1 and Γ_4 show different types of AFM orders.

Table 3.3. Real components of the BV of the allowed Ireps for the magnetic structure of the DPv polymorph of Mn_2CrSbO_6 oxide with a propagation vector κ = [½ 0 ½].

Irep / Symm	Γ_1	Γ_2	Γ_3	Γ_4
x, y, z	100 010 001	100 010 001	100 010 001	100 010 001
-x+1/2, y+1/2, -z+1/2	-100 010 00-1	-100 010 00-1	100 0-10 001	100 0-10 001
-x, -y, -z	100 010 001	-100 0-10 00-1	100 010 001	-100 0-10 00-1
x+1/2, -y+1/2, z+1/2	-100 010 00-1	100 0-10 001	100 0-10 001	-100 010 00-1

The use of Γ_2 in the Rietveld fit of the NPD data collected at 2K at D2B quickly converged. However, in order to simplify the determination of the accurate magnetic structure of the DPv polymorph of Mn_2CrSbO_6, the same model was used to refine the difference pattern resulting from subtracting the NPD data collected at 80 K to those measured at 2 K under the high intensity mode. By that, the nuclear structures of both the main phase and the detected secondary phases are cancelled and do not disturb the signal arising from the magnetic diffraction.

The *x* and *z* components of the discussed Γ_2 Irep were independently refined for both magnetic sites, what implies that the spins are confined to the *xz* plane. The resulting Fourier coefficients along both directions (C_1 and C_3 for *x* and *z* axes respectively) acquired similar values for both Mn- and Cr- sites but opposite in sign. Consequently, both coefficients were constrained to be the same, and thus to align with opposite values along the [101] direction: $C_{1\,(Mn)} = -C_{3\,(Mn)}$ and $C_{1\,(Cr)} = -C_{3\,(Cr)}$. The number of magnetic parameters is then simplified to one for Mn site and another one for Cr site, which resulting refinement is shown in Figure 3.4a. The modules of the spins can be calculated as the square root of the sum of the squared components along *x* and *z* directions: $\mu = \sqrt{C_1\mu_x^2 + C_3\mu_z^2}$ The resulting magnetic structure is depicted in Figure 3.4b. The magnetic moments of Mn^{2+} and Cr^{3+} cations amount to 4.8 (1) μ_B and 2.7 (1) μ_B respectively, which is in good agreement with their expected values at 2 K from the spin only 2S contribution (5 μ_B and 3μ_B respectively).

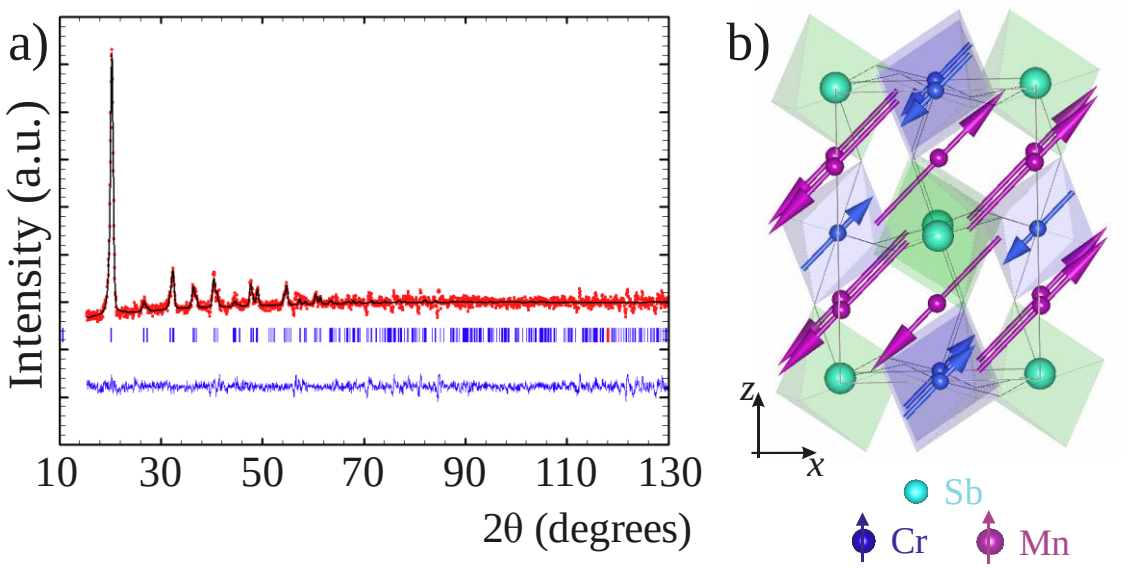

Figure 3.4. a) Rietveld refinement of the 2 K - 80 K NPD high resolution pattern profiles collected at D2B. The row of marks shows the position of the magnetic diffraction peaks. b) A portion of the magnetic structure determined from a), where Mn^{2+} and Cr^{3+} spins are depicted as purple and blue arrows respectively.

The spin canting originating the 0.2 μ_B net FM component observed from magnetisation measurements cannot be determined from NPD measurements, as the maximal resolution mode of D2B detects a minimum magnetic moment of ~ 0.4 μ_B. Although C1 and C3 were constrained to be the same, their independent refinement gives close but slightly different values. This indicates that, despite deviations are of the same order than the instrumental resolution Mn and Cr spins might not be perfectly aligned along [101] direction. Otherwise, both sublattices may be slightly deviated from each other. Therefore, a non-detectable FM component is allowed from the DM exchange interactions.

2.1.3 - Thermal stability

This study was developed through X-ray thermodiffraction. The thermal treatment consisted on heating ramp segments with a heating rate of 5 K / min, intercalated with 5 minutes of temperature stabilisation and diffraction collection every 50 K between 373 K and 1173 K. The results are shown in Figure 3.5, where the DPv polymorph remains stable up to T ~ 873 K. At this temperature, XRD patterns reveal the onset of a phase transition to the polymorph with ILO-type structure. The phase transition is completed at T ~ 973K, where no remnant diffraction peaks from the perovskite phase are appreciated.

It is worth noting that, for the best of our knowledge, this is the first experimental evidence for a DPv to ILO phase transition. According to theoretical predictions by Megaw [36] this transition is not possible through a second order transformation, as it implies the cationic exchange between Mn and the disordered Cr/Sb sites of the ILO structure. On the contrary, the topological transformation of the DPv is expected to originate a LNO-type structure [37,38], which is commonly observed as the quench product of these high pressure compounds [39]. Moreover, a second order transition has also

been observed between differently ordered corundum derivatives (NTO and ordered ILO structures) upon heating at ambient pressure [40]. This transition is proposed to occur through a large-scale cationic rearrangement which implies the ionic motion through different crystallographic sites. However, the occurrence of this transformation through direct cationic motion implies the need of starting from (NTO) and going to (ordered ILO) ordered configurations. In the case of the DPv to ILO transition, this requirement is not satisfied due to the disorder among Cr and Sb within the 6c (0 0 0.34) site in the ILO structure (see next section). Hence, this must be a first order transition, in which all thermodynamic parameters (enthalpy, entropy, energy, volume, etc.) are discontinuous.

The reason for the ILO preference over the LNO polymorph in this compound may reside on the charge-volume relationship for the different cations. As detailed in chapter 1, the average charge distribution of Mn_2MSbO_6 among A and B sites ($A^{2+}{}_2B^{4+}{}_2O_6$) is that usually originating ilmenite structures. In this particular compound, with M = Cr^{3+}, the size difference between both B-site cations is rather small. Consequently, a random distribution of Cr^{3+} ($^{VI}r_{Cr}{}^{3+}$ = 0.615 Å) and Sb^{5+} ($^{VI}r_{Sb}{}^{5+}$ = 0.610 Å) [14] is enhanced within (00z) layers, so that a maximal charge distribution can be tailored through ensuring the face sharing of all the $Mn^{2+}O_6$ and $Sb^{5+}O_6$ octahedra.

To conclude this section, it can be established that a compromise between pressure and temperature must be reached in order to isolate both the perovskite and the corundum derivative modifications. Increasing the synthesis pressure favours the preparation of the denser polymorph but the higher tilt of its octahedra minimises the DPv stability so, for this chemical composition in particular, heating the DPv polymorph at ambient pressure destabilises this structure and originates the ILO polymorph. The interest of this transition remains on the accessibility to the obtention of an additional polymorph with potential different properties. Furthermore, a probable reversibility of this phase transition by increasing pressure back to the optimal value provides access to two different structures which can be isolated and inter-converted [7].

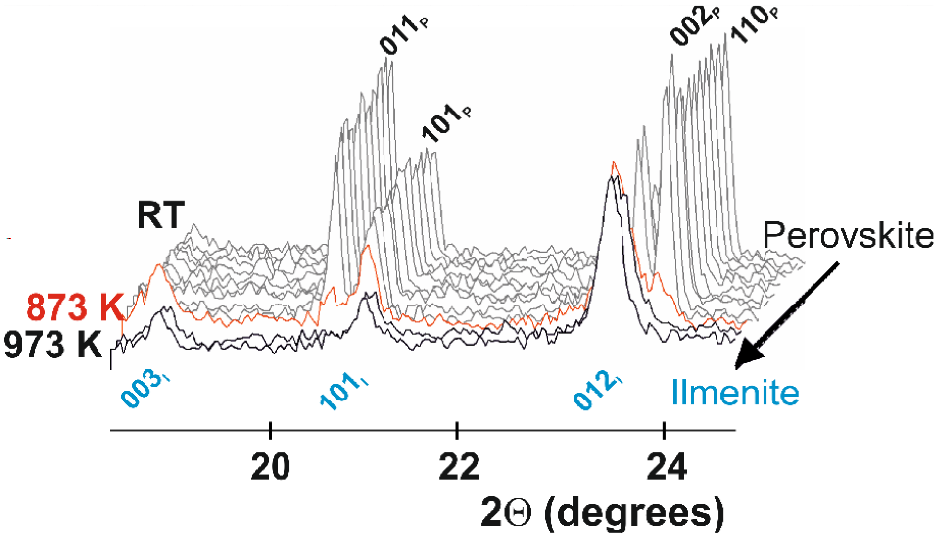

Figure 3.5. Magnification of the low angle region of the XRD patterns of Mn_2CrSbO_6 collected upon heating from room temperature up to 973 K. The red pattern shows the phase transition at 873 K and the main peaks of both polymorphs are identified with their corresponding $(hkl)_P$ (perovskite) and $(hkl)_I$ (ilmenite) Miller indices.

2.2- Ilmenite

2.2.1 - Synthesis and structural characterisation

The rhombohedral polymorph of Mn_2CrSbO_6 was observed under moderate pressure conditions. However, it could not be completely isolated as single phase through direct HPHT synthesis. Therefore, the ILO_Mn_2CrSbO_6 oxide was prepared through "hard-soft" chemistry [1,41,42]. As described in the previous section, the 'soft' thermal treatment of the metastable DPv polymorph synthesised under 'hard' high pressure conditions enables the phase transition to the most stable ILO structure. Its synthesis thus implies the application of 8 GPa and 1473 K to the homogeneous stoichiometric mixture of Mn_2O_3, Cr_2O_3 and Sb_2O_3 during 15 minutes in a Conac-type press followed by heating the resulting product under 973 K during 8h with intermediate grinding. Routine qualitative characterisation was developed through XRD. All the Bragg peaks could be indexed in the $R\bar{3}$ space group with an ilmenite structure (Figure 3.6a-top). The presence of a *c*-glide plane would imply additional systematic extinctions (hkil) with l odd, so the presence of those maxima in our experimental profiles may exclude the corundum ($R\bar{3}c$) and LNO ($R3c$) polymorphs. Therefore, alternating (00z) layers of different compositions can be distinguished through XRD. However, since Cr and Mn have similar atomic numbers (Z_{Cr} = 24 and Z_{Mn} = 25), similar diffraction patterns would be obtained for ilmenite with different antisite disorder, e.g. different ilmenite polymorphs with A = 2 Mn and B = Cr/Sb or A = Mn/Cr and B = Mn/Sb, where cations are disordered in mixed (00z) layers. Moreover, an NTO-type structure, where both (00z) layers are constituted by ordered cations, could also show a similar profile [2]. Therefore, the crystal structure of this compound cannot be undoubtedly determined only through XRD, so further structural characterisation is needed.

As pointed out for the Mn_2CrSbO_6 DPv polymorph, the neutron scattering lengths of these elements are all different enough to appreciate their order, provided the negative value of the coherent scattering length for Mn (-3.73 fm) in contrast to the positive ones for Cr (3.635 fm) and Sb (5.57 fm) [9]. Therefore, the Rietveld refinement of NPD data collected at room temperature at the high resolution D2B instrument (Figure 3.6a-bottom) confirmed the complete cationic distribution within the 6c (00z) site of the expected ILO model with $R\bar{3}$ space group and cell parameters a = 5.2084 (4) Å and c = 14.400 (1) Å. Mn locates at 6c site with z = 0.1411 (5) while Cr and Sb are disordered within 6c position with z = 0.3408 (5). Further structural details, including selected bond distances and angles and octahedral distortions, are summarised in Table 3.4. Two different views of the unit cell of the nuclear structure are depicted in Figure 3.6b. Minor amounts of secondary $MnCr_2O_4$ (4.2 %) and $MnSb_2O_4$ (4.4 %) phases were detected. Polyhedral distortions are usually found for corundum and its derivatives due to cation–cation repulsions across shared faces and edges of the octahedra. These were calculated by using equation *Eq. 3* and revealed regular BO_6 in contrast to highly distorted MnO_6 octahedra. The octahedral distortions of AO_6 octahedra are higher compared to those of BO_6 in high-pressure ILO silicates and germanates [43,44]. On the other hand $\Delta(AO_6) < \Delta(BO_6)$ is observed for titanates [45]. It is interesting to note that for ABO_3 ilmenites, where both (00z) layers are completely constituted by the same cation, the maximal difference among $\Delta(AO_6)$ and $\Delta(BO_6)$ is of one order of magnitude. Otherwise, the double ILO Mn_2CrSbO_6 shows a distortion mismatch of up to four orders of magnitude. The regular size of Cr/SbO_6 polyhedra ($\Delta = 2.5*10^{-7}$) may be expected due to the regular character of SbO_6 octahedra as determined in the previous section for the DPv polymorph ($7.4*10^{-6}$). This is a direct consequence of the large polarising effect of the

electronic configuration of the Sb^{5+} cation ([Kr] $4d^{10}$). Concerning Mn sites, the octahedral distortion $\Delta(MnO_6) = 1.1*10^{-3}$ is consistent with the values reported in the literature for ABO_3 ILO titanates [45]. Its higher distortion can be explained on the basis of fundamental chemistry: Mn^{2+} is a relatively large cation ($^{VI}r_{Mn}^{2+}$ = 0.83 Å) that in ILO is forced to be into a sixfold coordination. As detailed below, the octahedral distortion arises from the electrostatic repulsion between cations located into face sharing octahedra. When MnO_6 and Cr/SbO_6 share a face, the regular environment favoured by the covalency of Sb-O bonds and the lighter weight of Mn (Z_{Mn} = 25, $Z_B = (Z_{Cr} + Z_{Sb})/2$ = 37.5), makes the displacement of Mn easier than that of Sb. As a result, two different M-O bond lengths are found for Mn. The use of the experimental bond lengths to determine the oxidation states of cations from BVS calculations yields $Mn^{1.9+}$, $Cr^{2.9+}$ and $Sb^{5.2+}$, thus confirming the expected nominal values.

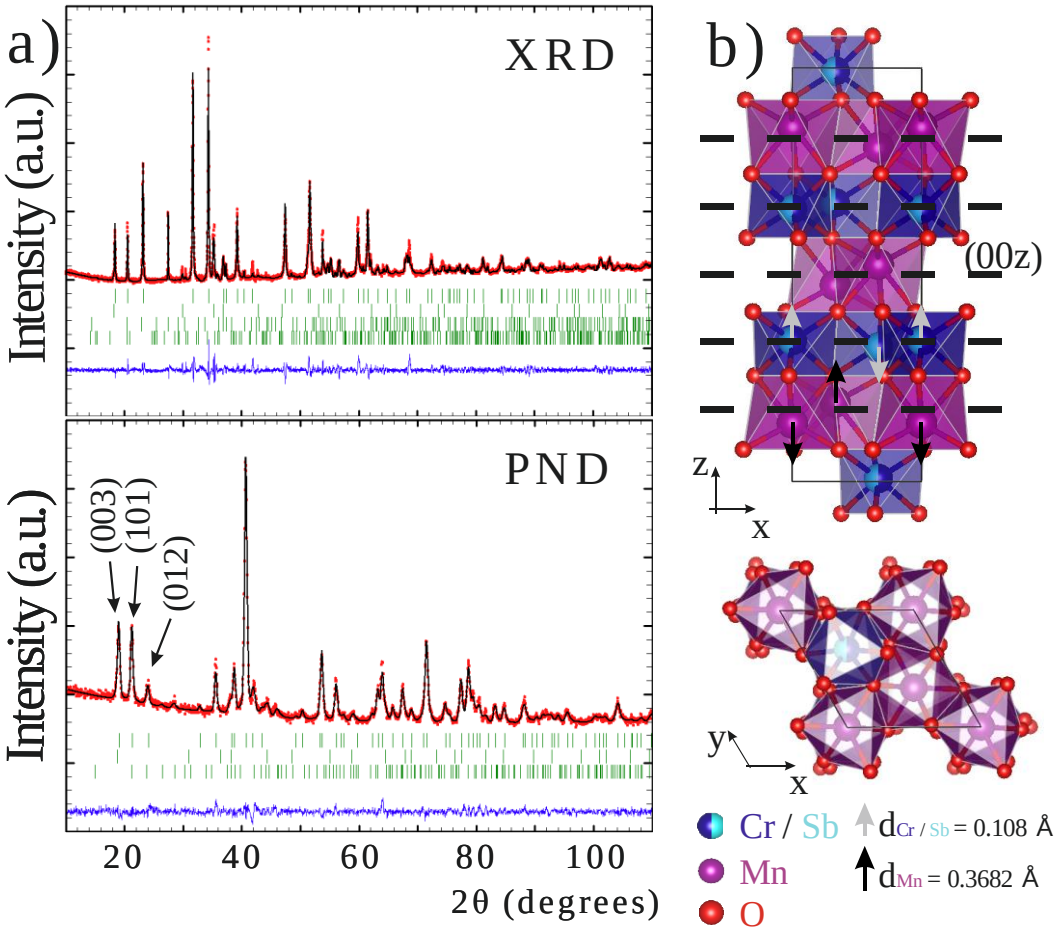

Figure 3.6. a) Rietveld refinements of Mn_2CrSbO_6 ILO polymorph from XRD (up) and NPD (bottom) data; $MnCr_2O_4$, Sb_2O_4 and $Mn_2Sb_2O_7$ secondary phases are included (2nd to 4th rows of Bragg positions respectively). b) Structural model determined from NPD. The displacement of the cations from (00z) layers is identified as d_M and schematised with black and grey arrows for Mn and Cr/Sb, respectively.

Table 3.4. Crystallographic parameters, selected bond distances and angles for the ILO polymorph of Mn_2CrSbO_6 as obtained from the Rietveld refinement of NPD data collected with high resolution at D2B at 300 K.[a)]

$R\bar{3}$	a = 5.2084 (4) Å		c = 14.400 (1) Å		
Atom-site	x	y	z	Occ	BVS
Mn– 6c	0	0	0.1411 (5)	1	1.9
Cr/Sb– 6c	0	0	0.3408 (5)	0.5/0.5	2.9/5.2
O– 18f	0.2875 (4)	-0.0285 (5)	0.2560 (2)	1	—

A-O	**d (Å)**	**B-O**	**d (Å)**
Mn - O (x3)	2.286 (6)	Cr/Sb - O (x3)	1.994 (5)
Mn - O (x3)	2.139 (4)	Cr/Sb - O (x3)	1.992 (4)
d_{av}.(Mn - O)	2.212 (2)	d_{av}.(Cr/Sb - O)	1.993 (2)
$\Delta(MnO_6)$	$1.1*10^{-3}$	$\Delta(Cr/SbO_6)$	$2.5*10^{-7}$

<Mn – O – Mn >	**<Cr – O – Cr >**	**< Mn – O – Cr >**
88.8 (2)	98.3 (2)	84.1 (2); 119.6 (1); 139.5 (2)

[a)] Fitting residuals: R_p= 3.51%, R_{wp}= 4.46%, R_B = 3.79% and R_F = 2.38%,. [b]$V_i = \Sigma_j S_{ij} i = \exp(r_0 - r_{ij}/0.37)$. Values calculated using r_{ij}= 1.79 for Mn^{2+}, 1.724 for Cr^{3+} and 1.942 for Sb^{5+}.

As introduced in chapter I, the main distortion parameter for the corundum-related structures arises from the cationic displacements. The cationic arrangement into the anionic sublattice of ILO can be described as face sharing octahedra along the *z* axis with a stacking sequence A-B-□-B-A-□, where □ stands for a vacant cationic position. Faced A- and B-site cations shift towards their nearest □ site along the *z* axis as a consequence of their electrostatic repulsion, what originates off-centred polyhedra. This effect is cooperative through the structure, as these stacking sequences are geometrically distributed within the unit cell so that every MO_6 octahedron shares an edge with three additional octahedra within the same (00z) layer. The resulting effect is the puckering of the (00z) layers through the alternated displacements of consecutive cations above and below their ideal z values (see the up-down black and grey arrows in the upper panel of Figure 3.6b).

This displacement can be calculated from the accurate atomic positions determined from the room temperature NPD data. The difference between the ideal z values (1/6 for Mn and 1/3 for Cr/Sb) and the experimental ones included in Table 3.4, determines their shift in atomic coordinate dimensions. Multiplying these values by the unit cell dimension along the shifting direction rescales the distortion to real space units. The resulting values are d_{Mn} = 0.360 Å and $d_{Cr/Sb}$ = 0.115 Å, comparable to those observed in other ilmenites. It is particularly interesting the comparison of the Mn_2CrSbO_6 distortion against that of $MnTiO_3$ [45]. The displacement of Mn^{2+} cations is almost the same in both compounds, but the substitution of Ti^{4+} by two different cations at BO_6 (Cr^{3+} and Sb^{5+}) with close ionic radii ($^{VI}r_{Ti}^{4+}$ = 0.605 Å, $^{VI}r_{Cr}^{3+}$ = 0.615 Å and $^{VI}r_{Sb}^{5+}$ = 0.61Å) [14] results in lower cationic displacements (less than a half of the original value) and octahedral distortions (which decrease four orders of magnitude). This tendency evidences the importance of the charge distribution within each (00z) layer and among them. The lower distortion in the ILO polymorph of Mn_2CrSbO_6 oxide evidences its higher stability, thus justifying the absence of any additional cationic arrangement within the Cr/Sb layer or even among Mn and Cr/Sb layers, which would originate the crystallisation of the compound in a different structural type (LNO or NTO).

Figure 3.7 shows two HRTEM images of the ILO polymorph of Mn_2CrSbO_6. Figure 3.7a depicts the $[2\bar{1}\bar{1}0]$ projection, which shows the regular staking of grey and dark rows of contrast along [0001] direction, thus confirming the alternation of subsequent (00z) layers of different compositions. The absence of any additional order within none of these layers, confirms the ilmenite-type structure, which structural model determined from NPD data is superimposed. Moreover, the structural details summarised in Table 3.4 were used as input for the HRTEM image simulation, showing a good matching with the experimental one for a defocus of -200 Å and a thickness of 57 Å.

Figure 3.7b shows the HRTEM micrograph along [0001] direction. Through this projection only the corundum-type arrangement can be observed, as the different cation sites are overlapped through the zone axis and only an averaged contrast is observed. The corresponding simulated image from the detailed structural features determined from NPD refinement is superimposed on the experimental image in the enlargement shown in the lower part of Figure 3.7b. As observed in the previous projection, both calculated and experimental micrographs fit. In an analogous manner, the [0001] projection of the structural model is also included in the figure.

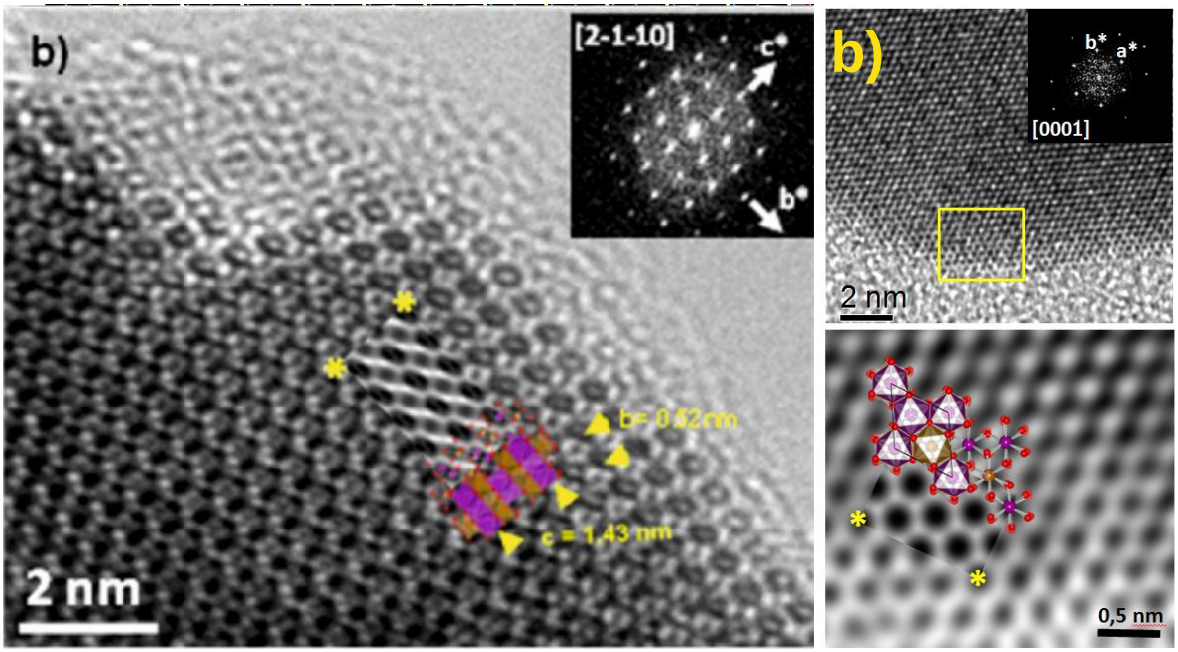

Figure 3.7. HRTEM images of the ILO polymorph of Mn_2CrSbO_6 along the $[2\bar{1}\bar{1}0]$ (a) and [0001] (b) zone axes. Figure b is enlarged below. Insets show the simulated images (delimited by yellow asterisks) calculated for a thickness of 57 Å and a defocus of -200 Å and the structural model obtained from the Rietveld refinements of NPD data.

2.2.2 - Magnetic behaviour

At a first sight, the magnetic susceptibility of the ILO polymorph of Mn_2CrSbO_6 (Figure 3.8a) resembles that observed for the perovskite related compound. A first small kink is observed at T_{N1} ~ 60 K, close to that of the DPv polymorph of Mn_2CrSbO_6. Consequently, the reminiscence of a non-detected amount of the DPv used as the precursor of the ILO modification was considered. However, NPD data collected at different temperatures discarded this hypothesis, as neither nuclear nor magnetic peaks could be assigned to the already characterised DPv_Mn_2CrSbO_6. A second magnetic transition stronger than the first one occurs below T_{N2} ~ 53 K, where the magnetic susceptibility increases and FC-ZFC curves diverge. The presence of a maximum at ~ 15 K and the low values of χ(~ 0.8 emu $mol^{-1} \cdot Oe^{-1}$) indicate the AFM nature of this transition, though the divergence of FC and ZFC curves reveal the presence of a FM component. The reciprocal susceptibility can be fitted to a CW behaviour for the 230 K – 300K temperature range (see Figure 3.8a-right axis). The total paramagnetic moment determined from this fitting is 8.8 (1) μ_B and the Weiss constant amounts to θ = -195.6 (1) K. The value of 8.8 μ_B is slightly lower than the theoretical one (9.2 μ_B), calculated from the stoichiometric contributions of Mn^{2+} (S = 5/2) and Cr^{3+} (S = 3/2) cations. This low value evidences the absence of large amounts of magnetic secondary phases, what constitutes another compelling reason not to assign the magnetic transition at T_{N1} to DPv_Mn_2CrSbO_6. Otherwise, it points to the existence of intrinsic AFM correlations below T_{N1}.

Field dependent magnetisation measurements are shown in Figure 3.8b for different temperatures up to H = 5 T. The AFM interactions are confirmed as the M shows a linear dependence with the magnetic field. Moreover, there exist a crossover between the M vs. H plots obtained at different temperatures below T_{N1}.when a critical magnetic field of 2.2 T is applied. This effect is often observed in AFM ground states when a magnetic field is applied parallel to the spin arrangement [ref]. There also exists a hysteresis in the magnetisation loop measured at 2 K, which reveals the presence of a net FM component with a coercive field of 300 Oe and a remanent magnetisation of 0.08 μ_B. It has been reported that the occurrence of two consecutive magnetic transitions, similar to those observed here, can be associated to the presence of temperature dependent spin reorientation transitions [46].

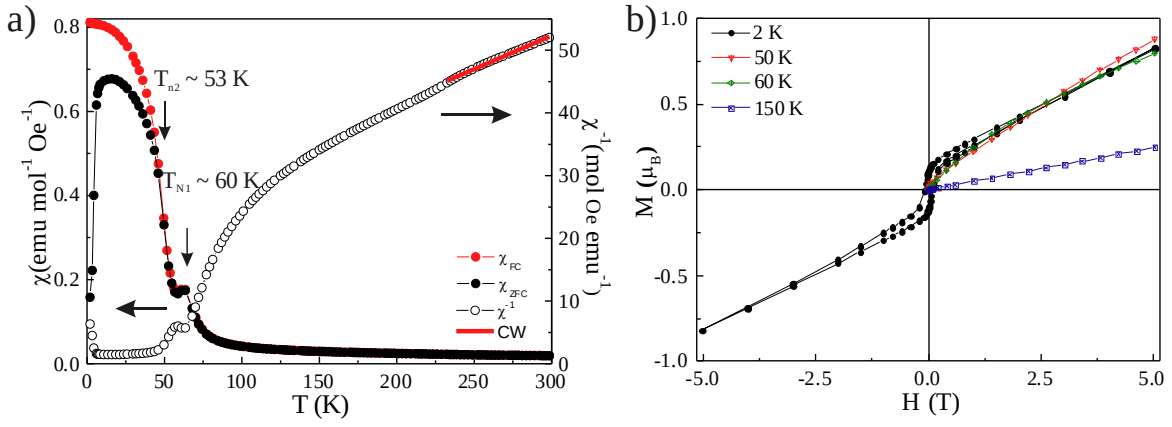

Figure 3.8. Magnetic behaviour of the ILO polymorph of Mn_2CrSbO_6 oxide in terms of the (a) magnetic susceptibility and (b) field dependent magnetisation measurements.

A complex behaviour is therefore predicted from the combination of susceptibility and magnetisation measurements, but the ordering of spins into the magnetic structure and its thermal evolution cannot be deduced from these measurements. Low temperature NPD studies were carried out in order to complete the magnetic characterisation of the sample. Figure 3.9a shows the Rietveld refinement of the NPD data collected at D1B at 60 K (up) and 1.5 K (bottom). The magnetic peaks observed at 1.5 K can be indexed with the propagation vector κ_{LT} = [0 0 0.54], where LT stands for low temperature. The symmetry analysis was performed using BasIreps software [35], resulting in the three different IReps indicated in Table 3.5. Both Mn and Cr sites are split into two independent sites, all of which allow these three Ireps. Γ_1 presents a unique magnetic component along the propagation vector direction. This Irep could only satisfy the propagation vector if all the Mn^{2+} and Cr^{3+} spins were aligned along the *z* axis with variable magnetic moments defining a cycloidal modulation of spins. The refinement of the neutron data require the antiparallel alignment of each magnetic site of both Mn and Cr, what clearly indicates that the cycloidal magnetic structure is not able to account for the measured magnetic intensities. The other two Ireps, Γ_2 and Γ_3, are more probable solutions, since they describe the confinement of the spins to the basal *xy* plane. The independent magnetic sites are allowed to acquire different orientations within the *xy* plane through the presence of different imaginary components along each of the equivalent directions. The difference between Γ_2 and Γ_3 Ireps is the direction towards which the rotation of the spins is propagated. However, the simple presence of these imaginary coefficients of the BV rotates the spins into stacked directions, while the description of a helix requires the introduction of a refinable rotation period. This can be done through the addition of a magnetic phase factor *(ϕ)*, which affects the Fourier components of the magnetic moment (*S*) as indicated in equation *Eq. 5*:

$$S_k = 1/2 * (R_k + iI_k) * e^{-2\pi i\phi} \quad Eq.\ 5$$

, where R_k and I_k are the real and imaginary components of the BV respectively. Γ_2 and Γ_3 cannot be distinguished from powder diffraction, so Γ_2 was selected to refine the helical model of the magnetic structure of the ILO polymorph of Mn_2CrSbO_6 from NPD data collected at 1.5 K (Figure 3.9a-bottom). The magnetic moments of the two independent sites for both Mn^{2+} and Cr^{3+} cations are constrained to be the same, since similar values were obtained when refined separately. Two different projections, along [010] and [001] directions, of the resulting magnetic structure are depicted in Figure 3.9b. The magnetic moments amount to μ_{Mn} = 4.53 (1) μ_B and μ_{Cr} = 2.79 (1) μ_B, in accordance to the expected values for Mn^{2+} (S = 5/2) and Cr^{3+} (S = 3/2).

Table 3.5. Real (BasR) and imaginary (BasI) components of the BV of the allowed Ireps for the magnetic structure of the ILO polymorph of Mn_2CrSbO_6 with propagation vector κ_{LT} = [0 0 0.54].

Irep / Symm	Γ_1	Γ_2	Γ_3
x, y, z			
Bas R	0 0 1	1.5 0 0	1.5 0 0
Bas I	0 0 0	-0.8660 -1.7321 0	0.8660 1.7321 0

In order to study the dynamics of the spin reorientation, short scans were collected every 2 K upon heating from 1.5 K up to 94 K at D1B. The thermal evolution of NPD patterns is depicted in Figure 3.9c, where a magnetic peak at ~ 5º and two magnetic satellites around (101) reflection are observed. Their diffuse intensities begin to appear at T_{N1}~ 60 K, and increase below T_{N2} ~ 53 K. The incommensurate propagation vector which indexes all the peaks at T_{N1} is κ_{HT} = [0 0 0.46], where HT stands for high temperatures. However, this magnetic propagation vector is not constant with temperature below T_{N2}. This feature is clearly observed for the magnetic peak appearing at low angles (~ 5 º), which is enlarged on the right panel of Figure 3.9c. It is worth noting that the propagation vector does not stabilise any commensurate cell (i.e. κ = [0 0 ½]), but it continuously changes with temperature through two consecutive magnetic transitions. This behaviour explains the observed complex magnetisation data shown in Figure 3.8. The refinement of each NPD patterns in the 1.5 K < T < 60 K temperature range provided independent κ values for all the measured temperatures. The resulting thermal dependence of the component along the *z* direction (κ_z) is depicted in Figure 3.9d. Below ~ 15 K the propagation vector and the position of the magnetic peaks seem stable, according to the temperature transition observed in χ *vs. T* curves.

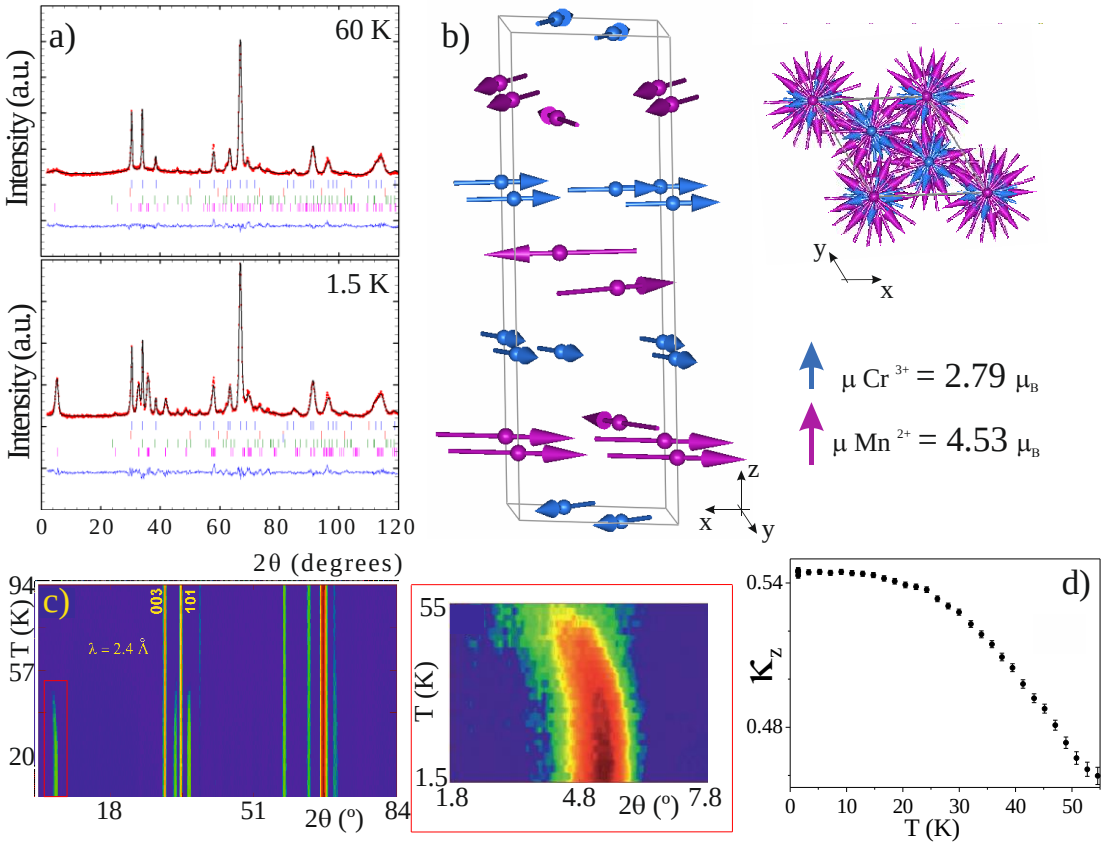

Figure 3.9. a) Rietveld refinements of the NPD data collected at D1B at 60 K (up) and 1.5 K (bottom) for ILO_Mn_2CrSbO_6 polymorph. b) Low temperature magnetic structure refined at 1.5 K. c) Thermal evolution of the NPD profiles between 1.5 K and 94 K; the thermal evolution of (00κ_z) reflection is enlarged on the right panel d) Thermal evolution of κ_z, below the spin reorientation at T_{N2} ~ 53 K: it varies from κ_{HT} = [0 0 0.46] (arising at T_{N1} ~ 60 K) to κ_{LT} = [0 0 0.54] (stabilised below ~15 K).

The origin of the helical structure can be explained in terms of the different magnetic interactions. It is worth noting that a wide number of different magnetic interaction paths are allowed in the corundum derivatives. These complex set of magnetic correlations, which can operate via direct cation-cation orbital overlapping and superexchange mechanisms [47], are further explained in Apendix II. There, a generalised view of the main interactions for both Mn^{2+} and M^{3+} sublattices is detailed in terms of the cationic orbital orientation. The magnetic interactions summarised in Apendix II can be used for all the corundum derivative structures by considering the preferences induced by the different cationic orders. ILO and NTO cases are particularised from that model.

Concerning the ILO_Mn_2CrSbO_6 polymorph, there is a strong competition between direct cation-cation and superexchange cation-anion-cation interactions. On the one hand, the so-called interlayer interactions (see top panels of Figure A2.1 in Apendix II) are those operating between Mn^{2+} and Cr^{3+} sublattices, taking into account the diamagnetic character of the Sb^{5+} cations. These magnetic interactions are governed by direct d^5-d^3 interaction through face sharing octahedra (d_{Mn-Cr} =2.88 (1) Å). An AFM ordering is favoured through the direct overlapping of the t_{2g} Mn - Cr orbitals along the *z* direction.: d_{xy} - d_{xy} , d_{xz} - d_{xz} and d_{yz} - d_{yz} [47]. This interaction can also develop via superexchange through p orbitals of the intermediate oxide anions. The orientation of the metal orbitals into the octahedral site determines that this superexchange interaction must occur through the e_g orbitals: d_z^2 - p - d_z^2 and $d_{x^2-y^2}$ - p - $d_{x^2-y^2}$. Since e_g orbitals of Cr^{3+} cation are empty, this superexchange interactions are relatively weak, what justifies the low value of the T_N attained in this oxide. The AFM nature of both direct and indirect interactions are cooperative [34].

On the other hand, the interactions within each type of magnetic sublattice occur between nearest neighbour Mn^{2+}-Mn^{2+} and Cr^{3+}-Cr^{3+} cations. These pairs of cations are located into edge sharing octahedra, where each octahedron shares a total of three edges with the three nearest octahedra of the same (00z) layer (see bottom panels of Figure A2.1 in Appendix II). Their magnetic interactions are also determined by the competition between direct and indirect correlations. The direct cation-cation interaction occurs via t_{2g}-d_{xy} or d_{xz} orbitals, while the superexchange interactions at ~ 90 º (see Table 3.4) are dominated by d_z^2 - p - $d_{x^2-y^2}$ and $d_{x^2-y^2}$ - p - $d_{x^2-y^2}$ interactions. Both direct and indirect interactions favour the AFM alignment of the spins within each sublattice.

In summary, both sublattices and their relative orientation should be antiparallel in the ILO structure. However, the cationic distribution prevents such a complete AFM behaviour: the stacking of consecutive (00z) layers originates the appearance of intercalated FM and AFM interlayer interactions (see Figure A2.2 in Appendix II). The coexistence of alternated FM and AFM spins into an hexagonal lattice interacting with another spin located at the centre of such a lattice, can be understood as two coexistent FM sublattices simultaneously coupled to the central spin in opposed directions. The described opposed FM sublattices, which form two twisted triangular lattices, induce a strong magnetic frustration. This frustration along with the magnetic dilution of the Cr^{3+} sublattice weakens the intralayer correlations. Therefore, the system stabilises by rotating FM spins within the *xy* plane, thus giving rise to the detailed helical magnetic structure. Upon cooling, the shorter Mn-Cr lengths elongate from 2.89 (1) Å (at room temperature) to 2.92 (1) Å (at 4 K), while the Mn-Mn (3.11 (1) Å) and Cr-Cr (3.01 (1) Å) remain approximately constant through temperature. Therefore, the interlayer interactions progressively weaken upon cooling while the strength of the interlayer interactions persists. This phenomenom induces the thermal dependence of the competition between Mn-Mn and Mn-Cr interactions, which results in the variation of κ_z.

Since Γ_2 and Γ_3 Ireps are not distinguishable, all the magnetic sites are forced to follow the same Irep, but the experimental data could also arise from the competition of the weak FM intralayer interactions with their AFM natural trend. This would rotate each Mn and Cr sites towards opposite directions, but the good fit of the simpler described model makes it the most probable solution.

3.-Mn_2FeSbO_6

3.1- Double perovskite

3.1.1 - Synthesis and structural characterisation

The synthesis of Mn_2FeSbO_6 also required the use of HPHT conditions. 5.5 GPa and 1523 K were applied during 15 minutes in a Conac-type press, after which the temperature was quenched and the sample was slowly depressurised. XRD measurements and further high resolution NPD data collected at D2B (Figure 3.10a) confirmed the crystallisation of a nearly pure DPv structure in the $P2_1/n$ space group with rock-salt order of Fe and Sb at the B sites. Complete structural details derived from the Rietveld fit of the high resolution NPD data are shown in Table 3.6. A 4 % of antisite disorder among Mn and Fe sites was determined from NPD provided their different scattering lengths (-3.73 fm and 9.45 fm respectively) [9]. The secondary phases included in the refinements, $MnFe_2O_4$ [48] and the high pressure polymorph of Mn_3O_4 [49], amount to < 1 % wt.

The cell parameters are slightly larger than those observed for the analogous Cr polymorph: a = 5.234 (1) Å, b = 5. 389 (1) Å, c = 7. 642 (1) Å and β = 90.372 (1)º. This difference is in accordance to the larger ionic radii of Fe^{3+} ($^{VI}r_{Fe}^{3+}$ = 0.645 Å *vs.* $^{VI}r_{Cr}^{3+}$ = 0.615 Å), which is also reflected in longer bond distances (see Table 3.6). BVS calculations result in a similar apparent over-bonding of Sb^{5+} cation due to its polarising effect.

The tilt angles, directly determined from the < B – O – B' > angles, are ϕ ~ 20.4 º and θ ~ 19.7 º, similar to those discussed for the DPv_Mn_2CrSbO_6 in accordance to their similar octahedral distortions, $\Delta(SbO_6) = 3.210^{-5}$ and $\Delta(FeO_6) = 2.8\ 10^{-4}$, obtained from *Eq. 3*. Figure 3.10b shows two different views of the DPv_Mn_2FeSbO_6 compound along [110] and [001] zone axes, where the $a^-a^-c^+$ tilt system can be observed.

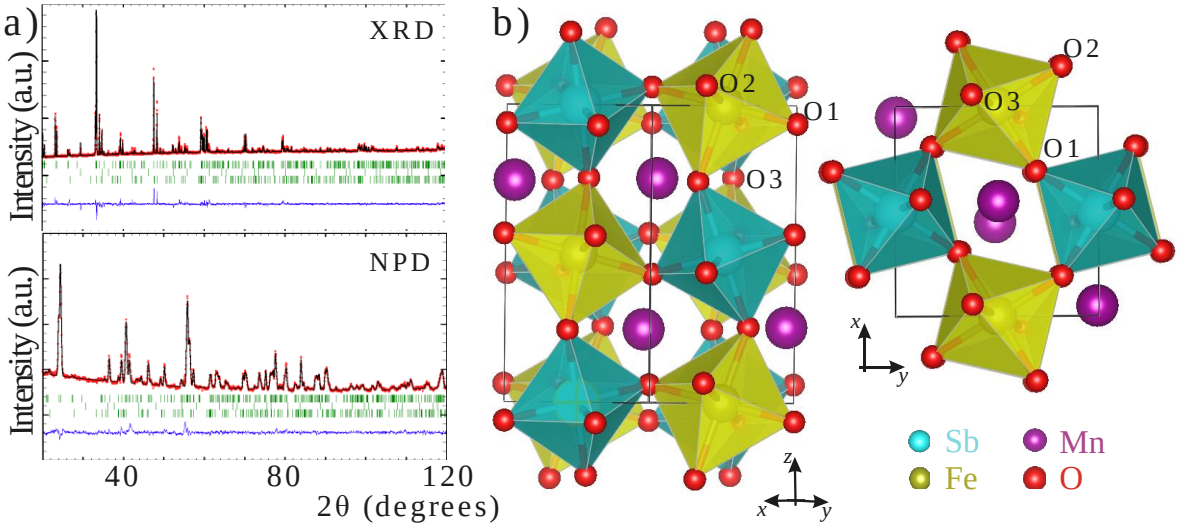

Figure 3.10. a) Rietveld refinements of Mn_2FeSbO_6 DPv polymorph from XRD (up) and NPD (bottom) data; $MnFe_2O_4$ and Mn_3O_4 secondary phases are included (2nd and 3rd rows of Bragg positions respectively). b) Structural model determined from NPD. $a^-a^-c^+$ out-of-phase and in-phase tilts along [110] and [001] directions can be observed in the left and right projections respectively.

Table 3.6.Crystallographic parameters, selected bond distances and angles for the DPv polymorph of Mn_2FeSbO_6 obtained from the Rietveld refinement of NPD data collected at D2B at 300 K.[a]

***P*2$_1$/n**	a = 5. 2341 (1) Å, b = 5. 3894 (1) Å, c = 7. 6415 (2) Å, β = 90.372 (2) º				
Atom-site	x	y	z	Occ	BVS
Mn/Fe– 4e	-0.007 (1)	0.0488 (9)	0.746 (1)	0.96/0.04	1.8
Fe/Mn– 2d	0.5	0	0	0.96/0.04	2.8
Sb – 2c	0	0.5	0	1	5.4
O_1 – 4e	0.3072 (9)	0.3081 (5)	0.9390 (6)	1	__
O_2 – 4e	0.3198 (9)	0.3080 (5)	0.5679 (6)	1	__
O_3 – 4e	0.8765 (6)	0.4450 (6)	0.7553 (5)	1	__

A-O	**d (Å)**	**B-O**	**d (Å)**
Mn- O_1	2.610 (8)	Fe- O_1 (x2)	1.997 (4)
Mn - O_1	2.191 (8)	Fe- O_2 (x2)	2.032 (5)
Mn- O_2	2.602 (8)	Fe- O_3 (x2)	2.080 (5)
Mn- O_2	2.158 (8)	d_{av}.(Fe - O)	2.036 (2)
Mn- O_3	2.221 (6)	Sb - O_1 (x2)	1.970 (5)
Mn- O_3	2.010 (8)	Sb - O_2 (x2)	1.980 (4)
d_{av}.(Mn- O)	2.299 (4)	Sb - O_3 (x2)	1.997 (5)
		d_{av}.(Sb - O)	1.982 (2)
Δ(FeO_6) =	$2.8*10^{-4}$	Δ(SbO_6) =	$3.2*10^{-5}$

< Mn-O_1-Fe >	**< Mn-O_2-Fe >**	**< Mn-O_3-Fe >**
81.6 (3); 113.5 (3)	82.1 (2); 103.5 (3)	91.2 (2); 105.1 (3)

[a]Fitting residuals: R_p= 3.77%, R_{wp}= 2.86%, R_B = 6.27% and R_F = 4.59%,. [b]$V_i = \Sigma_j S_{ij} i = \exp(r_0 - r_{ij}/0.37)$. Values calculated using r_{ij}= 1.79 for Mn^{2+}, 1.759 for $Fe^{3+}$and 1.942 for Sb^{5+}.

In accordance to the observed structural similarities between Mn_2MSbO_6 M = Cr and Fe double perovskite polymorphs, the HRTEM images collected for DPv_Mn_2FeSbO_6 display the same features observed for the M = Cr compound. The micrographs, not shown for that reason, correspond to a well ordered structure free from defects with similar contrast patterns and close periodicities to those explained in section 2 for the related Cr containing compound.

3.1.2 - Magnetic behaviour

The magnetic susceptibility data of the DPv polymorph of Mn_2FeSbO_6 oxide (Figure 3.11) show a complex behaviour. Direct susceptibility is affected by a high temperature contribution, assigned to the well-known ferromagnetic behaviour of $MnFe_2O_4$ oxide above room temperature [50]. This contribution was calculated for the small proportion determined from NPD and subtracted from the susceptibility data. After this correction, Figure 3.11a-top was obtained and the fitting of the reciprocal susceptibility to the Curie – Weiss law in the 250 K - 300 K temperature range yields a total magnetic moment μ_{exp} = 10.36 (1) μ_B and a Weiss constant θ = -17.4 (6) K. The experimental magnetic moment is close to the theoretical value expected for $2Mn^{2+}$ (S = 5/2) and Fe^{3+} (S = 5/2) sublattices (μ_{th} = 10.25μ_B). The negative value of θ and the presence of a maximum in the direct susceptibility point to the development of antiferromagnetic interactions below T_N ~ 55 K. This AFM behaviour is confirmed through the linear increase of field dependent magnetisation measurements (Figure 3.11b). The FM contribution above 200 K coming from the ~ 1% wt. of $MnFe_2O_4$ is μ = 0.05

μ_B. These observations are also in good agreement with those previously reported by Mathieu *et al*. [51].

However, a noticeable anomaly in magnetic susceptibility is observed at T ~ 160 K. At that temperature FC and ZFC data start to diverge pointing to the appearance of incipient FM interactions. However, no additional FM contribution is observed in the magnetisation curves below that temperature. This feature, assigned to a secondary phase by Tyutyunnik *et al*. [52], was further studied under *AC* conditions, which showed an unexpected maximum at that temperature raising an order of magnitude larger than that of the AFM transition in the imaginary contribution χ'' (see Figure 3.11a-bottom). The appearance of such an intense peak in the *AC* susceptibility measurements may originate an eventual MEC [53]. Consequently, the electric behaviour of the DPv_Mn_2FeSbO_6 was also analysed in terms of electric resistance measurements (detailed below).

A more detailed magnetic characterisation was carried out in terms of neutron diffraction at different temperatures. High resolution data were collected at D2B at room temperature, 70 K and 2 K. These patterns, depicted in Figure 3.11c-top, show clear magnetic peaks at 2 K in the low angle region, but only a bump at 70 K in the same angular range. This feature points to the existence of short range magnetic correlations, but no long range interactions are detected below the described anomaly at 160 K. These short range magnetic correlations could be explained on the basis of the onset of FM superexchange interactions through oxygen at 90º via pσ overlapping, favoured for d^5-d^5 interactions [34][3].

In order to check the accurate thermal dependence of the net magnetic behaviour of DPv_Mn_2FeSbO_6, its thermal diffraction was studied from NPD profiles collected each K upon heating from 1.5 K up to 60 K at D1B. As observed in Figure 3.11c-bottom, the magnetic peaks present in the 1.5 K pattern are not retained up to 60 K. Moreover, no differences are observed between the patterns collected at 140 K and 60 K, what confirms the absence of any magnetic long range order in that temperature range.

A careful examination of the complete thermodiffraction pattern, focussed in the 10 º - 60 º angular range up to 60 K in Figure 3.11d, showed neither the appearance of new magnetic peaks nor the increase of the intensity of the nuclear ones down to T_N ~ 55 K. The patterns collected at low temperatures clearly show the onset of magnetic diffraction peaks below T_N ~ 55 K and the increase of intensity of some nuclear peaks upon cooling.

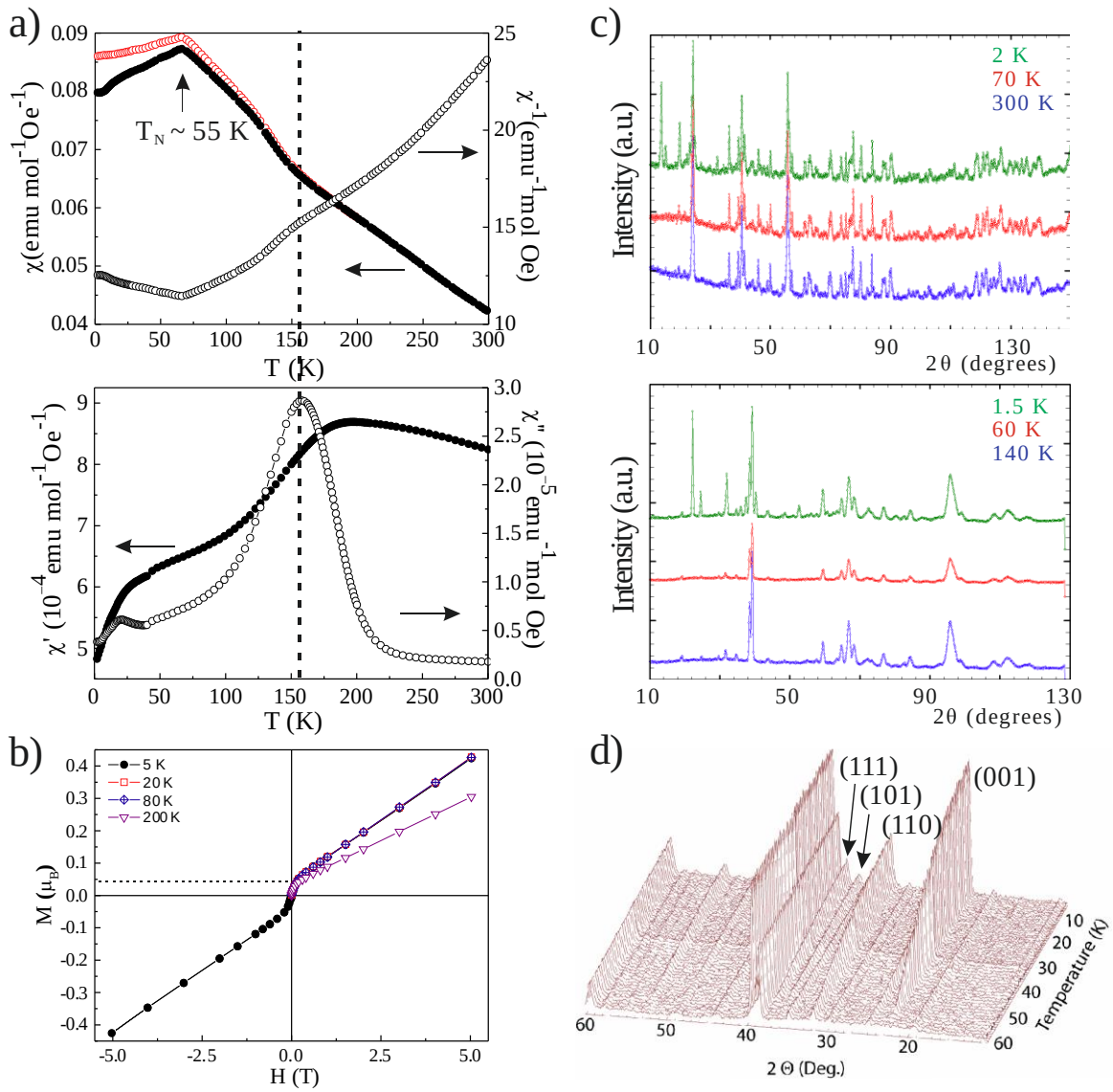

Figure 3.11. Magnetic behaviour of Mn_2FeSbO_6 double perovskite polymorph in terms of a) thermal dependence of the susceptibility under *DC* (top) and *AC* (bottom) conditions and b) field dependent magnetisation measurements. c) NPD profiles collected at 2 K, 70 K and 300 K at D2B diffractometer (top) and at 1.5 K, 60 K and 140 K at D1B instrument (bottom). d) Thermal evolution of the diffraction patterns collected each K at D1B focussed in the 10 º - 60 º angular range up to T = 60 K.

The determination of the magnetic structure at low temperatures was carried out through the Rietveld refinement of the high resolution NPD data collected at 2 K at D2B. All the magnetic peaks can be indexed with an incommensurate propagation vector along the *y* axis: $\kappa = [0\ 0.426\ 0]$. The symmetry analysis performed with BasIReps software [35] resulted in 2 possible Ireps, shown in Table 3.7. All the possible solutions imply the distinction of two independent sites for Mn^{2+} spins and another one for Fe^{3+} cation. Both Ireps contain three basis vectors determining the cooperative (FM) alignment of spins of equivalent positions along the propagation direction and their AFM coupling over the *xz* plane (Γ_1) or the other way around (Γ_2). Under any of them, the approaching procedure includes two main possibilities for refining these components:

i) Refining only Fourier coefficients C1 or C3 would originate a sinusoidal wave running along the *y* axis, with spins of variable modulus confined to the *x* or *z* axis respectively. Those waves would seem like that of Figure 3.12a-top for the FM aligned spins or as an envelope wave, as that schematised in Figure 3.12a-bottom, for the AFM phase. None of these sine waves seem probable solutions as, although they can fit the experimental data, the magnetic moments should vary between 0 and maximum values of $\mu_{(Fe^{3+})} = 5.3\ (2)\ \mu_B$ and $\mu_{(Mn^{2+})} = 7.0\ (1)\ \mu_B$ when confined to the *x* direction and $\mu_{(Fe^{3+})} = 4.5\ (2)\ \mu_B$ and $\mu_{(Mn^{2+})} = 9.1\ (1)\ \mu_B$ when confined to the *z* axis. These values are not realistic since both Mn^{2+} and Fe^{3+} expected magnetic moments are $\mu_{th.} = 5\ \mu_B$. Their large variation in these models seems to compensate the absence of an orthogonal contribution. Moreover, the similar behaviour of their BV under both Ireps point to the better combination of both contributions, as indicated in option ii).

ii) Refining both C1 and C3 coefficients simultaneously would materialise as a helix running parallel to the propagation vector direction. The restraint of both components to the same value originates a circular helix (Figure 3.12b-top) similar to that observed for the ILO polymorph of the Mn_2CrSbO_6 oxide, and the independent refinement of each coefficient originates an elliptical helix (Figure 3.12b-bottom). The differences between circular and elliptical helix magnetic structures are further discussed below.

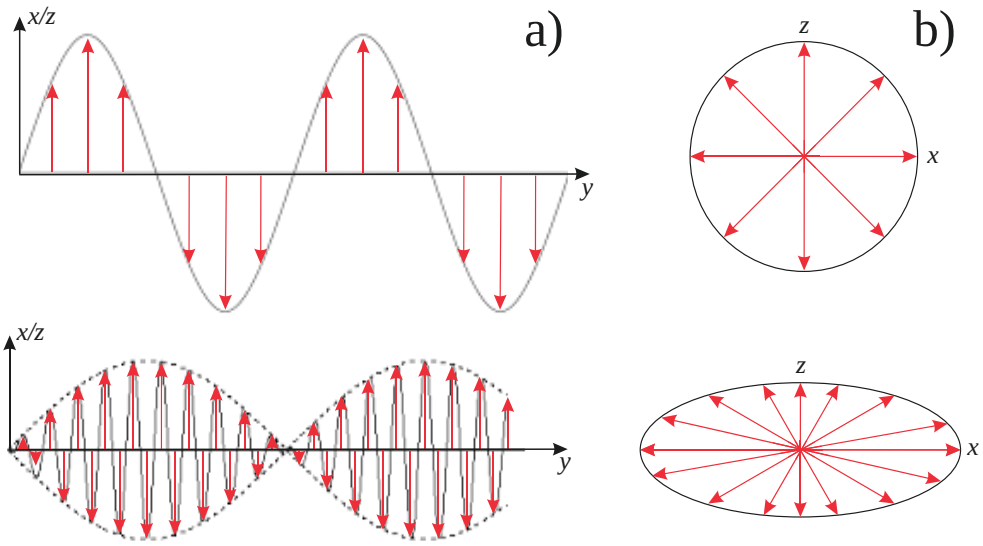

Figure 3.12. Schematic propagation along the *y* axis of the magnetic structures refined as a) FM (top) and AFM (bottom) sine-waves and b) circular (top) and elliptical (bottom) helices.

Table 3.7. Real (BasR) and imaginary (BasI) components of the BV of the allowed Ireps for the magnetic structure of the DPv polymorph of Mn_2FeSbO_6 with propagation vector κ = [0 0.426 0].

Irep / Symm	Γ_1
x, y, z	C1 C2 C3
Bas R	100 010 001
Bas I	000 000 000
-x+1/2, y+1/2, -z+1/2	C1 C2 C3 .
Bas R	-0.2304 0 0 0 0.2304 0 0 0 -0.2304
Bas I	0.9731 0 0 0 -0.9731 0 0 0 0.9731
	Γ_2
x, y, z	C1 C2 C3
Bas R	100 010 001
Bas I	000 000 000
-x+1/2, y+1/2, -z+1/2	C1 C2 C3 .
Bas R	0.2304 0 0 0 -0.2304 0 0 0 0.2304
Bas I	-0.9731 0 0 0 0.9731 0 0 0 -0.9731

The refinement of the helical model needs for the Irep Γ_2, since the use of the AFM one would originate two interpenetrated AFM spirals of Fe^{3+} and Mn^{2+} spins, rotating in the same direction. On the other hand, the restraint of antiparallel C1 and C3 components of Γ_2 originates satisfactorily the AFM contribution in a simple helix.

The first attempt to refine the described helical structure considered the constriction of both *x* and *z* components to a unique value, what resulted in a good fit for the 2 K data collected at D2B (Figure 3.13a-top). The resulting magnetic moments amount to 4.9 μ_B and 4.3 μ_B for Mn and Fe respectively. This magnetic structure can be described as a circular spiral, where all the spins, confined to the *xz* plane, rotate with a constant modulus (magnetic moment) describing a complete circle after ~ 2.35 unit cells along the *y* axis.

However, this refinement slightly improves when the magnetic contributions along *x* and *z* directions are allowed to be independent (see Figure 3.13a-bottom). In that case, an elliptical spiral is obtained, where the maximum components to the magnetic moments amount to 5.9 μ_B and 3.3 μ_B along *x* and *z* directions for Mn^{2+} and to 4.4 μ_B and 4.1 μ_B for Fe^{3+} along the same directions. Due to the negligible difference between the agreement factors of these two models from D2B data, the same refinements were carried out for the magnetic signal collected at D1B using a more suitable wavelength (2.52 Å). The larger wavelength used in this instrument allows a better resolution in the low angles range, in detriment of the high angles region, which is less useful for the magnetic superstructure determination.

Hence, a difference pattern was calculated by subtracting the diffraction profile collected at 140 K to that taken at 2 K. The unique contribution to this diffraction pattern comes from the magnetic phase. The positions of the three magnetic atoms and the peak shape determined from a previously optimised nuclear refinement of the 140 K data were used as starting parameters

Figure 3.13b shows the Rietveld refinements of the magnetic phase with both models. A better fit is obtained for the elliptical helix, with a magnetic reliability factor R_{mag} = 11% in contrast to the R_{mag} = 20% obtained for the circular helix. The magnetic structure at low temperatures is therefore

described as an elliptical helix of the Mn^{2+} and Fe^{3+} spins running through the *y* axis. The magnetic contributions of Mn^{2+} and Fe^{3+} spins along *x* and *z* directions are μ_x (Mn^{2+}) = 5.5 (1) μ_B, μ_z (Mn^{2+}) = 3.1(2) μ_B, μ_x (Fe^{3+}) = 4.6(1) μ_B and μ_z (Fe^{3+}) = 3.0 (2) μ_B. Two different views of this magnetic structure are depicted in Figure 3.13c.

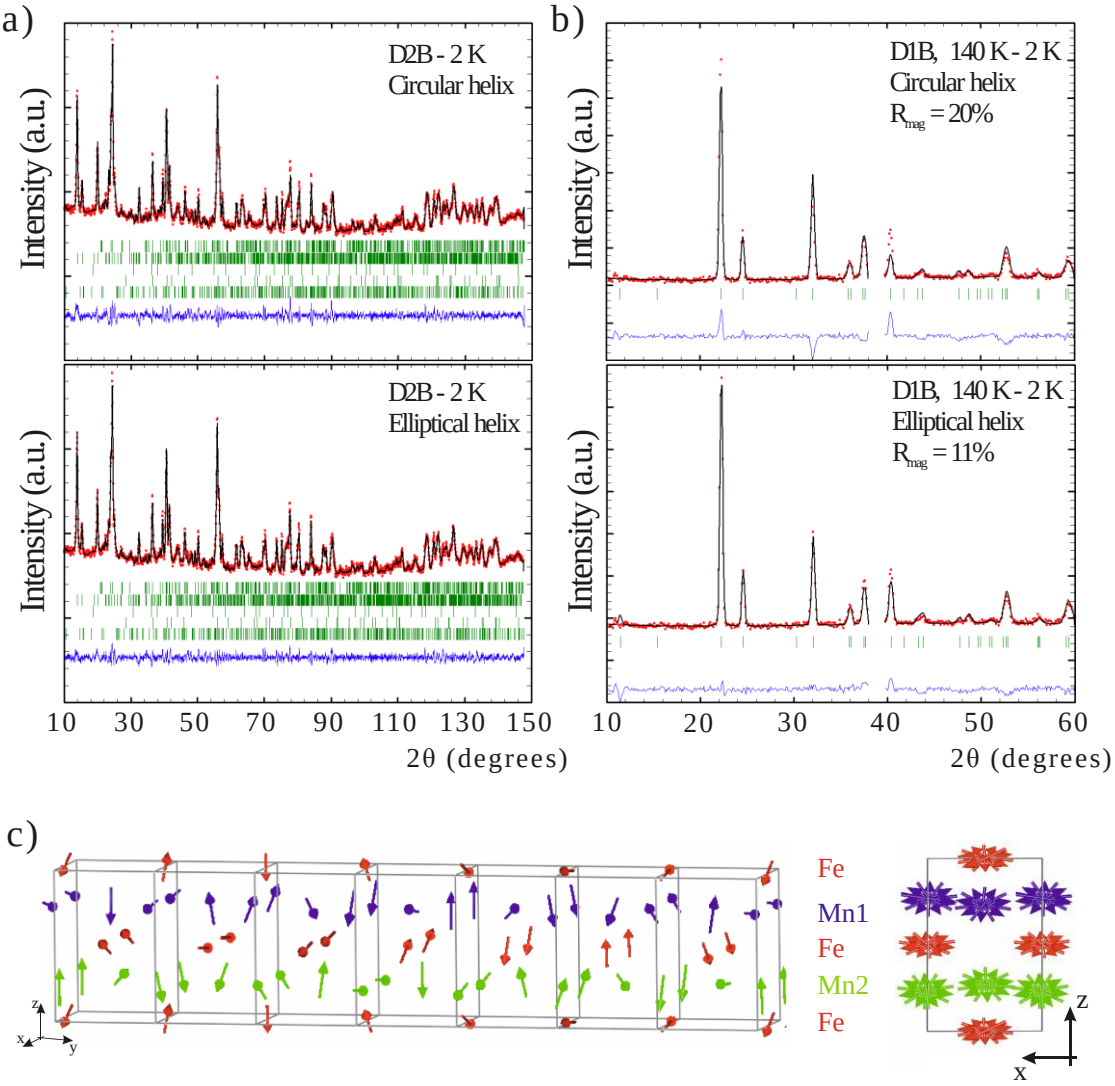

Figure 3.13. a) Rietveld refinements of the low temperature magnetic structure from D2B data collected at 2 K, using the circular helix (top) and the elliptical spiral (bottom) models. b) the same models are used to fit the single phase magnetic structure from the 2 K - 140 K D1B difference pattern. c) Two different views of the magnetic structure stabilised at low temperatures.

The origin of the described incommensurate helical magnetic structure may be the magnetic frustration induced by the competition between the two discussed short range magnetic interactions opposed in sign but equivalent in strength. On the one hand, AFM A-O-B superexchange interactions are operative between Mn^{2+} and Fe^{3+} spins. However, additional FM interactions are allowed in the Fe containing compound via pσ overlapping [34].

The presence of two extra electrons in the valence shell of Fe^{3+} cations respect to Cr^{3+}, strengthens the magnetic interactions in this DPv structure. As a consequence, the discussed short range magnetic interactions occur below 160 K, which is 100 K larger than the observed T_N of DPv_Mn_2CrSbO_6. However, the competition between the discussed AFM and FM short range interactions disrupts the development of long range AFM correlations, which do not occur down to $T_N \sim 55$ K, originating the described helical magnetic structure as consequence of magnetic frustration.

3.1.3 - Electric behaviour

As pointed out during the discussion on the magnetic behaviour, the slight magnetic response observed in *DC* susceptibility measurements is ascribed to the short range order of both the AFM matrix and the FM inhomogeneity. However, the appearance of such a sharp response in the *AC* data at T ~ 160 K compared to that observed at low temperature, points to the coexistence of these short range magnetic correlations with a transition of a different origin. It has been observed in the literature that the coexistence of two short range magnetic phases can originate a hysteresis loop in resistance measurements due to their different conductivities [54]. A similar behaviour could be expected for DPv_Mn_2FeSbO_6 in light of the experimental data, which may give rise to a magneto-electric coupling (MEC).

In order to check this assumption, resistance measurements were carried out using a Quantum Design PPMS. Conventional resistivity measurements [55] revealed the high resistivity of the sample. Therefore, a two - probe technique was used to measure tiny currents under large voltages (up to 20 V), applied by a Keithly 2410 SourceMeter [56]. This local sense mode allowed the accurate detection of currents in the picoamper range [57].

The results, depicted in Figure 3.14a, show a hysteretic behaviour of the resistance as a function of temperature. The hysteresis loop is centred at T ~ 160 K, coinciding with the described unexpected *AC* magnetic response. It is also worth noting that the clockwise sense of this loop is expected to get reversed under the application of a magnetic field, since the more conductive FM phase is enhanced at $H \neq 0$. In such conditions the thermal dependence of the resistance should follow a counter-clockwise loop as that schematised in Figure 3.14b, where the black curve identified with the number 1 represents the schematic resistance upon cooling and the red one identified with the number 2 indicates the lower resistance values expected upon heating.

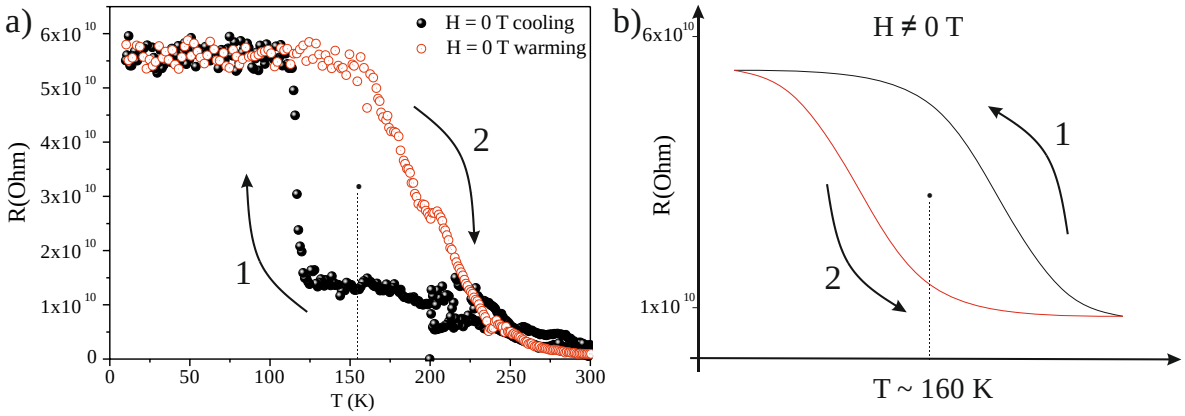

Figure 3.14. Electric behaviour of the DPv polymorph of Mn_2FeSbO_6 in terms of its resistance thermal evolution. a) experimental clockwise hysteresis loop upon cooling (1, black) and heating (2, red) at H = 0. b) scheme of the expected counter-clockwise behaviour under an applied magnetic field.

It is well known that the development of spiral spin structures can break inversion symmetry and generate multiferroicity [58]. In this context, Mathieu *et al.* [51] predicted a related helical magnetic structure for this compound through theoretical calculations and estimated an electronic polarisation P ~ 10 μC/m^2. However, it is remarkable that our experimental data do not show any evidences for an electric response at the magnetic ordering temperature. Otherwise, the cooperative long range magnetic order at T_N ~ 55 K deletes any differences between both FM and AFM short range magnetic phases, thus stabilising a constant average resistance.

The discussed results demonstrate that the substitution of M by different $3d^n$ transition metals induces notable functional modifications in Mn_2MSbO_6 DPv polymorphs. In this context, the results obtained for the M = Fe and Cr containing compounds should be compared. The use of M = Fe^{3+} induces the onset of disordered magnetic regions of different natures. Their competition has been found to give rise to both a magnetic and an electric response in a similar temperature range, thus originating an apparent small MEC. Since the magnitude of this possible effect is rather small, a further study including resistance measurements under an applied magnetic field has been considered not worthy. However, the composition-structure-properties relation determined from this study can be considered as a starting point to optimise the functional behaviour of these oxides in the search for new multiferroic materials.

The appearance of a more complex behaviour in DPv_Mn_2FeSbO_6 can be explained in terms of the isoelectronic character of $3d^5$ Fe^{3+} and $3d^5$ Mn^{2+} cations. In light of this trend, the enhancement of the proposed MEC can be pursued through the substitution of M by selected d^n ($n \neq 5$) transition metals large enough to induce higher antisite exchanges with Mn. The modulation of the A-B site exchange between non-isoelectronic cations is expected to induce varying magnetic interactions which could give rise to potential interesting properties. For instance, among the first transition metals the $3d^4$ Mn^{3+} cation (r = 0.645 Å) [14] is expected to have a better relation between the ionic radius and the electron configuration: its similar size respect to the discussed Fe^{3+} cation may not induce a larger A-B site exchange but its aliovalent configuration may enlarge the dielectric response. A comparable electron variation would be induced by substituting M by the $3d^6$ Co^{3+} cation, but its small size (r =

0.61 Å) is comparable to that of Cr^{3+} so it cannot be expected to get stabilised into the large A-site cuboctahedral void. On the other hand, the larger $3d^2$ V^{3+} (r = 0.64 Å) and d^1 Ti^{3+} (r = 0.67 Å) are prone to originate partial site exchanges but their scarce number of electrons will originate low magnetic moments and negligible MEC effects.

Therefore, it seems that the studied Mn_2FeSbO_6 composition is among the best candidates of the studied Mn_2MSbO_6 family to be multiferroic. It is now interesting to focus on the possibility of originating an enhanced functional behaviour of this compound upon inducing its phase transition into an ILO polymorph, in an analogous manner to that observed for the related DPv_Mn_2CrSbO_6. Provided the disordered configuration of Fe^{3+}/Sb^{5+} cations into the ILO modification, the random distribution of face-sharing d^5 Mn^{2+} - d^5 Fe^{3+} (paramagnetic) and d^5 Mn^{2+} - d^{10} Sb^{5+} (diamagnetic) dimmers could be subject of a local symmetry breaking under the application of an external magnetic field, what turns it into a potential multiferroic material of spin origin [59,60].The complexity of the proposed study relegates it to future work.

3.1.4 - Thermal stability

As previously explained for the isostructural compound with M = Cr, the thermal stability of the double perovskite polymorph of Mn_2FeSbO_6 has been studied through thermal diffraction. The same heating profile, with heating ramps of 5 K / min and diffraction measurements of 30 minutes every 50 K up to 723 K, was performed. Figure 3.15 shows the results obtained for the thermal evolution of this compound, where a similar phase transition to an ilmenite polymorph is observed. The transition starts at 573 K, depicted in red in Figure 3.15, when the intensity of the diffraction peaks of the perovskite structure sharply decrease and the most intense peaks of the ILO - type structure appear. The transformation is completed at 623 K, when only the diffraction peaks assigned to the ilmenite polymorph are observed.

The DPv to ILO transition was explained in section 2 for the Cr containing compound to imply the A / B sites exchange. The Rietveld refinements of DPv_Mn_2FeSbO_6 oxide showed a small proportion of A / B sites already exchanged, what evidences the major tendency of this compound to stabilise this site switching and justifies the lower temperature needed to induce this transition.

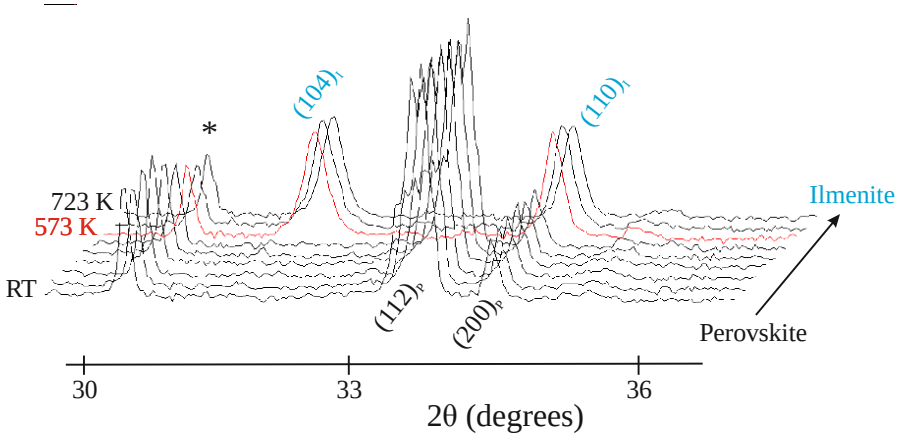

Figure 3.15. Thermal evolution of the XRD patterns of DPv_Mn_2FeSbO_6 upon heating at room pressure up to 723 K.

3.2- Ilmenite

3.2.1 - Synthesis and structural characterisation

The ILO polymorph of Mn_2FeSbO_6 oxide was synthesised under moderate pressure conditions. 3 GPa and 1473 K were applied to the homogeneous mixture of the binary oxides (Mn_2O_3, Fe_2O_3 and Sb_2O_3) in a Conac-type press. The synthesis process required 30 minutes to complete the solid state reaction, after which temperature was quenched and pressure was progressively suppressed.

The preliminary structural characterisation of this product, performed through XRD data, reveals that, in contraposition to the isostructural Mn_2CrSbO_6 oxide, Mn_2FeSbO_6 ilmenite polymorph can easily be isolated through this method. Consequently, although this compound can also be obtained from the high temperature phase transition of the high pressure DPv polymorph, the structural and functional studies of this compound presented along this subsection were carried out from the direct synthesis product. The use of higher pressures normally produces an increment of undesired secondary phases that will also be present after the thermal treatment to induce the phase transformation.

The Rietveld refinement of both XRD and high resolution NPD data collected at room temperature (Figure 3.16a) evidenced the crystallisation of the sample in the rhombohedral $R\bar{3}$ space group with cell parameters a = 5.2321 (2) Å and c = 14.3722 (8) Å. No difference can be appreciated between Mn and Fe in XRD as a consequence of their similar atomic numbers Z_{Mn} = 25 and Z_{Fe} = 26, as previously described for the analogous Mn_2CrSbO_6 oxide. Therefore, NPD is needed to complete the structural characterisation. The difference in the neutron scattering lengths allows to distinguish between the negative value of Mn sites (-3.73 fm) and the positive ones of Fe and Sb (9.45 fm and 5.57 fm respectively) [9]. Furthermore, a clear difference in the NPD patterns should be appreciated if Fe and Sb were somehow ordered, since the tabulated coherent neutron scattering length for Fe is about twice as long as that of Sb. The optimised structural model of ILO_Mn_2FeSbO_6 oxide, depicted in Figure 3.16b, is straightforward obtained by fitting the experimental data using the ILO_Mn_2CrSbO_6 structure as a starting model [1]. The structural features, including atomic positions and main interatomic distances and angles, slightly different from those of the isostructural compound with M = Cr, are detailed in Table 3.8.

The c cell parameter is similar to that observed for the ILO_Mn_2CrSbO_6, but a larger a value is obtained in agreement with the larger ionic radius of Fe^{3+} ($^{VI}r_{Fe^{3+}}$ = 0.645 Å, $^{VI}r_{Cr^{3+}}$ = 0.615 Å). The same tendency is found for the bond lengths, as the averaged value of the experimental Mn-O bonds is rather constant but the averaged M/Sb-O bonds increase 0.022 Å for M = Fe *vs.* M = Cr. The octahedral distortions, calculated from equation *Eq. 3*, are also similar for MnO_6 but up to three orders of magnitude higher for Fe/SbO_6 octrahedra than those of Cr/SbO_6. The difference on this distortion is induced by the larger displacement of B-site cations from their ideal sites in the centre of their octahedra. This value, determined from the difference between the ideal 1/6 and 1/3 z coordinate of the cationic positions and the experimentally determined accurate positions, are d_{Mn} = 0.403 Å and $d_{Fe/Sb}$ = 0.216 Å. As expected, the displacement of Mn^{2+} cations is not far away from that determined for the isostructural Cr containing compound (d_{Mn} = 0.360 Å), but Fe^{3+}/Sb^{5+} are farther displaced ($d_{Cr/Sb}$ = 0.115 Å) due to the different electronic environments of Cr^{3+} (d^3) and Fe^{3+} (d^5) cations: the electrostatic repulsion of Mn - Fe pairs is higher than that of Mn - Cr, what justifies the larger cation shifts and octahedral distortions found in ILO_Mn_2FeSbO_6. BVS calculations from M - O distances

using a standard interpolation method [13] yielded $Mn^{2.0+}$, $Fe^{3.0+}$ and $Sb^{4.9+}$, thus confirming their expected oxidation states into the nominal Mn_2FeSbO_6 composition.

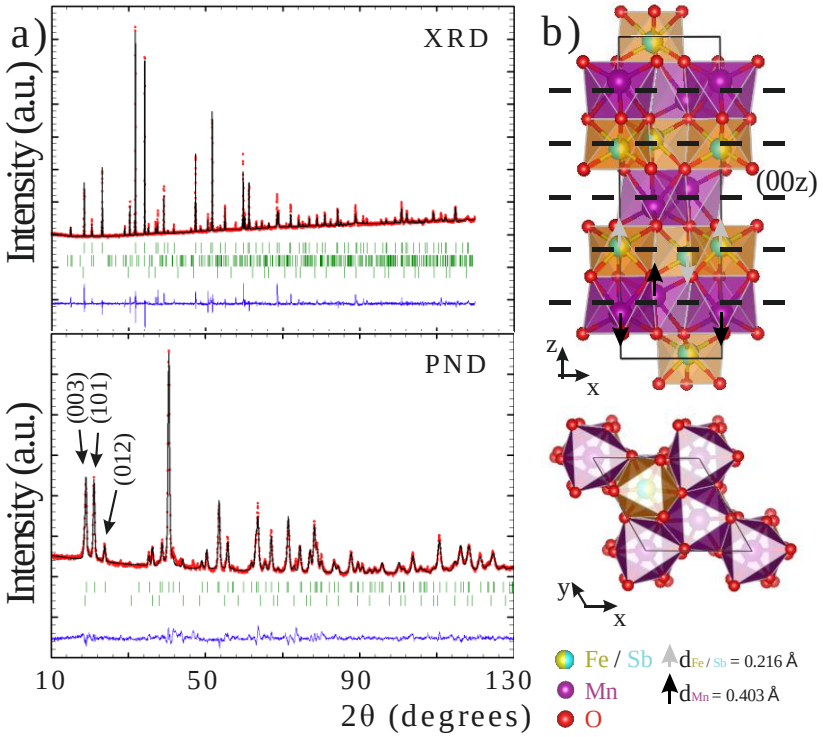

Figure 3.16. a) Rietveld refinements of the XRD (up) and NPD (bottom) data of ILO_Mn_2FeSbO_6. $MnFe_2O_4$ and Sb_2O_4 secondary phases are included (2nd and 3th rows of Bragg positions). b) Two different projections of the structural model determined from NPD, along [010] and [001] directions. The displacement of the cations from (00z) layers is identified as d_M and schematised as black and grey arrows for Mn and Fe/Sb, respectively.

Table 3.8.Crystallographic parameters, selected bond distances and angles for the ILO polymorph of Mn_2FeSbO_6 from the Rietveld refinement of NPD data collected at D2B at 300 K.[a]

$R\bar{3}$	a = 5.2321 (2)Å		c = 14.3722 (8) Å		
Atom-site	x	y	z	Occ	BVS
Mn– 6c	0	0	0.1384 (4)	1	2.0
Fe/Sb– 6c	0	0	0.3486 (2)	0.5/0.5	3.0/4.9
O– 18f	0.2897 (4)	-0.0211 (5)	0.2562 (2)	1	__

A-O	**d (Å)**	**B-O**	**d (Å)**
Mn - O (x3)	2.312(5)	Fe/Sb - O (x3)	2.059(3)
Mn - O (x3)	2.109 (3)	Fe/Sb - O (x3)	1.971(3)
d_{av}.(Mn - O)	2.215 (2)	d_{av}.(Fe/Sb - O)	2.015 (2)
Δ(MnO_6)	$2.1*10^{-3}$	Δ(Fe/SbO_6)	$4.8*10^{-4}$

<Mn – O – Mn >	**<Fe – O – Fe>**	**< Mn – O – Fe>**
90.3 (2)	98.0 (2)	118.2 (2); 127.7 (2)

[a]Fitting residuals: R_p= 3.4%, R_{wp}= 4.6%, R_B = 4.0% and R_F = 2.9%,. [b]$V_i = \Sigma_j S_{ij} i = \exp(r_0 - r_{ij}/0.37)$. Values calculated using r_{ij}= 1.79 for Mn^{2+}, 1.759 for Fe^{3+} and 1.942 for Sb^{5+}.

3.2.2 - Magnetic behaviour

The magnetic characterisation of the ILO_Mn_2FeSbO_6 sample was performed through temperature dependent magnetic susceptibility and magnetic field dependent magnetisation measurements. On the one hand, the direct susceptibility data, depicted in Figure 3.17a, show up to three different changes of slope. The first of them, enlarged on the inset, occurs at T ~ 500K. It appears as a very subtle response in the context of the large transitions observed at lower temperatures, though it is worth noting that the Curie constant above and below this transition changes from 11.38 to 10.57, what implies a variation of the magnetic moment of 0.35μ_B /f.u. This subtle but effective transition is assigned to an external parameter slightly affecting the magnetic susceptibility at that temperature. compound which will be further explored in future studies..

Concerning the other two magnetic transitions, a large ferrimagnetic coupling is observed at T_{N1} ~ 260 K, coincident with the observations predicted by Mathieu *et al*. [61], and a smaller inflection point appears at T_{N2} ~ 50 K. The linear fit of the reciprocal susceptibility data to the Curie-Weiss law in the 650 – 530 K temperature range yields a Weiss temperature θ = -464.4 K and a total magnetic moment μ_{exp} = 9.54 μ_B /f.u., in agreement with the expected $\mu_{th.}$ = 10.25 μ_B /f.u. for 2 Mn^{2+} and Fe^{3+}sublattices.

Field dependent magnetisation measurements, depicted in Figure 3.17b, show an S-shape plot at all the measured temperatures, with small coercive fields (~ 28 Oe) and saturation magnetic moments up to 4.5 μ_B at 2 K. The S-shape of these M *vs.* H curves indicates the absence of domains in the crystals, what added to the observed saturation value and to the nature of the transition observed at T_{N1} in magnetic susceptibility curves, point to the antiparallel arrangement of two FM sublattices. Such magnetic structure coincides with 2 Mn^{2+} (2*S = 2*5/2) opposed to Fe^{3+} (S = 5/2) spins, what originates a net FM contribution equivalent to that of an S = 5/2 cation.

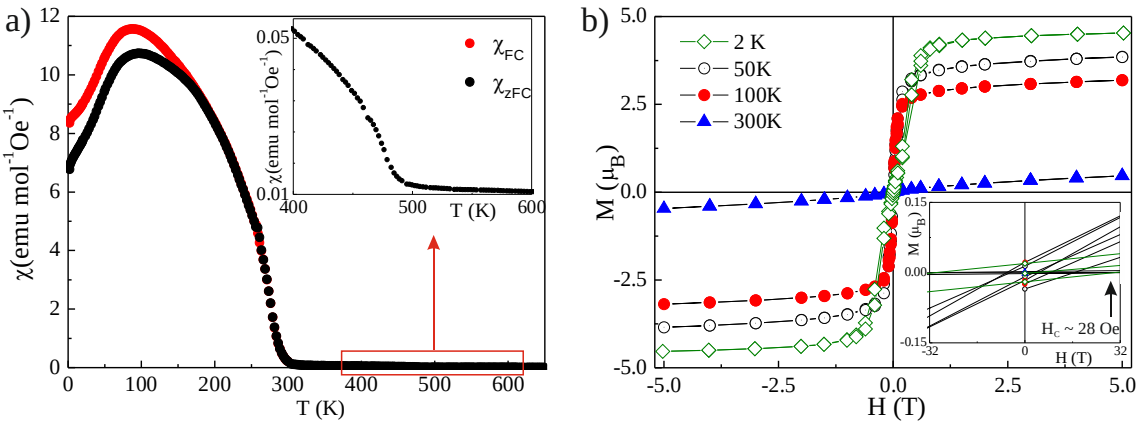

Figure 3.17. Magnetic behaviour of ILO_Mn_2FeSbO_6 in terms of a) thermal dependence of the magnetic susceptibility and b) field dependent magnetisation measurements. The insets show the enlargement of a) the high temperature magnetic transition and b) the small coercive field ~ 28 Oe.

In order to confirm this predicted magnetic structure and to determine the direction of the aligned spins, NPD patterns were collected at the high intensity D20 instrument every 0.7 K in the temperature range 280 K –4 K. Figure 3.18a shows a magnification of the low angle region of these diffraction patterns, where the nuclear (003) and (101) reflections are observed to increase their intensity below T_{N1}~ 260 K. Figure 3.18b shows a two-dimensional thermal evolution of these peaks, where the darkening of their red colour indicates their increase of intensity starting at ~ 275 K and stabilised at T_{N1}~ 260 K. This magnetic transition does not originate the appearance of any new Bragg peaks, what reveals a propagation vector κ_1 = [0 0 0].

High resolution NPD data were also collected at 150 K and 4 K at D2B diffractometer using wavelengths λ = 2.398 Å and 1.594 Å: the longer one is more suitable for discerning the magnetic peaks appearing at low angles and thus to determine the propagation vectors; otherwise, the shorter one is better for fitting the magnetic moments. The magnetic peaks at 150 K can be indexed with a propagation vector κ_1 = [0 0 0]. The symmetry analysis under this propagation vector for the atomic positions summarised in Table 3.8 yields six possible Ireps of one single BV for both Mn and Fe sites. As shown in Table 3.9a, three of them (Γ_2, Γ_4 and Γ_6) describe an AFM alignment of the spins and the other three (Γ_1, Γ_3 and Γ_5) describe a FM one. As deduced from the results of the M *vs.* H data, the magnetic structure should be ferro- or ferrimagnetic, for which the Ireps describing AFM structures can be excluded. Testing the FM Ireps by refining the 150 K data, it turned out that there is no spin contribution along the *z* direction, thus excluding Γ_1 too. Both Mn and Fe spins appear to follow the same Irep (Γ_3 or Γ_5), though they are independent magnetic sites and could behave in different manners. As discussed in the isostructural Mn_2CrSbO_6, these two Ireps (which are equivalent to the so-called Γ_2 and Γ_3 in the low temperature structure and the M = Cr compound) are undistinguishable, since they stand for the propagation of the same spin order towards opposite directions.

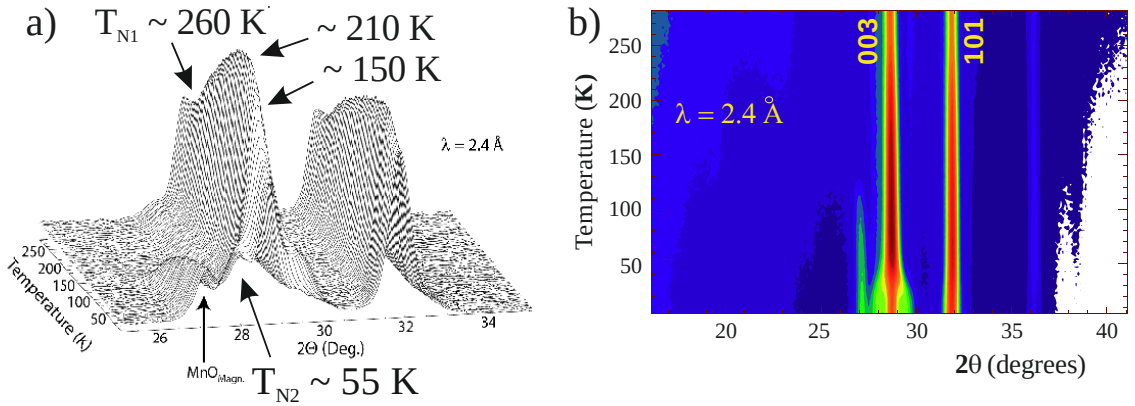

Figure 3.18. Thermal evolution of the NPD profiles of the ilmenite polymorph of Mn_2FeSbO_6 oxide enlarged for the low angles range. The spin reorientation is easily observed in Figure a), where the patterns obtained at the most significant temperatures are labelled: T_{N1} and T_{N2}, the beginning of the spin reorientation process and that at which the collineal structure has been refined (150 K).. The appearance of the magnetic satellites featuring the low temperature magnetic structure is evidenced in Figure b), where the thermal evolution of the diffraction peaks at low angles is depicted for the complete 280 K – 4 K temperature range. The peak appearing at T ~ 120 K is the main magnetic peak of the secondary MnO phase, that is only visible due to its strong magnetic contribution.

Table 3.9. Real (BasR) and imaginary (BasI) components of the BV of the allowed Ireps for the magnetic structures of the ILO polymorph of Mn_2FeSbO_6 from the symmetry analysis of NPD data collected at D2B at a) 150 K with propagation vector κ_1 = [0 0 0] and b) 4 K with propagation vector κ_2 = [0 0 δ].

a) 150 K , κ_1 = [0 0 0]			b) 4 K , κ_2 = [0 0 δ]	
Symm / Irep	x, y, z Bas R Bas I	-x, -y, -z Bas R Bas I	Symm / Irep	x, y, z Bas R Bas I
Γ_1	0 0 1 0 0 0	0 0 1 0 0 0	Γ_1	0 0 1 0 0 0
Γ_2	0 0 1 0 0 0	0 0 -1 0 0 0		
Γ_3	1.5 0 0 -0.8660 -1.7321 0	1.5 0 0 -0.8660 -1.7321 0	Γ_2	1.5 0 0 -0.8660 -1.7321 0
Γ_4	1.5 0 0 -0.8660 -1.7321 0	1.5 0 0 0.8660 1.7321 0		
Γ_5	1.5 0 0 0.8660 1.7321 0	1.5 0 0 0.8660 1.7321 0	Γ_3	1.5 0 0 0.8660 1.7321 0
Γ_6	1.5 0 0 0.8660 1.7321 0	1.5 0 0 -0.8660 -1.7321 0		

Therefore, the Rietveld refinement of the NPD data collected at 150 K (Figure 3.19a) was performed using Γ_3 Irep for both magnetic sites and constraining them to have opposite signs. This refinement resulted in a collinear ferrimagnetic structure, depicted in Figure 3.19b. The orientation of the spins along *x* or *y* directions cannot be distinguished from powder data due to their equivalent symmetry restrictions. Summarising, this structure can be described as the collinear alignment of spins along the *x* axis in two antiparallel ($2Mn^{2+}$ and Fe^{3+}) FM sublattices. The magnetic moments in this structure amount to 2.5 μ_B and 3.2 μ_B for Mn and Fe respectively. It is worth noting that these values are rather low but agree with the low saturation value in the magnetisation curves at this temperature.

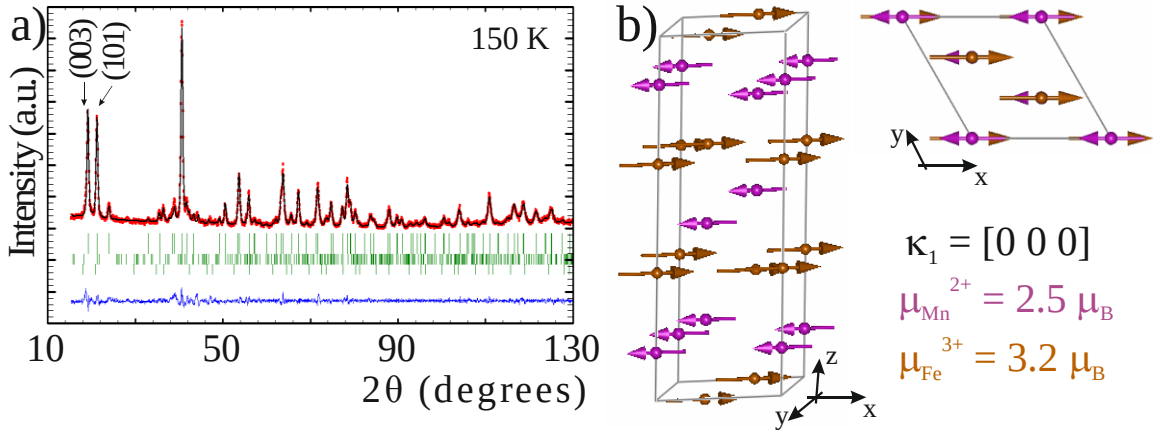

Figure 3.19. a) Rietveld refinement of the NPD data of ILO_Mn_2FeSbO_6 polymorph collected at 150 K at D2B. $Mn_2Sb_2O_7$ and MnO secondary phases are included (3rd and 4th rows of Bragg positions). b) Two different projections of the magnetic structure determined from a).

However, this structure does not represent the magnetic ground state of the system. Noticeable changes appear in the NPD data upon cooling down to 4 K, as evidenced in Figure 3.18. First, the MnO secondary phase becomes magnetic at ~ 120 K, as observed from the magnetic reflection arising at ~ 27 º. Afterwards, the ILO phase undergoes a second magnetic transition at ~ 50 K, where the described magnetic phase ruled by κ_1 = [0 0 0] turns into an incommensurate magnetic structure, as indicates the appearance of new satellite peaks around (003) reflection.

The high resolution NPD data collected at 4 K can be indexed with a propagation vector κ_2 = [0 0 0.07]. The magnetic symmetry analysis shows that the cation sites 00z and 00-z, which were coupled at 150 K, become now independent under the new propagation vector. Consequently, four independent magnetic sites are now based on three Ireps, summarised in Table 3.9b. The refinement of these data (Figure 3. 20a) assuming a low temperature magnetic structure related to the high temperature one, with spins on 00z and 00-z sites following the same Irep and having the same magnetic moment, reproduced very well the intensity of the new satellite peaks upon introducing a phase factor. Therefore, the main change happening at T_{N2} is the variation from the κ_{HT} = [0 0 0] to κ_{LT} = [0 0 δ], resulting in a helical structure running parallel to the *z* axis with the magnetic moments of both antiparallel Mn^{2+} and Fe^{3+} sublattices turning within the basal *xy* plane. Two different projections of this magnetic structure are depicted in Figure 3.20b.

It is worth noting that the refinement of the described model fitting the data collected under both wavelengths resulted in slightly different features. On the one hand, the shortest wavelength (λ = 1.594 Å) fits κ_{LT} = [0 0 δ] to δ = 0.069 and the magnetic moments to 4.8 (1) μ_B for Mn^{2+} sites and 4.7 (1) μ_B for Fe^{3+}. The included phase factor, required to fit this model as a consequence of the splitting of each Mn and Fe sites into two independent magnetic sites, describes the turning angle from 00z to 00-z sites. It refines to ϕ = 0.142 (3), which corresponds to a ~ 51 º turning angle. On the other hand, the use of the longest wavelength (λ = 2.398 Å) resulted in slightly reduced magnetic moments of 4.5 (1) μ_B for both Mn and Fe, a similar phase angle of ~ 53 º and a propagation vector κ_{LT} = [0 0 0.072]. Since the data taken at 2.398 Å have better resolution, they are more appropriate for determining the value of δ in the propagation vector. Otherwise, the data collected under 1.594 Å give more reliable magnetic moments due to their increased Q-range.

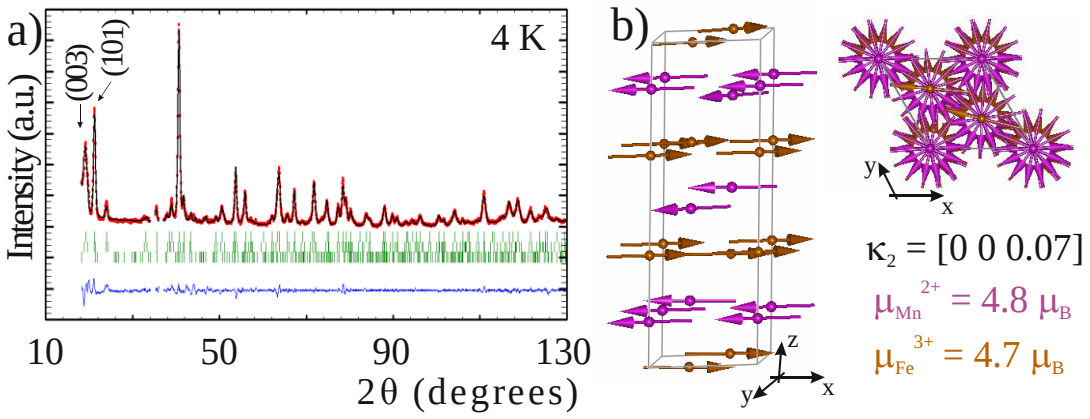

Figure 3.20. a) Rietveld fit of the 4 K NPD data of ILO_Mn_2FeSbO_6 collected at D2B. $Mn_2Sb_2O_7$ secondary phase is included (3rd row of Bragg positions). Two excluded regions mask the magnetic peaks of secondary MnO. b) Two different projections of the magnetic structure determined from a)

To sum up, this magnetic structure, depicted in Figure 3.20b, can be described as an incommensurate helix running along the *z* axis with a propagation vector κ_2 = [0 0 0.07]. Both Mn and Fe spins rotate within the basal *xy* plane under a magnetic phase factor ϕ = 0.142 (3), which defines a 51 º turning angle between the independent magnetic sites. The magnetic moments amount to 4.8 (1) μ_B/f.u. and 4.7 (1) μ_B/f.u. for Mn^{2+} and Fe^{3+} respectively, in good agreement with the expected 5 μ_B/f.u. for both S = 5/2 cations. This value is also in accordance to the saturation value of the magnetisation curve measured at 2 K.

In order to understand the origin of the spin reorientation of this sample, further discussion on the types of magnetic interactions is needed. The magnetic transition at 260 K is assigned to a ferrimagnetic behaviour, resulting from the antiparallel alignment of Mn and Fe sublattices. The magnetic structure determined from the refinement of 150 K data agrees with the predicted magnetic behaviour from susceptibility and magnetisation curves. As detailed for the analogous ILO_Mn_2CrSbO_6 compound and in Appendix II, the AFM interactions among Mn^{2+} and Fe^{3+} sublattices are governed by the direct overlapping of the t_{2g} orbitals which originates the direct cation-cation interactions through face sharing octahedra [47]. Moreover, these interactions are reinforced by superexchange interactions through oxygen via e_g orbitals [34] (see Appendix II for further details). In this case, both A (d^5 Mn^{2+})- and B (d^5 Fe^{3+})-site cations have half-filled d_z^2 and d_x^2-$_y^2$ orbitals, what justifies their stronger interaction and the consequently higher T_{N1} of this oxide: note that the ordering temperature of this transition increases 200 K upon substituting M = Cr ($3d^3$) by Fe ($3d^5$).

On the other hand, FM d^5-d^5correlations are observed within each magnetic sublattice. According to the nuclear structure, these coplanar cations should interact AFM either directly through the t_{2g} orbitals oriented towards the octahedral edge or through superexchange pathways. As detailed in Appendix II, both Mn_2CrSbO_6 and Mn_2FeSbO_6 ILO polymorphs show a strong competition between (00z) interlayer and intralayer interactions as a consequence of their incompatibility. Since not all the magnetic correlations in the corundum derivatives can be AFM, the discussed competition favours the antiparallel coupling between both sublattices, in expense of the interactions within a (00z) layer, which become forced to align FM.

Upon cooling, the Mn - Fe/Sb distances elongate but the Mn - Mn and Fe - Fe ones remain approximately constant, what makes both intralayer and interlayer interactions similar in strength but opposite in sign. Their enhanced competition thus gives rise to their magnetic frustration, what originates the development of a similar incommensurate helical modulation to that observed for the isostructural M = Cr compound. The progressive evolution of these magnetic exchanges resulted in the thermal dependence of the propagation vector in the Cr containing compound in a continuous magnetic transition, but apparently a single propagation vector for the helical magnetic structure should describe a more abrupt magnetic transition at low temperatures in the ILO_Mn_2FeSbO_6 oxide.

However, as pointed out from the analysis of the thermodiffraction patterns of Figure 3.18, a gradual spin reorientation occurs through a wide temperature range. In this scope, Mn^{2+} and Fe^{3+} spins may slowly rotate from their stacked antiparallel directions along the *x* axis of the commensurate magnetic structure appearing at T_{N1} ~ 260 K towards their independent orientations in the incommensurate helical magnetic structure determined at low temperatures. This subtle reorientation starts at T ~ 210 K, where a change on the intensity of the magnetic peaks is observed in the thermodiffraction. The intensification of this reorientation observed in the thermal evolution of the NPD patterns at ~ 180 K

agrees with the thermal dependence of the magnetic susceptibility data and with the magnetic field effect over the magnetisation measurements. However, the determination of a new propagation vector is not possible down to the so-called T_{N2} ~ 50 K, where satellite reflections appear around (003) peak. The small *z* component of the propagation vector determined at 4 K evidences the slow evolution of this spin reorientation upon cooling down to 4 K from the maximum intensity of the magnetic peaks arising at the first magnetic transition (260 K).

The low magnetic moments determined from the Rietveld refinement of the high resolution NPD data collected at 150 K can be explained in terms of this progressive rotation: in the model for the magnetic structure at that temperature Mn^{2+} and Fe^{3+} are restrained to be collinear, since their rotation within the *xy* plane is infinitesimal. For this reason, the lower intensity of the main magnetic peaks (003) and (101) refines to lower ordered moments, in the absence of new satellite reflections indicating the new direction of the already ordered spins.

The small δ value of the κ_2 defines the *c* parameter of the magnetic cell as 1/0.07 ~ 14.3 times larger than that of the nuclear cell, i.e. ~ 205 Å. The smaller propagation vector in ILO_Mn_2FeSbO_6 evidences a smaller magnetic frustration than that of ILO_Mn_2CrSbO_6. The interaction between Mn and Fe (00z) layers is stronger through the overlapping of two half-filled orbitals, what diminishes the magnetic frustration of this system. The result of this smaller frustration is the stabilisation of smaller rotation angles between consequent layers. On the other hand, the larger frustration of the Cr containing compound originates multiple helical magnetic structures of similar energy, which evolve with temperature. Provided the lower stability of each magnetic structure, this evolution occurs in a shorter temperature range: the magnetic structure of Mn_2FeSbO_6 is more stable, featuring its slow thermal evolution.

As proposed for the ILO_Mn_2CrSbO_6, the occurrence of a different magnetic structure with independent Mn^{2+} and Fe^{3+} magnetic sites following the undistinguishable Γ_2 and Γ_3 Ireps is tested. The refinement of this new model requires the combination of both bases into a single coIrep constituted by two BV. Mn1 (00z) and Fe2 (00z') magnetic sites are constrained to follow a counter-clockwise rotation through the BV corresponding to Γ_3 Irep and Mn2 (00-z) and Fe1 (00-z') sites rotate clockwise through the BV derived from Γ_2. Under these guides, the nearest neighbour spins within a common (00z) layer describe rotations towards opposite directions. This behaviour could be induced by their competing AFM nature and their FM orientation forced at high temperatures. In this case, the isoelectronic character of both cations allows the restriction of all the spins to the same value. This simplification reduces the magnetic parameters to one, since the only difference between both C1 and C2 coefficients is the sign which indicates the AFM coupling of Mn^{2+} and Fe^{3+} sublattices. The optimisation of this model (Figure 3.21) refines to a magnetic moment μ = 4.75 (2) μ_B, similar to those obtained from the original helical model ($\mu_{Mn^{2+}}$ = 4.8 μ_B and $\mu_{Fe^{3+}}$ = 4.7 μ_B).

These two solutions present not only similar magnetic moments, but also similar reliability factors. A smaller R_{mag} (6.32% *vs.* 7.04%) but larger R_p (3.81% *vs.* 3.65%), R_{wp} (5.25% *vs.* 4.93%) and χ^2 (4.1 *vs.* 3.62) values were obtained from the original model with the simple helix. These results are therefore similar, and the impossibility to discern clockwise or counter-clockwise rotations through powder diffraction points to the higher probability of the simpler structure described from the first refinement, where all the magnetic sites follow the same irreducible representation as they do at

higher temperatures. The available experimental techniques cannot discern both situations, but further neutron diffraction experiments should be collected on a single crystal ILO_Mn_2FeSbO_6.

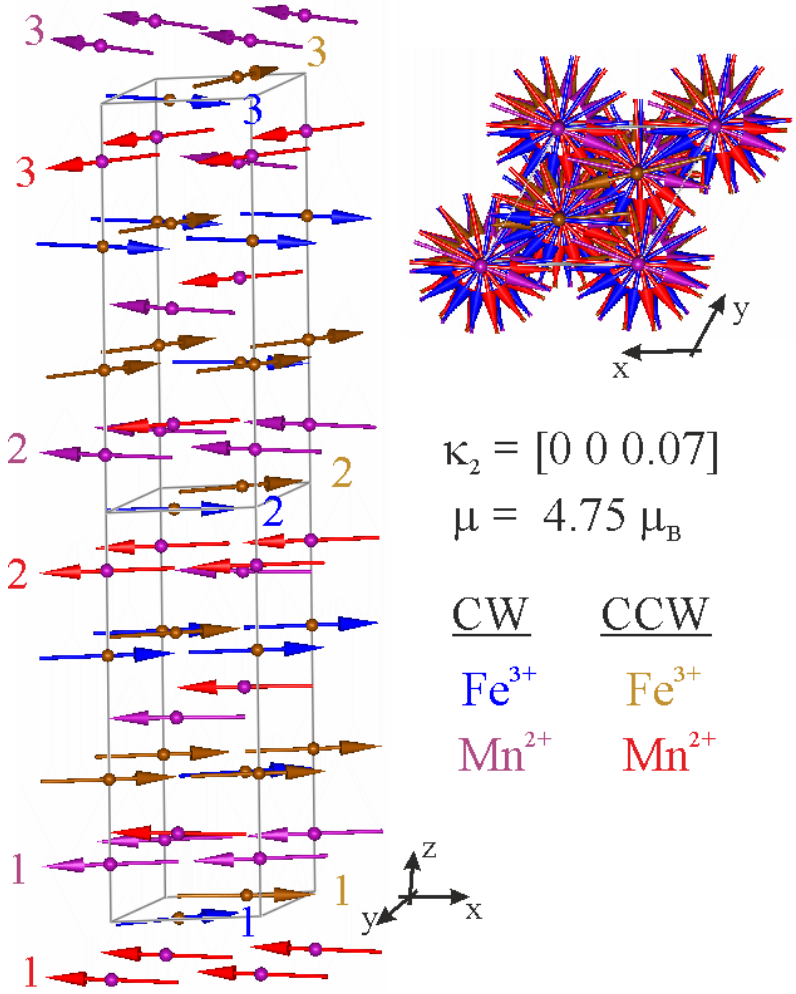

Figure 3.21. Alternative model for the low temperature magnetic structure of the ilmenite polymorph of Mn_2FeSbO_6 with independent magnetic sites for both Mn (purple and red) and Fe (blue and brown) rotating clockwise (CW) and counter-clockwise (CCW) respectively.

4.-Bibliography

[1] Dos santos-García A.J., Solana-Madruga E., Ritter C., Ávila-Brande D., Fabelo O., Sáez-Puche R. Synthesis, structures and magnetic properties of the dimorphic Mn_2CrSbO_6 oxide. Dalt. Trans. 2015;44:10665. doi:10.1039/c4dt03849e.

[2] Solana-Madruga E., Dos santos-García A.J., Arévalo-López A.M., Ávila-Brande D., Ritter C., Attfield J.P., et al. High pressure synthesis of polar and non-polar cation-ordered polymorphs of Mn_2ScSbO_6. Dalt. Trans. 2015;44:20441–8. doi:10.1039/c5dt03445k.

[3] Dos santos-García A.J., Ritter C., Solana-Madruga E., Sáez-Puche R. Magnetic and crystal structure determination of Mn_2FeSbO_6 double perovskite. J. Phys. Condens. Matter. 2013;25:206004. doi:10.1088/0953-8984/25/20/206004.

[4] Solana-Madruga E. Relación estructura - propiedades magnéticas en compuestos con estequiometría ABO_3 y sus derivados. Trabajo fin de licenciatura. 2012.

[5] Solana-Madruga E. Efecto de la presión sobre la estructura de compuestos con estequiometría ABO_3: Relación estructura – propiedades. Trabajo fin de máster. 2013.

[6] MALTA-Consolider. An introduction to high-pressure science and technology. 2016.

[7] Yusa H., Akaogi M., Sata N., Kojitani H., Yamamoto R., Ohishi Y. High-pressure transformations of ilmenite to perovskite, and lithium niobate to perovskite in zinc germanate. Phys. Chem. Miner. 2006;33:217–26. doi:10.1007/s00269-006-0070-5.

[8] Evans T., James P.F., Series L., Sciences P., Jan N., Society R., et al. A Study of the Transformation of Diamond to Graphite. Proc. R Soc. A 1964;277:260–9. doi:10.1098/rspa.1964.0020.

[9] Sears V.F. Neutron scattering lengths and cross sections. Neutron News 1992;3:26–37. doi:10.1080/10448639208218770.

[10] Vasala S., Karppinen M. $A_2B'B''O_6$ perovskites: A review. Prog. Solid State Chem. 2015;43:1–36. doi:10.1016/j.progsolidstchem.2014.08.001.

[11] Anderson M., Greenwood K., Taylor G., Poeppelmeier K. B-cation arrangements in double perovskites. Prog. Solid State Chem. 1993;22:197–233. doi:10.1016/0079-6786(93)90004-B.

[12] Retuerto M., Martínez-Lope M.J., García-Hernández M., Muñoz A., Fernández-Díaz M.T., Alonso J.A. Crystal and magnetic study of the disordered perovskites $Ca(Mn_{0.5}Sb_{0.5})O_3$ and $Ca(Fe_{0.5}Sb_{0.5})O_3$. Mater. Res. Bull. 2010;45:1449–54. doi:10.1016/j.materresbull.2010.06.036.

[13] Attfield J.P. Charge ordering in transition metal oxides. Solid State Sci. 2006;8:861–7. doi:10.1016/j.solidstatesciences.2005.02.011.

[14] Shannon R.D., Prewitt C.T. Effective Ionic Radii in Oxides and Fluorides. Acta Crystallogr Sect B-Structural Crystallogr. Cryst. Chem. 1969;B 25:925–46. doi:10.1107/s0567740869003220.

[15] Glazer A.M. The classification of tilted octahedra in perovskites. Acta Crystallogr Sect B Struct. Crystallogr. Cryst. Chem. 1972;28:3384–92. doi:10.1107/S0567740872007976.

[16] Retuerto M., Alonso J.A., García-Hernández M., Martínez-Lope M.J. Synthesis, structure and magnetic properties of the new double perovskite Ca_2CrSbO_6. Solid State Commun 2006;139:19–22. doi:10.1016/j.ssc.2006.05.011.

[17] Retuerto M., García-Hernández M., Martínez-Lope M.J., Fernández-Díaz M.T., Attfield J.P., Alonso J.A. Switching from ferro- to antiferromagnetism in A_2CrSbO_6 (A = Ca, Sr) double perovskites: a neutron diffraction study. J. Mater. Chem. 2007;17:3555. doi:10.1039/b705797k.

[18] Li M-R., Retuerto M., Deng Z., Stephens P.W., Croft M., Huang Q., et al. Giant Magnetoresistance in the Half-Metallic Double-Perovskite Ferrimagnet Mn_2FeReO_6. Angew. Chemie 2015;127:12237–41. doi:10.1002/ange.201506456.

[19] Arévalo-López A.M., Stegemann F., Attfield J.P. Competing antiferromagnetic orders in the double perovskite Mn_2MnReO_6 (Mn_3ReO_6). Chem. Commun. 2016;147:2–4. doi:10.1039/C6CC01290F.

[20] Okada T., Yagi T., Nishio-Hamane D. High-pressure phase behavior of $MnTiO_3$: decomposition of perovskite into MnO and $MnTi_2O_5$. Phys. Chem. Miner. 2011;38:251–8. doi:10.1007/s00269-010-0400-5.

[21] Johnson R.D., Chapon L.C., Khalyavin D.D., Manuel P., Radaelli P.G., Martin C.. Giant Improper Ferroelectricity in the Ferroaxial Magnet $CaMn_7O_{12}$. Phys. Rev. Lett. 2012;108:67201. doi:10.1103/PhysRevLett.108.067201.

[22] Prodi A., Daoud-Aladine A., Gozzo F., Schmitt B., Lebedev O., van Tendeloo G., et al. Commensurate structural modulation in the charge- and orbitally ordered phase of the quadruple perovskite $(NaMn_3)Mn_4O_{12}$. Phys. Rev. B 2014;90:180101. doi:10.1103/PhysRevB.90.180101.

[23] Prodi A., Gilioli E., Gauzzi A., Licci F., Marezio M., Bolzoni F., et al. Charge, orbital and spin ordering phenomena in the mixed valence manganite $(NaMn^{3+}_{(3)})(Mn^{3+}_{(2)}Mn^{4+}_{(2)})O_{12}$. Nat. Mater. 2004;3:48–52. doi:10.1038/nmat1038.

[24] Streltsov S.V., Khomskii D.I. Jahn-Teller distortion and charge, orbital, and magnetic order in $NaMn_7O_{12}$. Phys. Rev. B 2014;89:201115. doi:10.1103/PhysRevB.89.201115.

[25] Ozaki Y., Ghedira M., Chenavas J., Joubert J.C., Marezio M. High-pressure synthesis and bond lengths of calcium copper germanium oxide $[CaCu_3](Ge_4)O_{12}$. Acta Crystallogr Sect. B Struct. Crystallogr. Cryst. Chem. 1977;33:3615–7. doi:10.1107/S0567740877011686.

[26] Subramanian M.A., Sleight A.W. $ACu_3Ti_4O_{12}$ and $ACu_3Ru_4O_{12}$ perovskites: High dielectric constants and valence degeneracy. Solid State Sci 2002;4:347–51. doi:10.1016/S1293-2558(01)01262-6.

[27] Chen W., Mizumaki M., Seki H., Senn M.S., Saito T., Kan D., et al. A half-metallic A- and B-site-ordered quadruple perovskite oxide $CaCu_3Fe_2Re_2O_{12}$ with large magnetization and a high transition temperature. Nat. Commun 2014;5:3909. doi:10.1038/ncomms4909.

[28] Belik A.A., Matsushita Y., Tanaka M., Takayama-Muromachi E. Crystal structures and properties of perovskites $ScCrO_3$ and $InCrO_3$ with small ions at the A site. Chem. Mate.r

2012;24:2197–203. doi:10.1021/cm3009144.

[29] Belik A.A., Matsushita Y., Tanaka M., Takayama-muromachi E. High-Pressure Synthesis , Crystal Structures , and Properties of $ScRhO_3$ and $InRhO_3$ Perovskites. Inorg. Chem. 2013;52:12005–11.

[30] Belik A.A., Yi W. High-pressure synthesis, crystal chemistry and physics of perovskites with small cations at the A site. J. Phys. Condens. Matter. 2014;26:163201. doi:10.1088/0953-8984/26/16/163201.

[31] Thomas C.I., Suchomel M.R., Duong G.V., Fogg A.M., Claridge J.B., Rosseinsky M.J. Structure and magnetism of the A site scandium perovskite $(Sc_{0.94}Mn_{0.06})Mn_{0.65}Ni_{0.35}O_3$ synthesized at high pressure. Philos. Trans. R Soc. A Math. Phys. Eng. Sci. 2014;372:20130012. doi:10.1098/rsta.2013.0012.

[32] MacTempas User Manual. Berkley: 2016.

[33] Morrish A.H. The Physical Principles of Magnetism. New York: 1965.

[34] J.B. G. Magnetism and the chemical bond 1964:693. doi:10.1016/0029-5582(64)90241-X.

[35] Rodríguez-carvajal J. BasIreps: A program for calculating irreducible representation of little groups and basis functions of polar and axial vector properties. 2004.

[36] Megaw H.D. Ferroelectricity in crystals 1957.

[37] Inaguma Y., Tanaka K., Tsuchiya T., Mori D., Katsumata T., Ohba T., et al. Synthesis, structural transformation, thermal stability, valence state, and magnetic and electronic properties of $PbNiO_3$ with perovskite- and $LiNbO_3$-type structures. J. Am. Chem. Soc. 2011;133:16920–9. doi:10.1021/ja206247j.

[38] Navrotsky A. Energetics and Crystal Chemical Systematics among Ilmenite, Lithium Niobate, and Perovskite Structures. Chem. Mater. 1998;10:2787–93. doi:10.1021/cm9801901.

[39] Li M-R., Walker D., Retuerto M., Sarkar T., Hadermann J., Stephens P.W., et al. Polar and Magnetic Mn_2FeMO_6 (M=Nb, Ta) with $LiNbO_3$ -type Structure: High-Pressure Synthesis. Angew. Chemie. 2013;125:8564–8. doi:10.1002/ange.201302775.

[40] Li M.R., Retuerto M., Stephens P.W., Croft M., Sheptyakov D., Pomjakushin V., et al. Low-Temperature Cationic Rearrangement in a Bulk Metal Oxide. Angew. Chemie. - Int. Ed. 2016;55:9862–7. doi:10.1002/anie.201511360.

[41] Gopalakrishnan J. Chimie Douce Approaches to the Synthesis of Metastable Oxide Materials. Chem. Mater. 1995;7:1265–75. doi:10.1021/cm00055a001.

[42] Arévalo-López A.M., Rodgers J.A., Senn M.S., Sher F., Farnham J., Gibbs W., et al. "Hard-Soft" Synthesis of $SrCrO_{3-\delta}$ Superstructure Phases. Angew. Chemie. Int. Ed. 2012;51:10791–4. doi:10.1002/ange.201206203.

[43] Horiuchi H., Hirano M. $MgSiO_3$ (ilmenite-type): single crystal X-ray diffraction study. Am Mineral 1982;67:788–93. doi:10.1016/j.materresbull.2004.03.013.

[44] Susaki J., Konno M., Akimoto S. High-pressure synthesis and structural refinement of $CdGeO_3$ ilmenite. Zeitschrift Für Krist 1985;171:243–52.

[45] Liferovich R.P., Mitchell R.H. Rhombohedral ilmenite group nickel titanates with Zn, Mg, and Mn: Synthesis and crystal structures. Phys. Chem. Miner. 2005;32:442–9. doi:10.1007/s00269-005-0020-7.

[46] Ahmed N., Tsirlin A.A., Nath R. Multiple magnetic transitions in the spin -1/2 chain antiferromagnet $SrCuTe_2O_6$. Phys. Rev. B 2015;91:214413. doi:10.1103/PhysRevB.91.214413.

[47] Goodenough J.B. Direct cation- -cation interactions in several oxides. Phys. Rev. 1960;117:1442–51. doi:10.1103/PhysRev.117.1442.

[48] Wende C., Olimov K., Modrow H., Wagner F.E., Langbein H. Cation distribution, structure and magnetic properties of lithium manganese iron oxide spinel solid solutions. Mater. Res. Bull. 2006;41:1530–42. doi:10.1016/j.materresbull.2006.01.016.

[49] Moritomo Y., Ohishi Y., Kuriki A., Nishibori E., Takata M., Sakata M. High-Pressure Structural Analysis of Mn_3O_4. J. Phys. Soc. Japan 2003;72:765–6. doi:10.1143/JPSJ.72.765.

[50] Hu J., Qin H. Magnetic properties and magneto-transport in $MnFe_2O_{4-\delta}$ with tetragonal structure 2001;20:1531–2. doi:10.1023/A:1017999018593.

[51] Mathieu R., Ivanov S.A., Solovyev I.V., Bazuev G.V., Anil Kumar P., Lazor P., et al. Mn_2FeSbO_6: A ferrimagnetic ilmenite and an antiferromagnetic perovskite. Phys. Rev. B 2013;87:14408. doi:10.1103/PhysRevB.87.014408.

[52] Tyutyunnik A.P., Bazuev G.V., Kuznetsov M.V., Zainulin Y.G. Crystal structure and magnetic properties of double perovskite Mn_2FeSbO_6. Mater. Res. Bull. 2011;46:1247–51. doi:10.1016/j.materresbull.2011.04.001.

[53] Ziese M., Esquinazi P.D., Pantel D., Alexe M., Nemes N.M., Garcia-Hernández M. Magnetite (Fe_3O_4): a new variant of relaxor multiferroic? J. Phys. Condens. Matter. 2012;24:86007. doi:10.1088/0953-8984/24/8/086007.

[54] Dho J., Kim W.S., Hur N.H. Anomalous Thermal Hysteresis in Magnetization and Resistivity of $La_{1-x}SrxMnO_3$. Phys. Rev. Lett. 2001;87:187201. doi:10.1103/PhysRevLett.87.187201.

[55] Quantum Design. Physical Property Measurement System: Resistivity Option User ' s Manual. 1999.

[56] Keithley Instruments. Model 2400 Series SourceMeter User's Manual. 2002. doi:2400S-900-01.

[57] Keithley Instruments. 2410 and 2410-C SourceMeter ® Specifications:1–3.

[58] Radaelli P.G., Chapon L.C. Symmetry constraints on the electrical polarization in multiferroic materials. Phys. Rev. B - Condens. Matter. Mater. Phys. 2007;76:1–11. doi:10.1103/PhysRevB.76.054428.

[59] Khomskii D.I. Multiferroics: Different ways to combine magnetism and ferroelectricity. J. Magn. Magn. Mater. 2006;306:1–8. doi:10.1016/j.jmmm.2006.01.238.

[60] Tokura Y., Seki S., Nagaosa N. Multiferroics of spin origin. Reports Prog. Physics. 2014;77:76501. doi:10.1088/0034-4885/77/7/076501.

[61] Mathieu R., Ivanov S.A., Bazuev G.V., Hudl M., Lazor P., Solovyev I. V., et al. Magnetic order near 270 K in mineral and synthetic Mn_2FeSbO_6 ilmenite. Appl. Phys. Lett. 2011;98:202505-1-202505–3. doi:10.1063/1.3593194.

IV. Results and discussion

Mn_2MSbO_6 with M = d^0 transition metals

1.-General introduction

This chapter focuses on the detailed study of the structure – properties relation of Mn_2MSbO_6 oxides for M = Sc and the comparison with the moderate and the high pressure polymorphs of the M = Cr and Fe compounds. The increasing cationic radii induced further structural distortions and the increase of unpaired $3d^n$ electrons yielded more complex magnetic behaviours.

At a first sight, the diamagnetic character of the d^0 transition metal is expected to simplify the magnetic behaviour of the obtained polymorphs but the increase in size of the M^{3+} cation will keep enhancing the structural distortions, which may affect the magnetic correlations of the Mn^{2+} sublattice. Moreover, this detailed structure – properties relation will simplify the discussion of the results upon further substituting M by the $4f^n$ rare earth metals treated in the next chapter.

The synthesis of Mn_2ScSbO_6 under room pressure conditions was early performed by by Kosse *et al.* [1,2] and subsequently detailed by Ivanov *et al.* [3]. The conventional ceramic method yields the formation of a disordered ($R\bar{3}$) phase with a random distribution of Mn and Sc at the same crystallographic site that prevents the development of any long range magnetic order. However, the cationic arrangement into a RS-ordered DPv or into an ordered corundum derivative can be induced by its direct synthesis under HPHT conditions. Therefore, the high pressure polymorphs are expected to develop long range magnetic interactions [4].

The isolation of the ordered polymorphs of Mn_2ScSbO_6 required a large number of HPHT syntheses due to the broad range of phase coexistence between these three different polymorphs: the room pressure disordered phase ($R\bar{3}$), the NTO ($R3$) and the DPv ($P2_1/n$) modifications. The pressure-temperature-time phase diagrams are depicted in Figure 4.1, divided into two bidimensional graphs where pressure is represented in abscises axis and temperature (T, up) and reaction time (t, bottom) are represented on the *y* axis.

The experimental conditions are represented in Figure 4.1 as red and black circles for pure DPv and NTO phases respectively. On the other hand, mixed black and red circles correspond to products containing both polymorphs in different proportions. Their proportion is identified over or below the symbol with the % amount of the polymorph in which region is included. The 18 º - 36 º angular region of the most representative XRD patterns showing different proportions of the NTO and DPv polymorphs is depicted on the right-hand side of Figure 4.1 to show the effect of temperature (top panel), pressure (upper part of bottom panel) and time (bottom part). A single green square evidences the known disordered $R\bar{3}$ phase crystallising at room pressure and high temperature conditions.

The vast majority of the high pressure experiments as a resulted in the coexistence of NTO and DPv polymorphs as a consequence of their similar stabilities. This kind of behaviour is reflected in the phase diagrams as a dotted line indicating a broad phase boundary between these compounds. However, a progressively increasing proportion of the DPv polymorph is observed upon increasing pressure. This tendency is visible in both P-T and P-t diagrams, pointing to a preferred formation of the corundum derivative under moderate pressure conditions and that of the DPv modification at high pressures. This behaviour has been previously observed in the ILO and DPv polymorphs of Mn_2FeSbO_6 and Mn_2CrSbO_6 [5,6].

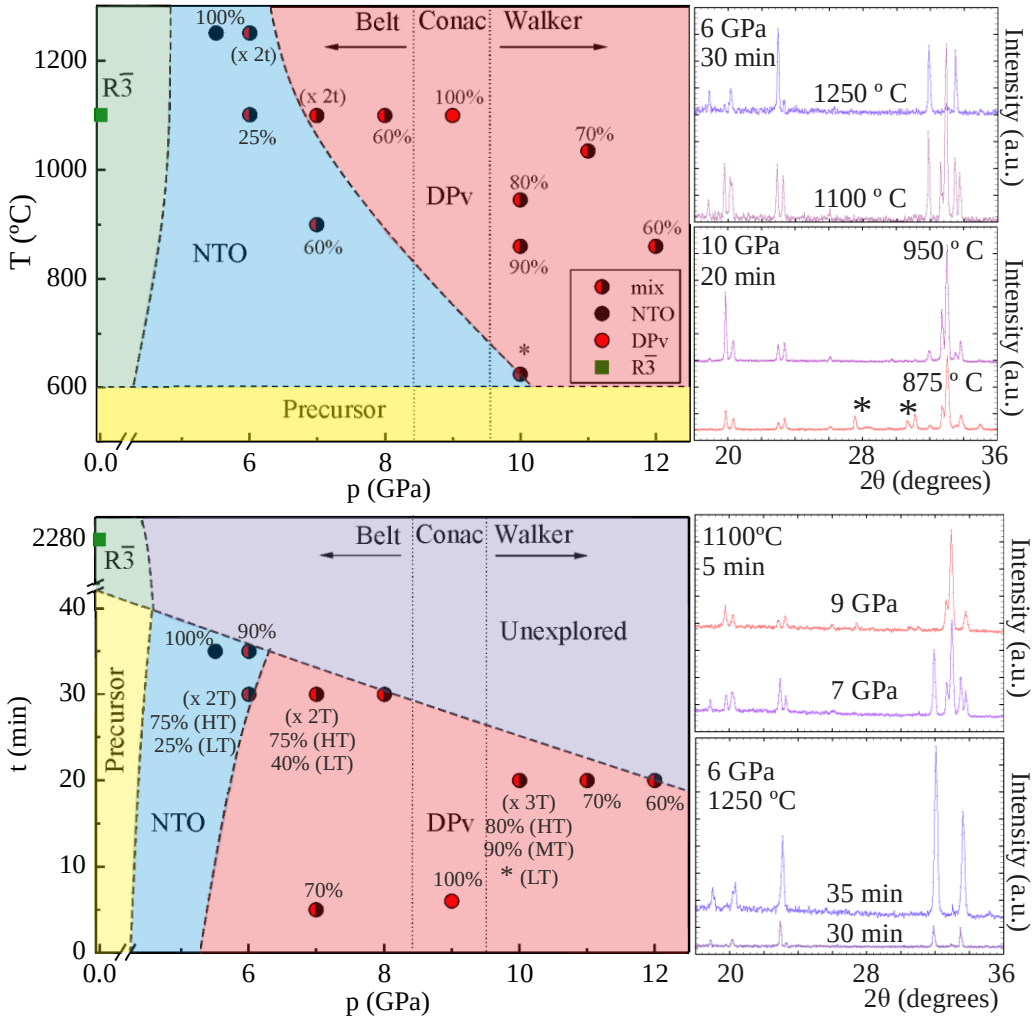

Figure 4.1. Pressure-Temperature (up) and pressure-time (bottom) phase diagrams for Mn_2ScSbO_6. The yellow region schematises the P, T and t conditions at which the precursor mixture does not react. At the green zone the disordered phase is formed, while blue and red regions stabilise the NTO and DPv polymorphs respectively. The purple one stands for unexplored conditions. The numbers above or below each point indicate the proportion of the NTO or the DPv phase in the blue and red zones respectively.

However, it is remarkable that all the syntheses tested above 9.5 GPa using a Walker module were found to apparently revert the observed pressure effect since larger amounts of NTO were found as a secondary phase. This apparent effect may not be attributed to an increasing pressure but as a result of slightly different T and t conditions used. It has been experimentally found during calibration test that temperature is subjected to gradients as high as 50 º C when the same electric power is applied.

In spite of the stabilising effect that the pressure exerts on DPv phase, high temperatures (1100 ºC) must be applied to isolate it as single phase. This conclusion comes straightforward from the experiments carried out at 9 – 12 GPa. The increase of pressure was evidenced to favour the DPv polymorph but pressing over the critical 9 GPa at lower temperatures does not preserve the DPv polymorph as a single phase. Moreover, the experiments developed at the moderate pressure of 6 GPa

show an inversion on the NTO:DPv (%) proportion from 75 :25 to 25: 75 upon lowering the synthesis temperature only 150 ºC.

The use of Clausius-Clapeyron relation (equation *Eq. 6*) and taking into account the experimental results for the observed NTO : DPv relative proportion under different pressure and temperature conditions, yield a tentative separation of the regions where each polymorph is stabilised in the P-T region, as depicted in Figure 4.1-top.

$$\frac{dP}{dT} = \frac{(S_i - S_j)}{(V_i - V_j)} = \frac{\Delta S}{\Delta V} \quad Eq.6$$

In this relation, P and T are the experimental pressure and temperature synthesis conditions and ΔS and ΔV are the change in entropy and volume between pairs of structures. Considering their relative densities, the molar volumes decreases in the order $V_{R\text{-}3} > V_{NTO} > V_{DPv}$ and taking into accoent the symmetries of these structures, the molar entropies might be expected to decrease in the order $S_{R\text{-}3} > S_{NTO} > S_{DPv}$ since higher symmetry tends to imply greater entropy [ref. libro Zircon]. The maximum entropy should not be interpreted as a maximum disorder, but as a maximum homogeneity of the atomic distribution. Therefore, for the phase boundary between R-3 and NTO structures one can expect $S_{R\text{-}3} > S_{NTO}$ and $V_{R\text{-}3} > V_{NTO}$ making ΔS and ΔV positive, so that dP/dT will be also positive for this boundary. However, the phase boundary between NTO and DPv has $S_{NTO} > S_{DPv}$ and $V_{NTO} > V_{DPv}$ making both ΔS and ΔV positive and therefore dP/dT positive. However, the experimental phase diagram between the NTO and the DPv phases shows a negative slope of the phase boundary contrary to our expectations. According to the results obtained from NPD, the cell-volume of NTO is higher than that of DPv, so it seems clear that ΔV is positive. The experimental negative Clapeyron slope of the NTO-DPv phase boundary, therefore requires that the molar entropy of DPv is greater than that of NTO ($\Delta S < 0$) which is counterintuitive given that DPv is the lower-symmetry phase.

It is notable that the metastable DPv polymorph does not transform into NTO at room pressure when increasing temperature (see section 3.3 concerning thermal stability of DPv_Mn_2ScSbO_6). This is in apparent contrast with the observed behaviour of the DPv_Mn_2MSbO_6 compounds with M= Cr and Fe, which transform tino their ILO derivatives. This ambiguity and the negative slope of the NTO-DPv phase boundary present a significant problem when evaluating the potential P-T relationships between ABO_3 systems. However, similar inconsistences have been also observed in ABO_4 compounds. For instance, the mineral thorite (zircon type-structure) transforms to huttonite (monacite type –structure) which has negative Clapeyron slope contrary to that calculated from equation *Eq.6* [7,8].

Regarding this anomaly, it is important to study the effect of the reaction time. The experiments included in the top panel of Figure 4.1 (T-P diagram) have not been performed at the same reaction times.The notation of experiments developed under the same P-T conditions and different (x*n t*) reaction times is labelled on the Figure. In this context, the bottom panel evidences that the DPv polymorph is formed at reduced time reaction while the NTO phase needs for longer times. This effect is reflected at the experimental point of 6 GPa/1250 ºC where the NTO structure is favoured but is relatively close to the stability limit (in pressure) of DPv. Therefore, certain amounts of DPv (~ 25 %) are found as a secondary phase within the main NTO. However, the maintenance of these conditions during 5 extra minutes decreases the DPv amount down to 10 %. This feature points to the strong time dependence of the NTO / DPv stability limit, which yields to a difficult control of the

synthesis conditions required to isolate both polymorphs. It seems that as it happened for Mn_2MSbO_6 (M = Cr, Fe) compounds, the DPv is the kinetic product and the moderate pressure polymorph is the thermodynamic preferred phase, that is, it has lower internal energy (U).

It is also worth noting that both the yellow and the purple regions of the phase diagrams depicted in Figure 4.1 are unexplored regions. The first one is identified as the experimental conditions unable to induce the reaction of the precursor mixture, which is expected to start at sufficiently high temperatures and /or reaction times. Under room pressure conditions, the disordered $R\bar{3}$ phase is described in the literature and checked from our experiment to occur at 1100 ºC. Although it has not been studied the stability of the disordered phase at lower temperatures, its synthesis through the ceramic method is not expected to be optimum below the melting point of Sb_2O_3 (655 ºC) [9].

Under high pressure conditions, the temperature needed to induce the reaction is usually lower [10], but the experiment carried out at 10 GPa and 625 ºC, identified in Figure 4.1 with an asterisk, did not complete the reaction of the precursor mixture into the high pressure polymorphs. For this reason, such temperature conditions are considered to be close to the boundary that defines the interplay between the yellow, blue and red regions.

The unexplored purple region showed in the P-t diagram should represent a set of experimental synthesis conditions which can stabilise higher distortions of the NTO and DPv phases or which could induce their phase transition into even denser modifications, such as post-perovskite structure.

Therefore, the next sections of this chapter focus on the structural characterisation and functional behaviour of the isolated NTO and DPv polymorphs of Mn_2ScSbO_6. The search for further functional phases and the complete understanding of the phase diagram of these oxides is still in progress and won't be treated at the current stage of this study.

2.-NTO_Mn_2ScSbO_6

2.1 – Synthesis and structural characterisation

The NTO polymorph of Mn_2ScSbO_6 was synthesised under HPHT conditions. The precursor mixture was prepared by grinding the stoichiometric amounts of the binary Mn_2O_3, Sc_2O_3 and Sb_2O_3 oxides under acetone in an agate mortar. The resulting homogeneous powder was pressed into a platinum capsule, placed in a Belt-type press at 5.5 GPa and 1523 K during 35 minutes. Once the reaction was completed, temperature was quenched and pressure was slowly released.

The preliminary structural characterisation of the moderate pressure polymorph of Mn_2ScSbO_6 oxide was performed by XRD.. The Rietveld refinement of these data (see Figure 4.2 top-left) can be fitted considering the ILO_Mn_2CrSbO_6 as a starting model [6]. All the reflections can be indexed with *R*3 space group and a= 5.4303 Å and c = 14.0609 Å lattice parameters. The *a* parameter is larger than those observed for Mn_2MSbO_6 with M = Cr and Fe, according to the bigger size of Sc^{3+} cation (0.745 Å [11]), but a shorter *c* length is observed. Despite the clear differences between the calculated and the experimental profiles, the reliability factors get acceptable values (R_p = 5.67, R_{wp} = 8.51 and χ^2 = 8.85). However, the large form and Bragg factors (R_f = 16.0 and R_B = 20.5) indicate the need for improving the crystallographic model. In fact, the refined atomic positions did not change substantially but their thermal factors had to be constrained (see Table 4.1a). The peak shape was adjusted with a Thompson-Cox-Hastings function but there is a mismatch in the relative intensities of some peaks between the theoretical and the experimental models. It is worth noting that the similar atomic XRD scattering factors of Mn (Z = 25) and Sc (Z = 21) do not allow a proper distinction and consequently the averaged profile observed from XRD could actually arise from structures with different cationic orders. On the other hand, their different NPD scattering lengths (-3.73 fm and 12.29 fm respectively) [12] are expected to solve this ambiguity.

Therefore, NPD data were collected at D2B at room temperature conditions in order to fully characterise the crystal structure. As it is clearly shown in Figure 4.2 top-right, the ILO model obtained by XRD does not fit the NPD reflections. Although there are some Bragg positions that correspond to a set of experimental maxima, there are large intensity differences between calculated and experimental reflections. The most surprising feature is the absence of (003) and (101) reflections in the NPD pattern, which appear for ILO ($R\bar{3}$) structures but do not emerge for corundum ($R\bar{3}c$) and $LiNbO_3$ – type (LNO, *R*3c) structures as indicated by the systematic absences induced by the presence of a glide plane (h0l and 0kl where l = 2n + 1).

It is mandatory that the crystal structure of the Mn_2ScSbO_6 polymorph satisfies both XRD and NPD data. On the one hand, the occurrence of (003) and (101) reflections, visible in the XRD pattern, points to an ILO structure [13], where AO_6 and BO_6 octahedra order alternatively along the *c* axis. On the other hand, the fitting of the NPD data requires a different cationic arrangement, where the atoms ordered along [012] direction give rise to an extinction of (003) and (101) reflections. Although both corundum and LNO structures are well-known to ban these maxima [14]. due to the presence of a *c*-glide plane, it is worth to analyse the resulting relative intensities of the XRD and NPD data to these models. The observed intensities in the NPD data reproduce well using a LNO-type model (see Figures 4.2-bottom and Table 4.1b) however the XRD pattern does not converge. It has to be pointed out that the large difference in the coherent neutron scattering lengths of Mn (negative) and Sc/Sb

(large positive values) layers may obscures the (003) and (101) planes, which may be thought of as arising from the sequential stacking of Sc (12.29 fm) and Sb (5.57 fm) along the *c* axis [12].

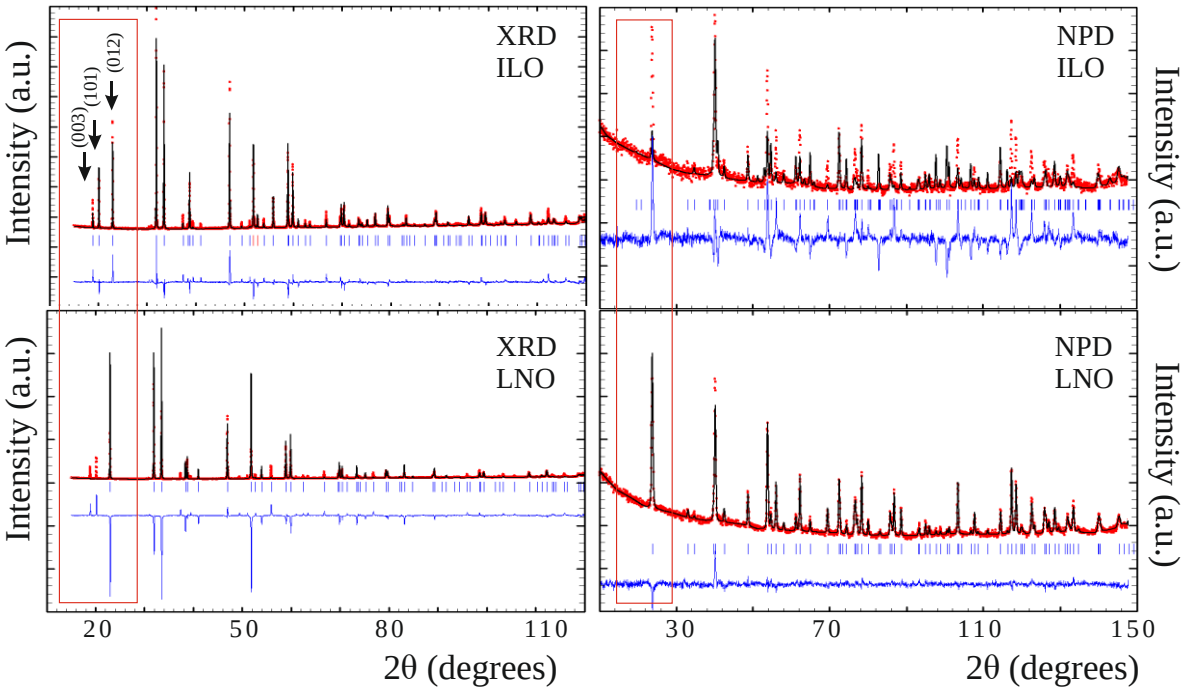

Figure 4.2. Rietveld refinements of XRD (left) and NPD (right) data of the moderate pressure polymorph of Mn_2ScSbO_6 fitted to an ILO (top) and a LNO (bottom) structures. The red rectangle highlights the (003), (101) and (012) Bragg peaks, which relative intensities point to an apparent ILO order through XRD and to an apparent LNO model from NPD results.

Table 4.1. Structural details resulting from the Rietveld fits of the XRD (a) and NPD (b) data of the rhombohedral polymorph of Mn_2ScSbO_6 to the apparent ILO and LNO-type structures respectively.*

a)XRD, $R\bar{3}$	a = 5.3403 (3) Å c = 14.0609 (1) Å		R_p= 5.67%, R_{wp}= 8.51%, R_F = 16.0%, R_B = 20.5% and χ^2 = 8.85		
Atom-site	x	y	z	Occ	Bov
Mn– 6c	0	0	0.1429 (3)	1	1.0
Sc / Sb– 6c	0	0	0.3591 (2)	0.5 / 0.5	1.0
O– 18f	0.2391 (8)	-0.0635 (9)	0.2495 (4)	1	1.0
b)NPD, *R*3c	a = 5.3408 (1) Å c = 14.0572 (4) Å		R_p= 3.21%, R_{wp}= 4.13%, R_F = 7.68%, R_B = 8.98% and χ^2 = 1.66		
Atom-site	x	y	z	Occ	Biso
Mn / B – 6a	0	0	0.2869 (7)	0.93 / 0.07 (1)	0.6 (2)
B / Mn– 6a	0	0	0.0000 (0)	0.93 / 0.07 (1)	0.92 (5)
O– 18b	0.0365 (5)	0.3219 (9)	0.0929 (4)	1	0.96 (4)

* The so called B site in the fitting of NPD to the LNO model stands for the disordered Sc^{3+} / Sb^{5+} cations localised at the (0 0 0) site and found in a 7% at the Mn site as a result of an antisite exchange.

The solution of this structure thus needs for a different space group which satisfies the described reflection conditions: it must allow cationic orders into intermittent layers of both {001} and {012} plane families. In order to satisfy these two conditions, the inversion centre and the glide plane must be excluded, what finally points to the *R*3 space group that is adopted by the Ni_3TeO_6 (NTO) compound [15]. The combined Rietveld fit of both XRD and NPD data using the *R*3 model is depicted in Figure 4.3a. The reliability factors of this refinement, summarised in Table 4.2 along with the resulting structural features, show the good accordance of the model to the experimental data from both patterns.

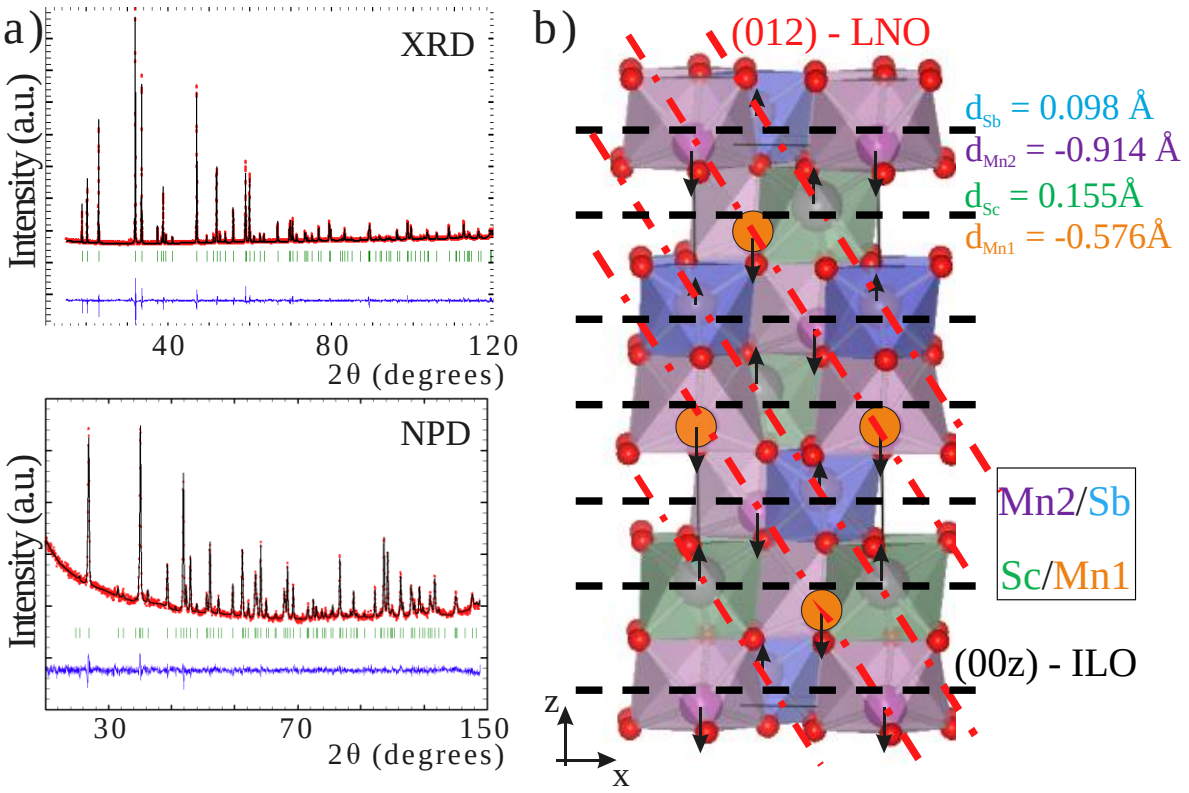

Figure 4.3. a) Rietveld refinements of XRD (top) and NPD (bottom) data collected at room temperature, fitted to a NTO-type structure. b) The structural model obtained from the combined refinement of both diffraction data. The black dashed and the red dashed-dotted lines showing the apparent ILO and LNO orders respectively. See the main text fir further details.

The optimised model resulting from the refinement is depicted in Figure 4.3b. The NTO structure can be described as an alternated stacking of Mn2 (purple) /Sb (blue) and Sc (green) / Mn1 (orange-sphered purple) octahedra along the *z* axis. There is a complete ordering within the (00z) layers between Mn1/Sc and Mn2/Sb. There, the apparent ILO stacking (detected through XRD) and LNO one (observed from PND) are schematised with black dashed lines and red dashed-dotted lines respectively. The first of them is broken by the order of MnO_6 -SbO_6 and ScO_6 -MnO_6 within each (00z) layer.

The final model clarifies the apparent contradiction between the XRD and NPD results. The (00z) layers alternate between Mn1/Sc and Mn2/Sb composition. For XRD, Sc (Z = 21) and Mn (Z = 25)

look similar when compared with the consecutive layer of Mn and Sb (Z = 50). Therefore, ILO-type ordering is apparent and the (003) and (101) reflections are observable. On the other hand, the difference in neutron scattering lengths for Mn, Sc and Sb (−3.73, 12.29 and 5.57 fm respectively) breaks the apparent inversion centre, as the (012) planes are alternatively constituted by Mn or by Sc/Sb, which makes the scattering distribution resemble that of an LN-type.

Table 4.2. Crystallographic parameters, selected bond distances and angles for the NTO polymorph of Mn_2ScSbO_6 from the combined Rietveld refinement of XRD and NPD data collected at 300 K.[a)]

R3	a = 5.3419 (5) Å			c = 14.0603 (2) Å	
Atom-site	x	y	z	Occ	BVS[b)]
Mn1– 3a	1/3	2/3	0.1619 (8)	1	1.89
Mn2 / Sc– 3a	2/3	1/3	0.3423 (8)	0.877 / 0.123	2.01
Sc / Mn2– 3a	0	0	0.2224 (8)	0.877 / 0.123	2.93
Sb– 3a	1/3	2/3	0.3823 (8)	1	5.18
O1– 9b	0.641 (1)	0.695 (2)	0.2926 (7)	1	__
O2– 9b	0.998 (2)	0.622 (2)	0.4555 (5)	1	__

A-O	**d (Å)**	**B-O**	**d (Å)**
Mn1 – O1 (x3)	2.42 (1)	Sc – O1 (x3)	2.04 (1)
Mn1 – O2 (x3)	2.09 (1)	Sc – O2 (x3)	2.18 (1)
Mn2 – O1 (x3)	2.12 (1)	Sb – O1 (x3)	2.02 (1)
Mn2 – O2 (x3)	2.31 (1)	Sb – O2 (x3)	1.98 (1)
$\Delta(Mn1O_6)$	$5.5*10^{-3}$	$\Delta(ScO_6)$	$1.1*10^{-4}$
$\Delta(Mn2O_6)$	$1.7*10^{-3}$	$\Delta(SbO_6)$	$1.1*10^{-4}$
< Mn1 – O1 – Mn2 > = 121.0 (4)		**< Mn1 – O2 – Mn2 >** = 118.4 (3)	

a) Fitting residuals: R_p= 3.04%, R_{wp}= 3.86%, R_B = 6.18% and R_F = 5.04%,.[b)] $V_i = \Sigma_j S_{ij} i = \exp(r_0 - r_{ij}/0.37)$. Values calculated using r_{ij}= 1.79 for Mn^{2+}, 1.849 for Sc^{3+} and 1.942 for Sb^{5+}

The structural parameters obtained from the Rietveld refinements are summarised in Table 4.2. The cations locate at 3a Wyckoff site and oxygen sites at 9b positions. As depicted in Figure 4.3b, the so-called Mn1 position (orange sphered purple octahedra) faces Sb (blue) along the *c* axis and Mn2 (purple) faces Sc (green). A 12.3% of site-selective antisite exchange has been found between Mn2 and Sc, but none between Mn1 and Sb.

As observed in corundum derivatives, cations are displaced from the centre of the octahedra.. These displacements, identified in Figure 4.3b as d_M, have been determined from the product of the *c* axis by the difference between the ideal and the experimental *z* coordinates of each atom, as it is often calculated for corundum derivatives [16]. The resulting values for Mn sites are exceptionally large: d_{Mn1} = 0.576Å and d_{Mn2} = 0.914Å. Both are much larger than the usual averaged displacements of Mn^{2+} cations in the related Mn_2MSbO_6 ILO polymorphs (0.360 Å and 0.403 Å for M = Cr and Fe, respectively) [6]. Their independent shifts for the related Mn_2FeMO_6 NTO phases (0.486 Å and 0.506Å for M = Mo and 0.449 Å and 0.544 Å for M = W) [17][18] are of the same order for d_{Mn1}, but d_{Mn2} attains the longest cationic displacement ever reported for the puckering of a corundum derivative [4]. Smaller non-quantifiable site-selective antisite exchanges between Mn2 and Fe sites are reported in the literature for Mn_2FeWO_6 NTO polymorph [18], while the lower Mn displacements in Mn_2FeMoO_6 are stabilised by a 7 % of Fe-Mo site exchange [17].

On the other hand, the displacements found for Sc (0.155Å) and Sb (0.098Å) are similar to those of Cr/Sb (0.115 Å) and Fe/Sb (0.216 Å) in the ILO related phases detailed in Chapter III. The disorder of the B-site cations in the ILO structures prevents the determination of the independent displacements of B and B' atoms, but the different atomic coordinates at the 3a site found in the NTO structure permits the distinction of the farther displacement of the larger Sc^{3+} cation faced to the most distorted Mn2 site and the smaller displacement of Sb^{5+} according to its smaller repulsion against Mn1 site. The same trend of shorter displacements for the B-site cation faced to the larger displaced Mn2 site is observed in other related NTO compounds.

These cation shifts defining the puckering of (00z) layers is directly related to the octahedral distortions, which are expected to further distort upon longer d_M. The experimental octahedral distortions included in Table 4.2 have been determined from equation *Eq. 3*:

$$\Delta = \frac{1}{n}\sum_{1}^{n}\left(\frac{d_i - \bar{d}}{\bar{d}}\right)^2 \quad Eq.3,$$

where d_i and $\bar{d}$ stand for the independent and averaged M-O distances respectively. Considering the discussed $\Delta(MnO_6)$ = 1.1 10^{-3} and 2.1 10^{-3} values of the related ILO polymorphs of Mn_2MSbO_6 (M = Cr and Fe respectively) as a reference [6], both $\Delta(Mn1O_6)$ and $\Delta(Mn2O_6)$ (5.5 10^{-3} and 1.7 10^{-3} respectively, see Table 4.2) follow the same trend. The similar octahedral distortions values found for $\Delta(ScO_6)$ and $\Delta(SbO_6)$ point to a similar stability of Sc^{3+} and Sb^{5+} cations in their independent sites. Their lower octahedral distortions compared to those of Mn sites are in good agreement with their shorter displacements into the puckered layers.

Concerning the M – O bond distances, all of the experimental values included in Table 4.2 are in accordance with the expected ones ($d(M\text{-}O)_{th.}$), which are calculated as the sum of the anionic radius and the ionic radii of the metals in the adequate oxidation state into a six-fold coordination environment [11]. On the one hand, $d(Sc\text{-}O)_{exp.}$ = 2.11 Å differs from the expected one ($d(Sc\text{-}O)_{th.}$ = $r_{Sc^{3+}}$ (0.745 Å) + $r_{O^{2-}}$ (1.40 Å) = 2.145 Å). The theoretical - experimental difference of 0.025Å can be explained from the antisite exchange with Mn^{2+}, which stabilises both the Sc and Mn2 sites: their cation displacements are minimised, thus favouring a higher coordination regularity and shorter M-O bond distances.

On the other hand, Sb - O averaged experimental bond distance through both oxygen sites is rather similar to the expected value, determined as $d(M\text{-}O)_{exp.}$ = $r_{Sb^{5+}}$ (0.60 Å) + $r_{O^{2-}}$ = 2.00 Å. In a similar manner, the experimental averaged $d(Mn\text{-}O)_{exp.} = \frac{d(Mn1\text{-}O)_{exp.} + d(Mn2\text{-}O)_{exp.}}{2}$ = 2.235 Å is close to the expected one: $d(Mn\text{-}O)_{th.}$ = $r_{Mn^{2+}}$ (0.83 Å) + $r_{O^{2-}}$ = 2.23 Å. However, it is worth noting that Mn1-O distance is elongated while Mn2-O bond length is shortened. As in the case of Sc, this difference can be attributed to the Mn2-Sc site-selective antisite disorder.

Moreover, the occurrence of an increasing antisite exchange was already discussed in chapter III through the Mn_2MSbO_6 series upon substituting M for transition metals of progressively increasing sizes. This size evolution implied a slight difference, of 0.03Å, between the two studied ILO polymorphs (M = Cr and Fe), but the larger difference between $r_{Fe^{3+}}$ (0.645 Å) and $r_{Sc^{3+}}$ (0.745 Å) induces the exponential site exchange of Mn and Sc from a hypothetical ILO-type structure. In fact, the NTO polymorph is related to an ordered-ILO structure, where the B/B' (00z) layer is constituted

by ordered cations with B-B'-□- sequence. The phase transition between both structures has been reported for Mn_2FeMoO_6 to occur through a cationic redistribution [19]. Therefore, the discussed 12.3% of antisite disorder in the NTO-type structure of Mn_2ScSbO_6 [4] can in fact be thought of as the remaining 12.3% of Sc in its ideal site of the related ordered ilmenite polymorph. This cationic redistribution stabilises the steric repulsions induced by the large volume of Sc^{3+} cation, which translates into the higher distortion of $Mn1O_6$ polyhedra (longer Mn-O bonds and higher Δ values), since Mn1 site is not stabilised via site exchange.

The oxidation states, determined from the bond distances through Bond Valence Sum calculations [20], resulted in the expected values for all the cation sites according to the nominal composition $Mn^{2+}{}_2Sc^{3+}Sb^{5+}O_6$.

The ordered decoration of the corundum lattice affords two candidate structures in the case of the Mn_2MSbO_6 oxides: ILO vs. NTO polymorphs. Density functional theory (DFT) calculations show that structures with only heteronuclear dimmers are more stable than structures with homonuclear pairs sharing faces [21].Therefore, Mn/Mn, Sb/Sb or M/M pairs should be avoided in all polymorphs when sharing faces. In light of this observation and provided the constant charge mismatches among the A^{2+}, B^{3+} and B'^{5+} cations, the driving force inducing the different cationic arrangements may be their size difference. As detailed in Chapter I, the highest chemical difference between the three different pairs of cations in Mn_2MSbO_6 oxides (Mn/Sb, Mn/M and M/Sb) is that of Mn^{2+}/Sb^5 which size difference into octahedral environments ($^{VI}r_{Mn^{2+}}$ = 0.83 Å and $^{VI}r_{Sb^{5+}}$ = 0.60 Å [11]) is 0.23 Å. Therefore, Mn^{2+} and Sb^{5+} always locate at face sharing octahedra. At this point, depending on the relative ionic radii of $M^{3+}$and Sb^{5+} (see Table 4.3), the compound will show different ordering preferences.

Table 4.3. Ionic radii in six-fold coordination of the different M^{3+} cations used in the Mn_2MSbO_6 compounds studied along the manuscript to crystallise with rhombohedral symmetry for the moderate pressure polymorph. Their size mismatches with Mn^{2+} (0.83 Å) and Sb^{5+} (0.60Å) cations are also indicated along with the favoured structure.

M^{3+}	$r^{(VI)}$ (Å)	A =Δr (M^{3+}-Mn^{2+}) (Å)	B = Δr (M^{3+}-Sb^{5+}) (Å)	A - B (Å)	Structure
Cr	0.615	0.215	0.015	0.20	ILO
Fe	0.645	0.185	0.045	0.14	ILO-antisite
Sc	0.745	0.085	0.145	-0.06	NTO-antisite

The structural model determined from XRD and NPD experiments has been confirmed by transmission electron microscopy studies. Figure 4.4a shows a representative HRTEM micrograph of the NTO-type polymorph of Mn_2ScSbO_6 through $[2\bar{1}\bar{1}0]$ zone axis. It shows an ordered structure free from any defects with periodicities of 5.3 Å and 14.1 Å that can be assigned to the *b* and *c* cell parameters respectively. The (0003) and $(01\bar{1}1)$ planes are identified in the FFT included as an inset on the upper-left corner. The model obtained from the Rietveld refinements and the simulated image using a defocus of -250 Å and a thickness of 43 Å, are also superimposed, showing a good fit with the experimental image.

However, the complete microstructural determination of this compound required the development of electron microscopy and microdiffraction studies. Figures 4.4b – d show SAED patterns which indicate the diffraction conditions hikl: -h+k+l=3n, hki0: -h+k=3n, 000l: l=3n, $h\bar{h}00$: h=3n and $h\bar{h}0l$, h+l=3n. Under these conditions, the only possible space groups are *R*3 and $R\bar{3}$. The lack of periodicity between the zero and the first order Laue zones (ZOLZ and FOLZ respectively) along the $[2\bar{1}\bar{1}0]$ zone axis depicted in Figures 4.4e and 4.4f points to the absence of a c-glide plane, in agreement with XRD. The comparison of the whole patterns of $[2\bar{1}\bar{1}0]$ and $[0\bar{1}\bar{1}1]$ (Figure 4.4g) zone axes shows the absence of a two-fold axis that unequivocally distinguishes between *R*3 and $R\bar{3}$ space groups, what confirms the absence of an inversion centre.

EELS analysis performed on several crystallites yields a + 2oxidation state for Mn. Figure 4.4h shows a representative EELS spectra where Mn-$L_{2,3}$ edge can be observed. The inset represents the L_3/L_2 ratio obtained from EELS spectra collected for standard binary Mn oxides. It will allow the determination of the correspondence between L_3/L_2 ratio with oxidation state of Mn. The blue cross points the experimental relation in the NTO polymorph of Mn_2ScSbO_6, which corresponds to a 100% of Mn^{2+} in agreement with the BVS calculations, derived from the Rietveld refinements.

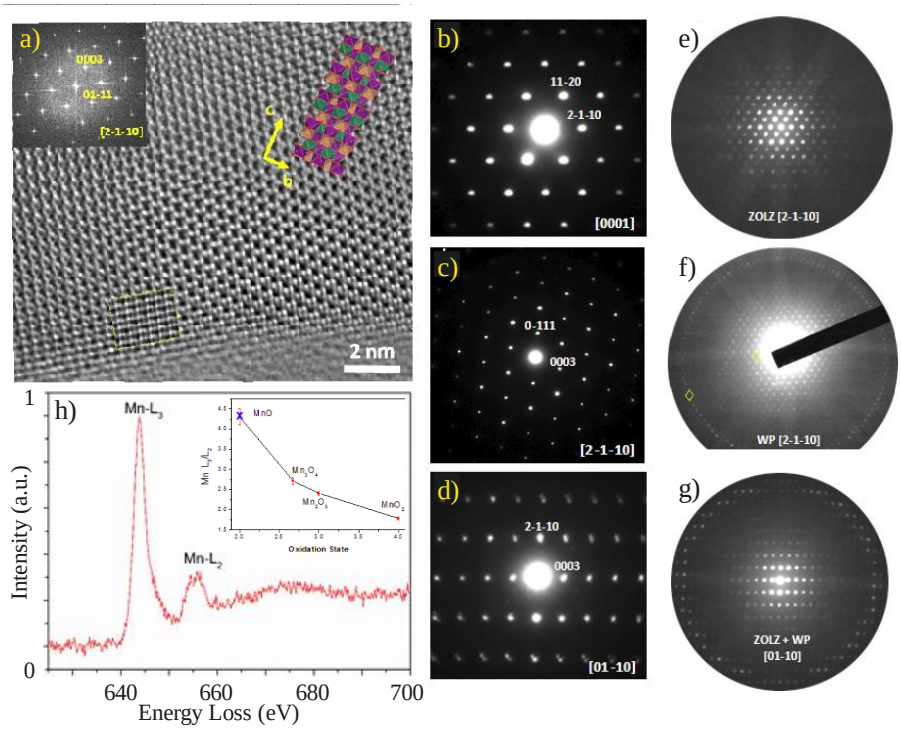

Figure 4.4. a) HRTEM image through the $[2\bar{1}\bar{1}0]$ zone axis. Insets show the FFT, the simulated image and the structural model fitting the experimental micrograph. b-d) SAED patterns for the NTO polymorph of Mn_2ScSbO_6 along[0001] (b), $[2\bar{1}\bar{1}0]$ (c) and $[0\bar{1}\bar{1}0]$ (d) zone axes. e-g) Microdiffraction patterns along $[2\bar{1}\bar{1}0]$ (e and f) and $[0\bar{1}\bar{1}0]$ (g). h) EELS spectrum obtained for the L-edge of Mn in the NTO_Mn_2ScSbO_6. The inset shows the standard L_3/L_2 ratio for binary Mn oxides and the experimental value for this sample (blue cross).

2.2 - Magnetic behaviour

The magnetic behaviour of the NTO polymorph of Mn_2ScSbO_6 was studied in terms of susceptibility and magnetisation measurements. The temperature dependence of the direct and reciprocal magnetic susceptibility data are depicted in Figure 4.5a, where an abrupt change of slope is observed below T_N ~ 42 K. The FC and ZFC plots do not diverge and the negative value of the Weiss constant (θ = -138 K), determined from the fit of the reciprocal susceptibility to a CW law in the temperature range 125 K - 300 K, points to the existence of AFM correlations. The magnetic moment determined from the CW fit amounts to 6.08μ_B / Mn^{2+} which is in good agreement with the expected spin only contribution for Mn^{2+} (5.92 μ_B). However, the magnetisation curve as a function of the magnetic field, depicted in Figure 4.5b, shows a S-shape feature below T_N (42 K), that indicates the existence of a net FM component with a remanent magnetisation of 0.62 μ_B at 2 K and a very small coercive field.

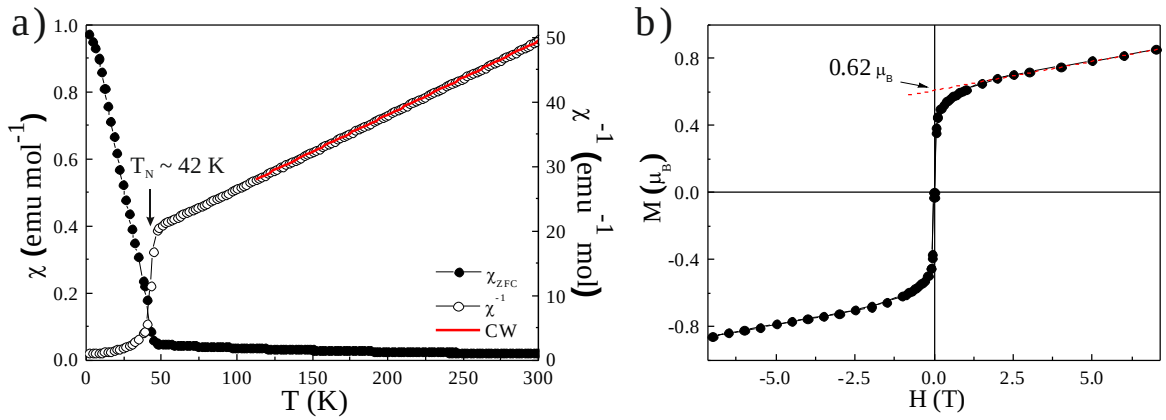

Figure 4.5. Magnetic behaviour of the Mn_2ScSbO_6 NTO polymorph in terms of a) thermal dependence of the susceptibility and b) field dependent magnetisation measurements at 2 K.

The presence of a single type of paramagnetic cation (d^5 Mn^{2+}) ordered in similar proportions into two different crystallographic sites points to two possible models which could originate the AFM behaviour: the antiparallel coupling of two FM sublattices or the AFM nature of both sublattices. However, as discussed along chapter III, the presence of a small FM component may originate from complex magnetic structures arising as a consequence of competing magnetic correlations. Therefore, in order to determine the magnetic structure of this compound, NPD data were collected at 4 K at D2B under high resolution.

Table 4.4.a) Real (BasR) and imaginary (BasI) components of the BV of the allowed Ireps for the magnetic structure of the NTO polymorph of Mn_2ScSbO_6 with propagation vector $\kappa = [0\ 0\ 0]$. b) The allowed Ireps with pure real components for the same magnetic structure.

a)	Irep / Symm	Γ_{1a}	Γ_{2a}	Γ_{3a}
	x, y, z			
	Bas R	0 0 1	1.5 0 0	1.5 0 0
	Bas I	0 0 0	-0.8660 -1.7321 0	0.8660 1.7321 0
b)	Irep / Symm	Γ_{1b}	Γ_{2b}	Γ_{3b}
	x, y, z			
	Bas R	0 0 1	1 1 0	0.577 -0.577 0
	Bas I	0 0 0	0 0 0	0 0 0

Γ_{1a} describes the spin orientation along the *z* axis, while Γ_{2a} and Γ_{3a} stand for the confinement of the spins along the *x* axis. Since the main magnetic peaks observed in the low temperature NPD pattern are those arising from (003) and (101) planes, Γ_{1a} can be directly ruled out: magnetic scattering contributions are operative in an orthogonal direction. As discussed in the previous chapter for the related Mn_2MSbO_6 ILO polymorphs Γ_{2a} and Γ_{3a} are undistinguishable from powder diffraction, as their BV only differ in their imaginary components. Note that the equivalency of *a* and *b* cell parameters implies the equivalency of both magnetic structures confining the spins either along *x* or *y* directions. Therefore, each of these structures would fit the (003) reflection by giving only half of the intensity to the (101) peak. Therefore the most possible solution is that combining both Ireps into one with spins bisecting the angle between *x* and *y* directions.

In order to simplify this approach, Sarah analysis software [22] has been used. The linear combination of the described Γ_{2a} and Γ_{3a} implies a tough process involving the imaginary components. These relations are automatically read from Sarah analysis results, which translates the imaginary components into real contributions by considering the relation between Γ_{2a} and Γ_{3a} through complex conjugation, using equations *Eq. 7* and *Eq. 8*:

$$\Gamma_b + \Gamma_b^* = 2BasR(\Gamma_a)\ \ Eq.\ 7;\quad -i\Gamma_b + (-i\Gamma_b^*) = 2BasI(\Gamma_a)\ \ Eq.\ 8$$

where Γ_a are the original Γ_{2a} and Γ_{3a} ($\equiv \Gamma_{2a}^*$) Ireps and Γ_b and Γ_b^* are the recombined Ireps summarised in Table 4.4b as Γ_{2b} and Γ_{3b}. Note that the resulting Γ_{2b} and Γ_{3b} Ireps already show a combined contribution aligned towards the [110] (Γ_{2b}) and the $[1\bar{1}0]$ (Γ_{3b}) directions with no imaginary components. The use of any of these Ireps should allow the fit of the experimental data, as it has been checked from the fit shown in Figure 4.6a using the combined Irep Γ_{2b}. Both Mn sites were constrained to order with the same magnetic moments towards opposite directions, what results in the magnetic structure depicted in Figure 4.6b. The magnetic moments, oriented along the bisecting direction of the basal *xy* plane, amount to 4.62(3) μ_B / Mn^{2+}. This value is in good agreement with the expected ordered magnetic moment ($5\mu_B$) of the d^5 Mn^{2+} cations (S = 5/2).

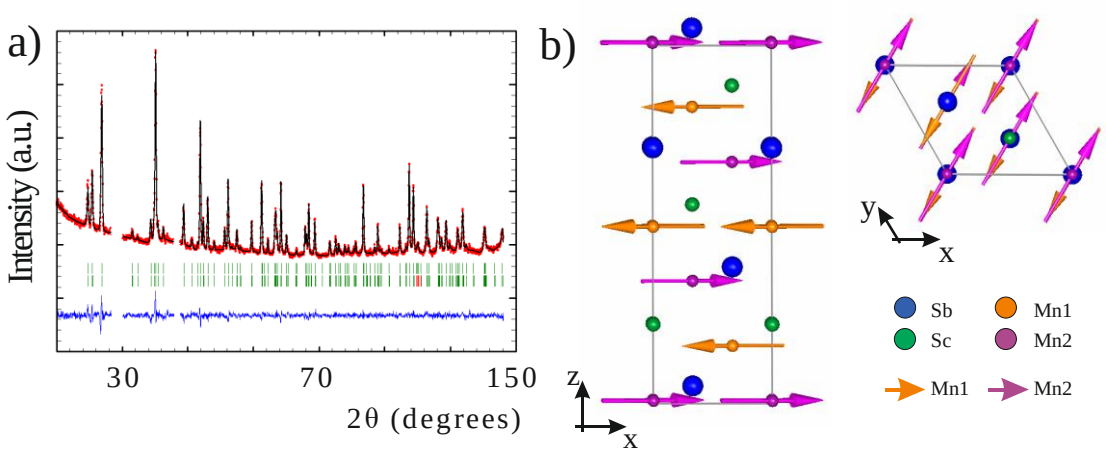

Figure 4.6. a) Rietveld refinement of the NPD data collected at 4 K at D2B for the NTO_Mn_2ScSbO_6. Two exclusion regions are used to neglect the presence of the signal from the vanadium can used as a sample holder. b) Magnetic structure determined from

The FM component observed from the magnetisation measurements can be explained in terms of the described magnetic structure with uncompensated magnetic moments arising from the site-selective antisite disorder: 12.3% * 4.62 μ_B = 0.57 μ_B at 4 K, which is close to the experimental FM component of 0.62 μ_B observed at 2 K. The expected maximal value for the completely ordered Mn^{2+} cations (5 μ_B) would induce a net FM contribution of 0.62 μ_B under this antisite proportion, what justifies the presence of this uncommon mechanism of inducing a net FM component.

It is worth noting that the occurrence of antisymmetric Dzyaloshinskii-Moriya exchange interactions was also considered as a possible origin of the FM contribution, but it is not allowed through this Irep, since it only permits the described spin direction. The independence of each magnetic site could induce a small canting of the spins through their different interactions within a sublattice and between them. However, the identical chemical and magnetic nature of both magnetic sites is only broken by the discussed antisite disorder. The slight canting arising from this effect would not be detectable from neutron diffraction. Moreover, the theoretical deviating angle between two consecutive AFM d^5 spins needed to induce a net FM component of 0.62 μ_B is 10.8 º, which is rather high for a canting angle. This hypothetical model needs for breaking the relation between Mn1 and Mn2 sites what is not possible under the determined propagation vector,. Therefore, the described AFM structure is accepted to induce the FM component simply from the site-selective antisite disorder.

Once the low temperature magnetic structure is determined, its thermal dependence has been studied in terms of the thermal evolution of the diffraction patterns. Figure 4.7a (top and bottom) shows the thermodiffractogram composed of a complete set of patterns measured every 1 K at D1B diffractometer. The intensity of the magnetic peaks increase upon cooling below T_N ~ 42 K. This value is consistent with the temperature transition deduced from susceptibility measurements and confirmed with the temperature evolution of the magnetic moment as depicted in Figure 4.7b. The described magnetic structure determined from high resolution NPD data collected at 4 K at D2B was used as a starting model for the refinement of the high intensity NPD data collected at 3 K at D1B. The resulting model was sequentially used for refining subsequent NPD data collected at progressively increasing temperatures. The gradual intensity difference is thus assigned to the slow

spin orientation while cooling below the transition temperature. The so – obtained thermal evolution of the magnetic moments is fitted to the critical law described by equation *Eq. 9*:

$$\mu(T) = \mu(0) * \left[1 - \frac{T}{T_C}\right]^{\beta} \quad Eq.\ 9,$$

where μ (T) and μ (0) are the magnetic moments at a generic temperature T and a hypothetical ideal value at 0 K; T_C is the critical temperature and β is a constant related to the magnetic lattice type. The data were fitted to this law in the $T_C/2 < T < T_C$ temperature range (21 K - 41 K), resulting in Néel temperature T_N = 42.0 K, in good agreement with the expected value from susceptibility data and the qualitative previous study of the thermal evolution of NPD data. β is optimised for 0.37, which is consistent with a 3D AFM Heisenberg behaviour, for which β = 0.36 is predicted.

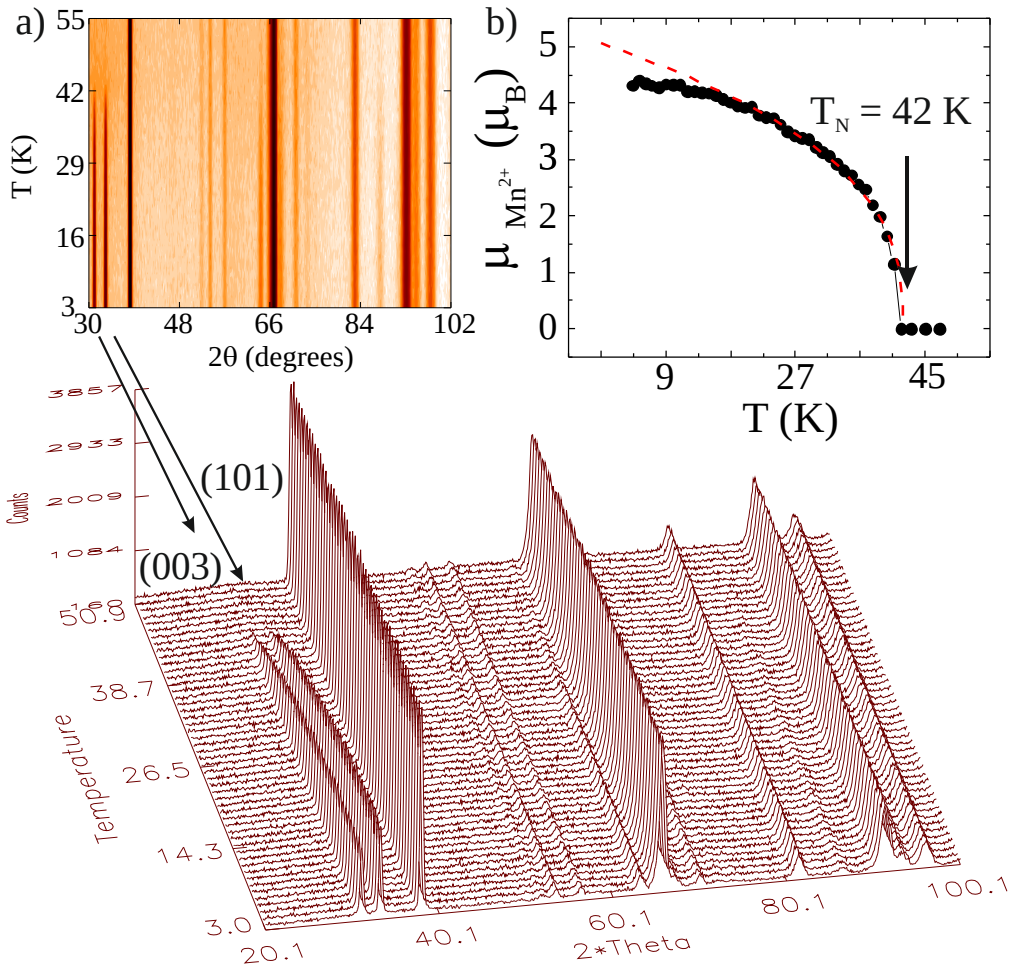

Figure 4.7 a) Thermal dependence of the NPD profiles of the NTO polymorph of Mn_2ScSbO_6 in two (up) and three (bottom) dimensions, showing the progressive increase of the magnetic peaks upon cooling. The main magnetic peaks (003) and (101) are labelled. b) Fit of the thermal dependence of the magnetic moment refined from the set of patterns collected at D1B.

2.3 - Electric behaviour

It is also significant that the polar symmetry of the NTO structure (*R*3) allows the existence of a net polarisation from the uncompensated cationic displacements along the *z* axis, as described from the nuclear structure. Herein the estimation of the expected polarisation is detailed, since the perpendicular nature of these two (magnetic and electric) ferroic components turn this material into a potential multiferroic.

In general terms, the net polarisation (P) can be calculated from equation *Eq. 10* according to the cationic displacements determined from the nuclear structure [23]:

$$P_{Rh.} = \frac{e}{V}\sum_i q_i \vec{r}_i \quad Eq.\ 10$$

In this equation *e* stands for the electron charge ($1.62\cdot10^{-19}$ C), *V* is the unit cell volume (347.467 (5) $Å^3$), q_i is the electronic charge of each (*i*) atom and $\vec{r}_i$ is their displacement along the *c* axis (expressed in Å). It is worth noting that the described rhombohedral unit cell is only one third of the complete hexagonal structure. Therefore, the triple amount of each cation will contribute to the net polarisation of the bulk material, i.e. $P_{Hx.} = 3\ P_{Rh.}$

The resulting polarisation is 28.3 μC/cm^2. This value is calculated from the solely cationic contributions, fixing the O2 position to its ideal 0.5 z coordinate. By that, the ideal position along the *c* axis for each (00z) layer can be determined as the middle distance between the reference O2 and the refined O1 position. This approximation, commonly used in the literature [18] still allows an accurate determination of the cationic displacements and, furthermore, permits to neglect the anionic contribution in the *P* estimation, thus simplifying the calculation.

The result is rather low compared to other corundum related compounds, such as the isostructural (NTO) Mn_2FeWO_6 (59.5 μC/cm^2) [18] and Mn_2FeMoO_6 (68 μC/cm^2) [17] compounds, the ordered-ILO polymorph of Mn_2FeMoO_6 (55 μC/cm^2) [19] or the LNO-structural type $LiNbO_3$ (67 μC/cm^2) [24].

Despite the apparently low spontaneous polarisation predicted for the NTO polymorph of Mn_2ScSbO_6, this result is very interesting in combination with the presence of a weak FM behaviour. The net FM component observed in Mn_2ScSbO_6 arising from the site-selective antisite disorder is confined into the *xy* plane. Both magnetic and electric components are therefore orthogonal magnitudes. This feature turns this material into a potential multiferroic, as highlighted in reference [4].

Attempts to measure the experimental polarisation dependence on the electric field (P(E)) were performed in terms of the voltage variation induced between the NTO_Mn_2ScSbO_6 pellet and a reference capacitor. An optimised homemade Sawyer-Tower circuit [25–27] was built with that purpose, but the obtained hysteresis loops cannot be properly assigned to a ferroelectric behaviour probably due to the P(E) measurements were performed in a polycrystalline sample [28].

3.-DPv_Mn_2ScSbO_6

3.1 – Synthesis and structural characterisation

The DPv polymorph of Mn_2ScSbO_6 was synthesised under extreme pressure and temperature conditions [4]. The precursor, prepared by grinding the stoichiometric amounts of Mn_2O_3, Sc_2O_3 and Sb_2O_3 oxides, was treated at 12 GPa and 1473 K for 20 minutes in a Walker-type multianvil apparatus. The sample was quenched by rapid cooling and the pressure was progressively released down to ambient conditions. The related NTO phase was found to coexist in variable proportions in all sets of experiments. Therefore, the combined Rietveld refinement of XRD and NPD patterns collected at room temperature (Figure 4.8a) include the NTO polymorph as secondary phase. The high pressure polymorph, with DPv structure (Figure 4.8b), crystallises in the $P2_1/n$ space group with cell parameters a = 5.2909 (3) Å, b = 5.4698 (3) Å, c = 7.7349 (5) Å and β = 90.165 (6) º. The structural features, including bond distances and angles, are summarised in Table 4.5. The rock-salt order of B and B' cations includes a 9.1 % of antisite disorder among Sc (B) and Mn (A) sites. This proportion agrees with the increasing antisite disorder observed among the studied Mn_2MSbO_6 series upon increasing the ionic radii of M. The described unit cell also increases according to the larger size of Sc^{3+} (r^{VI} = 0.745 Å) compared to those of Cr^{3+} (0.615 Å) and Fe^{3+} (0.645 Å) [11].

Concerning bond lengths, M-O distances are found to be longer for M = Sc than M = Cr and Fe, according to the discussed evolution of the ionic radii. On the other hand, Sb-O distances and octahedral distortions are similar to those observed for the Cr and Fe containing compounds. The sixfold coordinated Mn site shows Mn-O bonds slightly larger than expected (2.23 Å), which results as a consequence of the irregularity induced by the larger antisite proportion.

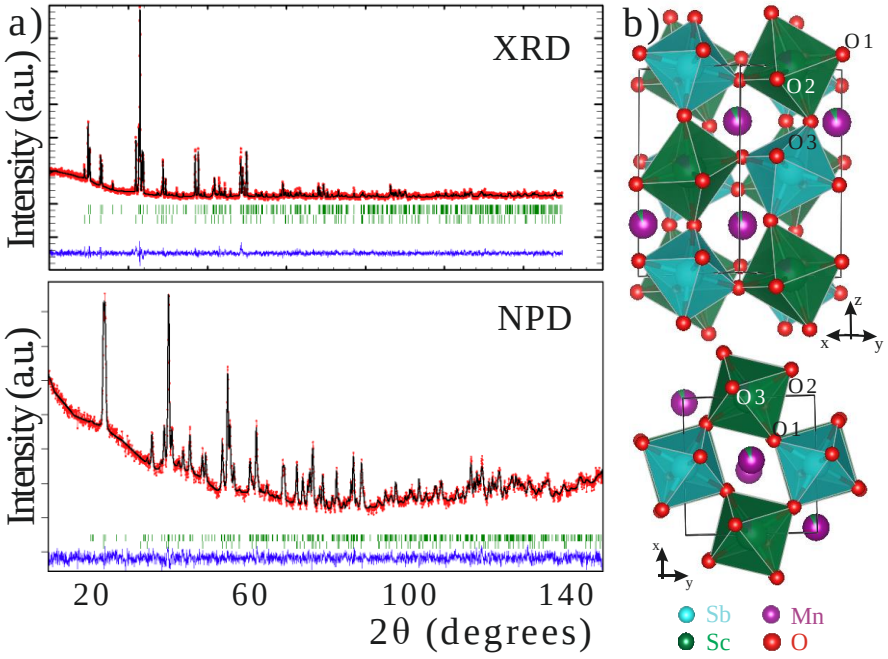

Figure 4.8. a) Rietveld refinements of Mn_2ScSbO_6 DPv polymorph from XRD (up) and NPD (bottom) data; the NTO polymorph is included as secondary phase. b) Structural model determined from a). $a^-a^-c^+$ out-of-phase and in-phase tilts along [110] and [001] directions can be observed in the left and right projections respectively..

Table 4.5. Crystallographic parameters, selected bond distances and angles for the DPv polymorph of Mn_2ScSbO_6 from the Rietveld refinement of NPD data collected at D2B at 300 K.[a)]

P*2$_1$/*n	a = 5.2909 (3) Å, b = 5.4698 (3) Å, c = 7.7349 (5) Å, β = 90.17 (1) º				
Atom-site	x	y	z	Occ	BVS
Mn / Sc– 4e	-0.009 (3)	0.038 (2)	0.749 (4)	0.909(4) 0.091(4)	1.7
Sc / Mn– 2d	0.5	0	0	0.409(4)/0.091(4)	2.9
Sb – 2c	0	0.5	0	0.5	5.3
O_1 – 4e	0.313 (2)	0.321 (2)	0.940 (1)	1	—
O_2 – 4e	0.327 (2)	0.307 (2)	0.570 (1)	1	—
O_3 – 4e	0.878 (1)	0.427 (1)	0.760 (2)	1	—

A-O	**d (Å)**	**B-O**	**d (Å)**
Mn - O_1	2.68 (3)	Sc - O_1 (x2)	2.07 (1)
Mn - O_1	2.77 (3)	Sc - O_2 (x2)	2.10 (1)
Mn - O_2	2.69 (3)	Sc - O_3 (x2)	2.15 (1)
Mn - O_2	2.12 (3)	d_{av}.(Sc - O)	2.11 (2)
Mn - O_3	2.21 (1)	Sb - O_1 (x2)	1.982 (9)
Mn - O_3	2.05 (2)	Sb - O_2 (x2)	1.99 (1)
d_{av}.(Mn - O)	2.42 (3)	Sb - O_3 (x2)	2.00 (1)
		d_{av}.(Sb - O)	1.99 (2)

$\Delta(ScO_6)$ =	$2.9*10^{-4}$	$\Delta(SbO_6)$ =	$1.6*10^{-5}$

< Mn-O_1-Mn >	**< Mn-O_2-Mn >**	**< Mn-O_3-Mn >**
76.5 (3); 149.6 (4)	82.1 (2); 105.5 (4)	82.8 (4); 122.8 (5)

[a)] Fitting residuals: R_p= 2.00 %, R_{wp}= 2.51 %, R_B = 6.04 % and R_F = 4.36%,. [b]$V_i = \Sigma_j S_{ij} i = \exp(r_0 - r_{ij}/0.37)$. Values calculated using r_{ij}= 1.79 for Mn^{2+}, 1.849 for $Sc^{3+}$and 1.942 for Sb^{5+}.

According to the general distortion trend, this compound shows ϕ ~ 19.5 º and θ ~ 21.5 º tilt angles, determined from the half difference of the experimental < B - O - B' > angles and the ideal 180 º. These values are similar to those observed for the DPv_Mn_2CrSbO_6 and Mn_2FeSbO_6, and the same $a^-a^-c^+$ tilt system operates, as observed in Figure 4.8b.

The oxidation states determined from BVS calculations are near the expected values for the nominal composition $Mn^{2+}{}_2Sc^{3+}Sb^{5+}O_6$ and confirmed by the EELS experiments performed on several crystals. The Mn-$L_{2,3}$ edge allows to perform the interpolation of the experimental L_3/L_2 ratio and then compare it to the calibration plot obtained from standard binary Mn oxides. This approach yields 100% of Mn^{2+} for the DPv polymorph of Mn_2ScSbO_6, as depicted in Figure 4.9a.

The structural and microstructural characterization of Mn_2ScSbO_6 DPv polymorph were also performed by SAED and HREM techniques. Figure 4.9b shows the HRTEM image along the [010] zone axis, where *a* (~ 5.2 Å) and *c* (~ 7.7 Å) cell parameters are identified through (100) and (001) directions. No extended defects are appreciated and both the simulated image, calculated with a defocus of -350 Å and a thickness of t = 30 Å, and the structural model obtained from the refinement of NPD data, show a good fit to the experimental micrograph.

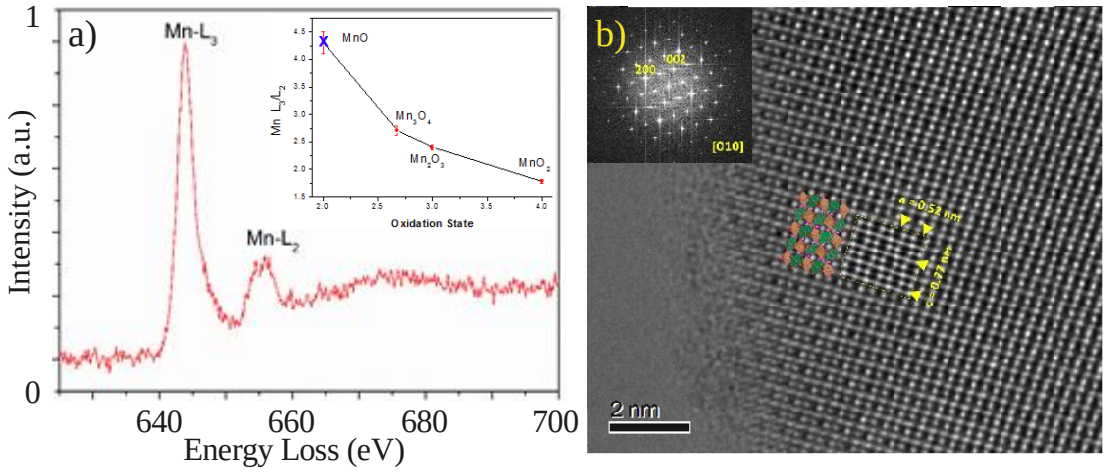

Figure 4.9. a) EELS spectrum for the L-edge of Mn in the DPv_Mn_2ScSbO_6 and experimental L_3/L_2 ratio (blue cross) interpolated into the standard values for binary Mn oxides (inset). b) HRTEM image along [010] zone axis; FFT, simulated image and the structural model included as insets.

3.2 - Magnetic behaviour

The magnetic behaviour of the DPv polymorph of Mn_2ScSbO_6 was studied by means of the temperature dependence of the magnetic susceptibility and field dependent magnetisation measurements, depicted in Figures 4.10a and 4.10b respectively. There exists a single magnetic transition, appreciated at T ~ 42 K, which correlates with the Néel temperature of the NTO modification: the presence of the secondary NTO phase masks the AFM transition of the DPv polymorph below T_N = 22.3 K, accurately determined from NPD data. The fit of the reciprocal susceptibility to a Curie - Weiss behaviour required an additional Temperature Independent Paramagnetism (TIP) contribution. This additional contribution converged to 0.00567 $emu^{-1}molOe$ and the resulting negative Weiss constant, θ = -94 K, points to the AFM behaviour of the DPv polymorph. The effective magnetic moment arising from this fit is $\mu_{exp.}$ = 5.5 μ_B / Mn^{2+}, slightly lower than the expected value ($\mu_{theor.}$ = 5.9 μ_B / Mn^{2+}) for S = 5/2.

The discussed AFM behaviour is confirmed in Figure 4.10b from magnetisation plots obtained above and below the transition. There is a linear increase of M with increasing H with the presence of a small FM contribution, which may arise from the NTO polymorph. A magnification of the low field region, is included in the inset of Figure 4.10b to clearly show the small curvature observed in the curves measured at 2 K and 20 K (black and red lines, respectively). A linear behaviour is observed for the M *vs.* H data measured at 40 K (blue line) since this temperature is near the T ~ 42 K of NTO.

The AFM interactions occur via Mn-O-Mn superexchange interactions through oxygen. The AFM character of these interactions, favoured by the long direct Mn-Mn distances (3.74 (2) Å; 3.9 (1) Å), is in good agreement with the expected behaviour for d^5-d^5 interactions at 90 º (see Table 4.5) [29].

It is reasonable that the low net component of the NTO modification cannot be detected in such a low proportion. Moreover, the 9.1% of Sc entering the Mn site in a disordered configuration in the DPv polymorph, turns some Mn (A) - O - Mn (A) effective interactions into the non-magnetic Mn (A) - O - Sc ones. The formation of additional Mn (A) - O - Mn (B) pathways as a consequence of the A-B

antisite exchange cannot originate long range interactions. Therefore, only a dilution effect is observed, justifying the low value of the experimental magnetic moment.

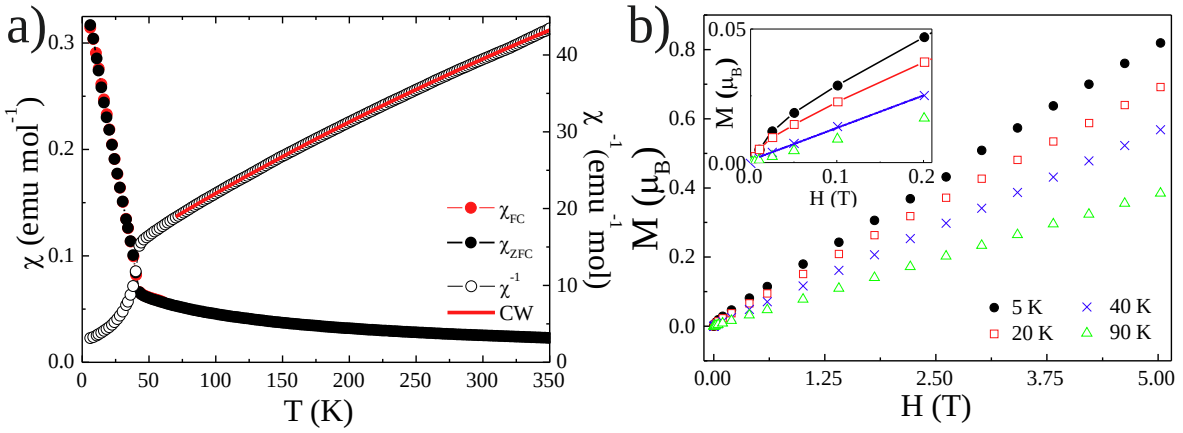

Figure 4.10. Magnetic behaviour of the Mn_2ScSbO_6 DPv polymorph in terms of a) thermal dependence of the susceptibility, measured under an applied magnetic field H = 3 kOe, and b) field dependent magnetisation measurements. The inset shows an enlargement of the low field region, where a small FM contribution from the NTO phase is observed.

The magnetic structure of the DPv_Mn_2ScSbO_6 was determined from the Rietveld refinement of the high intensity NPD data collected at 3 K at D1B and depicted in Figure 4.11a. All the magnetic peaks corresponding to the DPv phase can be indexed with the propagation vector $\kappa = [0\ 0\ 0]$. The symmetry analysis with BasIreps yields four possible Ireps of three BV each, summarised in Table 4.6. Since the imaginary contributions are 0 in all cases, only the real components are included in Table 4.6.

The presence of a single magnetic site involves four symmetry related spins into the unit cell. Since the magnetic unit cell must coincide with the nuclear one, the Ireps Γ_2 and Γ_4 can only satisfy the propagation vector if the spins were confined to the *xy* plane. The main magnetic peaks assigned to the DPv polymorph, as further detailed below from the thermal evolution of NPD data, are indexed (010) and (100). This means that a spin component orthogonal to both x and y directions is present. Therefore, Γ_2 and Γ_4 Ireps are directly discarded.

For analogous reasons, Γ_3 is also neglected, as its *z* component is FM, and it would only allow the AFM order along the *y* axis. Therefore, Γ_1, which allows the AFM alignment of spins into the *xz* plane, was selected to refine the low temperature NPD data.

The resulting magnetic structure, depicted in Figure 4.11b, can be described as an AFM arrangement of the Mn^{2+} spins confined to the *xz* plane. The ordered magnetic moment converged to 4.54 (1) μ_B, where the components along the *x* and *z* axes amount to 1.58 (1) μ_B and 4.26 (1) μ_B respectively, thus deviating the Mn^{2+} spins 20.34 (1) º far from the *z* axis. The resulting magnetic moment is rather low for the expected ordered value of Mn^{2+} (S = 5/2) cation, in accordance with the discussed magnetic dilution effect arising from the Sc/Mn antisite disorder: $5\mu_B - (9.1\% * 5\mu_B) = 4.55\mu_B$.

Table 4.6. Real components of the BV of the allowed Ireps for the magnetic structure of the DPv polymorph of Mn_2ScSbO_6 oxide with a propagation vector κ = [0 0 0].

Irep / Symm	Γ_1	Γ_2	Γ_3	Γ_4
x, y, z	100 010 001	100 010 001	100 010 001	100 010 001
-x+1/2, y+1/2, -z+1/2	-100 010 00-1	-100 010 00-1	100 0-10 001	100 0-10 001
-x, -y, -z	100 010 001	-100 0-10 00-1	100 010 001	-100 0-10 00-1
x+1/2, -y+1/2, z+1/2	-100 010 00-1	100 0-10 001	100 0-10 001	-100 010 00-1

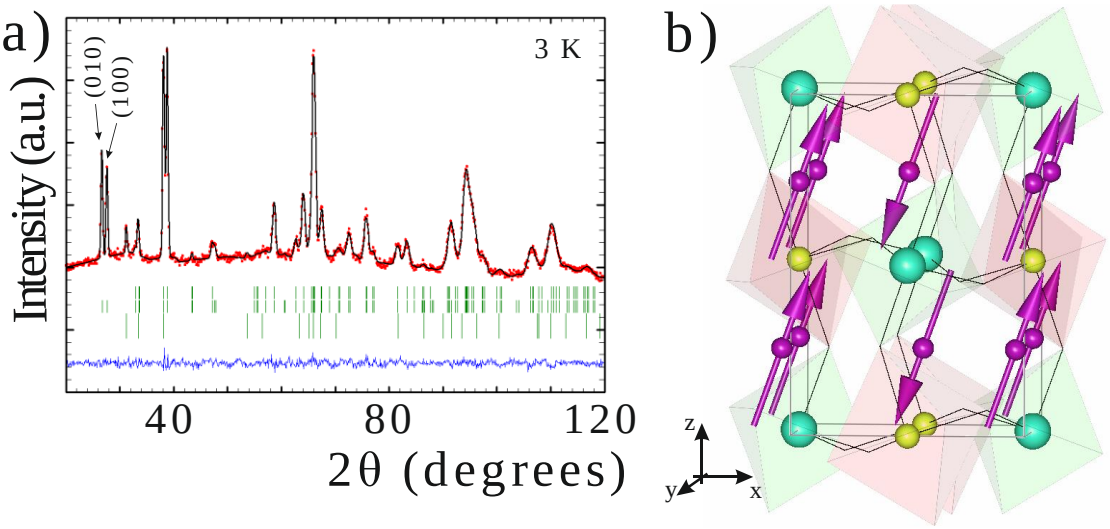

Figure 4.11. a) Rietveld refinement of the NPD data collected at 3 K at D1B for the DPv polymorph of Mn_2ScSbO_6. The two first rows of Bragg positions stand for the nuclear and magnetic structures of the DPv phase and the 3rd and 4th rows indicate the nuclear and magnetic structures of the NTO secondary phase. b) Magnetic structure of the DPv modification obtained from a).

The thermal evolution of the described magnetic structure has been studied from the evolution of the NPD data collected every 1 K at D1B upon heating from 3 K up to 30 K. The 2D thermodiffraction pattern, depicted in Figure 4.12a for the 20º - 50 º angular region, shows the nuclear peaks of both DPv and NTO polymorphs and the magnetic ones of the NTO phase present above 30K. The most intense peaks appearing at 2θ ~ 40 º are the nuclear $(002)_{DPv}$ + $(012)_{NTO}$ and the $(110)_{DPv}$. By cooling the sample below 42 K, the two main magnetic peaks of the NTO polymorph, $(003)_{NTO}$ and $(101)_{NTO}$, appeared. These are the lighter peaks appearing between 2θ = 28 º - 35 º, already observed at the top temperature of 30 K. By further cooling the sample, the magnetic $(010)_{DPv}$ and $(100)_{DPv}$ peaks appear below T_N ~ 23 K of the DPv polymorph.

The low temperature magnetic structure refined from the 3 K NPD data was used as a starting model for the refinement of the sequential thermal patterns. Figure 4.12b shows the fit of the resulting thermal evolution of the magnetic moments of the DPv_Mn_2ScSbO_6 to the same critical law used *(Eq. 9)* for the NTO polymorph. The results point to a T_N = 22.3 K and β = 0.37, in agreement to the 3D Heisenberg AFM behaviour.

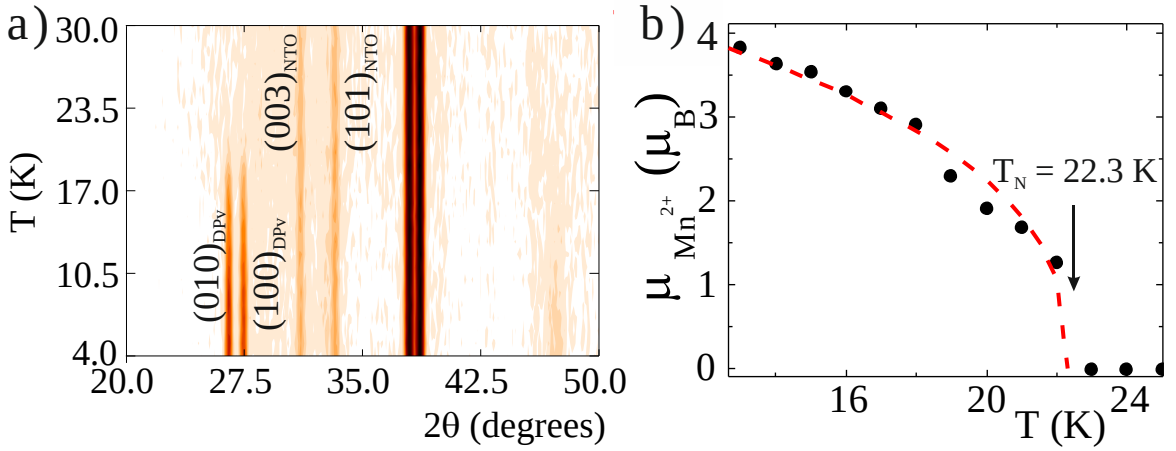

Figure 4.12. a) 2D thermal evolution of the NPD patterns collected at D1B for the DPv polymorph of Mn_2ScSbO_6 below 30 K, focused in the 20 º - 50 º angular region. The main magnetic peaks of both the DPv and the secondary NTO modifications are labelled. b) Fit of the thermal evolution of the magnetic moments of Mn^{2+} to the critical law (see text for a detailed explanation).

3.3 - Thermal stability

The thermal stability of the DPv_Mn_2ScSbO_6 was studied through thermal XRD. The compounds containing d^n transition metals were found to present a structural phase transition from the DPv structure to the ILO polymorph, which was the stable structure when synthesised under moderate pressure conditions. On the other hand, the synthesis of Mn_2ScSbO_6 under similar moderate pressure conditions induces the stabilisation of the NTO structure. The extreme cationic rearrangement needed to originate the NTO – type order from the DPv structure prevents the observation of such a structural transition. Otherwise, heat treatments have recently been found to induce large cationic rearrangements between different ordered corundum derivatives [19]. It is also notable that theoretical estimations [30], predict a DPv to LNO transition and the impossibility of a DPv to ILO transformation, which has indeed been demonstrated to occur [6]. It is worthwhile to highlight that the chemical equivalency of Mn1 and Mn2 crystallographic sites in the NTO polymorph of Mn_2ScSbO_6 in fact turns this material into an ordered LNO structure, for which the situation should be closer to that of the DPv to LNO transition. Therefore, it should be expected that the DPv to NTO phase transition was observed upon heating the high pressure polymorph under room pressure conditions.

However, the proposed phase transition is not observed from the experimental thermal XRD patterns, depicted in Figure 4.13. The absence of this transformation is explained in terms of the relative stability of both polymorphs. The metastable character of the DPv polymorph induces its decomposition into a mixture of variable proportion of cationic oxides at 773 K. However, it should be not forgotten that the NTO modification is featured by a high degree of distortion, translated into large displacements of the cations from their ideal sites in the centre of their octahedra. This large distortion cannot be stabilised with the only aid of the room pressure annealing, but apparently high pressures are also needed under the adequate temperature conditions.

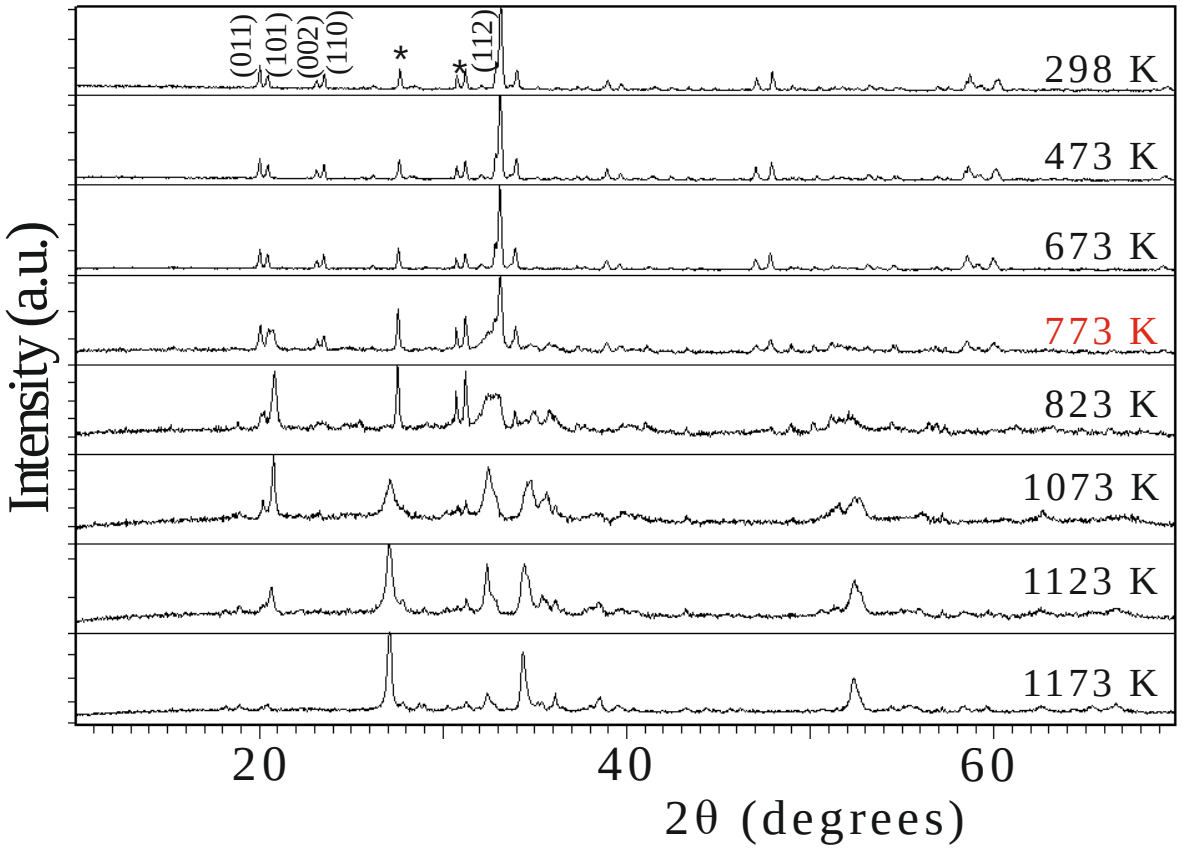

Figure 4.13. Thermal evolution of the XRD patterns of the DPv polymorph of Mn_2ScSbO_6 oxide. Above 773 K the DPv decomposes into $ScSbO_4$, $MnSb_2O_4$, Mn_3O_4, MnO, etc. XRD patterns were collected every 50 K. The patterns collected at 873 K - 1073 K are not shown since they are similar to the 823 K pattern.

4.-Bibliography

[1] Kosse L.I., Politova E.D., Chechkin V.V., Myzgin E.A., Medvedev B.S., Venevtsevae Y.N. Ferroelectric properties of compounds with magnesium ortho - tellurate structural type. Izv. Akad. Nauk. SSSR, Neorg. Mater. 1982;18:1879–82.

[2] Kosse L.I., Politova E.D., Venevtsev Y.N. Structural field boundaries and dielectric properties of compounds with the structure of magnesium orthotellurate type. Zhurnal. Neorg. Khimii. 1983;28:1689–94.

[3] Ivanov S., Nordblad P., Mathieu R., Tellgren R., Politova E., André G. Short-Range Spin Order and Frustrated Magnetism in Mn_2InSbO_6 and Mn_2ScSbO_6. Eur. J. Inorg. Chem. 2011;30:4691–9. doi:10.1002/ejic.201100381.

[4] Solana-Madruga E., Dos santos-García A.J., Arévalo-López A.M., Ávila-Brande D., Ritter C., Attfield J.P., et al. High pressure synthesis of polar and non-polar cation-ordered polymorphs of Mn_2ScSbO_6. Dalt. Trans. 2015;44:20441–8. doi:10.1039/c5dt03445k.

[5] Dos santos-García A.J., Ritter C., Solana-Madruga E., Sáez-Puche R. Magnetic and crystal structure determination of Mn_2FeSbO_6 double perovskite. J. Phys. Condens. Matter. 2013;25:206004. doi:10.1088/0953-8984/25/20/206004.

[6] Dos santos-García A.J., Solana-Madruga E., Ritter C., Ávila-Brande D., Fabelo O., Sáez-Puche R. Synthesis, structures and magnetic properties of the dimorphic Mn_2CrSbO_6 oxide. Dalt. Trans. 2015;44:10665. doi:10.1039/c4dt03849e.

[7] Ovsyannikov S.V., Trots D.M., Kurnosov A.V., Morgenroth W., Liermann H.-P., Dubrovinsky L. Anomalous compression and new high-pressure phases of vanadium sesquioxide, V_2O_3. J. Phys. Condens. Matter 2013;25:385401. doi:10.1088/0953-8984/25/38/385401.

[8] Fukunaga O., Yamaoka S. Phase transformations in ABO_4 type compounds under high pressure. Phys. Chem. Miner. 1979;5:167–77. doi:10.1007/BF00307551.

[9] SIGMA-ALDRICH. Materials Security Data Sheet. 2016.

[10] Rao C.N.R., J. Gopalakrishnan. New Directions in Solid State Chemistry. 1997.

[11] Shannon R.D., Prewitt C.T. Effective Ionic Radii in Oxides and Fluorides. Acta Crystallogr. Sect. B-Structural Crystallogr. Cryst. Chem. 1969;B. 25:925–46. doi:10.1107/s0567740869003220.

[12] Sears V.F. Neutron scattering lengths and cross sections. Neutron News 1992;3:26–37. doi:10.1080/10448639208218770.

[13] Wechsler B.A., Prewitt C.T. Crystal structure of ilmenite ($FeTiO_3$) at high temperature and at high pressure. Am. Mineral. 1984;69:176–85.

[14] Megaw H.D. A note on the structure of lithium niobate, $LiNbO_3$. Acta Crystallogr. Sect. A Cryst. Physics, Diffraction, Theor. Gen. Crystallogr. 1968;24:583–8. doi:10.1107/S0567739468001282.

[15] Newnham R.E., Meagher E.P. Structure of Ni_3TeO_6. Mater. Res. Bull. 1967;2:549–54.

[16] Liferovich R.P., Mitchell RH. Rhombohedral ilmenite group nickel titanates with Zn, Mg, and Mn: Synthesis and crystal structures. Phys. Chem. Miner. 2005;32:442–9. doi:10.1007/s00269-005-0020-7.

[17] Li M.-R., Retuerto M., Walker D., Sarkar T., Stephens P.W., Mukherjee S., et al. Magnetic-

Structure-Stabilized Polarization in an Above-Room-Temperature Ferrimagnet. Angew. Chem. Int. Ed. Engl. 2014;53:10774–8. doi:10.1002/anie.201406180.

[18] Li M.-R., Croft M., Stephens P.W., Ye M., Vanderbilt D., Retuerto M., et al. Mn_2FeWO_6: a New Ni_3TeO_6-Type Polar and Magnetic Oxide. Adv Mater. 2015: doi:10.1002/adma.201405244.

[19] Li M.R., Retuerto M., Stephens P.W., Croft M., Sheptyakov D., Pomjakushin V., et al. Low-Temperature Cationic Rearrangement in a Bulk Metal Oxide. Angew. Chemie - Int. Ed. 2016;55:9862–7. doi:10.1002/anie.201511360.

[20] Attfield J.P. Charge ordering in transition metal oxides. Solid State Sci. 2006;8:861–7. doi:10.1016/j.solidstatesciences.2005.02.011.

[21] Li M., Adem U., Mcmitchell S.R.C., Xu Z., Thomas C.I., Warren J.E., et al. A Polar Corundum Oxide Displaying Weak Ferromagnetism at Room Temperature.J. Am. Chem. Soc. 2012. doi:dx.doi.org/10.1021/ja208395z.

[22] Wills A.S. A new protocol for the determination of magnetic structures using simulated annealing and representational analysis (SARAh). 2000;278:680–1.

[23] Spaldin N.A. A beginners guide to the modern theory of polarization. J. Solid. State. Chem. 2012;195:2–10. doi:10.1016/j.jssc.2012.05.010.

[24] Hsu R., Maslen E.N., du Boulay D., Ishizawa N. Synchrotron X-ray Studies of $LiNbO_3$ and $LiTaO_3$. Acta Crystallogr. Sect. B 1997;53:420–8. doi:10.1107/S010876819600777X.

[25] Andika R., Toresano L., Hikam M., Soegijono B., Sudarmaji A. The Electrical Hysteresis Loop and Polarization Value of $BaZr_xTi_{1-x}O_3$ Multilayer Films Material at Different Annealing Temperature (x = 0.1 and 0.08) based on Sawyer Tower Circuit. 7th Int. Conf. Phys. Its Appl. 2014 (ICOPIA 2014) 2011;3:5714. doi:10.13140/RG.2.1.2911.1526.

[26] Ernst-Abbe-Hochschule Jena U. of A.S. Laboratory Experiments on Ferroelectricity Experiment. 1 2008:1–4.

[27] Ramay S., Anwar M.S. Synthesis and Ferroelectric Properties of KNO_3 films References and Essential Reading. 2010:331–8.

[28] Scott J.F. Ferroelectrics go bananas J. Phys.: Condens. Matter.;2008;21001:18–20. doi:10.1088/0953-8984/20/02/021001.

[29] Goodenough J.B. Magnetism and the chemical bond. 1964:693. doi:10.1016/0029-5582(64)90241-X.

[30] Megaw H.D. Ferroelectricity in crystals. 1957.

V.- Results and discussion

Mn_2MSbO_6 with M = $4f^n$ rare earths

1.-General introduction

This chapter focuses on the study of the Mn_2MSbO_6 system where M is substituted by a rare earth (R). The larger size of R respect to those of transition metals [1] and the presence of $4f^n$ electrons is expected to induce substantial differences regarding both the structures and the magnetic properties of these compounds, in comparison with those studied in the previous chapters.

As it was performed in the synthesis of previous Mn_2MSbO_6 compounds, the room pressure synthesis of these oxides was tested as a first approach. It was detailed in chapters III and IV that this test resulted either in the formation of a known disordered phase (M = Sc) or in the formation of non-desirable mixed oxides (M = Cr, Fe) when a transition metal is used. Otherwise, the large size of the R^{3+} cations stabilised a novel pyrochlore derivative with an unexpected stoichiometry: $(Mn_{0.66}R_{1.34})(Mn_{0.66}Sb_{1.34})O_7$. The fundamental interest on the chemistry ruling the stoichiometric and structural details of this eventual finding motivated the further study of these compounds, which includes the optimisation of their synthesis conditions, their structural characterisation and the determination of their magnetic behaviour. This study is reported in the next section of this chapter.

However, the main aim of introducing rare earths in this system is the preparation of new high pressure polymorphs stabilising the smaller Mn^{2+} cation into highly coordinated sites, such as the A site of a perovskite structure. Therefore, the third section of this chapter is devoted to the high pressure modifications of Mn_2MSbO_6 where M is a rare earth, which will be referred to as $MnRMnSbO_6$ in the following, since the large R^{3+} cations exchange sites with one of the smaller Mn^{2+} thus turning the general $A_2B_2O_6$ stoichiometry into $AA'BB'O_6$.

On the contrary to the observed metastability of Mn_2MSbO_6 oxides, where two different polymorphs can be stabilised under HPHT synthesis conditions, only the perovskite high pressure phase was found for a given $MnRMnSbO_6$ compound. Two perovskites with different symmetries are obtained under similar pressure and temperature conditions for the different members of the $MnRMnSbO_6$ series. Both polymorphs show rock-salt order of Mn and Sb into the B sites, while the large R^{3+} and the smaller Mn^{2+} cations are stabilised in the A site. It is detailed during the corresponding section how single crystal diffraction confirmed that the large size mismatch between Mn^{2+} and R^{3+} cations for the first members of the $MnRMnSbO_6$ family originates an additional simultaneous 1:1 order at the A sites. The reasons for the occurrence of this new type of combined A- and B-site orders into a so-called double double perovskite (DDPv) are also discussed. Moreover, the progressive distortion upon decreasing the size of R and the causes for the instability of this phase for the smaller R^{3+} cations are also detailed.

The magnetic properties of these compounds are studied and NPD experiments on the new structural type modification allowed the determination of their different magnetic structures and their thermal evolution.

2.-Room pressure: $(Mn_{0.66}R_{1.34})(Mn_{0.66}Sb_{1.34})O_7$ pyrochlores

2.1 - Synthesis and structural characterisation

Early attempts to synthesise $MnRMnSbO_6$ oxides through the conventional ceramic method starting from the homogeneous mixture of the Mn_2O_3, Sb_2O_3 and R_2O_3 binary oxides with Mn:R:Sb 2:1:1 stoichiometry yields a compound crystallising with pyrochlore structure (S.G. $Fd\bar{3}m$) as majority phase. The structural determination of this polymorph through the combination of different techniques (XRD, NPD, TGA and HRTEM and associated techniques), further detailed below, pointed to the real stoichiometric relation of the cations into these compounds as $(Mn_{0.66}R_{1.34})(Mn_{0.66}Sb_{1.34})O_7$.

The mentioned 2:1:1 relation is therefore not stabilised but a 1:1:1 one is formed instead. Consequently, half of the Mn in the precursor mixture is not introduced into the structure and nearly imperceptible amounts of Mn_2O_3 and Mn_3O_4 secondary phases, not even visible in the XRD patterns (see that of the Nd containing sample in Figure 5.1 as a representative example), were detected from NPD below their magnetic transition temperatures. The pure and nearly pure phases show, as observed in Figure 5.1, slightly different intensities, which prevented the fitting of the 2:1:1 stoichiometry through the Rietveld method.

The finding of the real stoichiometry of these compounds allowed the optimisation of their synthesis as pure $(Mn_{0.66}R_{1.34})(Mn_{0.66}Sb_{1.34})O_7$ phases, which involved the thermal treatment of the 1:1:1 stoichiometric mixture of Mn_2O_3, R_2O_3 and Sb_2O_3 under 1523 K during 48h in a conventional furnace. Previous decarbonation of the rare earth oxides was developed in all cases under 1173 K, except for R = Pr: the low stability of Pr_2O_3, which tends to oxidise to Pr_6O_{11}, requires 1323 K under a N_2/H_2 (5%) flow. The precursor mixtures were ground under acetone in an agate mortar and pelletized before subsequent treatments.

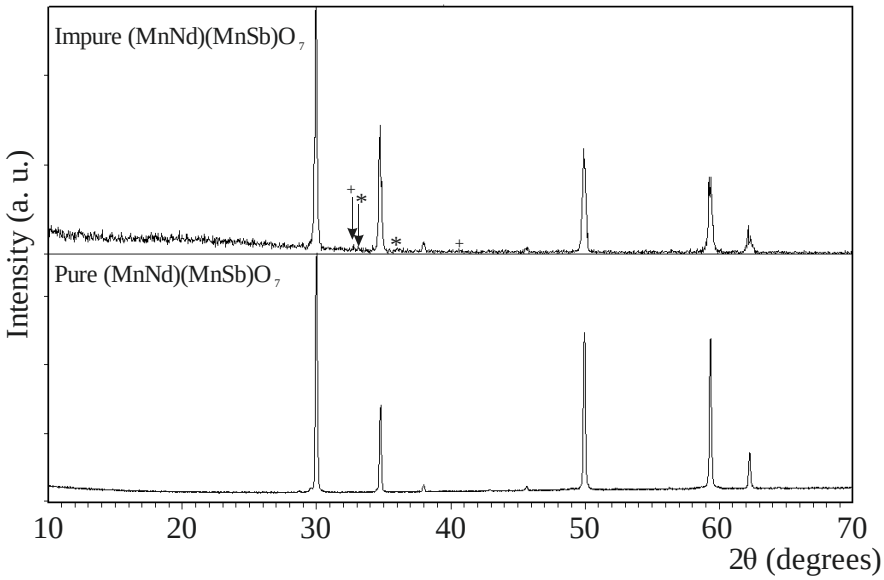

Figure 5.1. Compared XRD patterns of two $(Mn_{0.66}Nd_{1.34})(Mn_{0.66}Sb_{1.34})O_7$ pyrochlore phases: the one at the top is impurified with almost imperceptible amounts of Mn_2O_3 (*) and Mn_3O_4 (+); the bottom panel shows the pure compound.

The structural characterisation of all these compounds was carried out through the Rietveld refinement of XRD (R = Sm, Eu, Gd and Y, see Figure 5.2) and NPD (Figure 5.3) patterns collected at room temperature, using the cubic $A_2B_2O_7$ pyrochlore structure as a starting model. The R^{3+} and Mn^{2+} cations are located at the large A sites, while the octahedral voids are occupied by Mn^{3+} and Sb^{5+} cations. The cationic oxidation states were confirmed by EELS measurements for $(Mn_{0.66}R_{1.34})(Mn_{0.66}Sb_{1.34})O_7$ with R = Pr, Nd, Dy and Yb. Although these studies will be further detailed in the next pages, it is worth noting that Mn presents a mixed valence 2+ / 3+ state. Due to the smaller cationic radius of Mn^{3+} (0.645 Å) compared to that of Mn^{2+} (0.83Å) [1], it shows preference for the octahedral sites. Therefore, the discussed $(Mn_{0.66}R_{1.34})(Mn_{0.66}Sb_{1.34})O_7$ cationic proportion does not only fit the intensities of the XRD and NPD patterns, but it is also in good agreement with the results obtained from the electron microscopy studies.

The crystallographic details and reliability factors are summarised in Tables 5.1 and 5.2 respectively and the main interatomic distances and angles are shown in Table 5.3. In all of them, the results included for $(Mn_{0.66}R_{1.34})(Mn_{0.66}Sb_{1.34})O_7$ (R = Sm, Eu, Gd and Y) compounds are those of the refinements of their XRD data, since Sm, Eu and Gd are well known to absorb large amounts of neutron radiation [2], what prevented an easy collection of any NPD data, and Y was not measured for experimental scheduling reasons. Consequently, the accurate position of O1 (48f) site and the occupancies of each cation in 16c and 16d sites are not refined for these four compounds, but the values obtained for their nearest compositional neighbours are fixed. Only their cell parameters are thus fitted from their XRD profiles, what yields higher reliability factors.

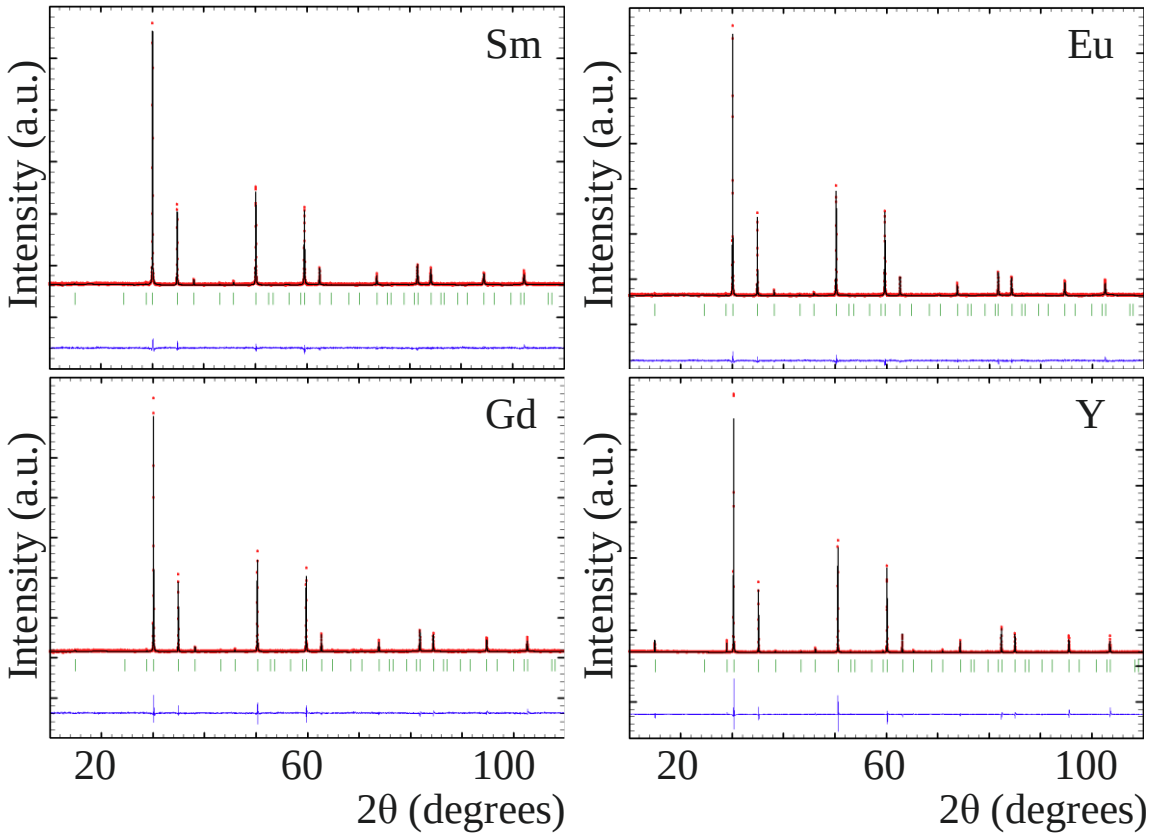

Figure 5.2. Rietveld refinements of the XRD data of $(Mn_{0.66}R_{1.34})(Mn_{0.66}Sb_{1.34})O_7$ R = Sm – Gd, Y.

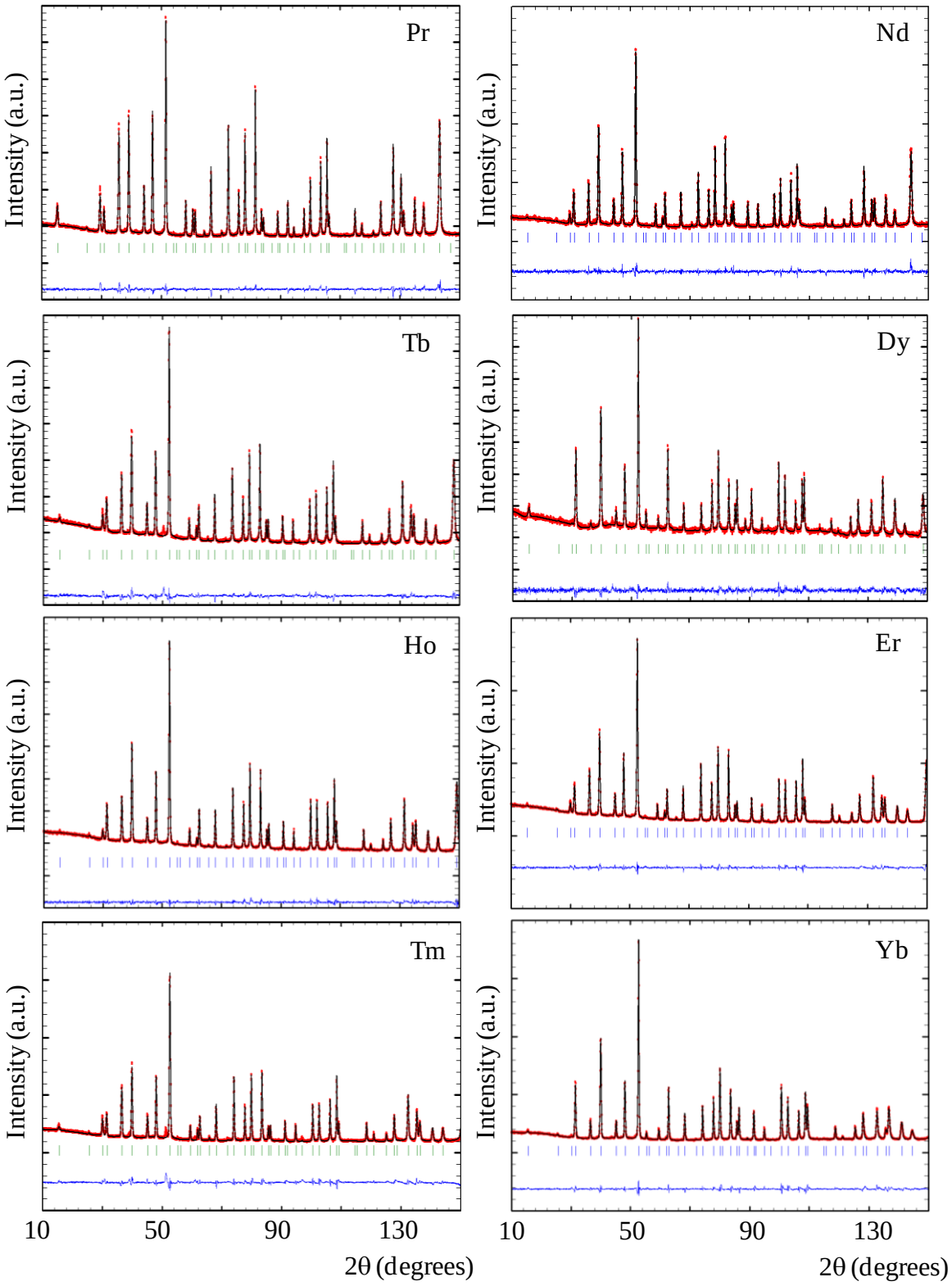

Figure 5.3. Rietveld refinements of the room temperature NPD data collected at D2B for $(Mn_{0.66}R_{1.34})(Mn_{0.66}Sb_{1.34})O_7$. R = Pr – Yb. The Figure continues on the next page for R = Lu.

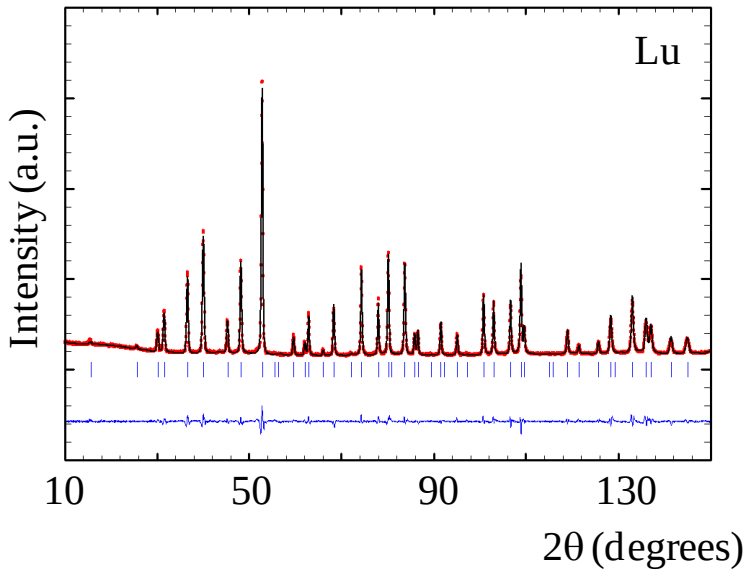

Figure 5.3. Rietveld refinements of the room temperature NPD data collected at D2B for $(Mn_{0.66}R_{1.34})(Mn_{0.66}Sb_{1.34})O_7$. R = Lu.

Table 5.1. Crystallographic details for the pyrochlore structure of the $(Mn_{0.66}R_{1.34})(Mn_{0.66}Sb_{1.34})O_7$ oxides from the Rietveld refinements of XRD and NPD data collected at room temperature. [a)]

***F*d-3m**		**$(Mn_{0.66}R_{1.34})(Mn_{0.66}Sb_{1.34})O_7$**			
Atom-site		x	y	z	Occ
Mn1/R– 16d		0.5	0.5	0.5	
Mn2/Sb– 16c		0	0	0	
O1 - 48f		x	0.125	0.125	0.25
O2 - 8b		0.375	0.375	0.375	0.04167
R	r (Å)	a (Å)	x (O1)	Occ 16d	Occ 16c
Pr	1.126	10.3512 (3)	0.3268 (1)	0.029/0.055	0.028/0.055
Nd	1.109	10.3285 (1)	0.3263 (1)	0.027/0.057	0.027/0.056
Sm	1.079	10.2790 (2)	0.326 (0)	0.027/0.057	0.027/0.056
Eu	1.066	10.2620 (1)	0.326 (0)	0.027/0.057	0.027/0.056
Gd	1.053	10.2542 (2)	0.326 (0)	0.027/0.057	0.027/0.056
Tb	1.04	10.2195 (1)	0.3288 (1)	0.022/0.048	0.035/0.062
Dy	1.027	10.2059 (1)	0.3292 (1)	0.027/0.056	0.029/0.054
Y	1.019	10.1896 (4)	0.329 (0)	0.027/0.057	0.028/0.056
Ho	1.015	10.1897 (3)	0.3297 (1)	0.027/0.057	0.028/0.056
Er	1.004	10.1745 (3)	0.3300 (1)	0.028/0.055	0.028/0.055
Tm	0.994	10.1585 (5)	0.3300 (1)	0.033/0.050	0.025/0.058
Yb	0.985	10.1435 (5)	0.3310 (1)	0.027/0.056	0.029/0.055
Lu	0.977	10.1329 (4)	0.3313 (1)	0.029/0.054	0.028/0.056

[a)] The details summarised for R = Sm, Eu, Gd and Y compounds result from the fit of XRD data.

Table 5.2. Reliability factors of the Rietveld refinements of $(Mn_{0.66}R_{1.34})(Mn_{0.66}Sb_{1.34})O_7$ from room temperature NPD and XRD data.

R	R_p /R_{wp} (%)	R_B /R_f (%)	X^2
Pr	2.99/3.86	2.54/1.75	2.98
Nd	3.69/4.71	2.89/2.11	1.75
Sm	2.70/3.94	6.14/5.89	2.43
Eu	2.32/3.27	5.95/4.18	1.60
Gd	2.67/4.45	6.84/7.33	3.63
Tb	2.94/3.95	5.56/4.60	4.72
Dy	2.66/3.38	3.10/2.15	1.79
Y	6.58/11.4	8.06/5.72	11.0
Ho	2.39/3.14	1.40/1.28	2.41
Er	2.56/3.38	2.21/1.55	3.59
Tm	3.86/5.56	5.91/4.66	10.0
Yb	2.92/3.99	1.64/1.42	5.32
Lu	3.45/4.64	1.93/1.45	5.77

Table 5.3. Main interatomic distances [a)] and angles [b)] in the pyrochlore structure of the $(Mn_{0.66}R_{1.34})(Mn_{0.66}Sb_{1.34})O_7$ oxides from the Rietveld refinements of NPD data collected at room temperature.

R	$d_{(A\text{-}O)th.}$ (Å)	$d_{(A\text{-}O)}$ (Å)	$d_{(B\text{-}O)}$ (Å)	<B-O1-B> (º)	<B-O1-A> (º)	<R-O1-A> (º)
Pr	2.471	2.487 (1)	1.991 (1)	133.6 (1)	106.06 (7)	90.8 (1)
Nd	2.459	2.479 (1)	1.989 (1)	133.3 (1)	106.13 (3)	91.0 (1)
Sm	2.439	_____	_____	_____	_____	_____
Eu	2.431	_____	_____	_____	_____	_____
Gd	2.422	_____	_____	_____	_____	_____
Tb	2.413	2.439 (1)	1.978 (1)	132.0 (1)	106.45 (3)	91.8 (1)
Dy	2.405	2.433 (1)	1.976 (1)	131.7 (1)	106.52 (6)	91.2 (1)
Y	2.399	_____	_____	_____	_____	_____
Ho	2.397	2.428 (1)	1.976 (1)	131.5 (1)	106.57 (1)	92.1 (1)
Er	2.389	2.422 (1)	1.974 (1)	131.3 (1)	106.61 (1)	92.2 (1)
Tm	2.383	2.418 (1)	1.971 (1)	131.3 (1)	106.61 (1)	92.3 (1)
Yb	2.377	2.410 (1)	1.972 (1)	130.7 (1)	106.73 (5)	92.6 (1)
Lu	2.371	2.406 (1)	1.972 (1)	130.6 (1)	106.76 (4)	92.7 (1)

[a)] The theoretical values for interatomic distances are determined from the sum of the averaged ionic radii of A / B site cations and oxygen anion: $r_{Aav.} = (2/3\ r_{R^{3+}}) + (1/3\ r_{Mn^{2+}})$; $r_{Bav.} = (2/3\ r_{Sb^{5+}}) + (1/3\ r_{Mn^{3+}}) = 0.615$ Å. The variable value of $d_{(A\text{-}O)th.} = r_{Aav.} + r_{O^{2-}}$ upon changing R is included in the Table; $d_{(B\text{-}O)th.} = r_{Bav.} + r_{O^{2-}} = 2.015$ Å.

[b)] <R-O2-R> = 109.5 (0), defines a regular $O2A_4$ tetrahedron.

The cell contraction of the pyrochlore structure (Figure 5.4a) can be appreciated through the lanthanide series. According to this contraction, O1 tends to displace towards higher values of its *x* coordinate, i.e. inner positions in the unit cell. Since O1 site describes the corner of the BO_6 octahedra (see the building blocks at the bottom of Figure 5.4b) and B site cations are located into a fixed position, this displacement is the responsible for the slight shortening of the experimental B-O bond distances (see Table 5.3), though the ionic radii of neither B nor O vary in this series. Otherwise, the A-O distances are expected to shorten with the decreasing cell volume, as the averaged ionic radii of the A site does change upon substituting the R^{3+} cations.

Although the M-O distances vary according to the lanthanide contraction, they diverge from their theoretical values. In the case of $d_{(B\text{-}O)}$, the experimental bond lengths summarised in Table 5.3 are shorter than the expected 2.015 Å value (see Table caption for details). This means that the six B-O1 bonds are effective, what translates into apparent high oxidation states for Sb^{5+} and Mn^{3+} from BVS calculations. On the other hand, the experimental A-O bond distances $d_{(A\text{-}O)}$ are slightly longer than their expected values ($d_{(A\text{-}O)th.}$) from the sum of the averaged A and O ionic radii. The experimental bond distances are averaged from six long A-O1 and two short A-O2 bonds, as dictated by the symmetry of this structure. Therefore, the A site is considered eightfold coordinated and the longer experimental distance means that the effective coordination number of A is lower than 8. However, the equivalency of the six long A-O1 bonds prevents lowering the coordination in the BVS calculation, what translates into apparent low oxidation states for R^{3+} and Mn^{2+} cations.

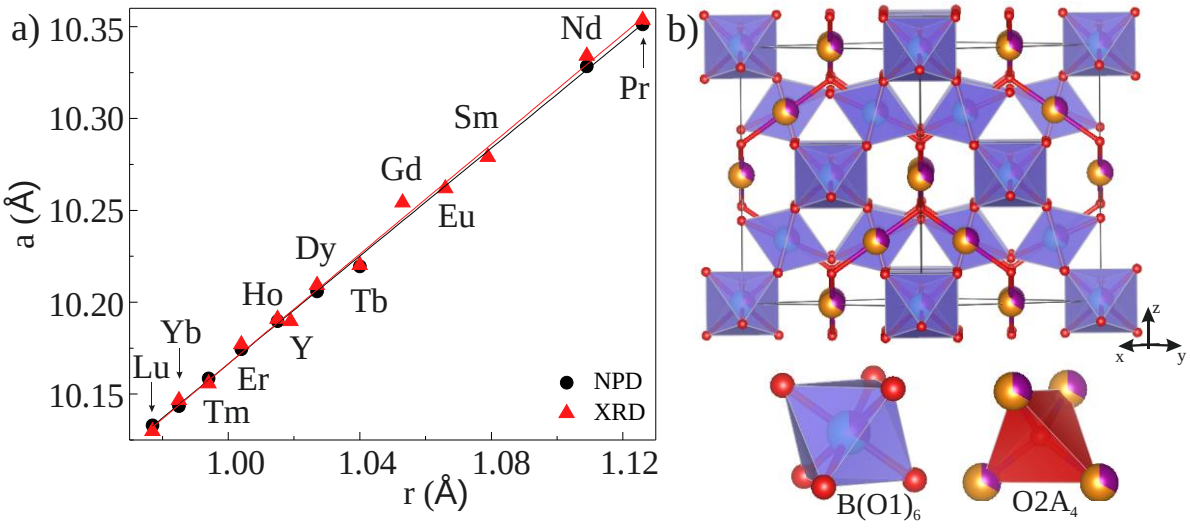

Figure 5.4. a) Evolution of the cell parameters obtained for the $(Mn_{0.66}R_{1.34})(Mn_{0.66}Sb_{1.34})O_7$ pyrochlores from the Rietveld refinement of XRD and NPD data collected at room temperature. b) Structural model obtained from the refinements. The octahedral $B(O1)_6$ and tetrahedral $(O2)A_4$ building blocks are shown at the bottom.

The oxidation states of Mn in these compounds were studied through EELS spectroscopy. The relative intensities of L_2/L_3 lines of Mn show a mixed valence +2 / +3 state. Figure 5.5a shows a representative profile of the discussed measurements for R = Nd. The proportion of both states is confirmed through the linear interpolation into the calibration curve depicted in Figure 5.5b. The experimental values, identified in Figure 5.5b with a red, blue, green and grey cross for R = Pr, Nd, Dy and Yb compounds, reveal averaged oxidation states for Mn of 2.7 (1), 2.51 (9), 2.60 (6) and 2.3 (1), respectively. Therefore, microscopy studies confirm that the Mn^{2+}:Mn^{3+} relation in these $(Mn_{0.66}R_{1.34})(Mn_{0.66}Sb_{1.34})O_7$ pyrochlores is 1:1 or very close to this proportion.

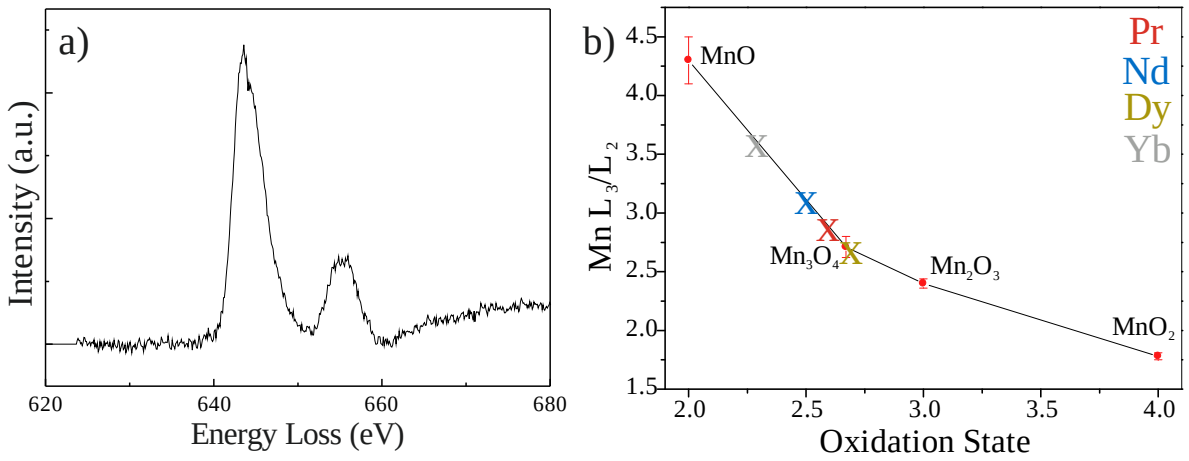

Figure 5.5. a) EELS spectrum obtained for the L-edge of Mn in the $(Mn_{0.66}Nd_{1.34})(Mn_{0.66}Sb_{1.34})O_7$ pyrochlore as a representative example. b) Calibration curve for the L_3/L_2 ratio of Mn from standard binary Mn oxides. The experimental values obtained for the R = Pr, Nd, Dy and Yb samples are interpolated, identified with a red, blue, green and grey cross respectively.

2.2 - Magnetic behaviour

The magnetic behaviour of pyrochlore oxides is usually governed by the geometrical frustration, a term applied to the situation in which a large fraction of magnetic sites is subject of competing constraints. In the pyrochlore structure, the magnetic A-site cations describe a tetrahedral lattice, where the < A - O - A > = 109.45 º angles favour AFM superexchange interactions but the tetrahedral arrangement of four equivalent spins prevents all of them to satisfy these AFM interactions. As a consequence, the described favoured AFM tetrahedral lattice originates frustrated systems.

These lattices often release their strain by stabilising a number of energetically equivalent spin orderings such as the so-called all in, all out or 2 in / 2 out configurations, where all the spins point towards /away the centre of the tetrahedron (as schematised in Figures 5.6a and 5.6b respectively) or they stabilise by acquiring equilibrated in/out pairs of spins (as schematised in Figure 5.6c).

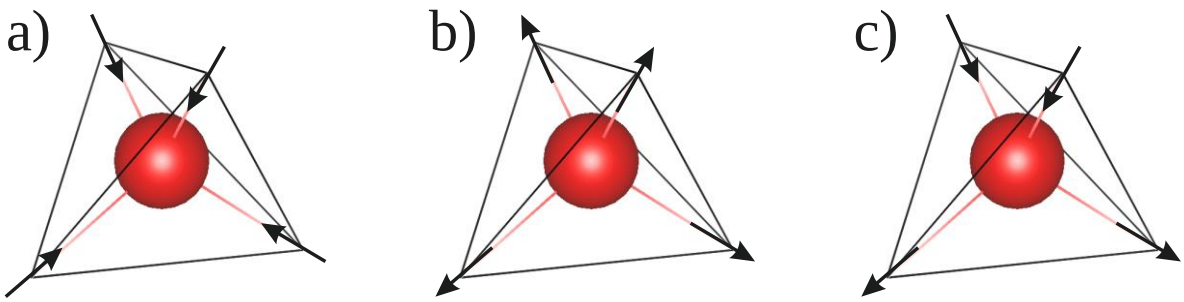

Figure 5.6. Frustrated AFM interactions in a tetrahedral lattice with all in (a), all out (b) and 2 in / 2 out (c) spin configurations.

The coexistence of these frustrated interactions in a pyrochlore structure with different paramagnetic cations into both A and B sites predicts a complex magnetic behaviour for $(Mn_{0.66}R_{1.34})(Mn_{0.66}Sb_{1.34})O_7$. On the one hand, the frustrated A sublattice contains disordered d^5 Mn^{2+} (1/3) and f^n R^{3+} (2/3) cations and, on the other hand, the B sublattice combines 1/3 of the d^4 Mn^{3+} cations disordered with 2/3 of the diamagnetic Sb^{5+} cations. Note that the cationic disorder among Mn^{3+} and Sb^{5+} into the B sites, favoured by their similar ionic radii (0.645 Å and 0.60 Å respectively [1]), induces a magnetic dilution effect on the B sites.

The *DC* magnetic susceptibility measurements of these compounds, depicted in Figure 5.7, show a Curie-Weiss behaviour for a wide temperature range. Table 5.4 shows the results of the CW fittings in the paramagnetic (~ 100 K – 300 K) region, along with the expected ($\mu_{th.}$) and the resulting effective ($\mu_{eff.}$) magnetic moments. In general terms, the low values of the Weiss temperatures evidence the low magnetic correlation of these compounds. These weak correlations develop at low temperatures, summarised in Table 5.4 as T_f for freezing temperature. It is worth noting that most of the experimental magnetic moments determined from these fits are in good agreement with their expected values, revealing their ideal paramagnetic behaviour for the indicated wide temperature range. Note that the R = Sm and Eu containing compounds are not fitted to the CW law since they typically show a Van-Vleck type temperature dependent paramagnetism due to their close energy levels ($\Delta E < k_B T$). Therefore, their experimental magnetic moments have been calculated at room temperature.

The magnetic susceptibility curves of $(Mn_{0.66}R_{1.34})(Mn_{0.66}Sb_{1.34})O_7$ with R = Nd, Tm and Lu compounds show a small magnetic transition at ~ 43 K, where FC and ZFC curves slightly diverge. Regarding the results detailed in the synthesis and structural characterisation subsection, this anomaly is assigned to a small amount of the ferrimagnetic Mn_3O_4 impurity (T_C = 43 K [3]), even though any magnetic peaks are observed in the NPD data collected at low temperatures (further detailed below).

However, the main magnetic feature of these compounds is their net maximum at T_f, enlarged in the insets of Figure 5.7. These maxima evidence a spin glass-like behaviour for $(Mn_{0.66}R_{1.34})(Mn_{0.66}Sb_{1.34})O_7$, according to their described tetrahedral frustrated magnetic sublattice [4].

The large susceptibility values reached in some of these pyrochlores (R = Gd, Tb, Dy, Ho and Er) point to the development of larger cluster-glass regions than those observed for the analogous oxides with other rare earths. Since the higher magnetisations are raised for the compounds containing rare earths of larger spin contributions, these results point to the glassy state favouring the parallel

alignment of the spins at low temperatures, which is confirmed from the field dependent magnetisation measurements later in this section.

Table 5.4. Freezing temperatures (T_f), Weiss constants (θ) and effective ($\mu_{eff.}$) and expected ($\mu_{th.}$) magnetic moments of $(Mn_{0.66}R_{1.34})(Mn_{0.66}Sb_{1.34})O_7$ pyrochlores.

R	T_f (K)	θ (K)	$\mu_{eff.}$ (μ_B)	$\mu_{th.}$ (μ_B)
Nd	< 2	-29.8	7.54	7.56
Sm [a)]	4.4	____	6.32	6.32
Eu [a)]	3.5	____	7.41	7.44
Gd	2.0	-1.3	11.07	11.07
Tb	5.0	-8.5	12.82	12.9
Dy	4.8	-10.5	13.77	13.8
Y	3.5	-23.4	6.23	6.24
Ho	3.6	-5.8	13.67	13.8
Er	< 2	-12.3	12.86	12.7
Tm	2.0	-31.5	10.93	10.8
Yb	2.0	-36.9	8.06	8.13
Lu	3.3	-25.7	6.23	6.24

[a)] Due to their typical Van-Vleck paramagnetic behavior, the effective magnetic moments of the R = Sm and Eu containing samples have been calculated at room temperature.

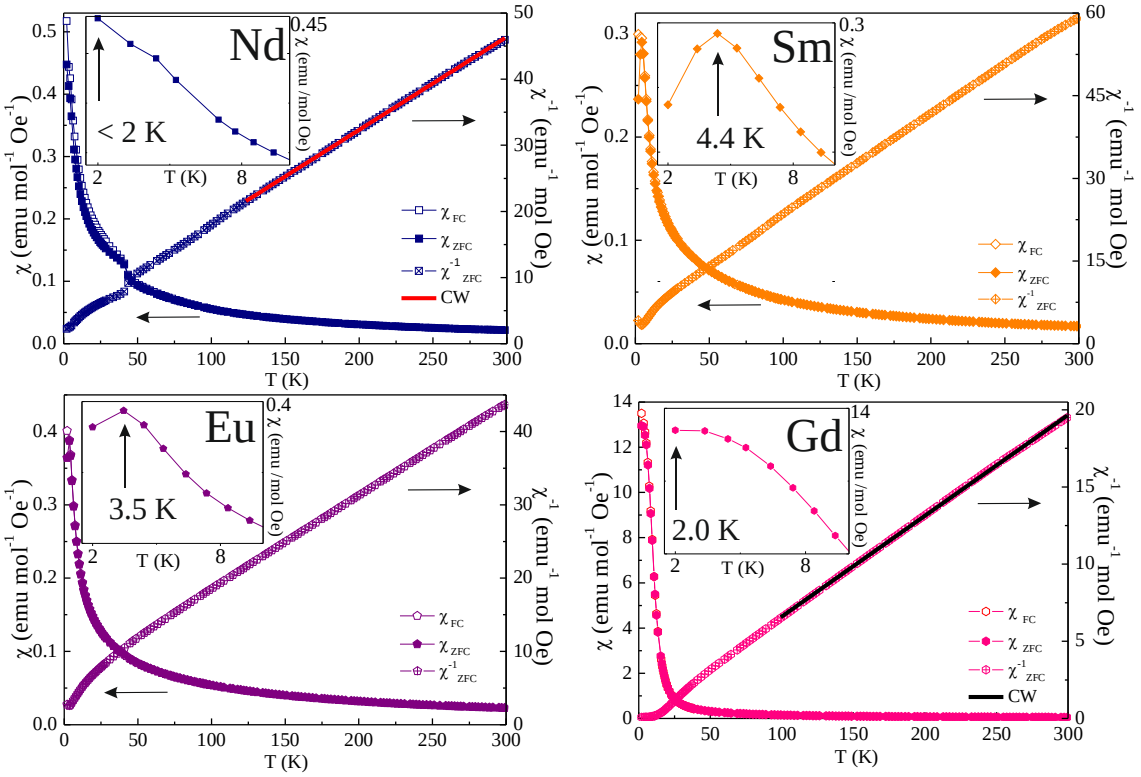

Figure 5.7. Direct (left axis) and reciprocal (right axis) magnetic susceptibility of $(Mn_{0.66}R_{1.34})(Mn_{0.66}Sb_{1.34})O_7$ pyrochlores with R = Nd-Gd. R = Tb-Lu continue in the next page. Their Curie-Weiss fits are depicted as a solid line over the χ^{-1} *vs.* T plot.

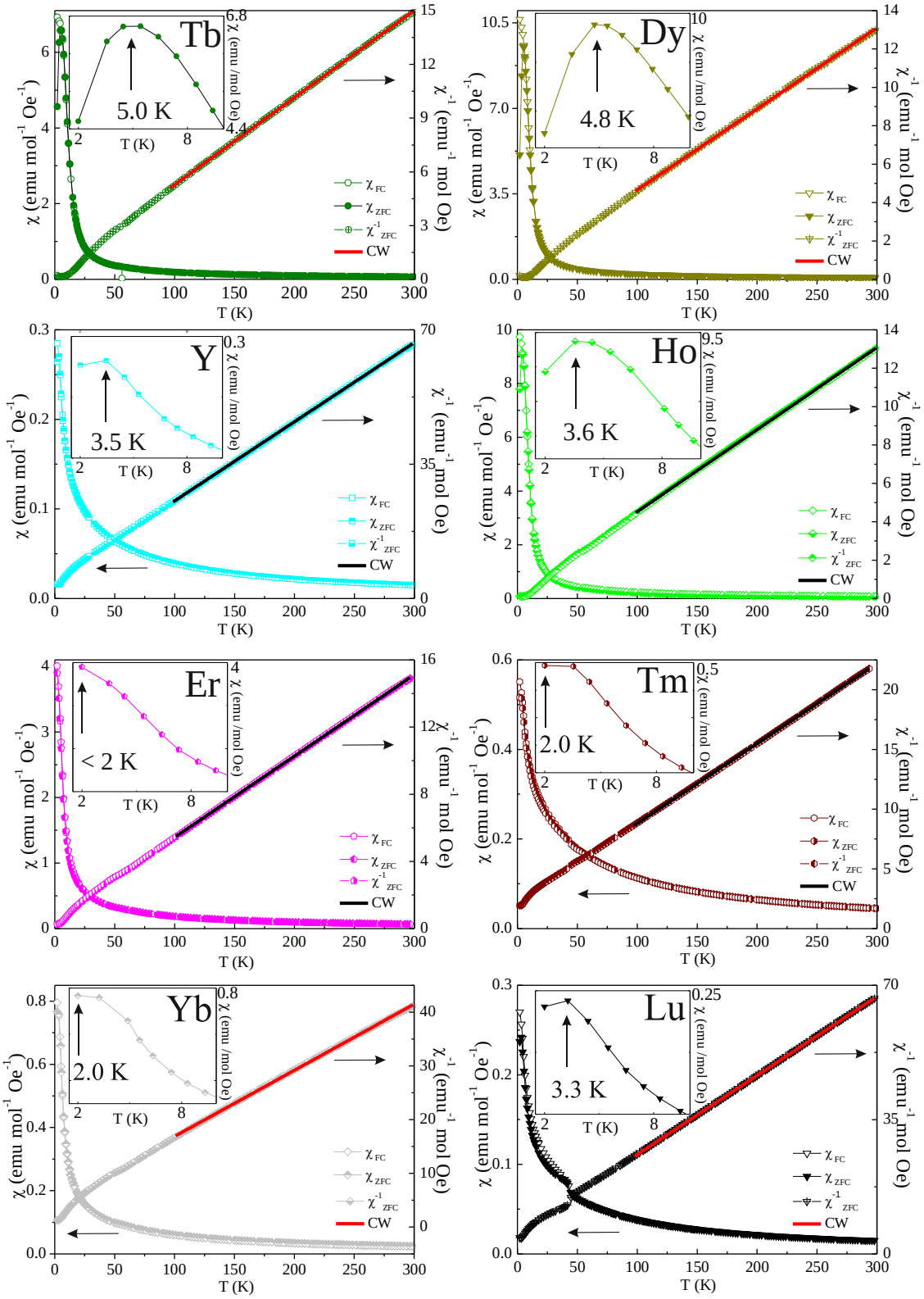

Figure 5.7. (Continuation) Direct (left axis) and reciprocal (right axis) magnetic susceptibility of $(Mn_{0.66}R_{1.34})(Mn_{0.66}Sb_{1.34})O_7$ pyrochlores for R = Tb-Lu, ordered for decreasing R ionic radius. Their Curie-Weiss fits are depicted as a solid line over the χ^{-1} *vs.* T plot.

It is also worth noting that the freezing temperatures summarised in Table 5.4 correspond to the maximum susceptibility values of the curves measured at 0.1 T. Such a high magnetic field cancels out the weak magnetic correlations of the spin glass state, for which not all the samples show a net maximum in susceptibility. Therefore, some of the T_f values indicated in Table 5.4 are indicated as below 2 K and cannot be determined under such a strong magnetic field, as evidenced in the enlargements of Figure 5.7 for R = Nd and Er containing compounds.

In order to further characterise the spin glass behaviour of these compounds a preliminary study including the evolution of T_f as a function of the magnetic field has been performed for R = Gd and Dy derivatives. As expected, this evolution, depicted in Figure 5.8, shows the increase of T_f for decreasing magnetic fields, which has been found to properly fit the Almeida-Thouless equation (*Eq 11*) [5], depicted in the insets of Figure 5.8:

$$H = (1 - T/T_F)^{3/2} \quad \textit{Eq. 11}$$

A similar behaviour is expected for the other $(Mn_{0.66}R_{1.34})(Mn_{0.66}Sb_{1.34})O_7$ pyrochlores. The use of lower magnetic fields permits the system to develop its weak correlations, thus increasing T_f. However, a further study of the spin glass-like behaviour of these systems must be confirmed by *AC* susceptibility measurements in future studies.

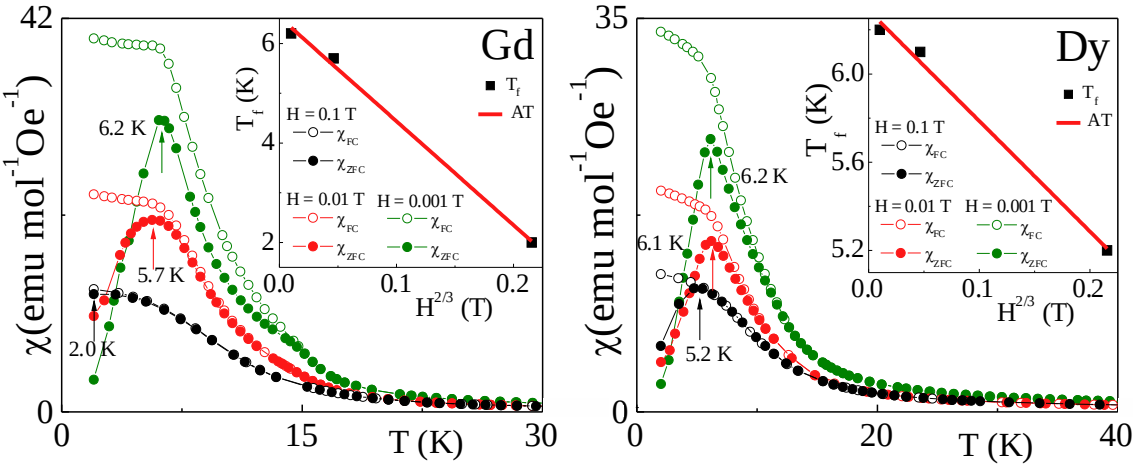

Figure 5.8. Evolution of the freezing temperature of the spin glass $(Mn_{0.66}R_{1.34})(Mn_{0.66}Sb_{1.34})O_7$ pyrochlores with R = Gd and Dy as a function of the applied magnetic field. The insets show the fits to the Almeida-Thouless (AT) equation.

According to the geometrical frustration, NPD data collected at low temperatures at the high intensity D1B instrument do not show any diffraction peaks arising from long range order. Otherwise, the difference patterns obtained by subtracting the 50 K data from those collected at 1.5 K only show undulations in the background signal (see Figure 5.9), revealing the occurrence of short range ordering. The coexistence of three different paramagnetic atoms (R^{3+}, Mn^{2+} and Mn^{3+}) among the different crystallographic sites of these compounds allows a number of different possible magnetic interactions, i.e. A - O - A, A - O - B and B - O - B, which can originate the observed short range correlations.

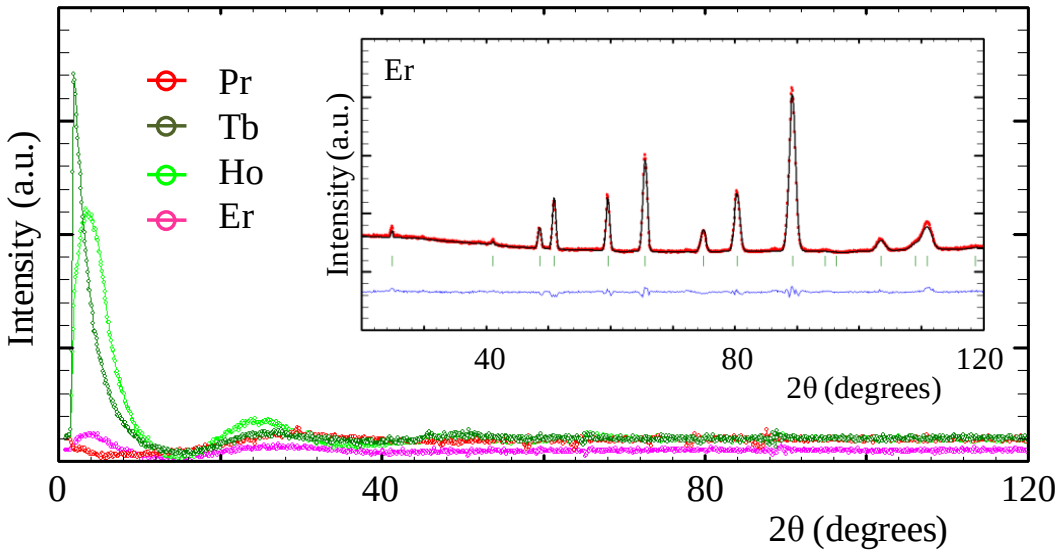

Figure 5.9. 1.5 K - 50 K NPD patterns for $(Mn_{0.66}R_{1.34})(Mn_{0.66}Sb_{1.34})O_7$ R = Pr, Tb, Ho and Er pyrochlores as representative examples of their short range order. The inset shows the Rietveld fit of the D1B NPD data collected at 50 K for the R = Er sample. This refinement was performed using the same structural model obtained from the fit of the room temperature NPD data collected at D2B.

The field dependence of the magnetisation curves of these compounds (Figure 5.10-left) reveals the development of large FM components at sufficiently low temperatures. Their high saturation magnetisations, reaching ~ 9 – 10 μ_B for R = Gd, Dy, Ho and Er, make these materials promising candidates as magnetocalorics [6]. Therefore, their magnetocaloric effect (MCE) has been studied from magnetisation measurements [7]. Multiple isothermal magnetisation curves have been measured at a PPMS-Quantum Design system up to H = 9 T. The magnetic entropy change (ΔS_M) has been determined from the numerical integration of equation *Eq. 12* [8,9]. The resulting magnetic entropy values, depicted in Figure 5.10-right, range from ~ (-12) J /kg K in the case of the Dy containing compound to ~ (-20) J /kg K observed in the Gd-one.

$$\Delta S_M(T)_{\Delta H} = \int_{H_1}^{H_2} \left(\frac{\partial M(T,H)}{\partial T} \right)_H dH \quad \textit{Eq. 12}$$

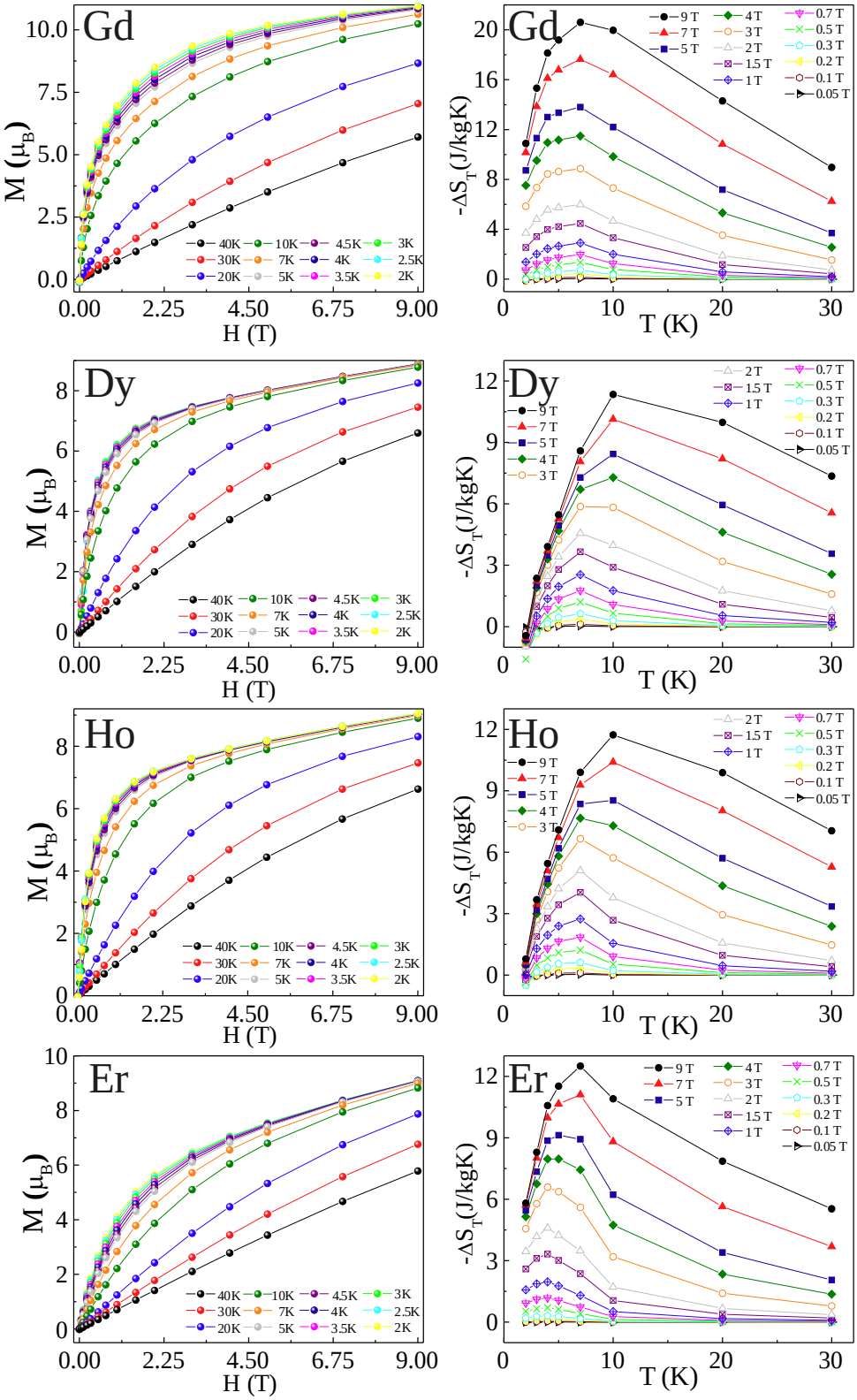

Figure 5.10. Field dependent magnetisation of $(Mn_{0.66}R_{1.34})(Mn_{0.66}Sb_{1.34})O_7$ pyrochlores with R = Gd, Dy, Ho and Er (left) measured at multiple temperatures. Magnetic entropy change (ΔS_M.) calculated from magnetisation measurements for selected ΔH values (right).

More precisely, these compounds show high entropy changes up to ~ 20.7 J/kgK (R = Gd), ~ 11.3 J/kgK (R = Dy), ~ 11.7 J/kgK (R = Ho) and ~ 12.5 J/kgK (R = Er) for $\Delta H = 9T$. These values are not comparable to those reached by typical long range ordered FM materials with giant magnetocaloric effect, such as Gd containing alloys, which can reach up to ~ 36 J/kgK for $\Delta H = 5T$ ($Gd_5Si_2Ge_2$) [10]. However, they can be considered rather high when compared to other oxides provided their magnetic frustration and dilution effects. In this context it is notable that the maximal magnetic entropy change (ΔS_{max}) of $(Mn_{0.66}Gd_{1.34})(Mn_{0.66}Sb_{1.34})O_7$ under a $\Delta H = 5T$ is only slightly lower than the reported value for the giant magnetocaloric zircon modification of $GdCrO_4$ (17.6 J/kgK *vs.* 18.8 J/kgK respectively) [11].

In order to determine the refrigerant capacity associated to these entropy changes, the relative cooling power (RCP) has been calculated from equation *Eq. 13*, where T_2-T_1 stands for the temperature range where $\Delta S = ½\ \Delta S_{max}$.

$$RCP = \int_{T_1}^{T_2} \Delta S_M \, dT \quad \textit{Eq. 13}$$

This temperature range, often considered as the useful regime of the material for magnetic refrigeration applications, is not easily determined for these curves due to their asymmetry. The Gd containing pyrochlore shows the most rounded plot, which half maximum value of entropy change ($\Delta S_{1/2}$) is achieved at T_2 = 27.5 K and T_1 < 2 K. The computerised integration assumes the approximation of the temperature limits to data points in the curves, so in this case the selected values are T_2 = 30 K and T_1 = 2 K. The selection of the temperature range for the different ΔH curves under this approximation evolves towards the shortening of the temperature window: for $\Delta H = 5$ T this window results in 20 K – 2 K but it closes to 10 K – 4 K for the smallest ΔH. The higher symmetry of the ΔS curves of this sample yields a relatively accurate determination of RCP values for the whole H margin, where only two points deviate from the general trend (see Figure 5.11-left). On the other hand, the same approach results in more irregular RCP values for the other compounds due to their less symmetric ΔS curves. All of them show maximal capacities between ~ 250 J/kg and ~ 550 J/kg, near the expected values for their use in magnetic refrigeration, which oscillate from ~ 100 J/kg to ~ 600 J/kg for the related $RCrO_4$ oxides [12].

Figure 5.11-right shows the Arrott plots, usually used to determine the accurate ordering temperature [13] and the order of the magnetic transition according to the Banerjee criterion [14,15]. The positive slope for all the curves both above and below the low temperature transition indicates their second order in all cases. As second ordered magnetic materials, the glassy magnetic materials have caused a wide interest for showing MCE over a much wider temperature range. Although the temperature range determined for these $(Mn_{0.66}R_{1.34})(Mn_{0.66}Sb_{1.34})O_7$ pyrochlores is relatively small, they present high electrical resistivity and high thermal stability, as detailed in the next subsection, what make these materials useful for low temperature applications such as He or H liquation.

The discussed magnetocaloric properties of these pyrochlores, depicted in Figure 5.11, can be enhanced by i) substituting Sb by a paramagnetic cation, ii) optimising the chemical composition at the A sites and iii) inducing amorphisation:

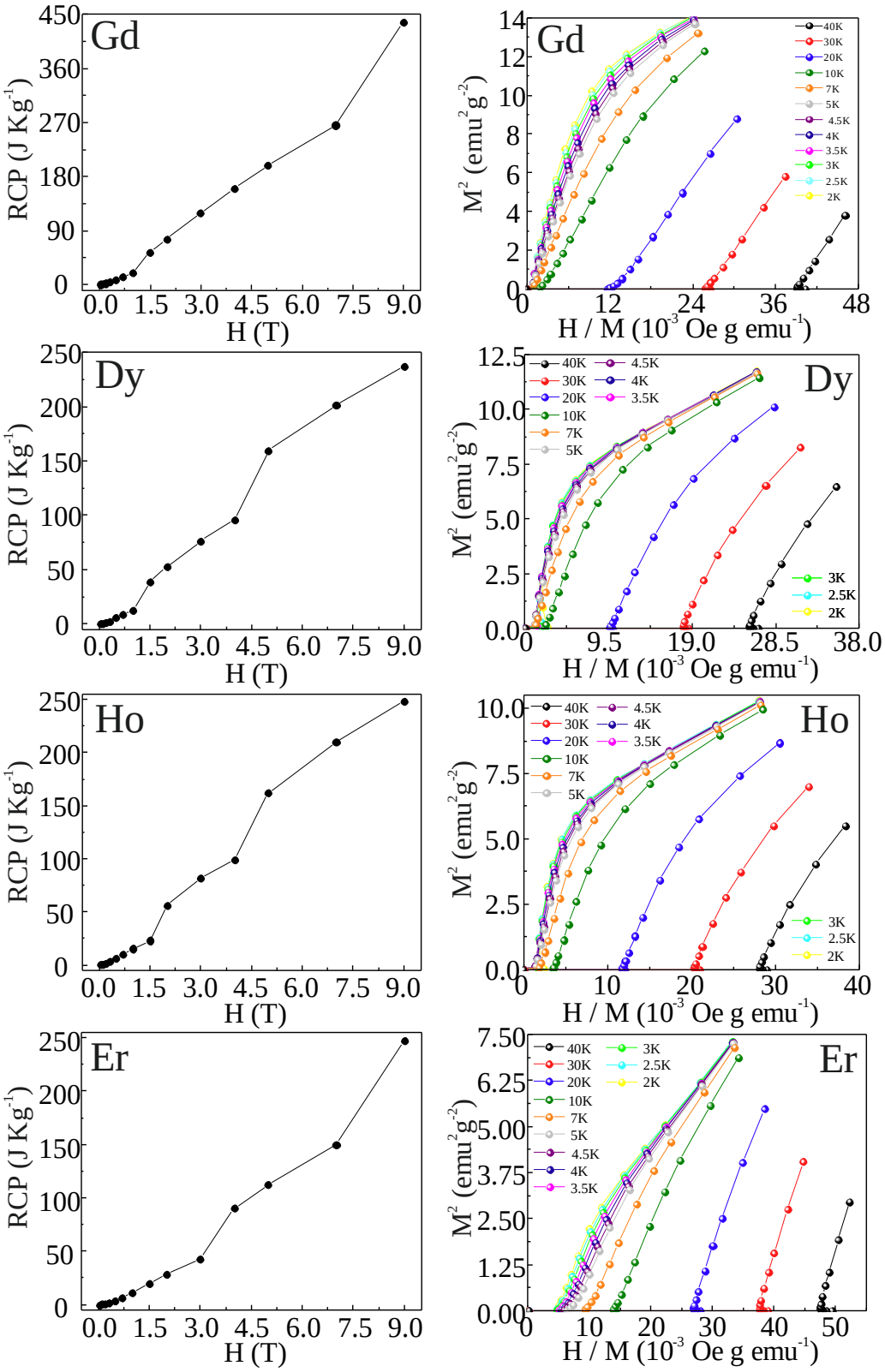

Figure 5.11. Relative cooling power (left) and Arrott plots (right) determined for $(Mn_{0.66}R_{1.34})(Mn_{0.66}Sb_{1.34})O_7$ pyrochlores with R = Gd, Dy, Ho and Er from their magnetisation measurements.

i) The substitution of the diamagnetic Sb^{5+} by a paramagnetic cation at the B sites. The introduction of another d^n metal compatible in size and charge with the Mn^{3+} of the rest of the B site, e.g. Ru^{5+} or Mo^{5+}, is expected to remove the B-site magnetic dilution thus facilitating the development of long range order magnetic interactions and consequently increasing the application temperature regime. Moreover, the introduction of additional paramagnetic transition metals is expected to enhance the polarisation of the rare earth through 3d-4f exchange interactions, thus optimising its influence on the MCE, as recently observed in the RMO_4 system [16].

ii) The partial substitution of a given R (let's say R1) by a different one (R2). This technique of combining different rare earths into a single phase is commonly used among the $RCrO_4$ as a chemical strategy for achieving broader temperature ranges of applicability [17]. For instance, the combination of Gd^{3+} and Tb^{3+} in this pyrochlore matrix may be expected to slightly sacrifice the magnitude of the ΔS_{max} in the advantage of widening the temperature window for $\Delta S_{1/2}$.

iii) The introduction of structural disordering or amorphisation by applying high pressures can also be expected to broaden the temperature range of applicability of the MCE for these $(Mn_{0.66}R_{1.34})(Mn_{0.66}Sb_{1.34})O_7$ pyrochlores, since higher entropy variations are intrinsically associated to the nature of the amorphous state.

2.3 - Thermal stability

As advanced, the structural stability of these pyrochlore phases has been studied under diverse conditions, including thermal treatments, high pressures and reducing atmospheres. Among them, only the heat treatment under reducing conditions yielded their decomposition into binary oxides. In fact, the application of a N_2/H_2 (5%) flow could not induce the decomposition process up to T = 1273 K, which is not completed until T > 1473 K as demonstrates the thermogravimetric analysis of Figure 5.12a.

The use of more extreme reducing agents, such as NH_3, induces an earlier degradation of these compounds, but they are still found to persist at T = 1073 K as pointed in Figure 5.12b-top for the R = Pr oxide. It is interesting to note that the R = Eu compound stabilises the pyrochlore structure as the main phase under the same environmental conditions. This treatment seems to induce the reduction of Eu^{3+} cations to Eu^{2+} resulting in the increase of the pyrochlore cell parameter from a ≈ 10.26 Å up to a ≈ 10.33 Å (see middle and bottom panels in Figure 5.12b).This reduction from $(Mn^{2+}_{0.66}Eu^{3+}_{1.34})(Mn^{3+}_{0.66}Sb^{5+}_{1.34})O_7$ stoichiometry could be achieved through three different mechanisms: i) the ammonolysis of the sample leading to a $(Mn^{2+}_{0.66}Eu^{3+}_{1.34-x}Eu^{2+}_{x})(Mn^{3+}_{0.66}Sb^{5+}_{1.34})O_{7-x}N_x$ pyrochlore; ii) removing O from the O2 sites originating an oxygen deficient pyrochlore with $(Mn^{2+}_{0.66}Eu^{3+}_{1.34-x}Eu^{2+}_{x})(Mn^{3+}_{0.66}Sb^{5+}_{1.34})O_{7-x/2}$ stoichiometry; or iii) the compensated oxidation of Mn^{2+} in the rest of the A sites, giving rise to a $(Mn^{2+}_{0.66-x}Mn^{3+}_{x}Eu^{3+}_{1.34-x}Eu^{2+}_{x})(Mn^{3+}_{0.66}Sb^{5+}_{1.34})O_7$ final composition. All of them would imply a change in the cell parameters, but the last one can be excluded as the presence of the mixed valence state of both A-site cations would be coupled to their divergence in size, probably inducing some additional order which is not observed through XRD. In order to distinguish between options i) and ii) further structural and functional studies are needed. The introduction of N^{3-} into the structure should imply an additional enlargement of the cell parameter ($r_{N^{3-}}$ = 1.46 Å *vs.* $r_{O^{2-}}$ = 1.38 Å) respect to that of the single reduction process proposed in ii), where the elimination of anions could induce a slight cell contraction partially compensating its expansion due to the larger ionic radii of Eu^{2+} (1.25 Å *vs.* 1.07 Å of Eu^{3+}) [1].

Heating these oxides under ambient pressure and in the absence of any gas flow do not induce any structural distortion at least up to the most extreme accessible temperature conditions in a conventional furnace (T > 1773 K), as shown in Figure 5.12c. This temperature is close to that needed for the isolation of $(Mn_{0.66}R_{1.34})(Mn_{0.66}Sb_{1.34})O_7$ pyrochlore pure phases.

Applying high pressure conditions up to 12GPa and ~ 1700 K (exemplified in Figure 5.12d for the R = Er compound) does not induce any structural phase transition into a DPv polymorph, which could have been expected from the traditional transformations of pyrochlores under high pressures [18]. However, the absence of any oxygen deficiency in these oxides and the unconventional stoichiometry into both A and B sites does not stabilise a DPv structure. In this context it should be noted that, consequently, the direct synthesis of high pressure DPv polymorphs of the initially sought Mn_2RSbO_6 stoichiometry was developed. The successful preparation and concomitant structural and functional study of these perovskites is carefully detailed in the next section of this chapter.

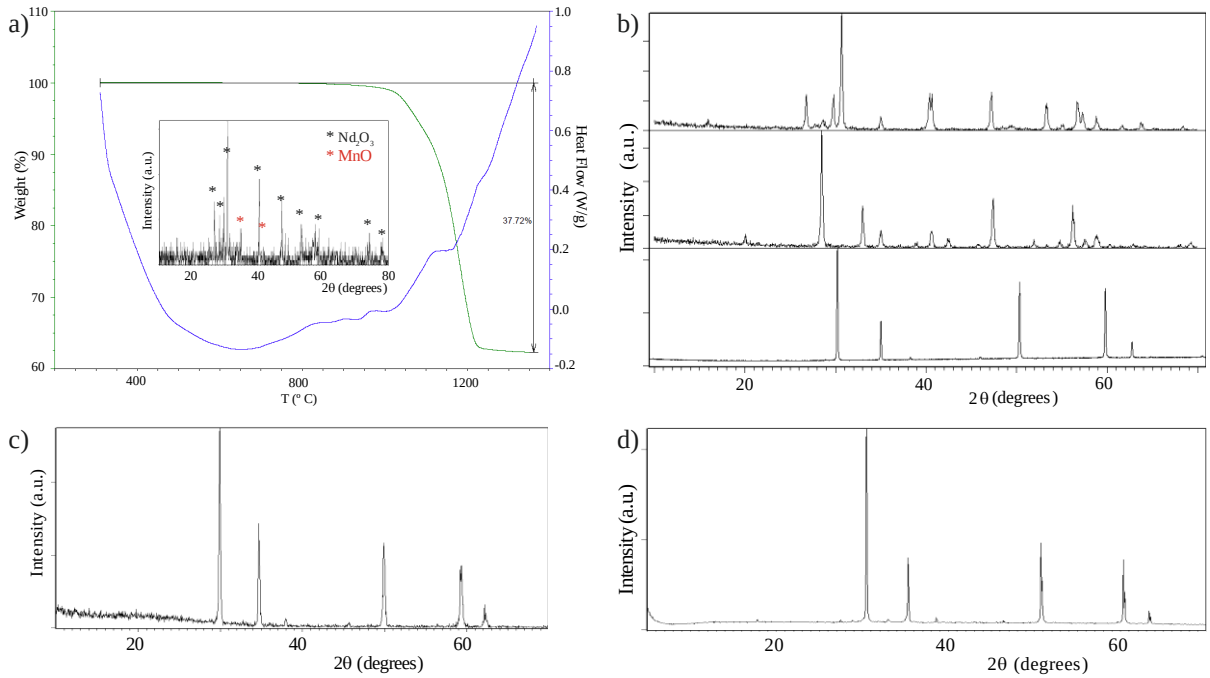

Figure 5.12. a) TGA profile for $(Mn_{0.66}Nd_{1.34})(Mn_{0.66}Sb_{1.34})O_7$ pyrochlore heated under a $H_2/N_2(5\%)$ flow. The inset in a) shows the XRD pattern of the resultant residue, which evidences the decomposition of the pyroclore into R_2O_3 + MnO (note that Sb is a volatile metal). b) XRD patterns of the $(Mn_{0.66}R_{1.34})(Mn_{0.66}Sb_{1.34})O_7$ R = Pr (upper panel) and Eu (middle panel) pyrochlores heated at T = 1073 K under a NH_3 flow. The bottom panel shows the original pure Eu containing compound before the amonolysis process. c) XRD pattern of a $(Mn_{0.66}R_{1.34})(Mn_{0.66}Sb_{1.34})O_7$ pyrochlore heated at 1773 K in a conventional furnace. d) XRD pattern of $(Mn_{0.66}Er_{1.34})(Mn_{0.66}Sb_{1.34})O_7$ pressed under 12 GPa and ~ 1700 K in a multianvil Walker module.

3.-High pressure: $MnRMnSbO_6$ double perovskites

3.1 - Synthesis and structural characterisation

The room pressure synthesis of $MnRMnSbO_6$ oxides through the conventional ceramic method yielded the pyrochlore derivatives detailed in the previous section. As it has been pointed out, applying high pressure (up to 12 GPa) and high temperature (up to 1700 K) to these phases did not result in any further phase transformation to a perovskite structure. Otherwise, the perovskite polymorphs of $MnRMnSbO_6$ need to be prepared through direct synthesis under HPHT conditions.

Applying similar pressures to those used in the syntheses of the related Mn_2MSbO_6 M = Fe, Cr and Sc compounds ($\leq$ 9 GPa), the experiments lead to the formation of an incipient perovskite - related structure in the presence of large amounts of pyrochlore derivative. In general, the entropy of the system decreases with its volume, what often favours the formation of high entropy phases, such as the perovskite structure. Therefore, due to the discussed broad *P- T* stability field of the pyrochlore structure, higher pressures are needed to synthesise pure $MnRMnSbO_6$ perovskite derivatives. The introduction of the large R^{3+} cations into the A site of the perovskite structure stabilises this denser polymorph, thus making it accessible as single phases at extreme pressure conditions (10 - 13 GPa).

Initial precursor powders were prepared by grinding the stoichiometric amounts of Mn_2O_3, Sb_2O_3 and R_2O_3 oxides. The oxidation states of the cations in the $MnRMnSbO_6$ perovskites resulted Mn^{2+}, R^{3+} and Sb^{5+} (as discussed later). Therefore, as in the previous Mn_2MSbO_6 oxides, the reaction taking place under high pressure conditions favours the reduction of Mn^{3+} to Mn^{2+} and the oxidation of Sb^{3+} to Sb^{5+}. However, the large size of the R^{3+} cations can only be stabilised in the cuboctahedral void, what means that a half of the B sites must be occupied by Mn. Since the octahedral coordination of the B sites can stabilise the Mn^{3+} of such a precursor, the final precursors used for the syntheses of $MnRMnSbO_6$ include the mixture of the stoichiometric amounts of R_2O_3, MnO and Sb_2O_5, where the cations in the reagents are already in their adequate oxidation states for the perovskite product. The use of this different precursor resulted in a better control of the synthesis conditions and avoided the presence of large amounts of non-desired secondary phases. A decarbonation process of the rare earth oxides was previously performed through their heat treatment in air at 1173 K and by heating Pr_6O_{11} at 1323 K under a N_2/H_2 (5%) flow in the case of Pr_2O_3. The best synthesis conditions resulted in 10 - 13 GPa (depending on the size of R^{3+}) and 1473 K. These conditions were applied during 20 minutes using a Walker-type module, after which temperature was quenched and pressure was slowly released.

One of the most important findings reached in this experimental work is that the crystal symmetry of the obtained perovskites is strongly dependent on the ionic radii of R^{3+}. On the one hand, the primary structural characterisation of these compounds through XRD revealed the formation of a conventional DPv structure for R = Eu and Gd, which diffraction patterns show a similar profile to those of the perovskite polymorphs of Mn_2MSbO_6 (M = Fe, Cr, Sc). On the other hand, the XRD profiles of $MnRMnSbO_6$ with R = La, Pr, Nd and Sm show superstructure peaks which will be later discussed to arise from the combination of the rock-salted order at the B sites with a columnar arrangement of the A-site cations. Figure 5.12 shows the final Rietveld fits of the XRD patterns collected at room temperature under synchrotron radiation at the high resolution endstation of BL04-MSPD beamline at ALBA lightsource [19]. TiO_2 coming from the detector (second row of Bragg positions) and

$RMnO_3$ (< 3% wt., third row) are included as secondary phases. The peaks marked with an asterisk are parasitic signals from the diffractometer (polyamide-imide Torlon).

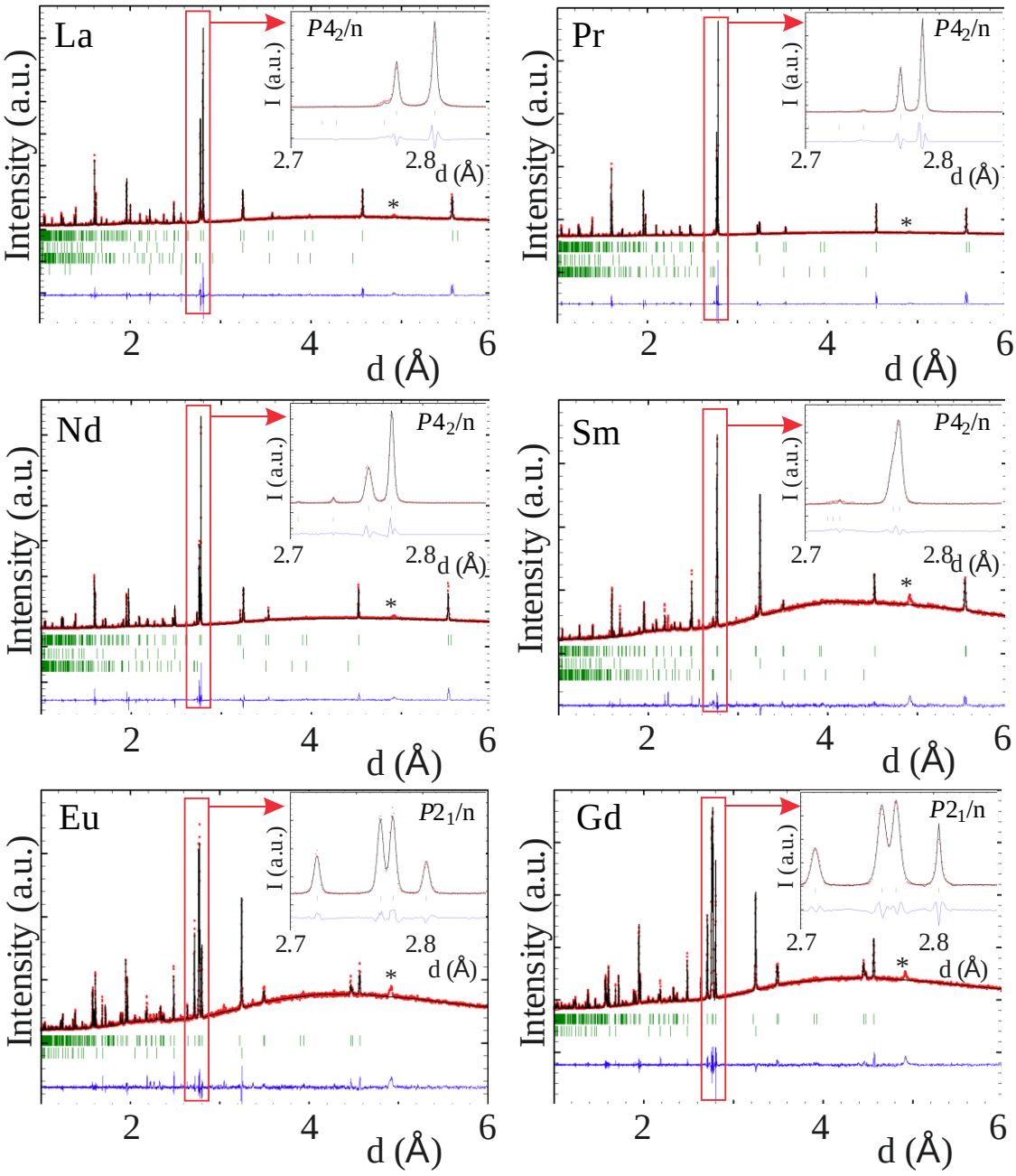

Figure 5.12. Rietveld refinements of the XRD data collected under synchrotron radiation for $MnRMnSbO_6$. The secondary phases included in the refinements are TiO_2 coming from the detector (second row of Bragg ticks) and $RMnO_3$ (< 3% wt., third row), and the peaks marked with an asterisk are parasitic signals from the diffractometer. The insets show an enlargement of the most intense region, highlighted with a red box in the main figure.

Concerning the Rietveld fit of the conventional DPv structure of the R = Eu and Gd containing compounds, depicted in Figure 5.13-bottom, the structural model of the related Mn_2MSbO_6 oxides was used as a starting point. As advanced, upon substituting M^{3+} by R^{3+} cations the large volume of rare earths prevents their accommodation into octahedral environments, for which R^{3+} cations usually occupy the A site of the perovskite structure (as it occurs, e.g. in the well-known manganites). Consequently, half of the Mn must be stabilised into the B sites, i.e. ordered with Sb in a rock-salt configuration.

The main crystallographic results fitted for these DPv_$MnRMnSbO_6$ (R = Eu and Gd) oxides are summarised in Table 5.5. A further study of the crystallographic details, including bond distances, angles and coordination environments, is detailed after the description of the new perovskite polymorph stabilised by $MnRMnSbO_6$ (R = La-Sm) so that the complete structural evolution induced by the substitution of R is studied.

Table 5.5. Crystallographic details for the monoclinic DPv structure of $MnRMnSbO_6$ (R = Eu, Gd) oxides from the Rietveld refinements of the powder XRD data collected under synchrotron radiation.

P*2$_1$/*n	**$MnRMnSbO_6$**				
Common positions	Atom-site	x	y	z	Occ
	Mn2 – 4d	0.5	0	0	0.5
	Sb – 4c	0	0.5	0	0.5
R	Atom-site	x	y	z	Occ
Eu	Mn/R – 4e	0.0126(5)	0.0544(2)	0.7475(4)	0.5
	O1 – 4e	0.311(3)	0.333(3)	0.962(3)	1
	O2 – 4e	0.344(3)	0.282(3)	0.564(2)	1
	O3 – 4e	0.886(2)	0.444(3)	0.772(2)	1
	Cell parameters	a (Å)	b (Å)	c (Å)	β (º)
		5.44032 (2)	5.60579 (2)	7.87820 (3)	90.269 (1)
	Atom-site	x	y	z	Occ
Gd	Mn/R – 4e	0.0123(3)	0.0571(2)	0.7474(3)	0.5
	O1 – 4e	0.297(2)	0.328(2)	0.946(2)	1
	O2 – 4e	0.331(2)	0.291(2)	0.566(2)	1
	O3 – 4e	0.892(2)	0.435(2)	0.770(1)	1
	Cell parameters	a (Å)	b (Å)	c (Å)	β (º)
		5.42201 (3)	5.60797 (2)	7.85407 (5)	90.309 (1)

Fitting residuals for Eu*:* R_p= 5.93%, R_{wp}= 8.43%, R_B = 10.9% and R_F = 13.5%.

Fitting residuals for Gd*:* R_p= 4.99%, R_{wp}= 7.24%, R_B = 4.36% and R_F = 3.59%

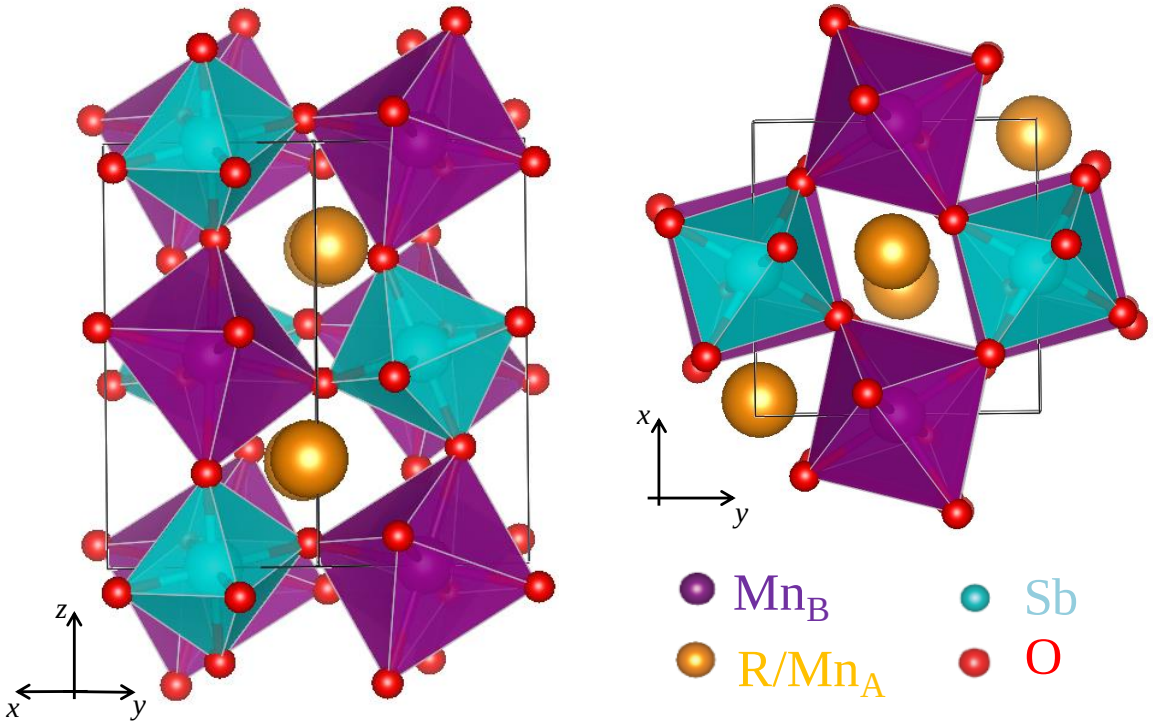

Figure 5.13. Structural model determined for the DPv polymorph of $MnRMnSbO_6$ (R = Eu and Gd) compounds from the Rietveld refinement of their XRD patterns collected under synchrotron radiation.

On the other hand, the routine powder XRD profiles of $MnRMnSbO_6$ with R = La, Pr, Nd and Sm showed the typical diffraction maxima of a perovskite structure coming from the conventional rock-salt order of the B-site cations (shortened as RS_B here). However, a carefully observation of the diffraction patterns revealed the appearance of a superstructure reflection at low angles, which indicates the possible stabilisation of an additional cation ordering.

In order to determine this new structure, ISOTROPY software [20] was used to check, in first place, the possible space groups that allowed symmetries for the simultaneous combination of cationic RS_B order with the three possible A-site arrangements, i.e. layered (L_A), columnar (C_A) and rock-salted (RS_A) and, afterwards, the tilt systems that originate additional distortions. Therefore, starting from the ideal $Pm\bar{3}m$ perovskite, the program gives R (½ ½ ½), M (½ ½ 0) and X (0 ½ 0) as the k-points in the Brillouin zone that can be assigned to the RS, C and L orders respectively in a related doubled cell. Each of these k-points was used to check the Ireps associated to them, which resulted in R2-, M4+ and X3- respectively for the A site (Wyckoff *b* position), and R1+ for the RS_B (Wyckoff *a* position). The combination of each of these Ireps for the different orders among A and A' cations with the R1+ determined for RS_B order, provided a list of possible subgroups, summarised in Table 5.6.

Table 5.6. ISOTROPY subgroups for the combination of i) rock-salted (RS), ii) columnar (C) and iii) layered (L) orders within the A site, with the RS order of B and B' cations in a double double perovskite (DDPv) derivative.

RS_A + RS_B		**C_A + RS_B**		**L_A + RS_B**	
Subgroup	Origin	Subgroup	Origin	Subgroup	Origin
F-43*m*	(0 0 0)	*Pn*-3*m*	(1 1 1)	*P*-43*m*	(-1/2 -1/2 -1/2)
		$P4_2/nnm$	(0 -1 -1)	$P4_2/mcm$	(0 1/2 1/2)
		$P4_2/mmc$	(1/2 1/2 0)	*P*4/*nmm*	(0 1/2 -1/2)
		Pnnn	(0 0 0)	*P*-42*m*	(1/2 1/2 1/2)
				Pccm	(0 1/2 1/2)
				*P*222	(-1/2 1/2 1/2)

In order to check these solutions, the experimental systematic absences were deduced from the profile fit of the routine experimental XRD data to the lowest symmetry (*P*-1): (00l) with l = 2n + 1 and (hk0) with h + k = 2n + 1. These extinction conditions point the presence of a screw axis perpendicular to a glide plane, what quickly excludes the RS_A + RS_B combination and leaves only three possible solutions: $P4_2/mmc$ and $P4_2/nnm$ for the C_A + RS_B combination and $P4_2/mcm$ for the L_A + RS_B ordering. Among them, $P4_2/nnm$ symmetry can be directly excluded, since it has additional elements of translational symmetry respect to those deduced from the *P*-1 profile fit. It is remarkable that the other two solutions also include additional extinctions, so further distortions affecting the anionic array will be needed. However, in order to check whether the A cations are ordered into columns or into layers, the $P4_2/mmc$ and $P4_2/mcm$ space groups were used to fit just the cationic ordering. These space groups are closely related by a change in the origin of the perovskite cell from (½ ½ 0) to (0 ½ ½), their *c*-glide plane being perpendicular to the *z*- or *y*-axis respectively. Therefore, the crystal unit cell is $a_p\sqrt{2} * a_p\sqrt{2} * 2a_p$ for the C_A + RS_B and $2a_p * a_p\sqrt{2} * a_p\sqrt{2}$ for the L_A + RS_B orderings. Figure 5.14 shows the refinements testing both crystallographic models, where it can be observed that only $P4_2/mmc$ was found to fit all the reflections arising from cationic ordering [21,22]. Otherwise, the combination of a diagonal cell and the L_A + RS_B orderings can only fit one of the cation order superstructure peaks. Therefore, the A-site arrangement in these doubly ordered perovskites must be columnar.

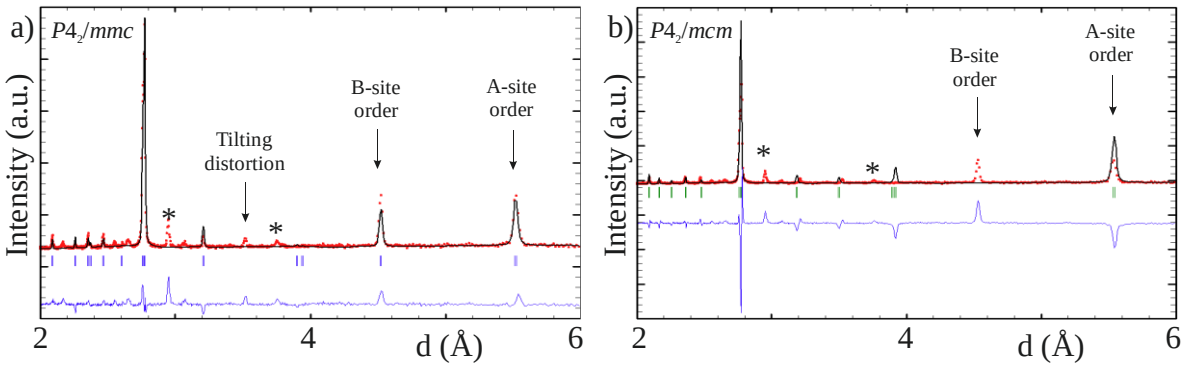

Figure 5.14. Fits of the XRD data of $MnNdMnSbO_6$ to the C_A + RS_B (a) and L_A + RS_B (b) models using the $P4_2/mcm$ and $P4_2/mmc$ space groups respectively.

Since not all the peaks of the diffraction pattern could be indexed with this space group (note the reflection labelled in Figure 5.14a at d ~ 3.53 Å), a structural distortion affecting the anionic sublattice is needed to decrease the symmetry of the cell. Therefore, a second symmetry analysis with ISOTROPY was performed, now considering both the C_A + RS_B cationic arrangements and the octahedral tilting. In this context, it is established that the three-dimensional Ireps for in-phase and out-of-phase octahedral tilts arising from the $Pm\bar{3}m$ parent group are M3+ and R4+ respectively [23,22,24]. Consequently, each of them has been combined with the cationic coupled orders, i.e. M4+ and R1+ for C_A + RS_B, resulting in the possible space groups summarised in Table 5.7.

Table 5.7. ISOTROPY subgroups for the combination of the columnar arrangement of A-site cations, rock-salted B-site cations and in-phase (left column) or out-of-phase (right) octahedral tilts in the DDPv structure of $MnRMnSbO_6$ (R = La, Pr, Nd and Sm).

C_A + RS_B + inph-tilt		**C_A + RS_B + oph-tilt**	
Subgroup	Origin	Subgroup	Origin
*P*n-3	(1 1 1)	*R*-3	(0 0 0)
$P4_2$/nnm	(0 -1 -1)	$P4_2$/n	(-1 -1 -1)
*C*ccm	(1/2 -1/2 0)	$P4_2$/m	(1/2 1/2 0)
*P*nnn	(0 0 0)	*C*2/c	(1/2 1/2 0)
		*P*2/c	(0 0 0)
		*C*2/m	(0 0 1)
		*P*2/m	(0 0 0)
		P-1	(0 0 0)

Taking into account the required presence of a screw axis perpendicular to a glide plane, most of the solutions shown in Table 5.7 can be discarded. In fact, only the $P4_2/n$ space group, including an out-of-phase tilt system, is a possible solution, since the $P4_2/nnm$ in-phase tilted system was already discarded in the previous step for inducing additional extinctions.

Therefore, the $P4_2/n$ space group has been found to fit all the reflections of the diffraction patterns of $MnRMnSbO_6$ (R = La, Pr, Nd and Sm) compounds with a $2a_p * 2a_p * 2a_p$ cell. According to the International Tables for Crystallography (Vol. A1) [25], the change from the diagonal cell ($a_p\sqrt{2} * a_p\sqrt{2} * 2a_p$) which supports the C_A + RS_B cationic arrangements (S. G. $P4_2/mmc$) to this doubled cell along the three crystallographic axes ($2a_p * 2a_p * 2a_p$) is possible because $P4_2/n$ is a maximal non-isomorphic subgroup of $P4_2/m$ (a'= 2a, b' = 2b), which is a subgroup of the discussed $P4_2/mmc$ fitting the cation order. The Rietveld refinements of their high resolution XRD data collected under synchrotron radiation were depicted in Figure 5.12 and their structural details are summarised in Table 5.8.

The Figure 5.15 shows the crystal structure of this new DDPv, that can be described as the combination of the conventional RS order of Mn_B (purple) and Sb (blue) among the B sites with the unusual columnar arrangement of Mn_A (green and grey) and R (orange) into the A sites. Mn_B and Sb locate into the 4c and 4d octahedral sites respectively, sharing corners along the three crystallographic axes. The $a^+a^+c^-$ tilt system associated to the oxygen displacements from their 8g site gives rise to three different cuboctahedral voids: two of them (2a and 2b Wyckoff sites) are fixed positions where Mn (Mn_A and $Mn_{A'}$ in Table 5.8 and Figure 5.15) sites into highly symmetric environments and the

third one (4e position) is an irregular site occupied by the large R^{3+} cation with a degree of freedom along the *z* direction. The mentioned regular coordinations of Mn in the A sites are shown in the lower part of Figure 5.15 to be tetrahedral (Mn_A, green) and square planar ($Mn_{A'}$, grey), which sequentially alternate along their columns. Therefore, these $MnRMnSbO_6$ (R = La, Pr, Nd and Sm) double double perovskites are notable not just for being the first examples of C_A + RS_B cation order combination in the perovskite family, but also for stabilising five different cationic environments, three of them for Mn^{2+} cations in octahedral, tetrahedral and square planar coordinations [26], as further discussed from the study of the M-O bond lengths.

The evolution of the cell parameters of $MnRMnSbO_6$ (R = La-Sm) agrees with the lanthanide contraction, as they concomitantly decrease with the substitution of R by progressively smaller rare earths. The transition from the DDPv to the simpler DPv structure for R^{3+} cations smaller than Sm (further explained below) is induced by the disorder of Mn_A, $Mn_{A'}$ and R into a single A site.

Table 5.8. Crystallographic details for the tetragonal $MnRMnSbO_6$ (R = La, Pr, Nd, Sm) oxides from the Rietveld refinements of the powder XRD data collected under synchrotron radiation.

P*4$_2$/*n	**$MnRMnSbO_6$**			
Atom-site	x	y	z	Occ
Mn_A – 2a	0.75	0.75	0.75	0.25
$Mn_{A'}$ – 2b	0.25	0.25	0.75	0.25
R– 4e	0.25	0.75	Z	0.5
Mn_B – 4c	0	0.5	0.5	0.5
Sb – 4d	0	0	0.5	0.5
O1 – 8g	x	y	z	1
O2 – 8g	x	y	z	1
O3 – 8g	x	y	z	1

R	a (Å)	c (Å)	Z	O1		O2		O3	
La	7.86342 (2)	8.02932 (3)	0.7751 (2)	x y z	-0.052(4) 0.545(4) 0.228(2)	x y z	-0.224(3) -0.041(2) 0.578(2)	x y z	-0.279(2) 0.080(2) -0.029(2)
Pr	7.83809 (1)	7.93135 (2)	0.7768 (1)	x y z	-0.047(2) 0.563(2) 0.228(2)	x y z	-0.226(2) -0.036(1) 0.580(1)	x y z	-0.264(2) 0.072(1) -0.030(1)
Nd	7.80354(2)	7.90375(1)	0.7777 (1)	x y z	-0.050(2) 0.559(2) 0.220(2)	x y z	-0.207(2) -0.017(2) 0.582(1)	x y z	-0.257(2) 0.075(1) 0.039(2)
Sm	7.82385 (3)	7.85109 (4)	0.7789 (3)	x y z	-0.055(5) 0.549(5) 0.220(3)	x y z	-0.182(3) -0.002(4) 0.586(3)	x y z	-0.257(4) 0.075(3) -0.034(3)

Fitting residuals for La: R_p = 8.41%, R_{wp} = 12.1%, R_B = 6.72% and R_F = 6.49%

Fitting residuals for Pr: R_p = 10.6%, R_{wp} = 15.5%, R_B = 7.94% and R_F = 8.63%

Fitting residuals for Nd: R_p = 7.06%, R_{wp} = 9.96%, R_B = 13.9% and R_F = 11.9%

Fitting residuals for Sm: R_p = 4.62%, R_{wp} = 6.75%, R_B = 10.2% and R_F = 16.7%

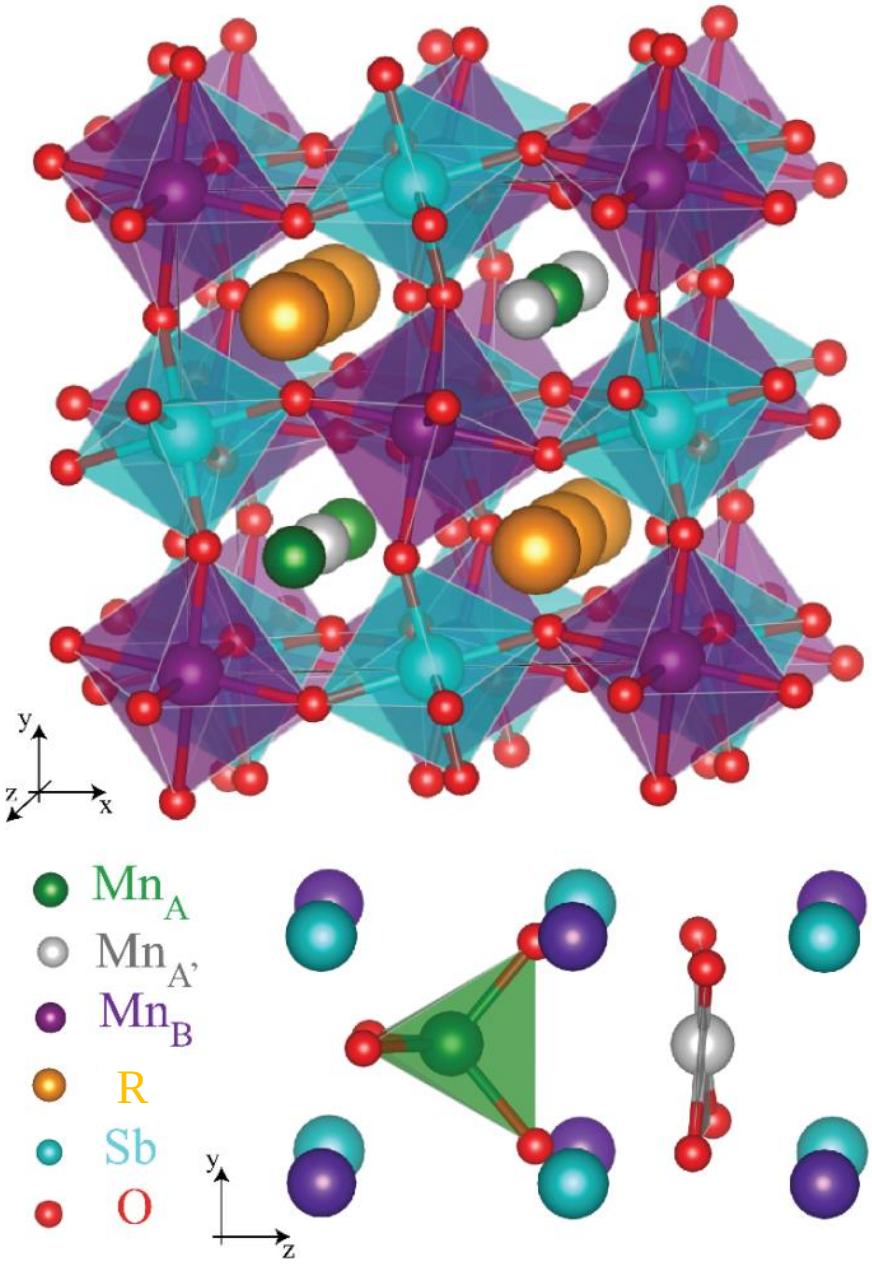

Figure 5.15. Structural model determined for the DDPv polymorph of $MnRMnSbO_6$ (R = La-Sm) compounds from the Rietveld refinement of their XRD patterns collected under synchrotron radiation.

The DDPv structure has also been tested through NPD and electron microscopy studies. NPD data were collected at WISH diffractometer at 200 K for $MnNdMnSbO_6$. The fit of the diffraction pattern, depicted in Figure 5.16a, supports the results obtained from the synchrotron XRD data. The considerable difference in the neutron scattering lengths of Nd (7.69 fm), Sb (5.57 fm), Mn (-3.73 fm) and O (5.8 fm) [2] confirms the different cationic sites, highlighting the occurrence of

independent columns occupied by the atoms with the highest scattering length and by those with a negative value. It is also possible to elucidate the rock-salt arrangement of B-site cations from the difference between Sb and Mn, as it was discussed in the previous chapters concerning Mn_2MSbO_6 (M = Sc, Cr and Fe) double perovskites. The scattering length of oxygen atoms allows the determination of accurate oxygen positions compared to those obtained from XRD. The atomic positions for O1, O2 and O3 sites summarised in Table 5.8 were updated after fitting the NPD of the R = Nd sample. It is worth noting that NPD data were also collected at 80 K at D20 instrument for $MnRMnSbO_6$ R = La and Pr compounds, which resulting oxygen positions supported these results.

A complete study of this new DDPv derivative was also performed through electron microscopy and its associated techniques. SAED patterns of $MnRMnSbO_6$ (R = Pr and Nd) were taken in a JEOL JEM2100 microscope operating at 200 kV with a double tilt (±45°) goniometer.

The diffraction patterns of a $MnNdMnSbO_6$ crystal, depicted in Figure 5.16b, can be indexed along $[110]_p$, $[100]_p$ and $[210]_p$ zone axes with a crystallographic $2a_p * 2a_p * 2a_p$ cell.

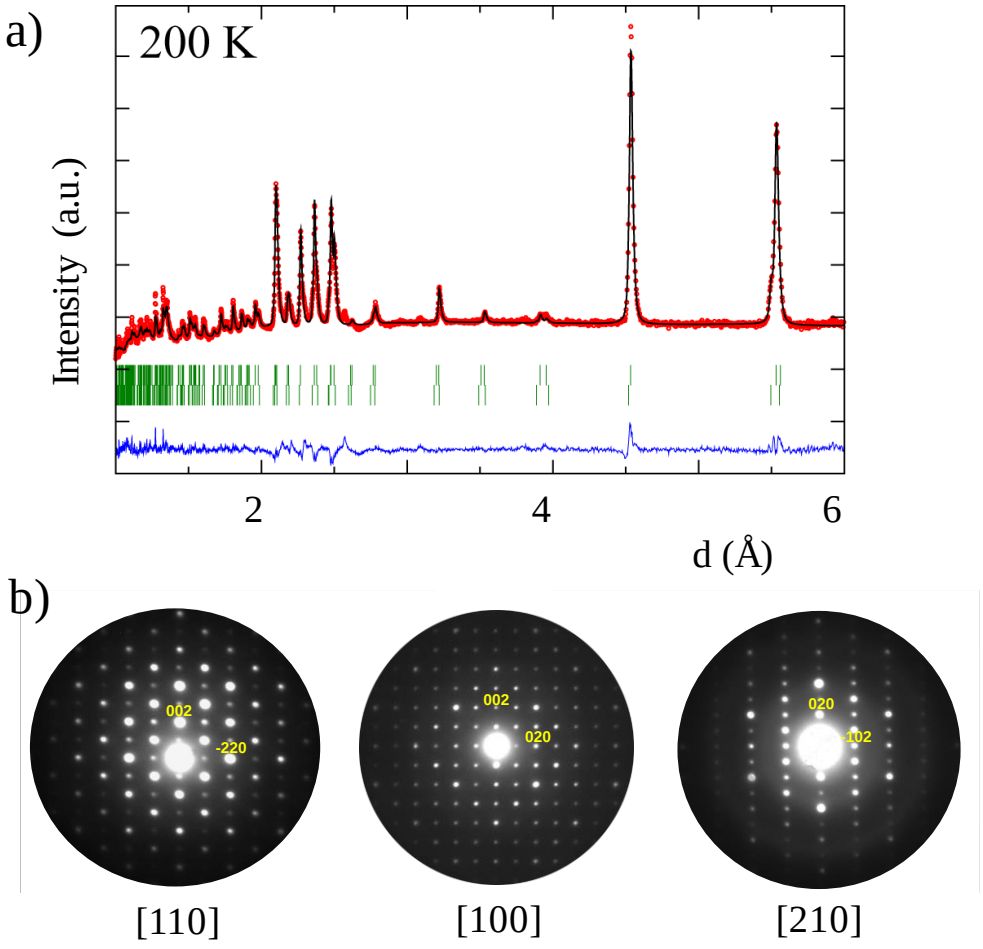

Figure 5.16. a) Rietveld refinement of the NPD data collected at 200 K for $MnNdMnSbO_6$ using the DDPv structural model. b) SAED patterns of a $MnNdMnSbO_6$ crystal along the $[110]_p$, $[100]_p$ and $[210]_p$ zone axes.

The new cationic arrangement determined from XRD and NPD was confirmed by transmission electron microscopy studies. Initial high resolution transmission electron microscopy (HRTEM) and electron energy loss spectroscopy (EELS) experiments were performed with a JEOL JEM 3000F microscope operating at 300 kV. Further Scanning-Transmission Electron Microscopy (STEM) images were collected in a JEOL JEM ARM200cF microscope with corrected aberration in the condenser lens, providing atomic resolution.

Figure 5.17 shows the STEM image of $MnPrMnSbO_6$ along [110] direction. The observed periodicities correspond to the *c* cell parameter (~ 7.9 Å) and the *xy* plane (~ 5.5 Å). A portion of the same crystallographic direction of the structure determined from XRD-NPD is superimposed, showing a good fit to the experimental image. The periodicity of equivalent B and A sites can be derived from [001] and $[\bar{1}10]$ directions respectively. The simulation of the HRTEM images, performed with MacTempas X software [27] using the refined structure from NPD data, is also included as an inset on the bottom-right corner of the micrograph, showing a good fit to the experimental data. The electron-rich Pr (Z = 59) and Sb (Z = 51) columns appear as bright spots while Mn are faint according to their low Z (25) number. The scanned intensities along *z*, depicted on the right hand side of the Figure 5.17a, show different profiles for subsequent columns, assigned to Sb-Mn_A-Mn_B-Mn_A-Sb and Mn_B-Pr-Sb-Pr-Mn_B, thus supporting the cationic ordering deduced from XRD and NPD.

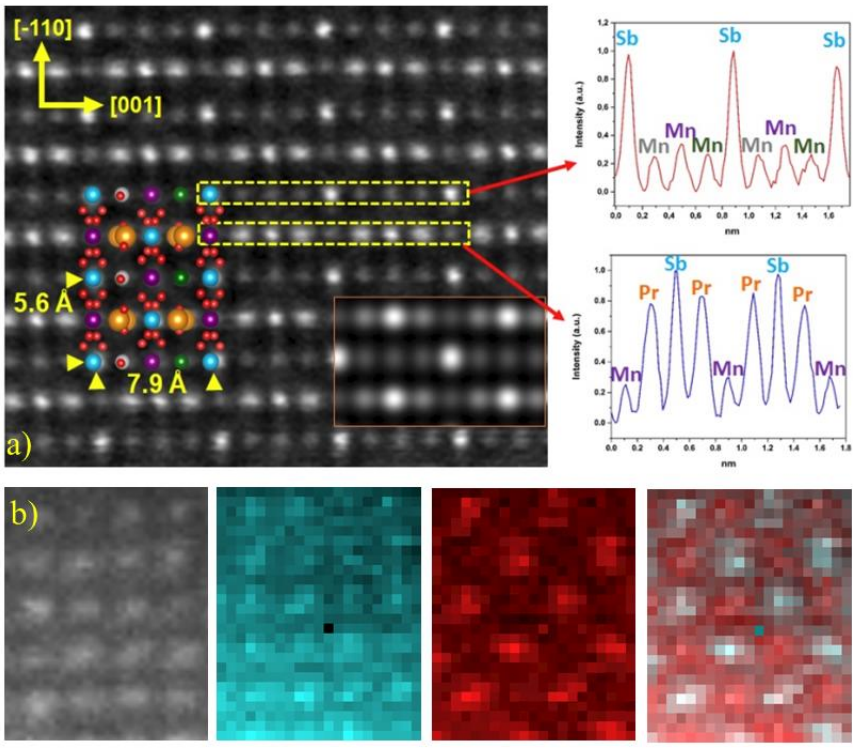

Figure 5.17. a) Atomic-resolution [110] TEM image of $MnPrMnSbO_6$ (left).The DDPv model and the simulated image (lower-right orange box) are included as insets, both fitting the experimental data. The scanned intensities (right) from the dashed box sections show different [001] repeat sequences revealing the columnar order of A-site cations. b) STEM image (grey, left) of $MnPrMnSbO_6$ along [010] zone axis and X-ray mappings fitted for Mn (blue) and Pr (red).

The X-ray mappings performed from STEM images collected along the [010] zone axis are shown in Figure 5.17b, where it can be observed that Pr atoms (red coloured) are only located at the A sites while Mn (blue) are stabilised at both A and B sites. The combination of both mappings into a single one, shown on the right panel of Figure 5.17b, fit the alternation of A (red) and B (blue) sites.

As indicated, EELS spectra were also collected for $MnRMnSbO_6$ (R = Pr and Nd) DDPv polymorphs in order to check the oxidation state of Mn. The results, exemplified in Figure 5.18 for a representative sample of $MnPrMnSbO_6$, show the typical ratio for the L_3/L_2 edge lines of Mn corresponding to Mn^{2+}. It is worth noting that the oxidation states determined from BVS calculations from the M-O bond distances from the Rietveld refinements of NPD and synchrotron XRD data are averaged values based on an ionic model. For this reason, the presence of a certain covalent character of these bonds affects the experimental averaged oxidation states, as it was discussed in detail for the DPv polymorph of Mn_2CrSbO_6 related compound in chapter III. Otherwise, the evidence of a 2+ state for Mn from more accurate EELS spectra confirms the expected $Mn^{2+}R^{3+}Mn^{2+}Sb^{5+}O_6$ nominal formula.

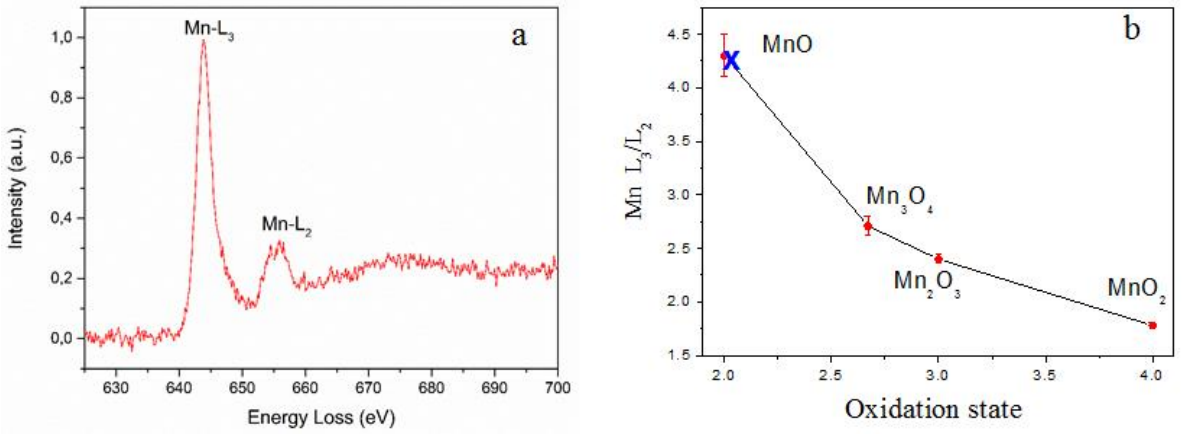

Figure 5.18. a) EELS spectrum for $MnPrMnSbO_6$ DDPv structure showing the Mn-L_2 and L_3 ionisation edges. b) Calibration curve for Mn oxidation states from the L_3/L_2 integrated intensity ratios for different binary Mn oxides. The experimental ratio for $MnPrMnSbO_6$ from figure a) is interpolated (blue cross), showing all Mn adopts 2+ state.

It is finally remarkable that during the final steps of the structural characterisation of this new DDPv derivative a single crystal of $MnNdMnSbO_6$ could be grown by slowly cooling the HPHT synthesis product. Single crystal XRD data were collected on a SuperNova X-ray Diffraction System (Oxford) and the structure was solved using the Superflip package in Jana2006 [28]. The structural details, including atomic coordinates, bond lengths, equivalent thermal factors and BVS calculations, are summarised in Table 5.9. In general terms, the discussed structural details determined from the Rietveld refinements of the powder XRD and NPD data and supported by microscopy studies, are undoubtedly confirmed from single crystal analysis [26].

Table 5.9. Refinement results for $MnNdMnSbO_6$ DDPv structure from single crystal XRD taken at 120 K under Mo K_α radiation. S.G. $P4_2/n$; a = 7.8225(5) Å, c = 7.9077(5) Å. Fitting agreement factors: R_{obs} = 2.24%, wR_2 = 5.04%, GOF = 1.20.

	x	y	z	$U_{eq.}$ [Å^2]	BVS
Mn_A	½	½	0	0.005	1.9
$Mn_{A'}$	0	0	0	0.019	1.8
Nd*	½	0	0.2674(4)	0.006	2.8
Mn_B	¾	¼	¼	0.006	2.2
Sb*	¼	¼	¼	0.003	5.4
O1	0.3194(3)	0.0097(3)	0.2820(3)	0.007	___
O2	0.4855(3)	0.2920(3)	0.1655(4)	0.009	___
O3	0.3192(4)	0.3004(4)	0.4855(3)	0.009	___

d_{A-O} (Å)		d_{B-O} (Å)	
Mn_A-O3 (x4)	2.110 (3)	Mn_B-O1(x2)	2.118(3)
$Mn_{A'}$-O2 (x4)	2.091 (3)	Mn_B-O2(x2)	2.199(3)
Nd-O1 (x2)	2.465 (3)	Mn_B-O3 (x2)	2.196(3)
Nd-O1 (x2)	2.397 (3)	Sb-O1(x2)	1.973(3)
Nd-O2 (x2)	2.536 (3)	Sb-O2 (x2)	1.987(3)
Nd-O3 (x2)	2.762 (3)	Sb-O3 (x2)	1.979(3)
Nd-O3(x2)	2.946 (3)		

* Small antisite disorders have been detected for Nd and Sb sites, which have 6.3 (6) % and 7.6 (6) % of Mn respectively.

Table 5.10 shows the interatomic M-O bond distances obtained from the NPD and synchrotron XRD diffraction patterns. The theoretical bond distances, calculated from the sum of the ionic radii of O and M in the adequate coordination number are 2.0 Å (Sb-O), 2.23 Å (Mn_B-O) and 2.06Å (Mn_A-O in the DDPv structure). The theoretical R-O distances for the six $MnRMnSbO_6$ compounds are also summarised in Table 5.10. According to these distances Sb and Mn_B are six-fold coordinated at the B-sites of both DDPv and DPv structures and there is a good agreement between the calculated and the theoretical values, since it can be observed that $(M\text{-}O)_{exp.} \sim (M\text{-}O)_{th.}$. On the other hand, different coordination environments are favoured for the A-site cations due to the large difference between the ionic radii of R^{3+} and Mn^{2+} cations, as mentioned during the description of the DDPv structure. Cooperative oxide displacements in the DDPv_$MnRMnSbO_6$ modification results in almost regular alternating tetrahedral and square-planar environments for the A-site Mn^{2+} cations that are located in two inequivalent sites within their column. In contrast, R^{3+} cations are 10-fold coordinated. The $MnRMnSbO_6$ DDPv structure is notable for having five different cation sites, three of them occupied by Mn^{2+} in tetrahedral, square-planar, and octahedral environments. Upon changing R for smaller cations, the optimisation of the octahedral tilt (discussed below) for the accommodation of the rare earth at the 4e position induces the concomitant distortion of the Mn A sites. The small size of the fourfold Mn (0.66Å) is adequate for the tetragonal and square planar coordinations in the sufficiently different voids of $MnRMnSbO_6$ (R = La, Nd and Pr) compounds, but in the case of R = Sm oxide it induces an increase of Mn_A-O distances, which become closer to the six-fold coordination of the monoclinic double perovskites, since the theoretical ionic radii of Mn^{2+} in such coordination amounts

to 0.96 Å. The increase on the coordination of Mn A sites in $MnSmMnSbO_6$ compensates by lowering the coordination of Sm^{3+} down to a near eightfold position.

Table 5.10. Experimental [a)] M-O interatomic distances for both tetragonal and monoclinic polymorphs of $MnRMnSbO_6$ determined from their Rietveld refinements.

R	d_{Sb-O} (Å)	d_{MnB-O} (Å)	d_{MnA-O} (Å)	$d_{MnA'-O}$ (Å)	$d_{R-O(exp.)}$ (Å)	$d_{R-O(th.)}$ (Å)
La	1.89	2.27	2.25	2.15	2.56	2.56
Pr	1.92	2.22	2.16	2.16	2.54	2.53
Nd	1.93	2.21	2.09	2.09	2.55	2.51
Sm	1.80	2.32	2.20	2.38	2.47	2.48
Eu	1.92	2.23	$d_{A-O(exp.)}$ = 2.39			2.41
Gd	1.94	2.21	$d_{A-O(exp.)}$ = 2.38			2.40

[a)] The theoretical values determined from $d_{M-O\ (th.)} = r_M + r_O$ are 2.00 Å, 2.23 Å and 2.06 Å for M = Sb, MnB and MnA/A' respectively. The expected value for the R-O distance for each R is included in the last column, where it is averaged with $d_{MnA-O\ (th.)}$ for the disordered A sites in the DPv $MnRMnSbO_6$ (R = Eu and Gd).

As it has been stated, there is and "order (DDPv) to disorder (DPv)" phase transition when the size of the R^{3+} cation decreases along the lanthanide series. Figure 5.19a shows two different regions of the synchrotron XRD patterns that highlight the evolution of the diffraction peaks upon substituting R for progressively smaller ones. The d = 4 - 6 Å region is depicted on the left-hand side of the figure, which shows the presence of $(110)_{DDPv}$ and $(111)_{DDPv}$ reflections arising from the C_A and RS_B arrangements respectively in the patterns of $MnRMnSbO_6$ (R = La-Sm). The small broad peak identified with an asterisk is a parasitic signal coming from the diffractometer. The $(110)_{DDPv}$ reflection associated to the A-site columnar ordering disappears when Sm is substituted by Eu and smaller rare earths. The $(111)_{DDPv}$ reflection splits into $(101)_{DPv}$ and $(011)_{DPv}$ as a consequence of lowering the symmetry from $P4_2/n$ to $P2_1/n$. The d = 2.7 – 2.85 Å region, enlarged on the right-hand side of Figure 5.19a, shows the evolution of the most intense peaks of the XRD patterns. The $(022)_{DDPv}$ and $(220)_{DDPv}$ reflections get closer from La down to Sm and finally splits into a doublet, identified as the $(112)_{DPv}$ + $(\bar{1}\bar{1}2)_{DPv}$ reflections of the DPv structure, for Eu and Gd. These two peaks are surrounded by another two assigned to the $(020)_{DPv}$ and $(200)_{DPv}$ crystallographic planes commonly observed in $P2_1/n$ double perovskites.

The progressive evolution of the cell parameters, summarised in Tables 5.5 and 5.8, is depicted in Figure 5.19b. The normalised c_n cell parameter of both the tetragonal DDPv and the monoclinic DPv polymorphs ($c_n = c/a_p$) decreases with the ionic radii of R. The change of trend coincides with the phase transition from the $P4_2/n$ to the $P2_1/n$ symmetries. A similar but smoothed effect is observed for the normalised a parameter (a_n), which splits into two (a_n and b_n) according to the monoclinic symmetry.

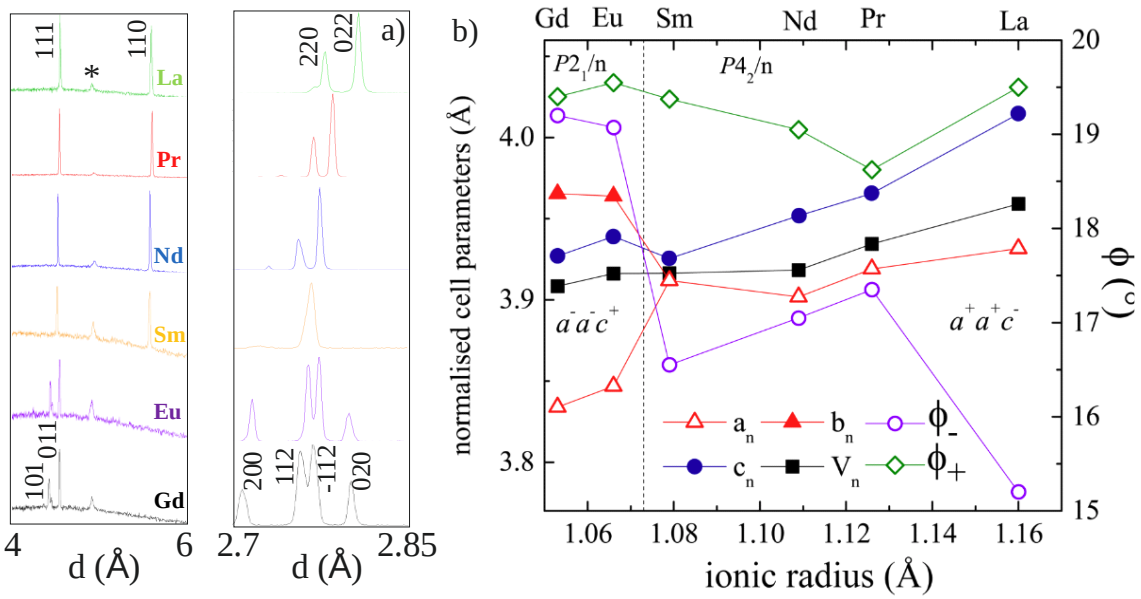

Figure 5.19. a) Enlargement of the 4 Å - 6 Å (left) and 2.7 Å – 2.85 Å (right) regions of the XRD profiles collected under synchrotron radiation, where the DDPv to DPv transition is observed. b) Evolution of the normalised cell parameters and volume (left axis) and the in-phase (Φ_+) and out-of-phase (Φ_-) octahedral tilt angles (right axis) as a function of the ionic radii of R^{3+} cations.

Coupled to this phase transition, a change of tilt system is observed from the $a^+a^+c^-$ associated to the tetragonal $P4_2/n$ space group to the $a^-a^-c^+$ featuring the monoclinic $P2_1/n$ one. It is worth noting that, as detailed in Chapter I, columnar A-site arrangements are stabilised by SOJT distortions and high tilt angles [29]. Among the few perovskites known to stabilise this type of order, the DPv $CaFeTi_2O_6$ is notable for being the first example of A-site columnar ordering associated to $a^+a^+c^-$ tilt system. The in-phase tilt in the basal plane (Φ_+) amounts to 16.5 º and the out-of-phase one (Φ_-) is 11.3 º [30]. The tilt values observed for the double ordered $MnRMnSbO_6$ compounds, which lowest values amount to $\Phi_+ = 18.6$ º and $\Phi_- = 15.2$ º, are rather high compared to those. These larger tilting angles are consistent with the stabilisation of the columnar order into the DDPv structure in spite of its high distortion, which involves the need for high pressure synthesis conditions[26].

The numeric results of the calculations of the depicted tilt angles of $MnRMnSbO_6$ perovskites are summarised in Table 5.11. The independent Φ_+ and Φ_- tilt angles have been determined from the half difference between the experimental $< B – O_n – B' >$ angles and their ideal 180 º value, as explained in Apendix I. The tilts parallel to the basal plane of the perovskite structure (θ) were calculated using the average of the $< B – O_n – B' >$ angles through O1 and O2 for the monoclinic DPv and through O2 and O3 for the tetragonal DDPv polymorph. The Φ_+ and Φ_- of $MnRMnSbO_6$ (R = Eu and Gd) adopt similar values as it occurred in the related Mn_2MSbO_6 (M = Cr, Fe, Sc) DPv where Φ_+ is identified as ϕ and Φ_- corresponds to θ [31–33] but they diverge for $MnRMnSbO_6$ (R = La - Sm). The tilt systems associated to these two space groups are reciprocal, i.e. the in-phase tilts along [110] and $[\bar{1}10]$ directions of the tetragonal polymorph (θ_2 and θ_3 in Table 5.12) become out of phase for the monoclinic distortion (θ_1 and θ_2) while the out-of-phase tilt along [001] in the former (ϕ_1) turns into an in-phase tilt (ϕ_3) as a consequence of the A-site cations disorder effect. Therefore, the tilt angle evolution can be considered as an order parameter for this phase transition.

Table 5.11. Distortion parameters for $MnRMnSbO_6$ as a function of the ionic radius of R and its difference with that of the A-site Mn^{2+} cation[a)]: In-phase and out-of-phase tilt angles (Φ_+, Φ_-) and octahedral distortion (Δ) of SbO_6 and MnO_6 determined from $\Delta = (1/n)*\sum[(d_{av}-d_i)/d_{av}]^2$.

R	r_R^{3+} (Å)	$r_R^{3+} - r_{MnA}^{2+}$ (Å)	Φ_+	Φ_-	Δ (SbO_6)	Δ (MnO_6)
La	1.16	0.50	19.50	15.20	$1.04*10^{-4}$	$5.6*10^{-5}$
Pr	1.126	0.46	18.63	17.35	$1.18*10^{-4}$	$3.95*10^{-4}$
Nd	1.109	0.45	19.05	17.05	$1.7*10^{-4}$	$1.6*10^{-3}$
Sm	1.079	0.42	19.38	16.55	$9.53*10^{-3}$	$7.07*10^{-3}$
Eu	1.066	0.106	19.55	19.08	$4.01*10^{-4}$	$6.95*10^{-4}$
Gd	1.053	0.093	19.40	19.20	$1.9*10^{-5}$	$7.1*10^{-5}$

[a)] The ionic radii for the fourfold coordinated Mn^{2+} cations in A sites of the tetragonal double double perovskites is 0.66 Å. The conventional higher coordination of Mn in the A-site disordered configuration stabilizes r = 0.96 Å.

It is also remarkable that SbO_6 and MnO_6 appear to show considerably different tilts for both modifications. The results obtained from the use of equation *Eq. #bla* of Apendix I, are summarised in Table 5.12. Higher values have been found for SbO_6 octahedra, but the averaged MnO_6/SbO_6 Φ_+ and Φ_- values are close to those determined from the $< B - O_n - B' >$ angles shown in Table 5.11. The trend of this evolution is that expected considering that the determination of the tilt angles from atomic positions is directly related to the difference between the expected and the experimental M-O distances, which are farther altered for M = Mn than for Sb, thus originating higher tilt angles for the more regular SbO_6 octahedra. The octahedral distortions (Δ) are also shown in Table 5.11, where their evolution upon substituting R for progressively smaller cations can also be observed: they increase from R = La to Sm despite the apparent higher symmetry of $MnSmMnSbO_6$, thus revealing an increasing distortion of the DDPv structure. After the phase transition into the monoclinic DPv derivative both octahedra become less distorted, achieving magnitudes comparable to those of Mn_2MSbO_6 (M = Cr, Fe, Sc) DPv [31–33].

Table 5.12. Independent tilt angles (º) of MnO_6 and SbO_6 octahedra in $MnRMnSbO_6$. In-phase and out-of-phase tilt angles (Φ_+, Φ_-) are labelled as a function of their propagation direction (ϕ along [001] and θ along [110] and [$\bar{1}$10]) and of their mediating oxygen (O_n mediates for ϕ_n and θ_n).

	Φ_-			Φ_+						
R	ϕ_1 (Mn)	ϕ_1 (Sb)	ϕ^*	θ_2 (Mn)	θ_2 (Sb)	θ_2	θ_3 (Mn)	θ_3 (Sb)	θ_3	θ^*
La	13.85	16.47	15.16	18.09	21.92	20.00	16.92	21.03	18.98	19.49
Pr	16.11	18.88	17.50	21.82	21.53	21.68	16.58	18.38	17.48	19.58
Nd	15.13	18.87	17.00	17.23	21.96	19.60	17.64	19.15	18.40	19.00
Sm	14.69	18.47	16.58	15.36	25.64	20.50	17.78	18.67	18.23	19.37
	Φ_+			Φ_-						
	ϕ_3 (Mn)	ϕ_3 (Sb)	ϕ^*	θ_2 (Mn)	θ_2 (Sb)	θ_2	θ_1 (Mn)	θ_1 (Sb)	θ_1	θ^*
Eu	17.98	21.15	19.57	17.90	22.21	20.05	17.21	18.99	18.10	19.08
Gd	18.00	20.88	19.44	18.66	21.57	20.12	17.22	19.66	18.44	19.28

[*] Note the averaged ϕ and θ values are comparable to the Φ_- and Φ_+ values respectively summarised in Table 5.11 for R = La - Sm compounds and to the corresponding Φ_+ and Φ_- for R = Eu-Gd.

3.2 - Magnetic behaviour

The magnetic behaviour of $MnRMnSbO_6$ compounds has been studied in terms of their temperature dependent magnetic susceptibility and field dependent magnetisation measurements. Figure 5.20 shows the thermal evolution of their direct (left axis) and reciprocal (right axis) susceptibilities and their corresponding fits to the Curie-Weiss law. These plots show a complex magnetic behaviour at low temperatures showing several consecutive magnetic transitions. Some of these transitions account to the presence of small amounts ($\leq 4\%$) of Mn containing compounds as $RMnO_3$ and MnO. Taking into account the magnetic behaviour of these secondary phases, two magnetic transitions can be assigned for most of the $MnRMnSbO_6$ oxides, i.e. R = Pr, Nd, Sm and Eu, attending to the paramagnetic nature of the rare earth element. On the other hand, R = La and Gd containing compounds show a single magnetic transition. This feature is associated to the diamagnetic character of La^{3+} and the absence of magnetic anisotropy of Gd^{3+} cations: the former implies the unique ordering of the Mn^{2+} magnetic sublattice and the latter favours the simultaneous order of R^{3+} and Mn^{2+} spins.

These materials are paramagnetic at high temperatures and the Curie-Weiss fit to 150-300 K reciprocal susceptibility gives negative values of the Weiss constant, pointing to the existence of antiferromagnetic interactions. The experimental paramagnetic moments are in good agreement with the theoretical values, although those of R= La, Pr, Sm and Eu compounds were determined at room temperature due to the presence of magnetic impurities (R = La) or to their frequently temperature dependent moments. The Néel temperatures for these single (T_{N1}) or consecutive (T_{N1} and T_{N2}) transitions have been determined from the first order differentiate of the reciprocal susceptibilities. These differentiates are included as black lines in Figure 5.20. The resulting ordering temperatures are summarised in Table 5.13 along with the fitting results for the Weiss temperature (θ) and the effective magnetic moment ($\mu_{eff.}$). Their expected values ($\mu_{th.}$), saturation magnetisations ($M_{sat.}$) and coercive fields (H_C) from M *vs.* H curves are also included in Table 5.13.

Table 5.13. Ordering temperatures, Weiss constant (θ), effective ($\mu_{eff.}$) and expected ($\mu_{th.}$) moments, saturation magnetisations [a)] and coercive fields (H_C) of $MnRMnSbO_6$ DDPv and DPv polymorphs.

R	T_{N1} (K)	T_{N2} (K)	Θ (K)	$\mu_{eff.}$ (μ_B)	$\mu_{th.}$ (μ_B)	M_0 / $M_{sat.}$	H_C (T)
La*	48	____	____	____	8.37	0.95 /____	0.02
Pr*	89	75	____	____	9.12	1.5 / 1.85	0.08
Nd	76	42	-80	8.9	9.14	1.2 / 2.1	0.20
Sm*	80	39	-128	8.3	8.5	0.12 /____	0.40
Eu*	61	38	____	____	9.05	0.30 /____	0.02
Gd	67.5	____	-32	11.1	11.53	5.3 / 5.8	____

[a)] M_0 stands for the remanent moment. * The effective magnetic moments could not ben determined due to the presence of secondary phases (MnO in R = La sample) or moments varying with temperature (R = Pr, Sm and Eu).

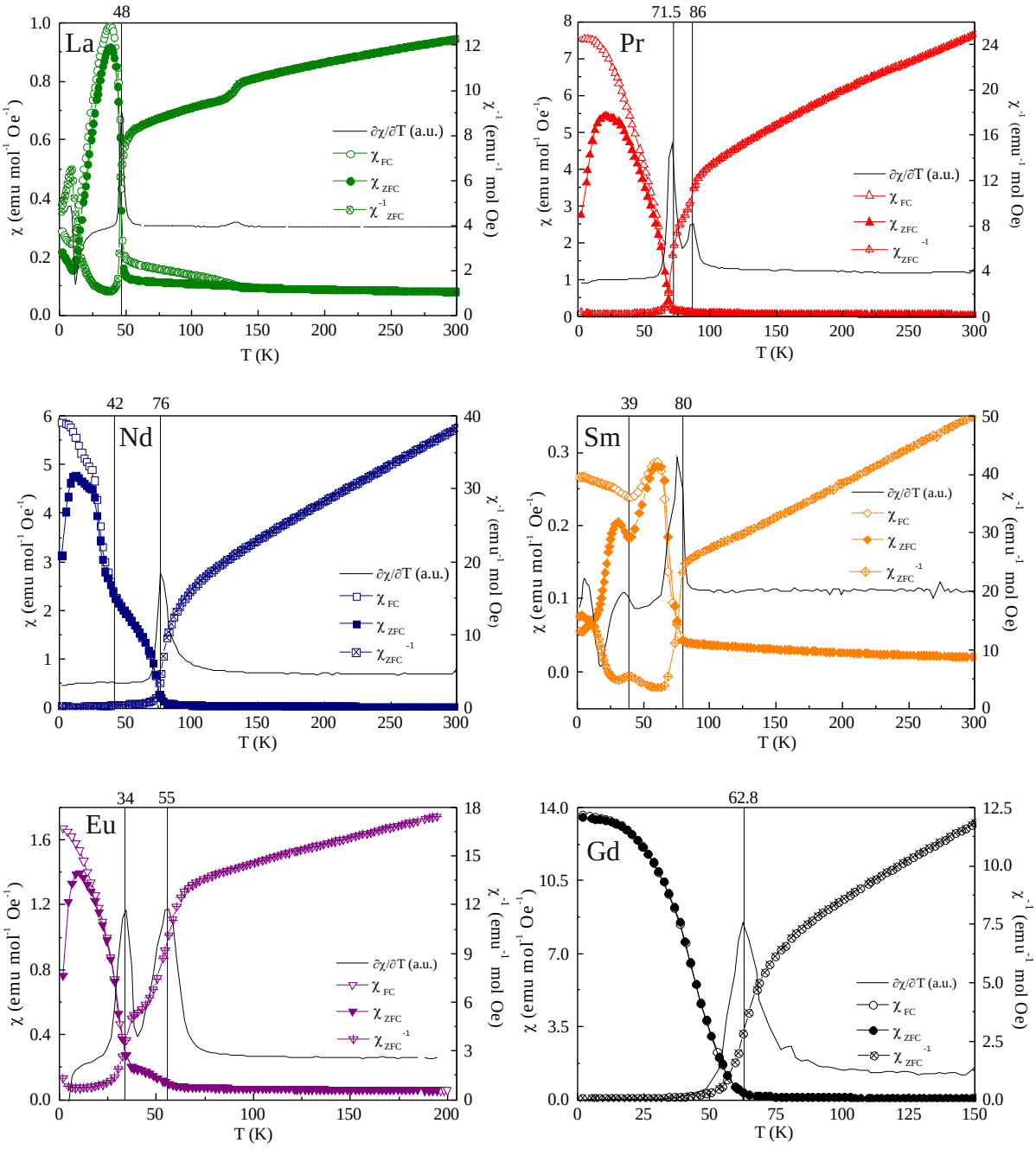

Figure 5.20. Magnetic behaviour of $MnRMnSbO_6$ DDPv and DPv compounds in terms of their direct (left axis) and reciprocal (right axis) magnetic susceptibility. The black line shows the first order differentiate of the χ^{-1} revealing the ordering temperatures.

Figure 5.21 shows the field dependence of the magnetisation of $MnRMnSbO_6$ at 2 K. A common feature observed for all the compounds is the presence of a net ferromagnetic component at 2 K, which agrees with their discussed susceptibility measurements.

Starting from $MnLaMnSbO_6$ compound, Mn^{2+} is the only paramagnetic cation at both A- and B-sites of the DDPv structure. Taking into account the small remanent moment (~ 0.95 μ_B) and the shape of the M *vs.* H plot, AFM behaviour with a small canting angle of the Mn spins may operate at low temperatures. This magnetic behaviour has been confirmed by the determination of the magnetic structure through NPD techniques. As it will be further discussed below, there exists an AFM ordering between Mn_A and Mn_B - ferromagnetic sublattices within the *xz* plane.

The introduction of a paramagnetic lanthanide increases the complexity of the magnetic behaviour of these perovskites. The M *vs.* H loops of R = Pr and Nd compounds show higher ferromagnetic components than that of the La containing compound, with remanent magnetisation values of 1.5 μ_B and 1.2 μ_B respectively. Both loops show small coercive fields (0.08 T and 0.20 T respectively), with an incomplete wasp-waisted shape that can be attributed to the coexistence of AFM and FM competing interactions [34]. Their saturation magnetisations ($M_{sat.}$ in Table 5.13) show net components that fit with the only contribution of ordered FM moments of the $4f^2Pr^{3+}$(gJ = 3.20 μ_B) and $4f^3Nd^{3+}$(gJ = 3.27 μ_B) cations, thus pointing to the AFM character of the Mn^{2+} sublattice. This hypothesis is further discussed in the magnetic structure determination section where below T_N, Mn^{2+}_A and Mn^{2+}_B spins couple AFM along the *z* axis and Pr^{3+} orders FM along the same crystallographic axis. The magnetic structure of the Nd containing compound at 2K is closely related to that of $MnPrMnSbO_6$, but the spins are located in the *xy* plane. It is interesting to note that $MnNdMnSbO_6$ compound presents a spin reorientation transition strongly influenced by the rare earth magnetic anisotropy, further discussed below

The magnetisation loop of the R = Sm compound does not saturate, what indicates its predominant AFM behaviour. However, a wasp waisted hysteresis loop is also observed at 2 K, resembling those observed for $MnRMnSbO_6$ R = Pr and Nd. Due to the high neutron absorption of Sm^{3+} [2] NPD measurements have not been performed to elucidate the magnetic structure of this compound. However, the magnetic behaviour can be explained if Mn^{2+} sublattices coupled AFM and the FM component arised from the FM character of Sm^{3+} spins, taking the magnetic structures of R= Pr and Nd compounds as a reference. The lower remanent magnetisation of this compound (see M_0 values in Table 5.13) is in good agreement with the theoretical net component associated to the $^6H_{5/2}$ ground term of Sm^{3+} (gJ = 0.71 μ_B).

In order to understand the origin of the AFM interactions, an analysis of the type and relative strength of the different possible magnetic interactions is performed. Table 5.14 summarises the M-O-M superexchange angles occurring among the different crystallographic sites. It is worth noting that the rock-salt order of B sites implies the need for supersuperexchange Mn_B-O-Sb-O-Mn_B pathways and the fourfold coordination of both Mn_A and $Mn_{A'}$ sites prevents their direct interaction, so neither A /A' nor B site Mn^{2+} cations can develop effective magnetic interactions with their equivalent sites. Therefore, the strongest magnetic interactions in these compounds are the A - O - B ones, which occur through angles near 90º, thus favouring their AFM matrix behaviour.

Table 5.14. Angles (º) mediating the main magnetic interactions in the DDPv and DPv structures of $MnRMnSbO_6$ compounds.

R	< R – O_n – Mn_B>			<Mn_A – O_1 - Mn_B>	<$Mn_{A'}$ – O_2 - Mn_B>
	O_1	O_2	O_3		
La	88.8 (3)	85.6 (3)	98.3 (3)	99 (1)	101 (1)
Pr	85.5 (3)	86.5 (3)	101.4 (3)	101.4 (3)	100.8 (3)
Nd	85.6 (3)	87.7 (3)	103.6 (3)	98.9 (3)	96.6 (3)
Sm	87.7 (4)	83.8 (4)	104 (1)	98.5 (4)	86 (1)
Eu	111.7 (3)	93.6 (3)	99.5 (3)	___	___
Gd	112 (1)	96 (1)	98.6 (3)	___	___

On the other hand, the DPv derivatives of the R = Eu and Gd compounds do not exhibit any significant hysteretic behaviour according to their low coercive fields, which amount to ~ 0.02 T and 7.3 * 10^{-4} T respectively. The magnetisation loop of the R = Eu compound does not saturate, indicating an AFM coupling between Mn-A and Mn-B sublattices, since the ground term of the Eu^{3+} cation ($^7F_0$) does not contribute to the ordered magnetic moment. The small FM component observed in this compound (~ 0.3 μ_B) can be explained in terms of the existence of a rather small canting angle between both Mn-sublattices. The magnetic moment at saturation in the hysteresis loop for the R= Gd compound measured at 2 K takes the value of ~ 5.8 μ_B. Assuming that Mn^{2+}_A and Mn^{2+}_B spins coupled AFM, as in the previous cases, and the net FM component was assigned to the FM ordering of Gd^{3+} spins, the saturation moment is smaller than gJ (7 μ_B). Since L = 0 for Gd^{3+}, an incomplete quenching of the angular moment does not exist for this ion taking into account that the ground term of the Gd^{3+} free ion is $^8S_{7/2}$. However, the cation disordering between Mn and Gd at the A site of the perovskite structure may have some influence on the magnetic ordering of both sublattices.

However, the proposed models for these two magnetic structures cannot be experimentally confirmed due to the high absorption of neutron radiation by Eu^{3+} and Gd^{3+} cations [2].

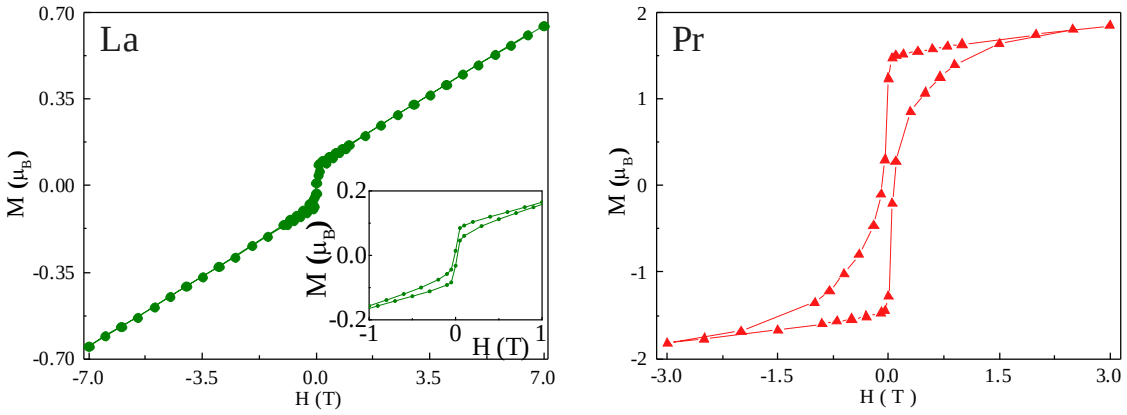

Figure 5.21. Field dependence of the magnetisation of $MnRMnSbO_6$ R = La and Pr DDPv at 2 K. The Figure continues on the next page for the rest of the rare earths.

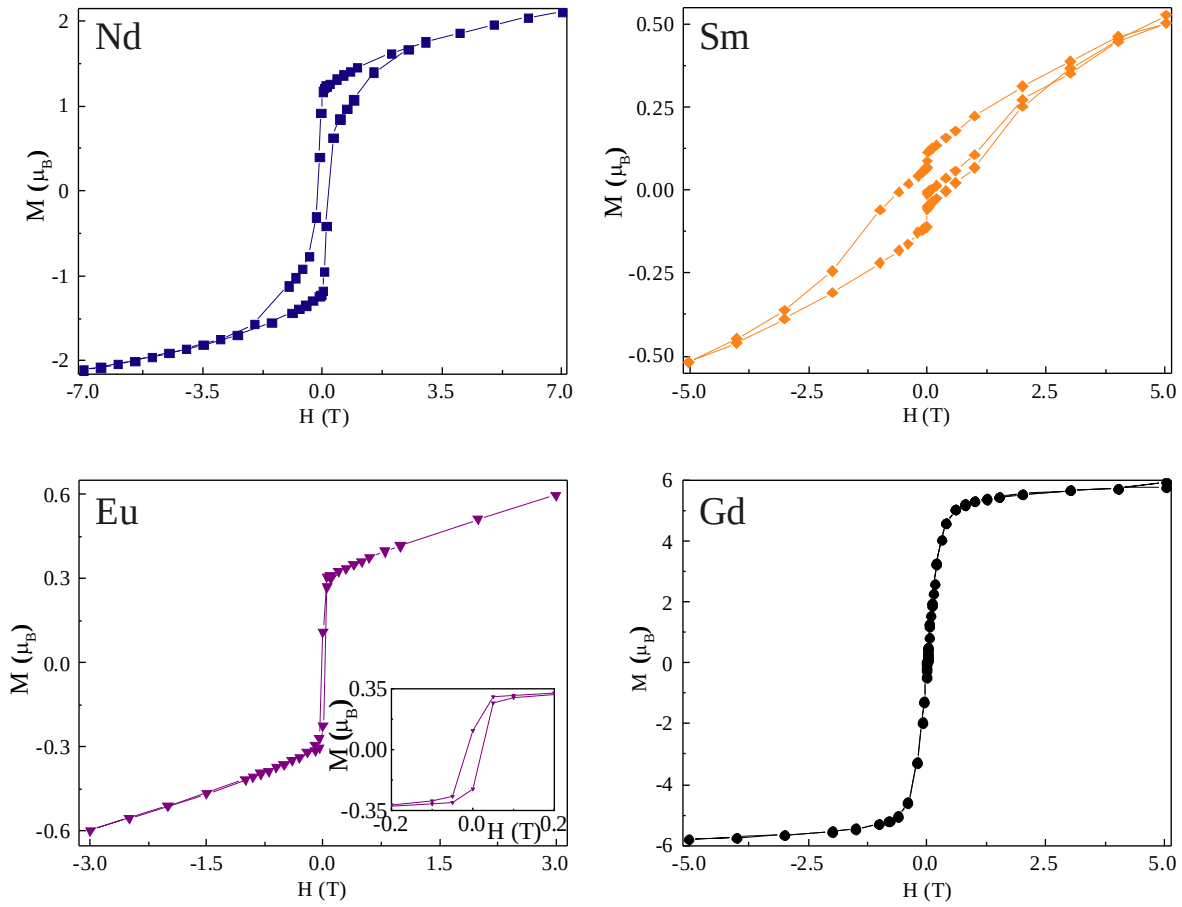

Figure 5.21. Field dependence of the magnetisation of $MnRMnSbO_6$ R = Nd and Sm DDPv and R = Eu and Gd DPv compounds at 2 K.

The magnetic structures of the DDPv modifications of $MnRMnSbO_6$ have been determined from NPD data collected at D20 (R = La and Pr) and WISH (R = Nd) instruments. The low temperature magnetic structures of $MnLaMnSbO_6$ and $MnPrMnSbO_6$ were characterised from the difference patterns obtained from subtracting the diffractograms collected at 80 K and 1.7 K. The high intensity of WISH data allowed the direct refinement of the data collected at 2 K for $MnNdMnSbO_6$ oxide. The patterns of these three compounds show similar magnetic reflections at low temperature but a notable difference can be observed at 3 Å < d < 6 Å region, which can be compared in Figure 5.22: there, a single peak appears for R = Pr but a doublet rises for R = La and Nd. These maxima have been indexed with a propagation vector κ = [0 0 0] as the (020) and (002) for La and Nd compounds and the (020) for Pr. Therefore, both Mn^{2+} and Pr^{3+} spins must be confined to the *z* axis in $MnPrMnSbO_6$. On the other hand the magnetic intensity of both magnetic peaks in $MnLaMnSbO_6$ and $MnNdMnSbO_6$ indicates that the spins must have a contribution along the *x* axis. However, under this constraint they could be oriented either parallel to the *x* axis or confined to the *xz* / *xy* planes, as the presence of a component along *x* already means the existence of a component perpendicular to both *y* and *z* directions.

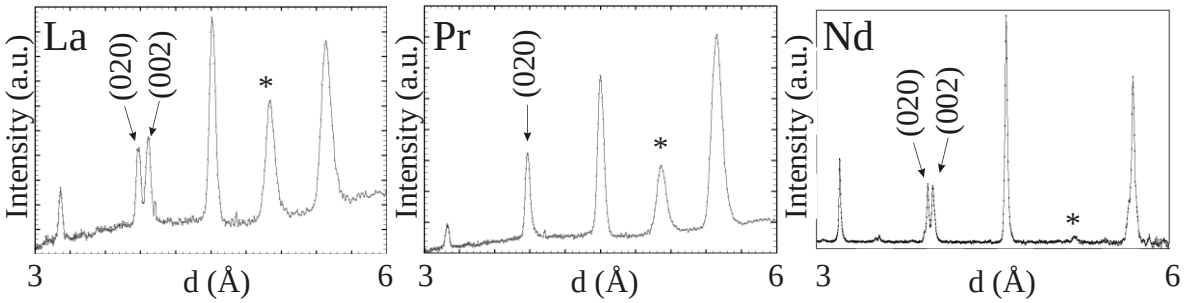

Figure 5.22. Compared low temperature NPD data for $MnRMnSbO_6$ R = La, Pr and Nd DDPv modifications focussed in the d = 3 Å - 6 Å region. The presence of both (020) and (002) magnetic peaks is observed for R = La and Nd, while only the (020) is present in the R = Pr compound. The asterisk identifies the main magnetic peak of the secondary MnO phase.

The symmetry analysis performed with BasIreps software [35] for $P4_2/n$ space group and [0 0 0] propagation vector yields a complex result including a number of different Ireps for each magnetic site ($Mn_{A}/_{A'}$, Mn_B and R), which are summarised in the a) part of Tables 5.15 – 5.17.

The $Mn_{A/A'}$ sites can follow six possible Ireps of individual Basis Vectors (BV), among which Γ_1, Γ_3 and Γ_7 stand for a FM alignment of the spins along the *z* direction (Γ_1) and confined to the *xy* plane (Γ_3 and Γ_7), while Γ_6, Γ_4 and Γ_8 describe their AFM behaviour along the same orientations respectively.

Table 5.15. a) Real (Bas R) and Imaginary (Bas I) components of the BV of the allowed Ireps for $Mn_{A/A'}$ magnetic sites of the DDPv polymorph of $MnRMnSbO_6$ with propagation vector κ = [0 0 0]. b) shows the recombined Ireps, where the imaginary components of Γ_3, Γ_4, Γ_7 and Γ_8 have been made real.

Irep / **a)** Symm	Γ_1	Γ_{3a}	Γ_{4a}	Γ_6	Γ_{7a}	Γ_{8a}
x, y, z						
Bas R	004	200	200	004	200	200
Bas I	000	0-20	020	000	020	0-20
-y,x+1/2,z+1/2						
Bas R	004	200	-200	00-4	200	-200
Bas I	000	0-20	0-20	000	020	020
Irep / **b)** Symm	Γ_1	Γ_{3b}	Γ_{4b}	Γ_6	Γ_{7b}	Γ_{8b}
x, y, z						
Bas R	004	400	400	004	0-40	000
Bas I	000	000	000	000	000	040
-y,x+1/2,z+1/2						
Bas R	004	400	-400	00-4	0-40	000
Bas I	000	000	000	000	000	0-40

Table 5.16. a) Real (Bas R) and Imaginary (Bas I) components of the BV of the allowed Ireps for MnB magnetic site of the DDPv polymorph of $MnRMnSbO_6$ with propagation vector $\kappa = [0\ 0\ 0]$. b) shows the recombined Ireps, where the imaginary components of Γ_3 and Γ_7 have been made real.

Irep / **a)** Symm	Γ_1	Γ_{3a}	Γ_5	Γ_{7a}
x, y, z				
Bas R	200 020 002	200 020 002	200 020 002	200 020 002
Bas I	000 000 000	000 000 000	000 000 000	000 000 000
-x+1/2, -y+1/2,z				
Bas R	-200 0-20 002	200 020 00-2	-200 0-20 002	200 020 00-2
Bas I	000 000 000	000 000 000	000 000 000	000 000 000
-y,x+1/2,z+1/2				
Bas R	200 0-20 002	000 000 000	-200 020 00-2	000 000 000
Bas I	000 000 000	0-20 200 00-2	000 000 000	020 -200 002
y+1/2,-x+1,z+1/2				
Bas R	-200 020 002	000 000 000	200 0-20 00-2	000 000 000
Bas I	000 000 000	-200 020 002	000 000 000	020 -200 00-2
Irep / **b)** Symm	Γ_1	Γ_{3b}	Γ_5	Γ_{7b}
x, y, z				
Bas R	200 020 002	400 040 004	200 020 002	000 000 000
Bas I	000 000 000	000 000 000	000 000 000	000 000 000
-x+1/2, -y+1/2,z				
Bas R	-200 0-20 002	400 040 00-4	-200 0-20 002	000 000 000
Bas I	000 000 000	000 000 000	000 000 000	000 000 000
-y,x+1/2,z+1/2				
Bas R	200 0-20 002	000 000 000	-200 020 00-2	0-4004000-4
Bas I	000 000 000	000 000 000	000 000 000	000 000 000
y+1/2,-x+1,z+1/2				
Bas R	-200 020 002	000 000 000	200 0-20 00-2	0-40040004
Bas I	000 000 000	000 000 000	000 000 000	000 000 000

As shown in Table 5.16, Mn_B-site spins can be completely defined by four three dimensional Ireps describing both their AFM alignment along the *x* (BV 1 of Ireps Γ_1 and Γ_5), *y* (BV 2 of Ireps Γ_1 and Γ_5) and *z* axis (BV 3 of Ireps Γ_3, Γ_5 and Γ_7) and their FM interactions along the *z* directions (BV 3 of Irep Γ_1) and confined to the *xy* plane (BV 1 and 2 of Ireps Γ_3 and Γ_7).

Concerning the R magnetic site, the Ireps needed for its complete description (summarised in Table 5.17) are closely related to those detailed for the $Mn_{A/A'}$ sites. The main difference is that the higher degree of freedom featuring R implies its higher multiplicity, what yields two noteworthy facts: i) two additional Ireps are now needed to describe the AFM behaviour along the *z* axis and ii) the Ireps describing the confinement of spins to the *xy* plane need a second BV.

In the a) part of all these Tables 5.15 – 5.17, some imaginary components are included. In order to simplify these complex Ireps by combining them into different Ireps with only real component, Sarah Representational Analysis software [36] was used to perform the symmetry analysis of these DDPv polymorphs as explained in detail in Chapter IV. The resulting Γ_{nb} Ireps are summarised in the b) part of the same tables.

Table 5.17. a) Real (Bas R) and Imaginary (Bas I) components of the BV of the allowed Ireps for R magnetic site of the DDPv polymorph of $MnRMnSbO_6$ with propagation vector $\kappa = [0\ 0\ 0]$. b) shows the complete set of Ireps after the combination of $\Gamma_3+\Gamma_7$ and $\Gamma_4+\Gamma_8$ Ireps, where the imaginary components have been made real.

Irep / **a)** Symm	Γ_1	Γ_2	Γ_{3a}	Γ_{4a}	Γ_5	Γ_6	Γ_{7a}	Γ_{8a}
x, y, z								
Bas R	002	002	200 020	200 020	002	002	200 020	200 020
Bas I	000	000	000 000	000 000	000	000	000 000	000 000
-y,x+1/2,z+1/2								
Bas R	002	002	000 000	000 000	00-2	00-2	000 000	000 000
Bas I	000	000	0-20 200	0-20 200	000	000	020 -200	020 -200
-x, -y, -z								
Bas R	002	00-2	200 020	-200 0-20	002	00-2	200 020	-200 0-20
Bas I	000	000	000 000	000 000	000	000	000 000	000 000
y, -x+1/2,z+1/2								
Bas R	002	00-2	000 000	000 000	00-2	002	000 000	000 000
Bas I	000	000	0-20 200	020 -200	000	000	020 -200	0-20 200
Irep / **b)** Symm	Γ_1	Γ_2	Γ_{3b}	Γ_{4b}	Γ_5	Γ_6	Γ_{7b}	Γ_{8b}
x, y, z								
Bas R	002	002	400 040	400 040	002	002	000 000	000 000
Bas I	000	000	000 000	000 000	000	000	000 000	000 000
-y,x+1/2,z+1/2								
Bas R	002	002	000 000	000 000	00-2	00-2	0-40 040	0-40 040
Bas I	000	000	000 000	000 000	000	000	000 000	000 000
-x, -y, -z								
Bas R	002	00-2	400 040	-400 0-40	002	00-2	000 000	000 000
Bas I	000	000	000 000	000 000	000	000	000 000	000 000
y, -x+1/2,z+1/2								
Bas R	002	00-2	000 000	000 000	00-2	002	0-40 040	040 0-40
Bas I	000	000	000 000	000 000	000	000	000 000	000 000

The Rietveld refinement of the magnetic structures of $MnRMnSbO_6$ DDPv polymorphs thus requires the combination of all these $\Gamma_1 - \Gamma_8$ Ireps into a single matrix. In light of the magnetic susceptibility and magnetisation measurements that point to the existence of a ferromagnetic component, the BV which stand for AFM interactions can be excluded from this analysis. Therefore, only Γ_1, Γ_{3b} and Γ_{7b} are needed for the refinement of the $Mn_{A/A'}$ spins and BV 3 of Γ_1 and BVs 1 and 2 of Γ_{3b} and Γ_{7b} can fully describe both the R and Mn_B sites. The combination of these 13 BV can be summarised, as shown in Table 5.18, into 5 basis functions (Ψ) where Ψ_1 attempt to the alignment of the spins along *z* direction and $\Psi_2 - \Psi_5$ describe the confinement of the spins into the *xy* plane.

Therefore, the determination of these magnetic structures consider the refinement of Ψ_1 for the NPD data which only show the magnetic peaks arising from the order of the spins along the *z* direction, as it is the case of the low temperature data of $MnPrMnSbO_6$ oxide. On the other hand, the combination of Ψ_2 and Ψ_5 or Ψ_3 and Ψ_4 are needed to solve the orientation of spins along the *x* and *y* directions respectively. In a similar manner, the confinement of the spins into the *xz* plane will be governed by the combination of Ψ_1, Ψ_2 and Ψ_5 basis functions. Note that Ψ_3 and Ψ_4 are included in this matrix for being co-Ireps of the related Ψ_2 and Ψ_5, but their mandatory combination for introducing a component along the *y* axis actually describe AFM orders, for which they can also be neglected.

Table 5.18. Recombined matrix including all the possible BV (in real components) of the allowed FM Ireps for the three different magnetic sites (A = $Mn_{A/A'}$, R and B = Mn_B) of the magnetic structures of the DDPv polymorph of $MnRMnSbO_6$ with propagation vector κ = [0 0 0].

Symm and site \ BF		Ψ_1	Ψ_2	Ψ_3	Ψ_4	Ψ_5
x, y, z	A	001	100	0-10	____	____
	R	001	100	010	____	____
	B	001	100	010	____	____
-y,x+1/2,z+1/2	A	001	100	0-10	____	____
	R	001	____	____	0-10	100
	B	001	____	____	0-10	100
-x, -y, -z	A	____	____	____	____	____
	R	001	100	010	____	____
	B	____	____	____	____	____
y, -x+1/2,z+1/2	A	____	____	____	____	____
	R	001	____	____	0-10	100
	B	____	____	____	____	____
-x+1/2, -y+1/2,z	A	____	____	____	____	____
	R	____	____	____	____	____
	B	001	100	010	____	____
y+1/2,-x+1,z+1/2	A	____	____	____	____	____
	R	____	____	____	____	____
	B	001	____	____	0-10	100

Only Mn^{2+} spins contribute to the $MnLaMnSbO_6$ magnetic behaviour, thus simplifying the determination of its magnetic structure. As deduced from the diffraction patterns, the occurrence of (020) and (002) reflections mean the localisation of the spins along the *x* direction or their confinement to *xy* / *xz* planes. Since the basis vectors of Table 5.18 revealed an AFM behaviour of the R and Mn_B sublattices along the *y* axis, the *xy* option can be discarded, so two single options are left. These two possibilities were tested for the 1.7 K - 80 K NPD difference pattern: on the one hand, the single spin contribution along the *x* axis was considered by refining Ψ_2 and Ψ_5 basis functions (Rietveld fit shown in Figure 5.23a); afterwards, these bases were combined with an additional component along the *z* direction through the use of Ψ_1, simulating by that the confinement of Mn^{2+} spins in the *xz* plane. The introduction of this additional component along the *z* axis was not found to improve the refinement. Otherwise, this component could not converge to a detectable value, but it amounts to ~ 0.6 (2) μ_B, which would approximately turn the spins ~ 7º respect to the *x* axis with a 33% of relative error. Moreover, this inaccurate component does not significantly affect the magnetic moment along *x*. On the other hand, Mn^{2+} spins order FM within its sites but coupled AFM along the *x* axis, as depicted in Figure 5.23b. The magnetic moments in the described magnetic structure converge to 5.1 (1) μ_B / Mn^{2+}.

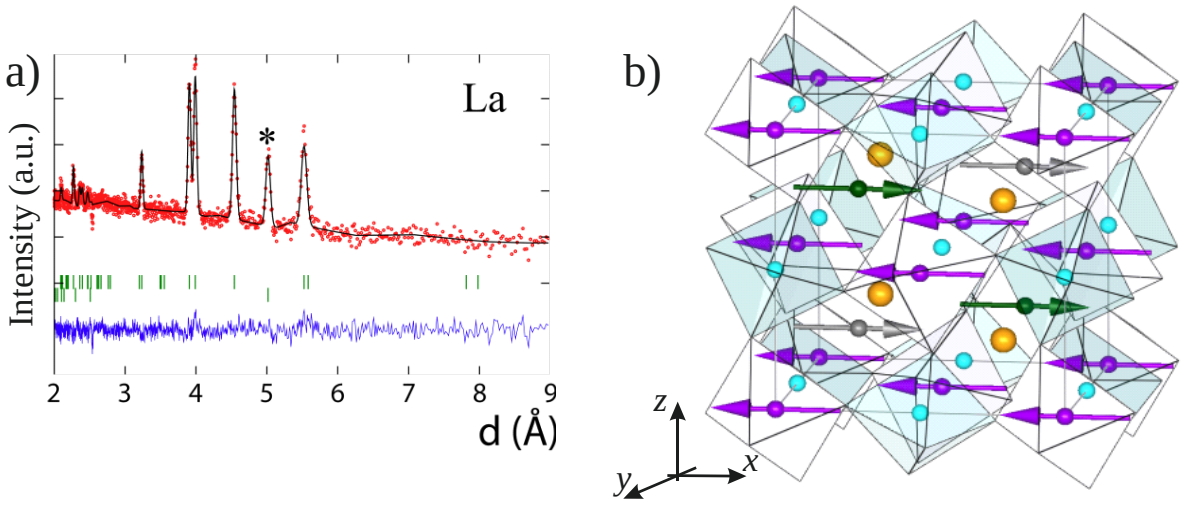

Figure 5.23. a) Rietveld refinement of the 1.7 K - 80 K difference pattern for NPD data collected at D20 for $MnLaMnSbO_6$. The asterisk highlights the ain magnetic peak of the MnO secondary phase. b) Magnetic structure of determined for $MnLaMnSbO_6$ from a). Purple arrows schematise the Mn_B-site spins and the green and grey ones do for Mn_A and $Mn_{A'}$ respectively. Orange spheres stand for La^{3+} cations and the blue ones for Sb^{5+}.

The refinement of the difference pattern of NPD data collected at 80 K and at 1.7 K at D20 for $MnPrMnSbO_6$ (Figure 5.24a - top) was performed using Ψ_1 for the three different magnetic sites since all the spins must be parallel to the *z* axis. Figure 5.24b shows a portion of the magnetic structure, where FM $Mn_{A/A'}$ moments are opposite to those of Mn_B cations along the *z* axis. On the other hand, Pr moments are parallel to Mn_B spins thus originating a net FM component. The refined magnetic moments amount to 5.0 (1) μ_B for Mn^{2+} cations and to 2.2 (1) μ_B for Pr^{3+} spins. The refinement of the complete set of NPD data collected at different temperatures in a sequential mode allowed the study of the thermal evolution of the magnetic moments. The resulting values of the magnetic moments, shown in Figure 5.24a-bottom, gradually increase upon cooling down to 1.7 K below T_N.

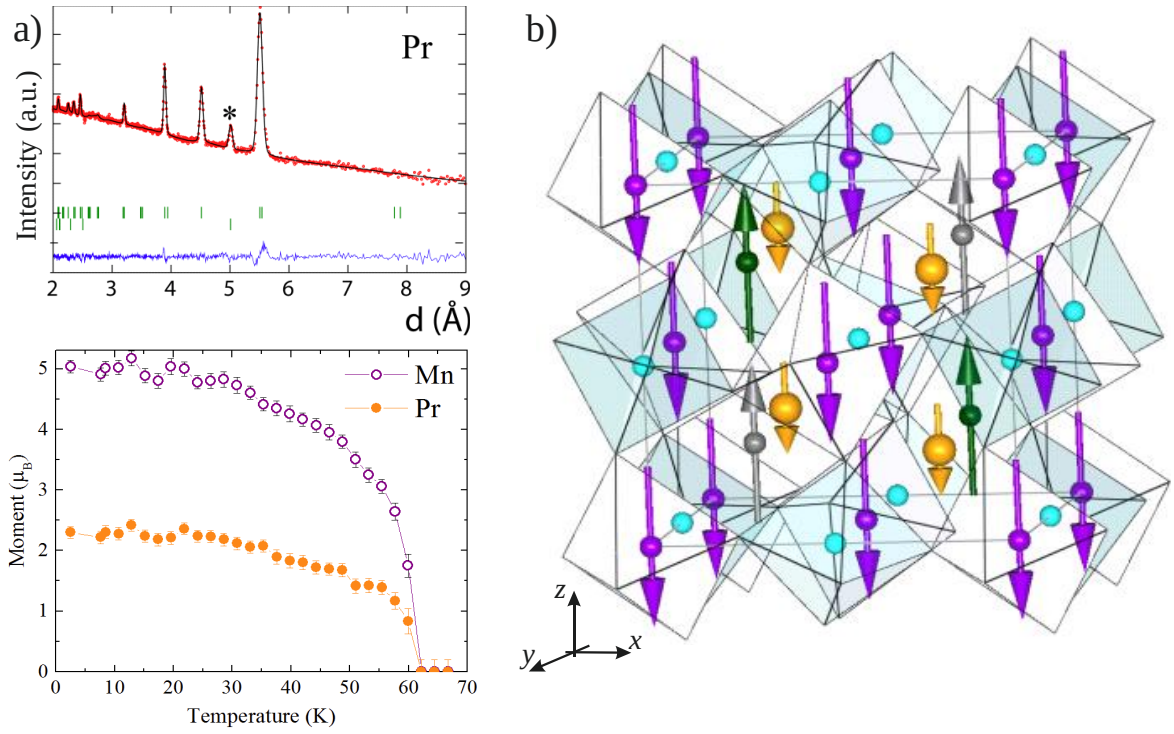

Figure 5.24. a) Rietveld refinement of the 1.7 K - 80 K difference pattern for NPD data collected at D20 for $MnPrMnSbO_6$(top) and thermal evolution of the magnetic moments (bottom). b) Magnetic structure of $MnPrMnSbO_6$ Determined from a). The same colour code used in Figure 5.23 is used here. The introduction of a paramagnetic rare earth gives rise to a net FM (orange arrows)

The determination of the magnetic structure of $MnNdMnSbO_6$ and its thermal evolution were performed in terms of high resolution NPD data collected at WISH instrument at different temperatures. As it has been pointed out before, the low temperature data show a similar profile to that of the related $MnLaMnSbO_6$ oxide, showing the (020) and (002) reflections. However, the diffraction pattern collected at 60 K shows the presence of a single magnetic peak in the 3.9 Å -3.95 Å region, as observed in the $MnPrMnSbO_6$ compound: the thermal evolution of this reflection is highlighted with an arrow in Figure 5.25a at 200 K (top, non-magnetic phase), 60 K (middle) and 2 K (bottom).

In order to determine the magnetic structures of this compound, we have first performed the Rietveld refinement of the NPD data collected at 60 K. Using the magnetic structure of $MnPrMnSbO_6$ as starting model the magnetic intensities quickly fit thus revealing the orientation of the magnetic moments of Mn^{2+} cations parallel to the *z* axis. Otherwise, Nd^{3+} spins do not order at this temperature, so the magnetic structure of $MnNdMnSbO_6$ at 60 K, shown in Figure 5.25b-top, can be described by the AFM coupling of $Mn_{A/A'}$ and Mn_B sublattices. Further NPD measurements performed at low temperatures showed the evolution of the (020) reflection, which progressively splits into two peaks. Figure 5.25c-left shows the superimposed NPD profiles collected at 80 K (red), 60 K (orange), 40 K (black) and 2 K (blue) focussed in the 3.85 Å < d < 4.05 Å range. There, the (020) reflection can be observed to increase in intensity down to 40 K. At this temperature, it has already reached its maximum intensity and the (002) peak has started to grow. Upon cooling down to 2 K, the (002) reflection becomes more intense, while the (020) one decreases back. As pointed out in Chapter III, the occurrence of consecutive magnetic transitions upon cooling is a sign of the development of spin reorientation transitions. The evidence of a spin reorientation from the described thermal evolution of the (020) and (002) magnetic reflections, motivated the Rietveld refinement of the diffraction pattern collected at 40 K, revealing a magnetic moment along the *z* axis and a perpendicular component along the *x* axis. These values are depicted in the right panel of Figure 5.25c, where the left axis shows the independent *x* (μ_x) or *z* (μ_z) contributions of the magnetic moments and the right axis indicates the net angle of Mn^{2+} spins respect to the *z* axis. In order to satisfy the magnetic reflections observed at 2 K, Mn spins must rotate towards the *x* axis, giving rise to a magnetic structure similar to that observed for $MnLaMnSbO_6$ compound. Therefore, the Rietveld refinement of the data collected at 2 K, depicted in Figure 5.25a-bottom, considered Ψ_2 basis function for $Mn_{A/A'}$ sites and Ψ_2 and Ψ_5 bases for Mn_B and Nd magnetic sites. Consequently, the resulting magnetic structure, depicted in Figure 5.25b-bottom, shows all the spins aligned along the *x* axis, where Mn^{2+} spins amount to ~ 4.4 (1) μ_B and those of Nd^{3+} to ~ 1.1 (1) μ_B. Therefore, the order of Nd below T_{N2} in the perpendicular direction to that adopted by Mn^{2+} is the responsible for the spin reorientation observed in this compound.

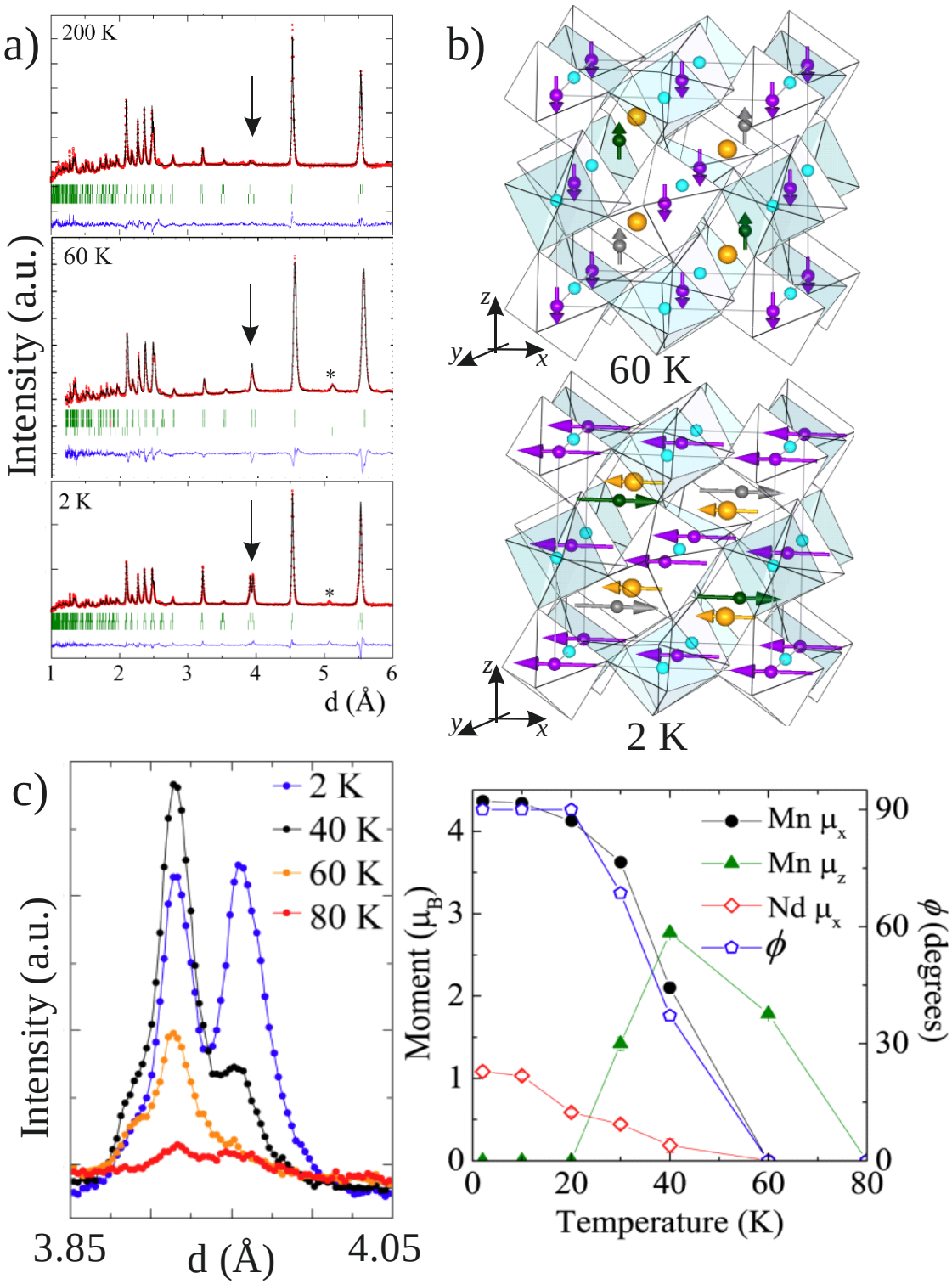

Figure 5.25. a) Rietveld refinements of NPD data collected at WISH instrument for $MnNdMnSbO_6$ at 200 K (top), 60 K (middle) and 2 K (bottom). b) Magnetic structures of $MnNdMnSbO_6$ at 60 K (top) and 2 K (bottom). c) Superposition of the NPD patterns collected at 80 K, 60 K, 40 K and 2K focused in the 3.9 Å < d < 3.95 Å region (left) and thermal evolution of the magnetic moments and their orientation (right).

The different orientation of the spins along *x* or *z* directions for these $MnRMnSbO_6$ oxides is own to the rare earth anisotropy. The magnetic anisotropy of R^{3+} cations is well known to favour either oblate or prolate charge clouds depending on the sign of the so-called second order Stevens coefficient (α_J): $\alpha_J > 0$ induces a prolate charge cloud which favours the orientation of spins parallel to the *z* axis, whereas $\alpha_J < 0$ stands for an oblate cloud supporting the confinement of the spins to the *xy* plane; $\alpha_J = 0$ does not induce any anisotropic behaviour, thus being associated to the spherical symmetry [37].

As a consequence, the easy magnetisation direction for a given rare earth element in hexagonal or tetragonal crystal structures is parallel or perpendicular to the *c* axis, usually attending this criterion. However, the interaction of this charge cloud of the 4f electrons with the electrostatic field of the ions surrounding the rare earth site can also produce a strong crystal field induced anisotropy. This effect depends on the nature of the electrostatic field associated to the point symmetry of the R-site in the hosting structure, i.e. in the crystallographic arrangement of atoms surrounding R, which in tetragonal structures such as that of the DDPv polymorphs of $MnRMnSbO_6$ oxides is defined by the second order crystal field parameter (V_2^o). Therefore, the relative strength of this factor (V_2^o) respect to the specific property of the rare earth (α_J) determines the sign and magnitude of the uniaxial anisotropy constant (K_1) through equation *Eq.14*:

$$K_1 = -\frac{3}{2}\alpha_J V_2^0 \left(r_{4f}\right)^2 \left[3J_z{}^2 - J(J+1)\right] \quad Eq.14$$

where r_{4f} is the ionic radii of the rare earth element and J and J_z are the crystal field splittings at room temperature and at zero temperature respectively. The energy of a given spin state is directly related to K_1 and to the sine of the angle existent between the orientation of the spin and the *z* direction.

The crystal field effect on the R^{3+} cations induces the splitting of its energetic states, which population is governed by Boltzmann statistics. Therefore, an R site subjected to a strong crystal field is often related to a thermally stable spin state (that favoured by the compromise between α_J and V_2^o). Otherwise, R sites under weak crystal fields have various states close in energy, which results in a larger temperature dependence of the net anisotropy. As a consequence, R^{3+} cations located at crystallographic sites with low crystal field effects may be expected to exhibit a reorientation of their easy magnetisation direction upon cooling down the sample. In this context, it is notable the case of R-Fe-B magnets (e.g. $Nd_2Fe_{14}B$), which often show spin-flop transitions at low temperatures and /or under high applied magnetic fields [38–40].

In the case of the DDPv structures of $MnRMnSbO_6$ compounds, three different magnetic behaviours have been found upon substituting R for different rare earths. The La containing compound does not show any anisotropic behaviour, according to the $\alpha_J = 0$ coefficient of La. There, both Mn^{2+} sublattices (that constituted by A / A' cations and that of B sites) align antiparallel to each other, as any d^5-d^5 superexchange correlations favours AFM interactions.

The substitution of La by Pr originates a completely different behaviour. The first remarkable difference is actually the ordering temperature, which rises up near twice as large as that of $MnLaMnSbO_6$.

Pr^{3+} cations are commonly found to exhibit large crystal field effects usually overcoming their small oblate-type anisotropy [41], which justifies the observed magnetic structure of $MnPrMnSbO_6$: the strong crystal field may induce a large splitting of the energetic states resulting in the localisation of

the $4f^2$ electrons in two atomic orbitals which symmetries may only be allow their interaction with B-site cations through the *z* axis. As a consequence, the easy magnetisation direction of Pr turns parallel to *z* and the strong coupling between 3d and 4f electrons orient Mn^{2+} sublattices in the perpendicular direction to that observed for the related $MnLaMnSbO_6$ oxide.

Further substituting La by Nd^{3+} cations, the strong anisotropy of this rare earth overcomes the crystal field splitting, what induces the explained thermal dependence of the anisotropy thus resulting in the expected spin reorientation. In this particular case, Mn^{2+} sublattices order along *z* at lower T_{N1}, due to the re-divergent tilt angles; cooling the sample below T_{N2} induces their strong interaction with the rare earth, which strong oblate anisotropy originates the observed spin reorientation.

4.-Bibliography

[1] Shannon R.D., Prewitt C.T. Effective Ionic Radii in Oxides and Fluorides. Acta Crystallogr. Sect. B-Structural Crystallogr. Cryst. Chem. 1969;B 25:925–46. doi:10.1107/s0567740869003220.

[2] Sears V.F. Neutron scattering lengths and cross sections. Neutron News 1992;3:26–37. doi:10.1080/10448639208218770.

[3] Chardon B., Vigneron F. Mn_3O_4 commensurate and incommensurate magnetic structures. J. Magn. Magn. Mater. 1986;58:128–34. doi:10.1016/0304-8853(86)90132-0.

[4] Mydosh J.A. Spin glasses: An experimental introduction. London & Washinton D.C.: 1993.

[5] Almeida J.R.L. De, Thouless D.J. Stability of the Sherrington-Kirkpatrick solution of a spin glass model. J. Phys. A. Math. Gen. 1978;11:983–90. doi:10.1088/0305-4470/11/5/028.

[6] Pecharsky V.K., Gschneidner J.R.K.A. Magnetocaloric effect and magnetic refrigeration. J. Magn. Magn. Mater. 1999;200:44–56. doi:10.1016/S0304-8853(99)00397-2.

[7] Pecharsky V.K., Gschneidner K.A. Magnetocaloric effect from indirect measurements: Magnetization and heat capacity. J. Appl. Phys. 1999;86:565. doi:10.1063/1.370767.

[8] Pecharsky V.K., Pecharsky V.K., Gschneidner K.A., Gschneidner K.A., Pecharsky A.O., Tishin A.M. Thermodynamics of the magnetocaloric effect. Phys. Rev. B - Condens. Matter. Mater. Phys. 2001;64:1444061–14440613. doi:10.1103/PhysRevB.64.144406.

[9] Entropy variation calculation software n.d.

[10] Pecharsky A.O., Gschneidner K.A., Pecharsky V.K. The giant magnetocaloric effect of optimally prepared $Gd_5Si_2Ge_2$. J. Appl. Phys. 2003;93:4722–8. doi:10.1063/1.1558210.

[11] Palacios E., Tomasi C., Sáez-Puche R., Dos santos-García A.J., Fernández-Martínez F., Burriel R. Effect of Gd polarization on the large magnetocaloric effect of $GdCrO_4$ in a broad temperature range. Phys. Rev. B - Condens. Matter. Mater. Phys. 2016;93:1–8. doi:10.1103/PhysRevB.93.064420.

[12] Bellouz R., Oumezzine M., Hlil E.K., Dhahri E. Effect of Cr substitution on magnetic and magnetic entropy change of $La_{0.65}Eu_{0.05}Sr_{0.3}Mn_{1-x}Cr_xO_3$ (0.05???x???0.15) rhombohedral nanocrystalline near room temperature. J. Magn. Magn. Mater. 2015;375:136–42. doi:10.1016/j.jmmm.2014.09.053.

[13] Arrott A., Noakes J.E. Approximate equation of state for nickel near its critical temperature. Phys. Rev. Lett. 1967;19:786–9. doi:10.1103/PhysRevLett.19.786.

[14] Mira J., Rivas J., Rivadulla F., Vázquez-Vázquez C., López-Quintela M.A. Change from first- to second-order magnetic phase transition in $La_{2/3}(Ca,Sr)_{1/3}MnO_3$ perovskites. Phys. Rev. B - Condens. Matter. Mater. Phys. 1999;60:2998–3001. doi:10.1103/PhysRevB.60.2998.

[15] Burrola-Gándara L.A., Santillan-Rodriguez C.R., Rivera-Gomez F.J., Saenz-Hernandez R.J., Botello-Zubiate M.E., Matutes-Aquino J.A. Comparison of the order of magnetic phase transitions in several magnetocaloric materials using the rescaled universal curve, Banerjee and mean field theory criteria. J. Appl. Phys. 2015;117:1–5. doi:10.1063/1.4918340.

[16] Midya A., Khan N., Bhoi D., Mandal P. 3d-4f spin interaction induced giant magnetocaloric effect in zircon-type $DyCrO_4$ and $HoCrO_4$ compounds. Appl. Phys. Lett. 2013;103:1–5. doi:10.1063/1.4819768.

[17] Dong Q.Y., Ma Y., Ke Y.J., Zhang X.Q., Wang L.C., Shen B.G., et al. Ericsson-like giant magnetocaloric effect in $GdCrO_4$-$ErCrO_4$ composite oxides near liquid hydrogen temperature. Mater. Lett. 2015;161:669–73. doi:10.1016/j.matlet.2015.09.070.

[18] Ramesha K., Sebastian L., Eichhorn B., Gopalakrishnan J. Perovskite and pyrochlore modifications of Pb_2MnReO_6: Synthesis, structure, and electronic properties. Chem. Mater. 2003;15:668–74. doi:10.1021/cm0207494.

[19] ALBA Lightsource n.d. http://www.cells.es/en/beamlines/bl04-mspd.

[20] Campbell B.J., Stokes H.T., Tanner D.E., Hatch D.M. ISODISPLACE: A web-based tool for exploring structural distortions. J. Appl. Crystallogr. 2006;39:607–14. doi:10.1107/S0021889806014075.

[21] Anderson M., Greenwood K., Taylor G., Poeppelmeier K. B-cation arrangements in double perovskites. Prog. Solid State Chem. 1993;22:197–233. doi:10.1016/0079-6786(93)90004-B.

[22] Barnes P.W., Lufaso M.W., Woodward P.M. Structure determination of A_2M_3+TaO_6 and A_2M_3+NbO_6 ordered perovskites: Octahedral tilting and pseudosymmetry. Acta Crystallogr. Sect. B Struct. Sci. 2006;62:384–96. doi:10.1107/S0108768106002448.

[23] Howard C.J., Stokes H.T. Group-Theoretical Analysis of Octahedral Tilting in Perovskites. Acta Crystallogr. Sect. B Struct. Sci. 1998;54:782–9. doi:10.1107/S0108768198004200.

[24] Stokes H.T., Hatch D.M., Campbell B.J. ISOTROPY Tutorial. 2013.

[25] Crystallography TIUO. International Tables for Crystallography Volume A: Space-Group Symmetry. 2005. doi:10.1107/97809553602060000100.

[26] Solana-Madruga E., Arévalo-López Á.M., Dos santos-García A.J., Urones-Garrote E., Ávila-Brande D., Sáez-Puche R., et al. Double Double Cation Order in the High-Pressure Perovskites $MnRMnSbO_6$. Angew. Chemie. - Int. Ed. 2016;55:9340–4. doi:10.1002/anie.201603526.

[27] Mac Tempas X. Version 2.3.7. A program for simulating HRTEM images and diffraction patterns. n.d.

[28] Superflip Package. JANA 2006 n.d.

[29] King G., Woodward P.M. Cation ordering in perovskites. J. Mater. Chem. 2010;20:5785. doi:10.1039/b926757c.

[30] Leinenweber K., Parise J. High-Pressure Synthesis and Crystal Structure of $CaFeTi_2O_6$, a New Perovskite Structure Type. J. Solid State Chem. 1995;114:277–81. doi:10.1006/jssc.1995.1040.

[31] Dos santos-García A.J., Solana-Madruga E., Ritter C., Ávila-Brande D., Fabelo O., Sáez-Puche R.. Synthesis, structures and magnetic properties of the dimorphic Mn_2CrSbO_6 oxide. Dalt. Trans. 2015;44:10665. doi:10.1039/c4dt03849e.

[32] Dos Santos-García A.J., Ritter C., Solana-Madruga E., Sáez-Puche R. Magnetic and crystal structure determination of Mn_2FeSbO_6 double perovskite. J. Phys. Condens. Matter. 2013;25:206004. doi:10.1088/0953-8984/25/20/206004.

[33] Solana-Madruga E., Dos santos-García A.J., Arévalo-López A.M., Ávila-Brande D., Ritter C., Attfield J.P., et al. High pressure synthesis of polar and non-polar cation-ordered polymorphs of Mn_2ScSbO_6. Dalt. Trans. 2015;44:20441–8. doi:10.1039/c5dt03445k.

[34] Stoyanova-Lyubenova T., Dos santos-García A.J., Urones-Garrote E., Torralvo M.J., Alario-Franco M.Á. High-pressure synthesis, structural and complex magnetic properties of the ordered double perovskite Pb_2NiReO_6. Dalton Trans. 2014;43:1117–24. doi:10.1039/c3dt52073k.

[35] Rodríguez-carvajal J. BasIreps: A program for calculating irreducible representation of little groups and basis functions of polar and axial vector properties. 2004.

[36] Wills A.S. A new protocol for the determination of magnetic structures using simulated annealing and representational analysis (SARA h) 2000;278:680–1.

[37] Skomski R., Sellmyer D.J. Anisotropy of rare earth magnets. J. Rare Earths 209AD;27:675–9.

[38] Oesterreicher H., Spada F., Abache C. Anisotropic and high magnetization rare earth transition metal compounds containing metalloids. Mater. Res. Bull. 1984;19:1069–76.

[39] Abache C., Oesterreicher J. Magnetic anisotropies and spin reorientations of $R_2Fe_{14}B$-type compounds. J. Appl. Phys. 1986;60:3671–9. doi:10.1063/1.337574.

[40] Coey JMD. New Permanent Magnet Materials. Phys. Scr. 1987;T19:426–34.

[41] Sachidanandam R., Yildirim T., Harris A.B., Aharony A., Entin-Wohlman O. Single-ion anisotropy , crystal-field effects , spin reorientation transitions , and spin waves in R_2CuO_4 , R ⁄ Nd , Pr , and Sm …. Phys. Rev. B 1997;56:260–86. doi:10.1103/PhysRevB.56.260.

VI.- Conclusions

The Mn_2MSbO_6 (M = Cr, Fe and R- Rare earth element) family of oxides has been studied. Their synthesis under different pressure conditions has provided access to different polymorphs, which structural characterisation in terms X-ray and neutron diffraction techniques revealed the coherent evolution of the structural features as a function of the M^{3+} cation size. Moreover, the relation between these structural features and the magnetic properties has been established through the compared magnetic behaviour of the isostructural compounds with different compositions. The main conclusions arising from the obtained results are summarised as follows:

- The relatively small ionic radius of Mn^{2+} requires high pressures to be stabilised at highly coordinated crystallographic sites. However, the introduction of the much larger R^{3+} lanthanide cations, which necessarily locates at the biggest cation position thus mixing with Mn, increases the averaged ionic radii of the A-site cations. This feature has allowed the preparation of a new series of compounds with pyrochlore structure at room pressure conditions 1523 K. The discussed low stability of Mn^{2+} at the large A sites of this structure has been found to originate an unexpected stoichiometry, determined as $Mn_{0.66}R_{1.34}Mn_{0.66}Sb_{1.34}O_7$. It is notable that this composition hosts the highest proportion of Mn^{2+} at the A site of a non-deficient $A_2B_2O_7$ pyrochlore derivative up to date (33%). It is also interesting that these compounds are extremely stable under heat, pressure, oxidising and even reducing environments.

The well-known geometric frustration of the tetrahedral lattice adopted by the pyrochlore structure coupled to the mixed 2+ and 3+ oxidation state of Mn and the presence of rare earth elements, gives rise to strongly frustrated magnetic systems. As a consequence, exotic magnetic properties are observed in these compounds, including spin-glass behaviour and a large magnetocaloric effect which rises up to 20.7 J /K kg for the R = Gd containing compound.

- On the other hand, the substitution of M by smaller transition metals does only originate a Mn_2MSbO_6 room pressure polymorph in the case of M = Sc. This room pressure phase is centrosymmetric ($R\bar{3}$) with disordered cations into a single crystallographic position and do not show any long-range magnetic interactions. Although the use of smaller $3d^n$ transition metals do not originate any room pressure polymorph, but the thermal treatment only yields a mixture of undesired oxides, the synthesis of these Mn_2MSbO_6 under high pressure and high temperature conditions leads to the isolation of various polymorphs.

- Corundum derivatives are stabilised under moderate pressure conditions, i.e. 3 GPa – 5 GPa. Among them, different ordered derivatives have been characterised depending on the relative size and charge mismatches of the involved cations. In this context, ilmenite-type structures ($R\bar{3}$) are formed for M = Cr and Fe. These compounds show alternated layers constituted by Mn and disordered M/Sb octahedra. The complex nature of the magnetic interactions in this structure includes direct and superexchange correlations between Mn-Mn, M-M and Mn-M. The competition of some of these interactions, which are all favoured to be AFM, originate the appearance of incommensurate helical magnetic structures below T_N ~ 60 K and T_N ~ 260 K in the case of M = Cr and Fe respectively. It is worth noting that, although the small value of the propagation vector of ILO_Mn2FeSbO6 (κ = [0 0 0.07]) prevented its determination down to relatively low temperatures (T_{N2} ~ 55 K), the large frustration of these systems has been found to induce the thermal dependence of the propagation vector of ILO_Mn_2CrSbO_6, which varies from κ_{HT} = [0 0 0.46] to κ_{LT} = [0 0 0.54].

- Upon substituting M by the larger Sc^{3+} cation an additional cationic order is induced, thus crystallising with the Ni_3TeO_6-type structure (*R*3), where the alternated (00z) layers are constituted by ordered Mn/Sc and Mn/Sb. The further cationic order in this corundum derivative

breaks the inversion symmetry, for which the uncompensated puckering of the cations induces a spontaneous polarisation, estimated in 28.3 $\mu C/cm^2$. An unexpected net FM component has been found in this compound to arise below $T_N \sim 42$ K from an unusual site-selective antisite disorder (12.3%), what coupled to the mentioned polarisation turns this compound into a potential multiferroic material.

- It is also worth noting that the long-range centrosymmetric ilmenite polymorphs can also be expected to break the local symmetry under an applied magnetic field coupled to the development of a helical magnetic structure. This possibility, which unfortunately has not been studied along this dissertation, could imply the finding of multiferroicity of spin origin. This potential multifunctionality, achievable at unprecented temperatures in the case of the ferrimagnetic Mn_2FeSbO_6 compound ($T_N \sim 260$ K), could set the basis for a new pathway in the search for multifunctional materials.

- The synthesis of Mn_2MSbO_6 under higher pressure conditions (8 GPa – 13 GPa) induces the crystallisation of perovskite derivative polymorphs. These compounds show conventional B-site rock-salt ordered double perovskite structures for M = Cr, Fe, Sc, Eu and Gd. The substitution of M for larger rare earths has been found to stabilise a new type of doubly ordered perovskite derivative combining the rock-salt order of Mn^{2+} and Sb^{5+} at the B sites with an unusual columnar order of Mn^{2+} and R^{3+} at the A sites. Moreover, it is worth noting that these $MnRMnSbO_6$ (R = La, Pr, Nd, Sm) are not only the first double – double – perovskites showing this type of combined order but also five independent cation sites, three of them occupied by Mn in tetrahedral, square planar and octahedral coordinations.

- Regarding the magnetic properties and the magnetic structures of these high pressure polymorphs, both simple and complex behaviours have been determined as a function of the nature of the substituted M^{3+} cation. In this context, the $3d^0$ Sc^{3+} has allowed to determine the magnetic behaviour of the Mn^{2+} sublattice, which shows simple AFM interactions below $T_N \sim 23$ K. A similar AFM behaviour is observed for the M = Cr oxide below $T_N \sim 60$ K, where the combination of two AFM sublattices originates a small canting of the spins. The introduction of two extra electrons in M = Fe allows not only the AFM interactions observed for Mn_2ScSbO_6 and Mn_2CrSbO_6 but FM superexchange correlations are also permitted via pσ exchange below T ~ 160 K. The coexistence of these two competing interactions similar in strength but opposite in sign originates a magnetic frustration which translates into the development of an incommensurate helical magnetic structure below the ordering temperature $T_N \sim 55$ K.

- The introduction of lanthanide cations has been observed to induce complex magnetic behaviours attending to the magnetic anisotropy of the rare earths. The magnetic structures of the new $MnRMnSbO_6$ (R = La, Pr and Nd) have been determined from neutron diffraction. All of them show collinear structures with two opposed ferromagnetic Mn^{2+} sublattices and the spins of the paramagnetic R^{3+} cations aligned parallel to one of them. Surprisingly, a spin reorientation process has been found for $MnNdMnSbO_6$ but not for $MnPrMnSbO_6$. This difference is assigned to the competition between the magnetic anisotropy of R^{3+}, which induces the spin reorientation in the case of R = Nd at $T < 42$ K , and their crystal field effect, which large value masks the small anisotropy of R = Pr already coupled to the Mn^{2+} sublattice at ~ 62 K.

Appendix I

Determination of tilt angles in DPv and DDPv polymorphs

It was pointed out in Chapter III that the tilt angles determined for all the DPv and DDPv polymorphs studied in this project are determined from the half difference between the experimental < B - O - B' > angles through different O sites and their ideal 180º value. Provided that the tilt systems can be very complex, combining both in-phase and out-of-phase distortions of different magnitudes along each crystallographic direction [1], this calculation method may look extremely simplified. For instance, it is worthwhile to highlight that the cooperative octahedral rotation strictly defining the tilt angles is related to three pseudo-cubic axes, namely $[001]_C$ (ϕ), $[110]_C$ (θ) and $[111]_C$ (Φ) [2]. However, a single tilt value (ϕ) is often reported for conventional DPv structures. Although this approach has traditionally been used for determining tilt angles of orthorrombic and monoclinic perovskites [3,4], different methods could yield either more accurate tilt angles or acceptable values through a more pleasant process. Consequently, their reliability are now discussed and tested.

Therefore, the main aims of this appendix are to set the structural features which can be used to calculate the tilt angles, discuss the different methods arising from those features and compare the effectiveness of all of them. With this purpose, a general view of the perovskite structure is first considered, with no dependence on the different cationic orders or the $a^-a^-c^+$ *vs.* $a^+a^+c^-$ tilt systems achieved in DPv and DDPv polymorphs respectively.

In this context, since the three described tilt angles are related through structural parameters, all of them can be calculated from i) lattice dimensions, ii) bond angles and iii) the relation between atomic positions. Along this appendix, these three methods are detailed and the reliability of their results is discussed and compared from a generalised point of view, so that the conclusions arising from this discussion are valid for all the DPv and DDPv polymorphs. Further discussion on the particular tilt angles of Mn_2MSbO_6 DPv and $MnRMnSbO_6$ DDPv structures studied in this work is detailed in chapters III - V.

i) As a first attempt to check the magnitude of these tilt angles, the relation among the lattice parameters (see equations Eq.*15*-*Eq.17*) is the easiest and the most direct determination, as only a profile fit of diffraction data should be enough to calculate them. However, it is notable that this method only considers the cell dimensions but not the atomic coordinates, in contrast with the other two methods, which consider the relative location of cations and anions into the unit cell. For this reason, the tilt angles determined from the use of these equations are less accurate, as widely demonstrated for diverse orthorrombic *Pbnm* perovskites [2], and are not always consistent with those determined through the other two methods, as it is the case of the highly distorted DPv structures studied in chapters III and IV.

$$\cos\phi = \frac{a\sqrt{2}}{c} \quad Eq.15 \; ; \cos\theta = \frac{a}{b} \quad Eq.16 \; ; \; \cos\Phi = \frac{a^2\sqrt{2}}{bc} \quad Eq.17$$

ii) The second method determines the cooperative tilting of two corner-sharing octahedra (BO_6 and $B'O_6$), which are connected through an oxygen atom (O_n). For the ideal cubic perovskite *B*- and *B'*- site cations, which are occupied by undistinguishable elements, are perfectly aligned through a single intermediate O atom along the three crystallographic directions, resulting in ideal angles of 180º. On the other hand, the geometric distortion of this cubic structure arising either from atomic displacements or from B / B' cation order, deviates the octahedral tilting angle from this ideal value. The difference between the ideal and the experimental < B - O_n - B' > angles is the sum of both BO_6 and $B'O_6$ octahedral deviations (see Figure A1.1a). However, the mere < B - O_n - B' > angle does not distinguish among the different deviations of B and B' cations from

their ideal sites, but a unique value is obtained for their combination. Therefore, 180º - < B - O_n - B' > is mathematically approximated to the double product of equally tilted BO_6 and $B'O_6$ octahedra, i.e., it is considered twice as large as the individual octahedron tilt about the studied direction, as indicated in equation *2*. The accuracy of the so-calculated tilt angles is better than that of method i), but no differences can still be set for the different types of octahedra through this method. Therefore, equation *2* is ideally suited for B-site disordered perovskites or when similar tilts are expected for both BO_6 and $B'O_6$ octahedra, e.g., conventional orthorrombic *Pbnm* perovskites.

$$\phi = \frac{180^{o} - < B - O - B' >}{2} \quad Eq.4$$

iii) The determination of independent displacements of each oxygen atom (O_n) from their ideal positions provides the most precise values of the octahedral rotations. The global equation for an isolated polyhedron can be deduced through classical trigonometry: ϕ angle is schematised in Figure A1.1b, where it is highlighted in red as the angle formed between the theoretical (th.) and the experimentally observed (exp.) B - O bonds. These bonds can be determined from vectorial calculation as the difference between B and each of the O positions ($O_{th.}$ and $O_{exp.}$). Applying basic trigonometry to the triangle enclosed by $(B\text{-}O)_{th.}$, $(B\text{-}O)_{exp.}$ and $(O_{th}\text{-}O_{exp})$, the general expression for equation *Eq.25* is deduced straightforward:

The first approximation needed is the relation between the theoretical and the experimental B-O distances. Provided that the theoretical value, determined from the sum of the B and O ionic radii, is commonly used as the top limit to define whether B and O are bonded or not, it is reasonable that the enlargement of this theoretical value is not possible. However, from a mathematical point of view the theoretical to experimental shortening can also be thought of as its negative elongation. This approximation allows a simple generalisation of the tilt angle depicted in Figure A1.1c.

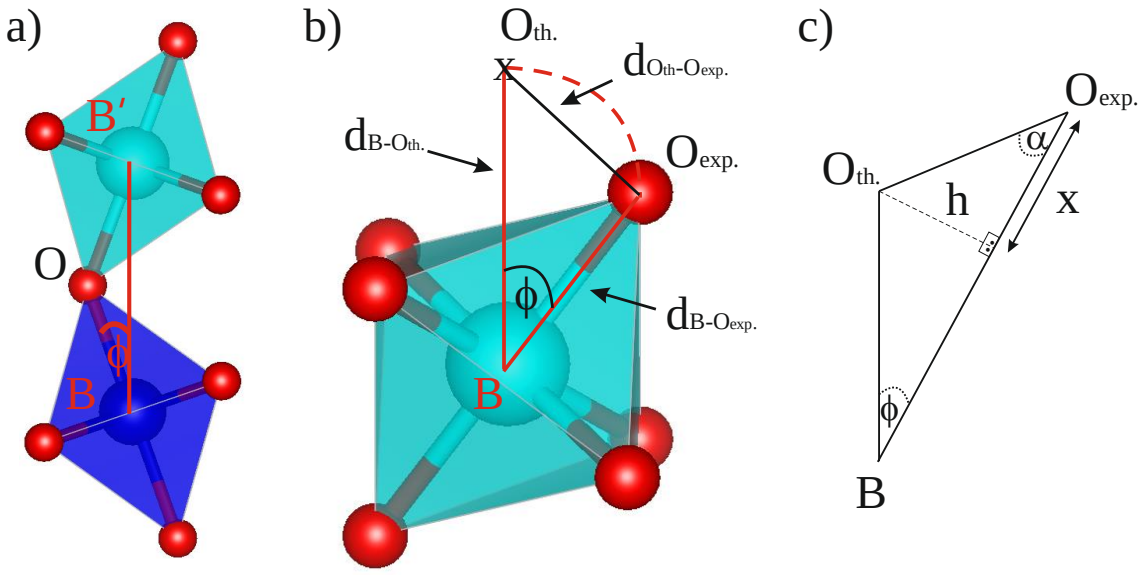

Figure 3.2.Schematic views of the tilt angles as determined through methods ii and iii: a) depicts a common ϕ for BO_6 and $B'O_6$ octahedra while b) and c) the independent tilt for an individual polyhedron. The trigonometric relations between the ϕ tilt angle and the atomic positions of a B-site cation bonded to an O anion is generalised in c) for any Pv derivative (see text for details).

There, using trigonometry one can define the height (h) of the B $O_{th.}O_{exp.}$ triangle as the distance which joins $(B\text{-}O)_{exp.}$ and $O_{th.}$ under a 90º angle. Note that the so-called x segment is the mathematical parameter which will be negative under the shortening of the experimental B-O bond length. The sine and cosine of ϕ (tilt angle) and α (the other acute angle) are defined through equations *bla-bla*.

$$\sin(\phi) = \frac{h}{d(B - O_{th.})} \quad Eq.18 \; ; \; \sin(\alpha) = \frac{h}{d(O_{th.} - O_{exp.})} \quad Eq.19$$

$$\cos(\phi) = \frac{d(B - O_{exp.}) - x}{d(B - O_{th.})} \quad Eq.20 \; ; \; \cos(\alpha) = \frac{x}{d(O_{th.} - O_{exp.})} \quad Eq.21$$

Since both h and x are constants, these four equations can be simplified into two:

$$\sin(\phi) * d(B - O_{th.}) = \sin(\alpha) * d(O_{th.} - O_{exp.}) \quad Eq22$$

$$d(B - O_{exp.}) - \left[\cos(\phi) * d(B - O_{th.})\right] = \cos(\alpha) * d(O_{th.} - O_{exp.}) \quad Eq.23$$

The theoretical and experimental B-O bond distances are known values and the $O_{th.}$-$O_{exp.}$ distance can also be determined from the relation between the expected O position and the real one determined from the Rietveld fit of the high resolution NPD data. Therefore, equations *Eq.22* and *Eq.23* constitute a system of two equations with two unknown parameters (ϕ and α). The trigonometric relation between sine and cosine ($\sin^2(\alpha) + \cos^2(\alpha) = 1$) allows the expression of *Eq.24* equation in terms of sin (α) and sin (ϕ) as:

$$d(B - O_{exp.}) - \left[\left(\sqrt{1 - \sin^2(\phi)}\right) * d(B - O_{th.})\right] = \left(\sqrt{1 - \sin^2(\alpha)}\right) * d(O_{th.} - O_{exp.}) \quad Eq.24$$

Using *Eq.22* to substitute sin (α) into *Eq.24* equation and operating the resulting expression in subsequent steps we can finally express ϕ in terms of the three known parameters in equation *Eq.25*:

$$d(B - O_{exp.}) - \left[\left(\sqrt{1 - \sin^2(\phi)}\right) * d(B - O_{th.})\right] = \left[\sqrt{1 - \left(\frac{\sin(\phi) * d(B - O_{th.})}{d(O_{th.} - O_{exp.})}\right)^2}\right] * d(O_{th.} - O_{exp.})$$

$$d^2(B - O_{exp.}) + \left[\left(1 - \sin^2(\phi)\right) * d^2(B - O_{th.})\right] - 2 * \left[d(B - O_{exp.}) * d(B - O_{th.}) * \sqrt{1 - \sin^2(\phi)}\right] =$$
$$= \left[1 - \left(\frac{\sin(\phi) * d(B - O_{th.})}{d(O_{th.} - O_{exp.})}\right)^2\right] * d^2(O_{th.} - O_{exp.})$$

$$d^2(B - O_{exp.}) + d^2(B - O_{th.}) - \sin^2(\phi) * d^2(B - O_{th.}) - 2 * d(B - O_{exp.}) * d(B - O_{th.}) * \sqrt{1 - \sin^2(\phi)} =$$
$$= d^2(O_{th.} - O_{exp.}) - \left(\sin^2(\phi) * d^2(B - O_{th.})\right)$$

$$d^2(B-O_{exp.}) + d^2(B-O_{th.}) - d^2(O_{th.}-O_{exp.}) = 2*d(B-O_{exp.})*d(B-O_{th.})*\sqrt{1-\sin^2(\phi)}$$

$$\sin^2(\phi) = 1 - \left[\frac{d^2(B-O_{exp.}) + d^2(B-O_{th.}) - d^2(O_{th.}-O_{exp.})}{2*d(B-O_{exp.})*d(B-O_{th.})}\right]^2 \quad Eq.25$$

Equation *Eq.25* relates the tilt angle along a given direction with the expected and real atomic positions. The described mathematical approximations make it applicable for both the axial direction and the equatorial plane of the octahedron. Therefore, both ϕ and θ angles can be determined from equation *Eq.25*.

It is worth noting that the symmetry restraints of a conventional rock-salt ordered *P2₁/n* DPv structure locate B and B' sites at fixed special positions, which also happens for B-site disordered orthorhombic perovskites and for the complex DDPv structures described in chapter V. Nevertheless, the use of equation *Eq.25* must be carefully considered for perovskites crystallising with different symmetries, as each space group localises B, B' and O atoms in different positions. For instance, the equatorial tilt angle (θ) may be differently defined whether directly through one single type of O atom (e.g., in the orthorhombic perovskites) or through two different O_n sites (e.g., tetragonal or monoclinic double perovskites) as the average of two related θ_n values. In this context, note that the name of the axial and equatorial oxygen positions used in the Mn_2MSbO_6 and $MnRMnSbO_6$ monoclinic DPv and tetragonal DDPv derivatives in chapters III-V is different: ϕ angle is defined by O1 or O3 sites for DDPv and DPv polymorphs respectively, and θ angle is defined by the averaged θ_2 and θ_3 angles independently determined through O2 and O3 sites for the DDPv derivative, while θ_1 and θ_2 angles calculated through O1 and O2 sites are averaged for the determination of the equatorial θ tilt angle in the conventional DPv polymorphs.

The three described calculation methods have been used for the determination of the tilt angles of Mn_2CrSbO_6 DPv polymorph in chapter III, in order to compare their reliability. The conclusion arising from those results is that method i) yields diverging results compared to the other two methods. Therefore, as expected it is the worst option, though it provides a tentative magnitude from simple calculations using the lattice parameters, which are accessible from a profile fit. The advantage of the third method is that it provides independent values for both ϕ and θ tilt angles for each type of B / B' sites. This method is the most adequate for complex perovskite derivatives where BO_6 and $B'O_6$ are expected to have very different rotations. For this reason, the independent tilt angles of Mn^{2+} and Sb^{5+} are discussed in chapter V for the $MnRMnSbO_6$ DDPv polymorphs. However, in the case of the monoclinic DPv structures, where both octahedra are rotated under similar angles, method ii) is discussed to be the best option. It results in similar values than those obtained from the most accurate method iii), which determination is tougher: the use of equation *Eq.25* requires the previous calculation of some parameters, including not only the experimental B-O length but also its expected value and the vectorial relation between each of the ideal and real oxygen positions; on the other hand, the tilt determination from method ii) only requires to know the averaged < B - O - B' > angle for applying equation *Eq.4*

AI. 1.- Bibliography:

[1] Glazer A.M. The classification of tilted octahedra in perovskites. Acta Crystallogr. Sect. B Struct. Crystallogr. Cryst. Chem. 1972;28:3384–92. doi:10.1107/S0567740872007976.

[2] Mitchell R.H. Perovskites: Modern and Ancient. Ontario, Canada: Almaz Press; 2002.

[3] Kojitani H., Shirako Y., Akaogi M.. Post-perovskite phase transition in $CaRuO_3$. Phys. Earth Planet Inter. 2007;165:127–34. doi:10.1016/j.pepi.2007.09.003.

[4] Retuerto M., García-Hernández M., Martínez-Lope M.J., Fernández-Díaz M.T., Attfield J.P., Alonso J.A. Switching from ferro- to antiferromagnetism in A_2CrSbO_6 (A = Ca, Sr) double perovskites: a neutron diffraction study. J. Mater. Chem. 2007;17:3555. doi:10.1039/b705797k.

Appendix II

Magnetic interactions in ordered corundum derivatives

The magnetic behaviour of the studied ordered corundum derivatives ILO_ Mn_2MSbO_6 (M = Cr, Fe) and NTO_Mn_2ScSbO_6 were discussed in chapters III and IV respectively. The use of NPD revealed their complex magnetic structures below their respective ordering temperatures. Among these complex structures incommensurate helical spin arrangements and temperature dependent propagation vectors have been found in these ilmenites. The origin of these complex behaviours is explained in terms of the coexistence of competing interactions similar in strength but opposed in sign, giving rise to geometrically frustrated lattices.

The origin of these magnetic behaviours is explained in terms of the wide number of different magnetic interaction paths. A general view of these coexistent interactions can be described from the orbital orientations and their possible interactions. Figure A2.1 shows the four different connexions between the four possible cation sites (which stand for a maximum of four magnetic sites). Two main types of magnetic interactions can be distinguished with no dependence on the nature of the cations that occupy each site: the so-called interlayer interactions (upper panel in Figure A2.1), which take place between face- or corner-sharing octahedra of consecutive (00z) layers, and the so-called intralayer interactions (bottom panel), which develop between two cations located into edge-sharing octahedra within a (00z) layer. It is worth noting that the scheme in Figure A2.1 exemplifies these interactions into an ILO structure, since the simplest 1:1 cation order is considered to occur into parallel A and B (00z) layers. However, this basic model can be used to understand the magnetic correlations of different ordered corundum derivatives, where the maintenance of a common anionic packing can be considered the parental structure and the different cationic arrangements will give rise to interactions of different natures (FM *vs.* AFM) and/or strengths, what will govern the magnetic behaviour of each compound.

In order to understand the discussed interactions, the first step is to identify them in terms of the orbital overlapping. The scope of this Appendix is therefore to set where do the interacting orbitals point, how do they interact and which is the origin of the observed functional evolution.

Regarding this objective, it is worthwhile to remind that the atomic orbitals are split in an octahedral environment into a more stable triply degenerate t_{2g} level and a less stable doubly degenerate e_g one, as a result of the crystal field. This splitting induces the orientation of the e_g (d_z^2 and $d_{x^2-y^2}$) orbitals towards the oxide anions, so that the four M-O bonds constituting the equatorial plane of the octahedron arise from the M $d_{x^2-y^2}$ - O p orbital overlapping and the two axial M-O bonds are formed by the interacting M d_z^2 and O p orbitals.

The corundum parental structure is usually described as an hexagonal closed packing of anions with 2/3 of the octahedral sites occupied by cations so that two consecutive occupied octahedral voids share an edge within the (00z) layer and a face along the *z* axis. The cationic orbitals into those octahedra are oriented, taking into account the discussed crystal field effect, as depicted in Figure A2.1. Two types of connections arise from this anionic array for both intralayer and interlayer interactions. One octahedron is connected to another one from the next (00z) layer through face sharing, which is the nearest neighbour, and to a next nearest neighbour via corner sharing. Concerning the interactions within a common (00z) layer, an octahedron is connected to another three by sharing edges: two of them are oblique edges, which connect the axial oxygen of the octahedra with one of the equatorial plane, while the third one is one of the four edges describing the equatorial plane of the octahedra.

Attending to this classification, the interactions depicted in Figure A2.1 are divided into four quadrants, organised in the same order from the top-left panel to the bottom-right one. Each of

these panels schematises both superexchange interactions through oxygen and direct cation-cation interactions when present.

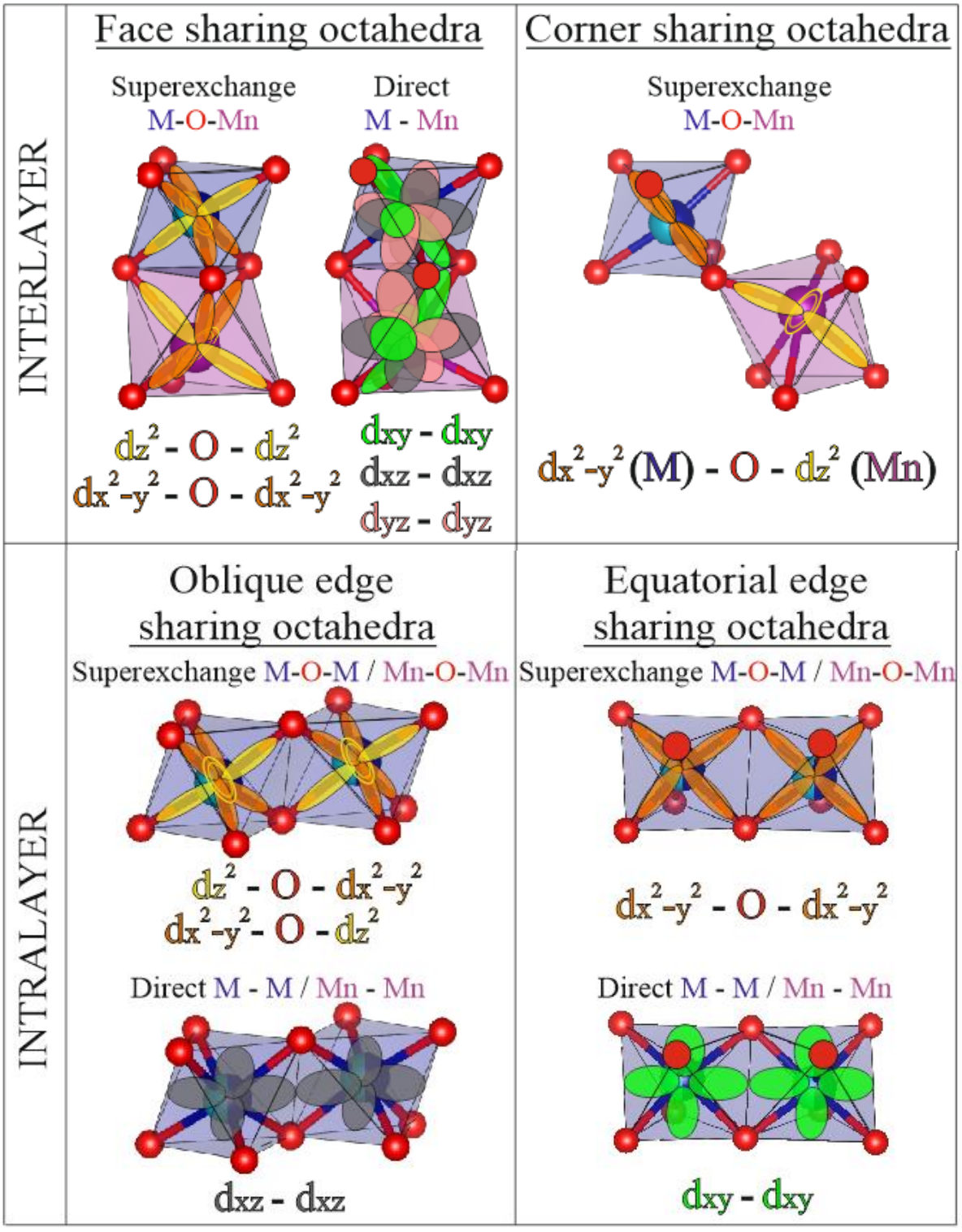

Figure A2.1. Interlayer (up) and intralayer (bottom) connections between all the possible magnetic sites into a corundum derivative structure, where the term *layer* stands for (00z) basal planes. Both superexchange and direct cation-cation interactions are schematised. The former occur via e_g-p(O)-e_g d_{z^2} (yellow) and / or $d_{x^2-y^2}$ (orange) orbitals while the latter imply t_{2g}-t_{2g} d_{xy} (green), d_{xz} (grey) or d_{yz} (pink) direct orbital overlap.

In the ILO type structure, where cations order into alternated (00z) layers, A and B magnetic sublattices are ruled by the so-called intralayer interactions. The interlayer interactions dictate how these sublattices are coupled among them. The magnetic behaviour of both ILO_Mn_2MSbO_6 (M = Cr, Fe) polymorphs can thus be explained from these set of interactions.

The magnetic interaction between Mn^{2+} (purple) and M^{3+} (blue) cations through face-sharing octahedra can be expected to occur via superexchange or direct exchange mechanisms, as both have connected pathways through properly oriented atomic orbitals. As observed in the upper-left panel of Figure A2.1, their indirect correlation via cation-anion-cation superexchange is accessible through three possible paths involving the e_g-e_g electron delocalisation. The d_z^2 (yellow) and the d_x^2-$_y^2$ (orange) orbitals of both M and Mn can interact through the mediation of a p-oxygen orbital. This Mn ($3d^5$)-M interaction at ~ 90º angle, is expected to be AFM for both M = Cr^{3+} ($3d^3$) and Fe^{3+} ($3d^5$) [1]. The empty e_g orbitals of Cr^{3+} ($3d^3$) make this interaction weak for ILO_ Mn_2CrSbO_6.

Otherwise, the half-filled t_{2g} orbitals favouring the direct Mn-M magnetic interaction via d_{xy}-d_{xy} (green) d_{xz}-d_{xz} (grey) and d_{yz}-d_{yz} (pink) direct overlapping originates the AFM coupling of both M = Cr^{3+} and Fe^{3+} cations with the Mn^{2+} sublattice with similar strengths. The direct orbital overlapping of the two interacting cations is much stronger than their superexchange interactions. Therefore, the global interlayer interaction operative in both compounds is the antiparallel orientation of Mn^{2+} and M^{3+} sublattices ruled by their direct relation. The similar sign of both superexchange and direct interactions is cooperative in both cases, which justifies the 200 K decrease observed for the ILO_Mn_2CrSbO_6 ordering temperature respect to that of the isostructural Fe containing compound, according to the weak Mn-O-Cr superexchange interaction.

An additional interlayer interaction is further developed between corner-sharing octahedra. As depicted in the upper-right panel of Figure A2.1, these two octahedral sites are released to show superexchange interactions through their single connecting oxygen. Since the M-O bonds which define these interactions are constructed on e_g metallic orbitals partially overlapping with the p orbitals of oxygen at < Mn - O - M > ~ 120º angle (119.1 (1) º and 118.4 (1) º for M = Cr and Fe respectively), these Mn-M interactions are much weaker and can be considered even negligible compared to those occurring between face-sharing octahedra, especially in the case of M = Cr^{3+}. However, the discussed structural features would favour an AFM behaviour, in agreement with the ruling cation-cation interactions between face-sharing octahedra [2].

The magnetic interactions ruling the magnetic behaviour of each sublattice are depicted in the bottom of Figure A2.1. As advanced, the magnetic nuclei within a lattice are connected through edge-sharing octahedra, among which two types of edges can be distinguished: on the left-hand side of the figure superexchange and direct cation-cation exchange interactions are schematised for the oblique edge-sharing octahedra. A similar scheme is depicted on the right-hand side of the figure for equatorial edge-sharing octahedra.

Both indirect interactions through oxygen involve e_g d_z^2 - d_x^2-$_y^2$ or d_x^2-$_y^2$ - d_x^2-$_y^2$ orbitals. These interactions, which occur through the p oxygen orbitals via ~ 90º angles are AFM in nature for both Mn^{2+} and M^{3+} sublattices. It is notable that these indirect exchanges, along with the direct ones, are diluted in the M^{3+} sublattices as a consequence of the cationic disorder of the paramagnetic $3d^n$ M^{3+} and the diamagnetic $3d^{10}$ Sb^{5+} into a common atomic position. Moreover, the accurate < M - O - M > angles which determine the superexchange correlation of nearest neighbour M^{3+} spins are 98.2 (3)º and 98.0 (2)º for M = Cr and Fe compounds respectively These angles are less favorable than those observed for < Mn - O - Mn > in the Mn^{2+} sublattice,

89.1 (2)º and 90.3 (2)º in the M = Cr and Fe compounds respectively, which are closer to the ideal 90º ruling the AFM behaviour.

On the other hand, as discussed for the interlayer interactions, the superexchange correlations are weaker than the direct cation-cation interactions. In the intralayer case, these interactions involve d_{xz}-d_{xz} and d_{xy}-d_{xy} t_{2g} orbitals, which are half-filled for the three Mn^{2+}, Cr^{3+} and Fe^{3+} cations. This feature makes these interactions relatively strong, which in principle should originate the AFM ordering of both magnetic sublattices in these ILO structures.

Therefore, the detailed mechanisms stand for the AFM behaviour of both magnetic sublattices and their AFM coupling through all the possible interacting pathways. However, it is worth noting that the cationic distribution into the parent corundum structure cannot satisfy the antiparallel alignment of the spins in all the cationic sites. This incompatibility arises from the geometrical frustration schematised in Figure A2.2.

On the one hand, the rhombohedral arrangement of these structures originates hexagonal lattices into (00z) layers, where the centre of each hexagon is an empty octahedron. The AFM behaviour of a single layer is accessible, as depicted in Figure A2.2a, due to the vacant positions. For instance, simple ilmenites such as $MnTiO_3$, where the magnetic sites locate at a single (00z) layer, are reported in the literature to show AFM collinear structures . However, the expected combination of two AFM sublattices stacked along the *z* axis is not possible under this geometry. A similar scheme superimposes in Figure A.2.2b three consecutive (00z) layers, two of them (black and blue ones) belong to the A magnetic sublattice and the intermediate one (red) represents the B magnetic sublattice. The three of them consider AFM intralayer interactions, as those of Figure A2.2.a, and are oriented so that all face-sharing A-B octahedra are AFM. It is this strong interlayer interaction which determines the competition between AFM and FM couplings of similar strengths between A- and B-site corner-sharing octahedra: even though the detailed orbital symmetry favours the cooperative AFM coupling, the described hexagonal geometry necessarily involves the parallel orientation of a B-site spin respect to three alternated corner-sharing A-site spins of each neighbouring (00z) layer. Since all the cationic positions within a layer are undistinguishable in a ILO-type structure, their coexistent FM and AFM alignments to the next magnetic sublattice is geometrically frustrated.

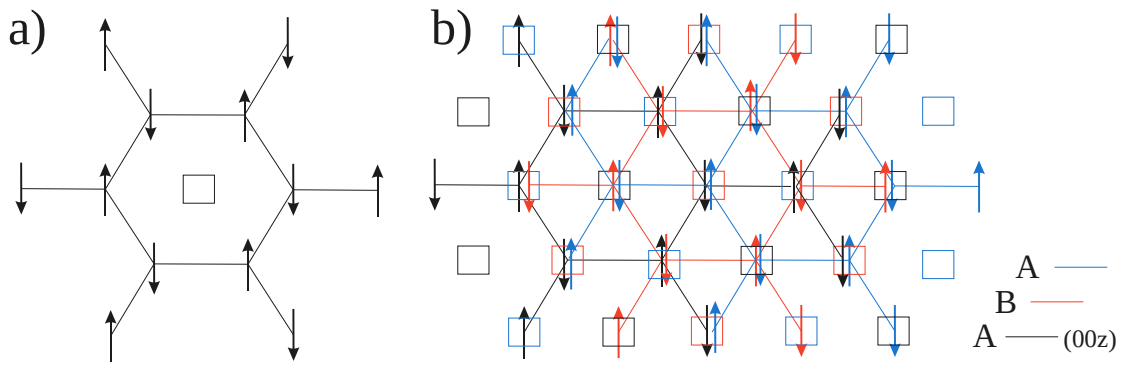

Figure A2.2. a) Scheme showing an AFM order of spins within a (00z) layer in a corundum-related structure. b) shows the superposition of three consecutive AFM layers as that depicted in a). The intermediate (red) layer is constituted by B-site spins while those on top of and below it (blue and black respectively) constitute the A-site magnetic sublattice. A complete antiparallel alignment between A and B sublattices is evidenced to be not possible in this simple scheme, since a red arrow is always parallel to three alternated nearest-neighbour blue and black arrows.

The described magnetic frustration prevents the structure to satisfy all the AFM interactions, what induces the competition between inter- and intralayer exchanges. In this context, their relative strengths are the determinant factor in the net magnetic behaviour of these compounds. On the one hand, the magnetic correlations within a lattice have been identified as relatively strong AFM, since a direct cation-cation t_{2g} orbital overlapping connects each magnetic site with the three edge-sharing octahedra of the same (00z) layer. However, the magnetic dilution effect of the M^{3+} magnetic sublattice makes this behaviour weaker than expected. On the other hand, the direct t_{2g} orbital interaction ruling the interlayer AFM behaviour is much stronger, provided that it is reinforced by three cooperative orbital overlaps among each pair of face-sharing octahedra. Even though the magnetic dilution of the M^{3+} sublattice also affects these interactions, the magnetic frustration induced by the incompatibility of inter- and intralayer behaviours favours the preferential Mn-M coupling due to its discussed stronger character. Therefore, the collinear AFM coupling of Mn^{2+} and M^{3+} FM sublattices observed for the high temperautre magnetic structure of ILO_Mn_2FeSbO_6 polymorph can be stabilised.

However, upon cooling down, the structural features evolve to stabilise the unit cell contraction. In this process, the Mn-M lengths between face-sharing octahedra increase from 2.89 (1) Å and 3.02 (1) Å at room temperature to 2.92 (1) Å and 3.08 (1) Å at 4 K for M = Cr and Fe respectively. Otherwise, the Mn-Mn and M-M distances remain approximately constant (the variation is found in the third decimal number) to the room temperature values: 3.11 (1) Å and 3.01 (1) Å respectively for Mn_2CrSbO_6 and 3.14 (1) Å and 3.05 (1) Å for Mn_2FeSbO_6. These differences weaken the interlayer interactions while keeping the intensity of the intralayer ones. As a consequence both interactions compete, which results in the frustration of the Mn-M AFM coupling and the concomitant rotation of the spins into an incommensurate helix which propagates along the *z* axis.

The propagation vector of this incommensurate structure is evidenced to be strongly temperature dependent for Mn_2CrSbO_6. This finding, accompanied by its larger κ_z value, reveals a much stronger frustration than that of Mn_2FeSbO_6. In this context, it is worth noting that the ordering temperature of the Fe containing compound, discussed to be 200 K higher than that of the Cr containing sample due to the presence of two e_g electrons, is close to room temperature (260 K). This high temperature minimises the competition between the magnetic interactions ruling the magnetic behaviour of each sublattice and their coupling, thus allowing the refinement of the NPD data collected at 150 K under a high resolution mode with the collinear commensurate structure discussed in chapter III. However, the detection of the incommensurate structure at low temperatures with such a small propagation vector (κ_z = 0.07), the small values of the magnetic moments(2.5 μ_B and 3.2 μ_B for Mn^{2+} and Fe^{3+} respectively) and the evidence of the onset of a spin reorientation transition at T ~ 200 K point to a similar behaviour to that observed for Mn_2CrSbO_6: the detected collinear magnetic structure could actually be already incommensurate, with a smaller propagation vector and a slight and non-detectable rotation of spins. Note that the low temperature propagation vector of Mn_2FeSbO_6 stands for a magnetic unit cell ~ 14 times longer than the crystalline unit cell along the *z* axis, in contraposition to the ~ 2 times magnetic cell of Mn_2CrSbO_6. This difference supports the much stronger frustration of the Cr containing compound, which could agree with the proposed similar thermal evolution of ILO_Mn_2FeSbO_6.

The substitution of M by Sc^{3+} discussed in chapter IV induce the preferential crystallisation of a NTO structure, instead of the ILO one acquired by Mn_2MSbO_6 M = Cr and Fe compounds. The diamagnetic character of the $3d^0$ Sc^{3+} cation simplifies the magnetic behaviour to an AFM commensurate structure constituted by a single magnetic lattice. The different cationic distribution in this corundum derivative originates a different definition of the main magnetic interactions, which can anyway be explained on the basis of the same orbital relations depicted in Figure A2.1.

Two independent Mn^{2+} sites are now stabilised, which are discussed in chapter IV to be always located into alternated (00z) layers and sharing their octahedral face with Sb (the so-called Mn1 site) and Sc (Mn2 site). As a result, their only connection among all the described inter- and intralayer interactions is the octahedral corner-sharing one. Therefore, the only magnetic interactions developed in this compound are $3d^5$-$3d^5$ superexchange e_g-e_g delocalisation through oxygen at ~ 90 º angles, which induces the antiparallel alignment of both Mn sites.

The main conclusion arising from this study is the strong dependence of the functional evolution not only on the nature of the constituting elements but also on the structural features. The apparently large differences observed among the isostructural Mn_2CrSbO_6 and Mn_2FeSbO_6 compounds are now justified to arise from similar magnetic behaviours between differently occupied electron configurations. On the other hand, the magnetic behaviour of a differently ordered structural derivative has also been justified in terms of the same interaction pathways. The magnetic behaviour of any corundum derivative polymorph with $A_2BB'O_6$ composition can therefore be predicted from the interplay of these interaction pathways. Moreover, the competition among these wide number of magnetic exchanges can give rise to simple FM or AFM behaviours in simple ABO_3 oxides or to complex frustrated systems for more complex compositions .-

AII.1 – Bibliography:

[1] Goodenough J.B. Magnetism and the chemical bond. 1964:693. doi:10.1016/0029-5582(64)90241-X.

[2] Goodenough J.B. Direct cation- -cation interactions in several oxides. Phys Rev 1960;117:1442–51. doi:10.1103/PhysRev.117.1442.

[3] Wechsler B.A., Prewitt C.T. Crystal structure of ilmenite ($FeTiO_3$) at high temperature and at high pressure. Am Mineral 1984;69:176–85.

Appendix III

Publications arising from this thesis

Magnetic and crystal structure determination of Mn_2FeSbO_6 double perovskite

2013 J. Phys.: Condens. Matter 25 206004

(http://iopscience.iop.org/0953-8984/25/20/206004)

J. Phys.: Condens. Matter **25** (2013) 206004 (6pp) doi:10.1088/0953-8984/25/20/206004

Magnetic and crystal structure determination of Mn_2FeSbO_6 double perovskite

A J Dos Santos-García[1,3], C Ritter[2], E Solana-Madruga[1] and R Sáez-Puche[1]

[1] Departamento de Química Inorgánica, Facultad de Químicas, Universidad Complutense de Madrid, E-28040 Madrid, Spain
[2] Institut Laue–Langevin, F-38042 Grenoble Cedex, France

E-mail: aj2santosgarcia@gmail.com and aj.dossantos@upm.es

Received 18 February 2013, in final form 4 April 2013
Published 25 April 2013
Online at stacks.iop.org/JPhysCM/25/206004

Abstract
The perovskite form of the Mn_2FeSbO_6 oxide has been obtained at 5.5 GPa and 1523 K. X-ray and neutron diffraction data reveal that this compound crystallizes in the monoclinic $P2_1/n$ space group with $a = 0.5234$ nm, $b = 0.5389$ nm, $c = 0.7642$ nm and $\beta = 90.372°$ lattice parameters. AC and DC magnetic susceptibility measurements suggest the existence of a complex magnetic behavior below 200 K. The magnetic structure has been determined and can be described on the basis of an elliptical spiral with an incommensurate propagation vector, $k = [0, 0.426, 0]$, where the magnetic moments of $2Mn^{2+}$ and Fe^{3+} cations are confined to the *ac*-plane.

(Some figures may appear in colour only in the online journal)

1. Introduction

The perovskite-type structure is one of the typical polymorphs exhibited by oxides with ABO_3 stoichiometry. Compounds crystallizing in this structure have been widely studied for a long time due to their interesting physical properties including superconductivity, magnetoresistance, ferroelectricity and thermoelectricity among others [1–5]. From the crystallographic point of view, the ideal crystal cubic structure can be described by a three-dimensional array of corner sharing BO_6 octahedra where the A sites are occupied by larger cations which are surrounded by 12 oxygen anions in cubo-octahedral coordination. However, substitutional derivatives of the 'simple' ABO_3 structure, for instance perovskites in which the substitution occurs only at the B site, e.g. $A(B'_{0.5}B''_{0.5})O_3$, results in perovskites of lower symmetry [6, 7].

In particular, $A^{2+}(Fe_{0.5}Sb_{0.5})O_3$ perovskites have been synthesized at ambient pressure for A = Ca [8] and Sr [9] and at higher pressures for A = Mn [10]. $Ca(Fe_{0.5}Sb_{0.5})O_3$ is an orthorhombic disordered perovskite characterized by the presence of antiferromagnetic Fe-rich islands, and $Sr(Fe_{0.5}Sb_{0.5})O_3$ and $Mn(Fe_{0.5}Sb_{0.5})O_3$ are ordered double perovskites, so the formula can be rewritten as Sr_2FeSbO_6 and Mn_2FeSbO_6 respectively; both were reported to be antiferromagnets [11]. The physical properties of the Mn_2FeSbO_6 phase are of interest, since $S = 5/2$ Mn^{2+} moments can couple directly to the $S = 5/2$ Fe^{3+} states, leading to complex magnetic order. Moreover, the Sb^{5+} is prone to form strongly covalent bonds to oxygens, while Mn^{2+}, being smaller than other divalent A cations, is expected to increase the electron–electron correlations in this compound [12].

We describe here an investigation of the crystal structure and of the magnetic properties of this 'A-site' manganite synthesized under high pressure conditions. The powder neutron diffraction experiments allowed determining the complex magnetic structure of this compound.

[3] Present address: Chemistry and Polymers Department, (EUITI) Polytechnic University of Madrid, C/Ronda de Valencia, 3. E-28012 Madrid, Spain.

Dalton Transactions

PAPER

View Article Online
View Journal

Cite this: DOI: 10.1039/c4dt03849e

Synthesis, structures and magnetic properties of the dimorphic Mn_2CrSbO_6 oxide†

Antonio J. Dos santos-García,*[a] Elena Solana-Madruga,[b] Clemens Ritter,[c] David Ávila-Brande,[b] Oscar Fabelo[c] and Regino Sáez-Puche[b]

Received 15th December 2014,
Accepted 19th January 2015

DOI: 10.1039/c4dt03849e

www.rsc.org/dalton

The perovskite polymorph of Mn_2CrSbO_6 compound has been synthesized at 8 GPa and 1473 K. It crystallizes in the monoclinic $P2_1/n$ space group with cell parameters a = 5.2180 (2) Å, b = 5.3710(2) Å, c = 7.5874(1) Å and β = 90.36(1)°. Magnetic susceptibility and magnetization measurements show the simultaneous antiferromagnetic ordering of Mn^{2+} and Cr^{3+} sublattices below T_N = 55 K with a small canting. Low temperature powder neutron diffraction reveals a commensurate magnetic structure with spins confined to the ac-plane and a propagation vector κ = [1/2 0 1/2]. The thermal treatment of this compound induces an irreversible phase transition to the ilmenite polymorph, which has been isolated at 973 K and crystallizes in $R\bar{3}$ space group with cell parameters a = 5.2084 (4) Å and c = 14.4000 (11) Å. Magnetic susceptibility, magnetization and powder neutron diffraction data confirm the antiferromagnetic helical ordering of spins in an incommensurate magnetic structure with κ = [00 0.46] below 60 K, and the temperature dependence of the propagation vector up to κ = [00 0.54] at about 10 K.

Introduction

Keeping up with the demands of today's society relies heavily on technological innovation and product development. The search for new materials constitutes therefore one of the fundamental aspects of Solid State Chemistry. The studied materials are usually functional, in the sense that they have some practical utility derived from the properties of the solid, that is, magnetism, ferroelectricity, superconductivity, *etc*. Lately, there has been a blossoming of multifunctional materials that combine two or more of these properties. In particular, multiferroic materials combine ferromagnetism and ferroelectricity, thereby allowing the control of a magnetic response through the application of an electric field.[1,2] In this context the most studied compounds are those derived from the archetypal ABO_3 perovskite which may combine two sublattices, one ferroelectrically active (d^o-closed shell cation) and the other magnetically ordered (d^n-open shell cation).[3] The special requirement for the simultaneous presence of closed and open d-shell cations directs the search for new materials displaying both properties.[4] In this sense, high pressure has been widely used to induce phase transformations and synthesize new compounds.[5] Fig. 1 shows a drawing of a set of ABO_3 compounds which, according to their Goldschmidt tolerance factor ($t = (r_A + r_O)/\sqrt{2}\,(r_B + r_O)$) where r_A, r_B and r_O are the ionic radii of A and B cations and oxygen respectively) crystallize with different crystal structures. For the ideal cubic perovskite, t is unity, although diverse distorted perovskite structures of lower symmetry can exist for values greater than

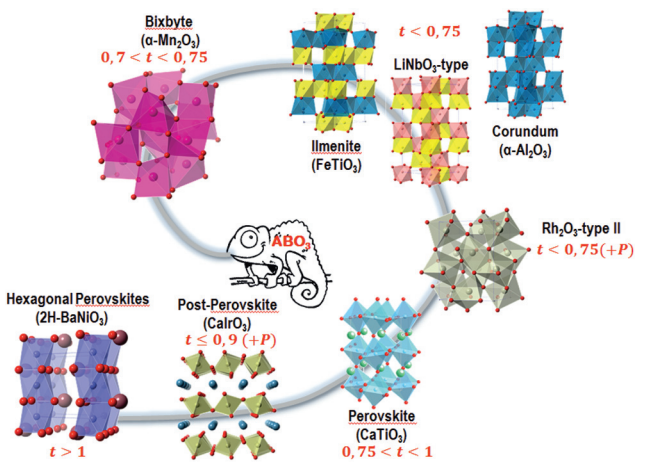

Fig. 1 Symmetry adopted by ABO_3 oxides as a function of Goldschmidt tolerance factor, t. A structural type can also be accessible by high pressure phase transformation (+P).

[a]Departamento de Ingeniería Mecánica, Química y Diseño Industrial, E.T.S.I.D.I, Universidad Politécnica de Madrid, 28012, Spain. E-mail: aj.dossantos@upm.es
[b]Departamento de Química Inorgánica, Facultad de Ciencias Químicas, Universidad Complutense de Madrid, 28040, Spain
[c]Institut Laue-Langevin, 38042 Grenoble Cedex, France

†Electronic supplementary information (ESI) available: XRD data, HRTEM micrographs in different orientations, magnification of the $M(H)$ data for ilmenite compound, reciprocal susceptibility and χT *vs.* T plots as well as different views of the magnetic structures. See DOI: 10.1039/c4dt03849e

Dalton Transactions

PAPER

Cite this: *Dalton Trans.*, 2015, **44**, 20441

High pressure synthesis of polar and non-polar cation-ordered polymorphs of Mn_2ScSbO_6†

E. Solana-Madruga,*[a] A. J. Dos santos-García,[b] A. M. Arévalo-López,[c] D. Ávila-Brande,[a] C. Ritter,[d] J. P. Attfield[c] and R. Sáez-Puche[a]

Received 4th September 2015,
Accepted 12th October 2015

DOI: 10.1039/c5dt03445k

www.rsc.org/dalton

Two new cation-ordered polymorphs of Mn_2ScSbO_6 have been synthesised at high-pressure. At 5.5 GPa and 1523 K Mn_2ScSbO_6 crystallizes in the Ni_3TeO_6-type structure with the polar *R*3 space group and cell parameters a = 5.3419 (5) Å and c = 14.0603 (2) Å. Below T_C = 42.0 K it exhibits ferrimagnetic order with a net magnetization of 0.6μ_B arising from unusual site-selective Mn/Sc disorder and is thus a potential multiferroic material. A double perovskite phase obtained at 12 GPa and 1473 K crystallizes in the non-polar $P2_1/n$ monoclinic space group with cell parameters a = 5.2909 (3) Å, b = 5.4698 (3) Å, c = 7.7349 (5) Å and β = 90.165 (6) °. Magnetization and neutron diffraction experiments reveal antiferromagnetic order below T_N = 22.3 K with the spins lying in the *ac* plane.

I. Introduction

Material properties are dependent upon atomic arrangement and the degree of order can be tailored by controlling the pressure–temperature conditions and bulk composition. At a given pressure *P* and temperature *T*, there are different possible atomic arrangements that correspond to local minima of free energy, the lowest-energy conformation being the thermodynamically-stable phase. However, high pressure and high temperature (HPHT) synthesis conditions may favour higher-energy minima and metastable phases, making them kinetically stable under ambient conditions and therefore recoverable.

Amongst transition metal oxides, HPHT helps to stabilize unusual oxidation states and environments that result in useful properties, *e.g.* the room temperature ferromagnetic metal CrO_2.[1] Moreover, HPHT promotes interesting structural mechanisms. The ilmenite (IL) $FeTiO_3$, for example, crystallizes in the space group $R\bar{3}$ with Fe and Ti stacked into alternate layers along the *c*-axis.[2] It transforms into an unquenchable distorted perovskite (Pv) structure (space group *Pbnm*) at 16 GPa and converts back into a polar $LiNbO_3$-type (LN, space group *R*3*c*) with Fe and Ti cations being ordered in the same layers.[3,4]

Moreover, ABO_3 oxides with Mn^{2+} on the A site are of fundamental interest due to the electronic and magnetic phenomena that emerge from the coupling of spin, charge and orbital degrees of freedom. HPHT conditions are often needed to stabilize $MnBO_3$ materials, *e.g.* perovskite-type $MnVO_3$ with an incommensurate magnetic structure and metallic conductivity,[5] and $LiNbO_3$-type $MnTiO_3$-II with a weak ferromagnetism through anisotropic exchange interactions.[6] The use of HPHT on ordered quaternary systems ($AA'B_2O_6$ or $A_2BB'O_6$) is a relatively less explored area with only a few reports.[7,8] Amongst these, $Mn_2FeB'O_6$ (B′ = Ta and Nb) with a LN-type structure[9] or (B′ = Mo, W) with the Ni_3TeO_6-type (NTO)[10,11] order shows polar and magnetic properties, while Mn_2BSbO_6(B = Fe and Cr) shows polymorphism between the IL- and double perovskite-types (DPv) depending on whether they are synthesized at moderate (3–5 GPa) or higher pressures (5.5–8 GPa).[12,13]

In this work, we present the order–disorder effects on the high pressure polymorphs of Mn_2ScSbO_6 oxide. Mn and Sc cations are randomly distributed in a corundum-related type structure when this material is synthesized under ambient conditions and it shows no long-range magnetic ordering.[14] The double perovskite (DPv) can be achieved with pressures higher than 10 GPa, but below 5.5 GPa the polar NTO-structure is obtained. NTO_Mn_2ScSbO_6 shows an unusual ferrimagnetism due to partial substitution of non-magnetic Sc^{3+} at just one of the two Mn^{2+} sites, whereas DPv_Mn_2ScSbO_6 is antiferromagnetic. Combined X-ray and powder neutron diffraction refinements and electron micro-diffraction experiments confirm the non-centrosymmetry of the NTO_Mn_2ScSbO_6 polymorph allowing a structural polarization that is predicted to

[a]*Dpto. Química Inorgánica, Universidad Complutense de Madrid, Av. Complutense sn, 28040-Madrid, Spain. E-mail: esolana@ucm.es*
[b]*Dpto. Ingeniería Mecánica, Química y Diseño Industrial, Universidad Politécnica de Madrid, C/ Ronda de Valencia 3, 28012-Madrid, Spain*
[c]*Centre for Science at Extreme Conditions and School of Chemistry, University of Edinburgh, Mayfield Road, EH9 3JZ, UK*
[d]*Institut Laue-Langevin, 38042 Grenoble Cedex, France*
† Electronic supplementary information (ESI) available. CCDC 1428909–1428911. For ESI and crystallographic data in CIF or other electronic format see DOI: 10.1039/c5dt03445k

Double Perovskites

International Edition: DOI: 10.1002/anie.201603526
German Edition: DOI: 10.1002/ange.201603526

Double Double Cation Order in the High-Pressure Perovskites $MnRMnSbO_6$

*Elena Solana-Madruga, Ángel M. Arévalo-López, Antonio J. Dos Santos-García, Esteban Urones-Garrote, David Ávila-Brande, Regino Sáez-Puche, and J. Paul Attfield**

Abstract: *Cation ordering in ABO_3 perovskites adds to their chemical variety and can lead to properties such as ferrimagnetism and magnetoresistance in Sr_2FeMoO_6. Through high-pressure and high-temperature synthesis, a new type of "double double perovskite" structure has been discovered in the family $MnRMnSbO_6$ (R = La, Pr, Nd, Sm). This tetragonal structure has a 1:1 order of cations on both A and B sites, with A-site Mn^{2+} and R^{3+} cations ordered in columns and Mn^{2+} and Sb^{5+} having rock salt order on the B sites. The $MnRMnSbO_6$ double double perovskites are ferrimagnetic at low temperatures with additional spin-reorientation transitions. The ordering direction of ferrimagnetic Mn spins in $MnNdMnSbO_6$ changes from parallel to [001] below $T_C = 76$ K to perpendicular below the reorientation transition at 42 K at which Nd moments also order. Smaller rare earths lead to conventional monoclinic double perovskites (MnR)$MnSbO_6$ for Eu and Gd.*

ABO_3 perovskite oxides are a versatile class of materials with many notable physical and chemical properties. Further important variation arises from cation ordering within the basic structural arrangement. A 1:1 cation order in perovskites can occur in (100) layered, (110) columnar, or (111) rock salt arrangements, with cations ordered parallel to the cubic perovskite planes indicated. All three types have been observed for both A-cation-ordered $AA'B_2O_6$ and for B-ordered $A_2BB'O_6$ double perovskites,[1] amongst which layered $AA'B_2O_6$ and rock salt $A_2BB'O_6$ orders are the most common.[2] However $AA'BB'O_6$ "double double perovskites" with simultaneous 1:1 cation order at both A and B sites are much rarer, and only one of the nine possible combinations has previously been reported. This type combines the common (100) A-cation layered and (111) rock salt B-cation orders in several examples, such as $NaLaMgWO_6$ and $NaLaScNbO_6$.[3,4] We report herein a new double double perovskite type that has been discovered as part of an investigation of perovskites with Mn^{2+} ions at A sites.

A^{2+} cations in perovskites synthesized at ambient pressure are typically large, nonmagnetic atoms, such as A = Ca, Sr, Ba, Pb. However, materials with the smaller high-spin Mn^{2+} ion at A sites have been synthesized under high-pressure and high-temperature conditions. This may introduce additional magnetic functionality as found in $MnVO_3$ perovskite which is metallic due to itinerancy of the V^{4+} $3d^1$ states as in $CaVO_3$ and $SrVO_3$, but also has coexisting helimagnetic order of localized $S = 5/2$ Mn^{2+} spins.[5] Several $Mn_2BB'O_6$ double perovskites have also been synthesized at high pressures.[6,7] Mn_2FeSbO_6 has low-temperature incommensurate antiferromagnetic Mn spin order.[8] Mn_2FeReO_6 has a high Curie temperature of 520 K and similar ferrimagnetic and spin-polarized conducting properties to the much-studied magnetoresistive material Sr_2FeMoO_6, but also shows a novel switch from negative to large positive magnetoresistances at low temperatures driven by Mn^{2+} spin ordering.[9,10] In contrast, Mn_2MnReO_6 (Mn_3ReO_6) shows successive antiferromagnetic ordering transitions for Re and Mn spins at 99 and 109 K, respectively.[11] Our subsequent investigation of possible rare earth (R) double perovskites Mn_2RSbO_6, reported herein, has led to the discovery of a new double double perovskite type for $MnRMnSbO_6$ with large R cations, as well as more conventional (MnR)$MnSbO_6$ double perovskites formed for smaller rare earth metal ions.

$MnRMnSbO_6$ materials were synthesized at 10 GPa pressure and 1473 K in a Walker-type multianvil apparatus. Further experimental details are given in the Supporting Information. Small single crystals of $MnNdMnSbO_6$ were separated from the Pt capsule following a slow cooling experiment. Powder X-ray diffraction patterns (Figure 1 a, b) collected at the ALBA synchrotron showed that two different perovskite-related structures are formed, with large cations (R = La, Pr, Nd, or Sm) giving rise to one type of structure, whereas the smaller Eu and Gd centers lead to the formation of a different arrangement. The latter structure was identified as a conventional $A_2BB'O_6$ double perovskite with a typical monoclinic $P2_1/n$ distortion. Mn^{2+} and R^{3+} cations are disordered over the A sites while Mn^{2+} and Sb^{5+} have rock salt order over B and B′ sites.

The new double double $MnRMnSbO_6$ perovskite superstructure adopted by large R cations was solved through X-

[*] Dr. Á. M. Arévalo-López, Prof. J. P. Attfield
Centre for Science at Extreme Conditions (CSEC) and School of Chemistry, University of Edinburgh
Mayfield Road, Edinburgh EH9 3JZ (UK)
E-mail: j.p.attfield@ed.ac.uk
E. Solana-Madruga, Dr. D. Ávila-Brande, Prof. R. Sáez-Puche
Dpto. Quimica Inorganica I, Fac. Quimicas
Universidad Complutense de Madrid
28040 Madrid (Spain)
Dr. A. J. Dos Santos-García
Dpto. Ingeniería mecánica, química y diseño industrial, ETSIDI
Universidad Politécnica de Madrid
28012 Madrid (Spain)
Dr. E. Urones-Garrote
Centro Nacional de Microscopía Electrónica
Universidad Complutense de Madrid
28040 Madrid (Spain)

Supporting information for this article can be found under: http://dx.doi.org/10.1002/anie.201603526. Open data for this article are at: http://dx.doi.org/10.7488/ds/1408.

